POLITECNICO DI TORINO

Master's Degree in Aerospace Engineering

Master's Degree Thesis

Mission Analysis tool completion: Solar indices investigation for Low Earth Orbits and occultations implementation

Supervisor
Prof. Lorenzo Casalino

Thales Alenia Space tutors
Ing. Cosimo Chiarelli
Dr. Valeria Catullo
Ing. Marco Berga

Candidate
Oscar Savarino

December 2019

Page intentionally left blank

Acknowledgements

I would like to thank the main reference figure I had in the company, Dr. Valeria Catullo, who followed me throughout the entire period of the thesis, from the preliminary studies, to the test part and implementation of the occultations in the software, up to the drafting and revision of the written thesis. To her I owe a great deal, her vast experience in the space sector combined with her immense willingness and clear and exhaustive dialectics, has allowed me to increase my wide-ranging knowledge.

I also thank my supervisor at the Polytechnic of Turin, prof. Lorenzo Casalino, for his willingness to check and revise the thesis and for giving me valuable advice on the drafting of the same.

Finally, I would like to mention and thank my office manager, Ing. Cosimo Chiarelli, and Ing. Marco Berga, my second tutor, for their support and for following me during my stay at the company.

Turin, December 5th , 2019

SUMMARY

Page intentionally left blank

1 ABSTRACT

The work of the thesis has been developed in collaboration with Thales Alenia Space Italia during a 7-month internship, from April 1st to November 29th, 2019.

The thesis mainly reports about two topics: the Earth's atmosphere, the empirical models that model it with their solar and geomagnetic indices and their forecast methods, first, and then the occultation of planets and stars by the Moon as seen from the spacecraft's telescopes.

The two topics are involved in a Thales Alenia Space's internal software, named NODES. It is a numerical orbit determination software used for years inside the company in Fortran code, but recently translated into MATLAB language, and used to simulate the spacecraft's orbit when it is influenced by external variable perturbations.

The first topic is particularly important for a Low Earth Orbit Mission Analysis, as the drag is one of the main factors that influences the spacecraft's orbit, and causes the orbit altitude to decay. The drag is strictly connected to the density of the atmosphere that varies based on the layers in which the spacecraft flies; the density is influenced by the solar activity, such as solar flares, for instance, and by the geomagnetic activity. Therefore, models such as Jacchia-Bowman 2006 and Jacchia-Bowman 2008, or NRLMSISE-00, are investigated to find which one has the best performances in modelling the atmosphere's density. In the phase of orbit propagation, it is very important to predict short-term and long-term solar and geomagnetic indices, and that is what is examined, i.e. the forecast method on which the three previous models rely on.

The second topic is a completion of the NODES code in order to improve it. First, the passages of the Moon in the Field of View of the spacecraft’s telescope or Star Tracker, mounted on two different axes of the satellite, were studied; then the occultation of planets or stars by the Moon were studied, during the motion of the satellite on its orbit. In the end, two other scripts were written, one for the observation of the sky, returning which stars and planets are occulted by the Moon during each time step, and the second is to be launched after the main analysis, in a later time, but the scope is always to see if the Moon has occulted any celestial body.

Moreover, a considerable part of the work was dedicated to the software testing in order to find any bugs and to improve its performances. The main focus was on the atmosphere models (Jacchia-Bowman 2006 and Jacchia-Bowman 2008) and how they model the density of the atmosphere layers, paying particular attention to solar maximums and geomagnetic storm events.

2 THALES ALENIA SPACE: THE COMPANY

Thales Alenia Space is the company created by Alcatel Alenia Space after the French group Thales acquired the entire shareholding of the French company Alcatel in the two joint ventures with the Italian holding Leonardo (ex Finmeccanica) in the space sector. The company is the largest producer of satellites in Europe specialized in the aerospace, space, defense, security and transport sectors.

Of the two joint ventures of the so-called French-Italian Space Alliance, Thales Alenia Space represents the side aimed to the space flight manufacturing sector, including project, development, integration, testing and post support - launch of an entire extra-atmospheric system (artificial satellites, interplanetary probes, space observatories, inhabited infrastructures, ...), including the realization of its sub-systems and electronic equipment. The other side is Telespazio, which is oriented to space services.

The holdings of the two groups in the above-mentioned companies are divided as follows:

- Thales Alenia Space is 67% owned by Thales and 33% by Leonardo;
- Telespazio is 33% Thales and 67% Leonardo.

In 2016, Thales Alenia Space had a total of 7980 employees, spread across 14 industrial sites in Europe (France, Italy, Spain, Belgium, United Kingdom, Germany) and in the USA. Of these, around 2100 are located in the 4 Italian sites (Rome, Turin, Milan, L'Aquila). [W1]

3 WHAT IS NODES?

The software NODES (Numerical Orbit Determination for Earth Satellites) has been used in TAS-I for more than thirty years as the baseline software for Mission Analysis activities. More than one mission analyst brought his own contribution to adapt it to the new standards and for the needs of the working projects.

This tool computes the orbital propagation of a spacecraft, given a certain amount of data (position, shape, etc.) and considering the forces due to the external perturbations of the space environment. It focuses only on terrestrial satellites.

Written in Fortran 77 and running on Linux, it uses a Runge-Kutta integrator to solve the system of equations describing the orbital propagation. It needs the standard mathematical library in double precision, IMSLD.

Through the years, many options have been added or updated to the simple propagation, based on the detailed data furnished by specific missions. For instance, ESA GOCE project was strongly pushing for detailed drag computation, ESA INTEGRAL for antenna switching, ASI Symbol X for multiple burns around the apses line, ESA LOFT for satellite axes pointing on predefined stellar sources, etc.

If NODES is one of the most complete, accurate and fastest software for this kind of studies, it is also an ageing tool fully mastered by only several people in the Mission Analysis team and extended to many missions without a good generalization of the processes.

The diversity of the routines – usually several copies of the same function adapted to a specific mission – the oldness of the language, and the needs to update the models – once more – to comply with the latest standards, led to the proposal of a new version of the software, more modern, easier and up-to-date. It was chosen to do it on MATLAB, an easy-to-use environment widely adopted by science and engineering companies, and to leave the restraining Linux. [1]

4 ECSS – SPACE ENVIRONMENT

Figure 4.1 - ECSS logo

ECSS (European Cooperation for Space Standardization) is a cooperative effort of the European Space Agency, national space agencies and European industry associations for the purpose of developing and maintaining common standards to use in all space activities. The ECSS frequently publishes Standards, to which contractors working for ESA must adhere to.

The Standard used for the activity of my thesis is the “ECSS-E-ST-10-04C – Space environment”. This standard forms part of the System Engineering branch (ECSS-E-10) of the Engineering area of the ECSS system. Its first version was published in January 21st, 2000 with the name of ECSS-E-10-04A; the second version was published in November 15th, 2008 with the name of ECSS-E-ST-10-04C – for easiness named ECSS 2008. The version used in this document, named ECSS 2019, is the draft for a future version, probably published by the end of 2019, as a review or update of the 2008 issue. In this way, all the consideration that will be done by taking in account this Standard, should be revised when the publication is effective.

The Standard ECSS-E-ST-10-04C is one of the series of ECSS Standards intended to be applied together for the management, engineering, product assurance and sustainability in space projects and applications. Requirements in this Standard are defined in terms of what shall be accomplished, rather than in terms of how to organize and perform the necessary work. This allows existing organizational structures and methods to be applied where they are effective, and for the structures and methods to evolve as necessary without rewriting the standards.

This standard is intended to assist in the consistent application of space environment engineering to space products through specification of required or recommended methods, data and models to the problem of ensuring best performance, problem avoidance or survivability of a product in the space environment.

The space environment can cause severe problems for space systems. Proper assessment of the potential effects is part of the system engineering process as defined in ECSS-E-ST-10.

This is performed in the early phases of a mission when consideration is given to e.g. orbit selection, mass budget, thermal protection, and component selection policy. As the design of a space system is developed, further engineering iteration is normally necessary with more detailed analysis.

In this Standard, each component of the space environment is treated separately, although synergies and cross-linking of models are specified. Informative annexes are provided as explanatory background information associated with each clause.

This Standard applies to all product types which exist or operate in space and defines the natural environment for all space regimes. It also defines general models and rules for determining the local induced environment.

The natural space environment of a given item is that set of environmental conditions defined by the external physical world for the given mission (e.g. atmosphere, meteoroids and energetic particle radiation). The induced space environment is that set of environmental conditions created or modified by the presence or operation of the item and its mission (e.g. contamination, secondary radiations and spacecraft charging). The space environment also contains elements which are induced by the execution of other space activities (e.g. debris and contamination).

4.1 Gravity

This ECSS tells that for Earth orbits, a model shall be applied that fulfils the following rules:

1. The model is a global and static model;
2. The model is based on GRACE or GOCE data
3. The model is published at: http://icgem.gfz-potsdam.de/tom_longtime
4. The model is described by spherical harmonic coefficients up to at least degree and order of 70.

For example, the EIGEN-GL04C model fulfils given requirements. Developed by C. Förste in 2006, it is based on data coming from Grace and Lageos. It has a spatial resolution in latitude and longitude of 1° × 1° (corresponding to degree × order = 360 × 360). For other planetary environments no standard gravity model exists.

Hereunder there is a graphical representation of the geoid undulations using EIGEN-GL04C model (note that geoid heights are exaggerated by a factor 10.000):

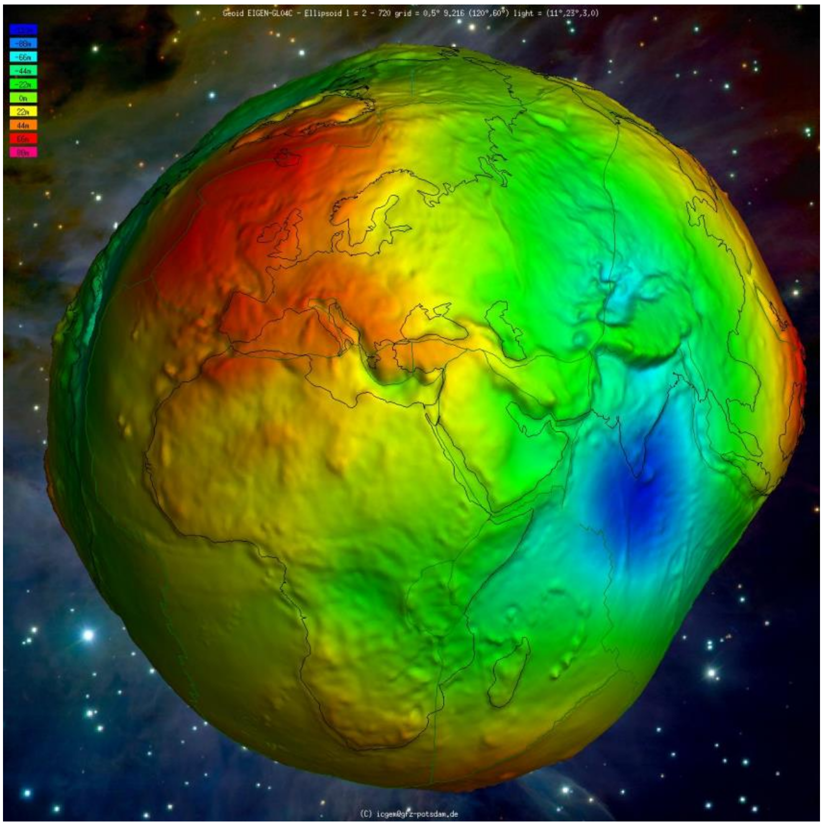

Figure 4.2 - Geoid EIGEN-GL04C (part 1)

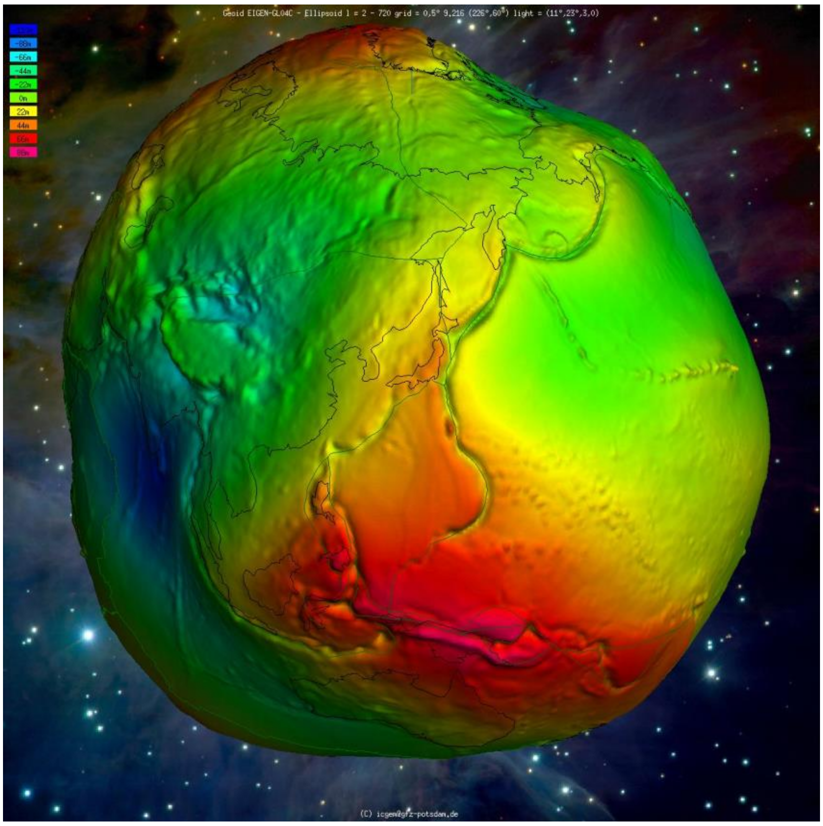

Figure 4.3 - Geoid EIGEN-GL04C (part 2)

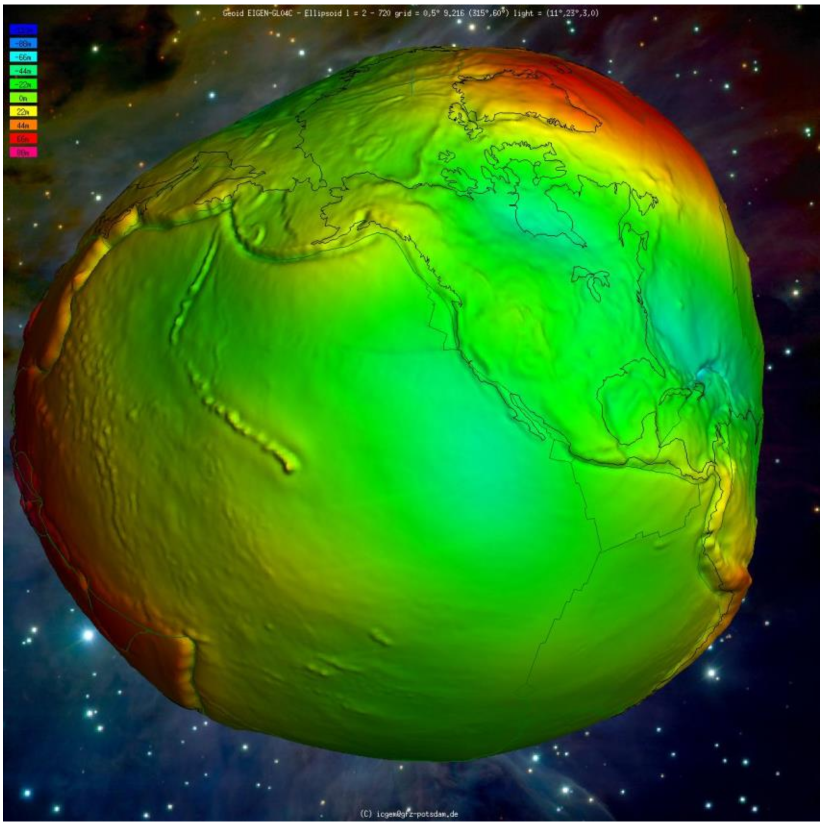

Figure 4.4 - Geoid EIGEN-GL04C (part 3)

Comparing with the ECSS 2008, it was noticed that the model did not change; moreover, while in 2008 this model was mandatory to use, now the standard allows us to choose among other models. However, because of the fact that the NODES software was tested with this model previously and gave acceptable results, it was chosen not to replace it. ECSS 2019 also suggests considering the EIGEN-6C4 model based on GOCE mission data because it has a resolution up to 2190 in degree and order (sub-degree, ~10 km resolution) and it is one of the latest state of the art for gravity model applications.

The Standard gives also other information about.

1. Tides: data on gravitational effects from tides and on Earth orientation parameters shall be obtained from the International Earth Rotation Service IERS;

2. Third body: for third body gravitational perturbations the Development Ephemerides data on planets (DE-430) and the Lunar Ephemerides data (LE-430) shall be used. These two types of ephemerides changed from ECSS 2008, they were numbered 405. For this reason, the new ephemerides have been downloaded and the software was updated.

4.2 Neutral atmosphere

4.2.1 Wind model

The wind model HWM-07 (Horizontal Wind Model) is a comprehensive empirical global model of horizontal winds in the mesosphere and thermosphere (middle and upper atmosphere). It is based on accumulated measurements made using a variety of observational techniques, including satellite, radar, and ground-based optical remote sensing. The model is used to provide the necessary winds, accounting for time, space and geophysical variations, for many ionospheric and dynamical calculations. It provides meridional (+ northward) and zonal (+ eastward) speed and covers all altitude regions. This is the wind model indicated in ECSS 2019 while in the previous Standard had chosen the HWM-93. Although HWM-07 is a new option for the ECSS, NODES code is already updated with this last model, thanks to the foresight of previous developers in keeping the software up-to-date by searching for new model updates. This is also due to the fact that the last wind model dated back to 1993, so it was foreseeable that the ECSS would have replaced it with a newer model as soon as a new standard had been issued. And so it was done. However, ECSS 2019 allows also to use, as an alternative to HWM-07, the HWM-93 model.

4.2.2 Models of Earth’s atmosphere

ECSS 2008 stated that the NRLMSISE-00 model shall be used for calculating both the neutral temperature and the detailed composition of the atmosphere instead the JB-2006 model shall be used for calculating the total atmospheric density above an altitude of 120 km. Moreover, it stated that for altitudes below 120 km, NRLMSISE-00 shall be used for calculating the total air density.

ECSS 2019 instead reports that the NRLMSISE-00 model shall be used for calculating the neutral temperature, the total density and the detailed composition of the atmosphere. It gives also the chance to use another model: in fact it suggests to use the JB-2006 model or JB-2008 model for calculating the total atmospheric density above an altitude of 120 km. It doesn’t mention anything about altitudes below 120 km.

In both documents, ECSS states that the NRLMSISE-00 model for species densities shall not be mixed with the JB-2006 model for total density.

Under these conditions, the following atmosphere partition was chosen:

- For altitudes below 800 km, the NRLMSISE-00 model is used as it calculates the molecular weights of the air components useful for the “free molecular flow” formulation for drag computation; it is more accurate and it calculates the contribution to the drag force of the collisions of air molecules on every elementary surface of the S/C.

- For altitudes above 800 km, the use of JB2006 or JB2008 is preferred because the drag contribution is not such important and the basic formula for drag force computation is sufficient; it thus requires the calculation of the total density only.

This partition seems to be the best and, as the chapter below explains, it was adopted to avoid the problem that the NRLMSISE-00 model diverges at high altitudes; moreover, to better compute density, and thus the drag force, JB2008 model's usage is recommended as it is more accurate than both NRLMSISE-00 and JB2006.

In NODES software, there was left the possibility of choosing all the three models because each of them gives good results.

Owing to these new features, the Technical Note and the User Manual of the NODES software have been corrected and updated. However, once the new ECSS standard is released, the NODES software and the just mentioned technical documentation must be revised to approve or modify and, eventually, update the relative parts. [2] [3]

4.3 Updates

At November 29th, 2019, no official version of "ECSS-E-ST-10-04C – Space environment" is issued yet.

5 ANALYSIS OF MODELS OF EARTH’S ATMOSPHERE

5.1 Atmosphere’s structure

An atmosphere is a layer or a set of layers of gases surrounding a planet and it is held in place by the gravity of the body. The atmosphere of Earth protects life on the planet by creating pressure allowing for liquid water to exist on the Earth's surface, absorbing ultraviolet solar radiation, warming the surface through heat retention (greenhouse effect), and reducing temperature extremes between day and night (the diurnal temperature variation).

Earth’s atmosphere consists of a number of layers that differ in properties such as composition, temperature and pressure. In general, air pressure and density decrease with altitude in the atmosphere. However, temperature has a more complicated profile with altitude, and may remain relatively constant or even increase with altitude in some regions. Because the general pattern of the temperature/altitude profile is constant and measurable by means of instrumented balloon soundings, the temperature behaviour provides a useful metric to distinguish atmospheric layers. In this way, Earth's atmosphere can be divided into five main layers, which are the troposphere, stratosphere, mesosphere, and thermosphere and exosphere. From highest to lowest, the five main layers have these measures:

- Exosphere: 700 to 10.000 km
- Thermosphere: 80 to 700 km
- Mesosphere: 50 to 80 km
- Stratosphere: 12 to 50 km
- Troposphere: 0 to 12 km

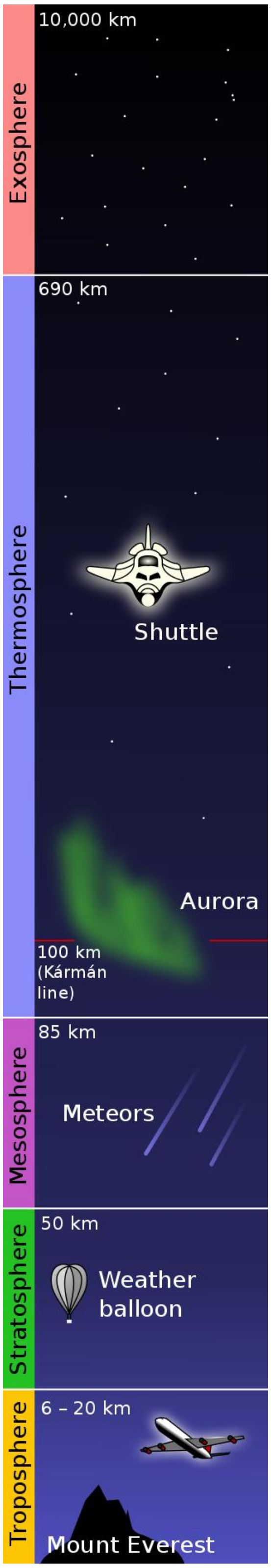

Figure 5.1 - Atmosphere structure

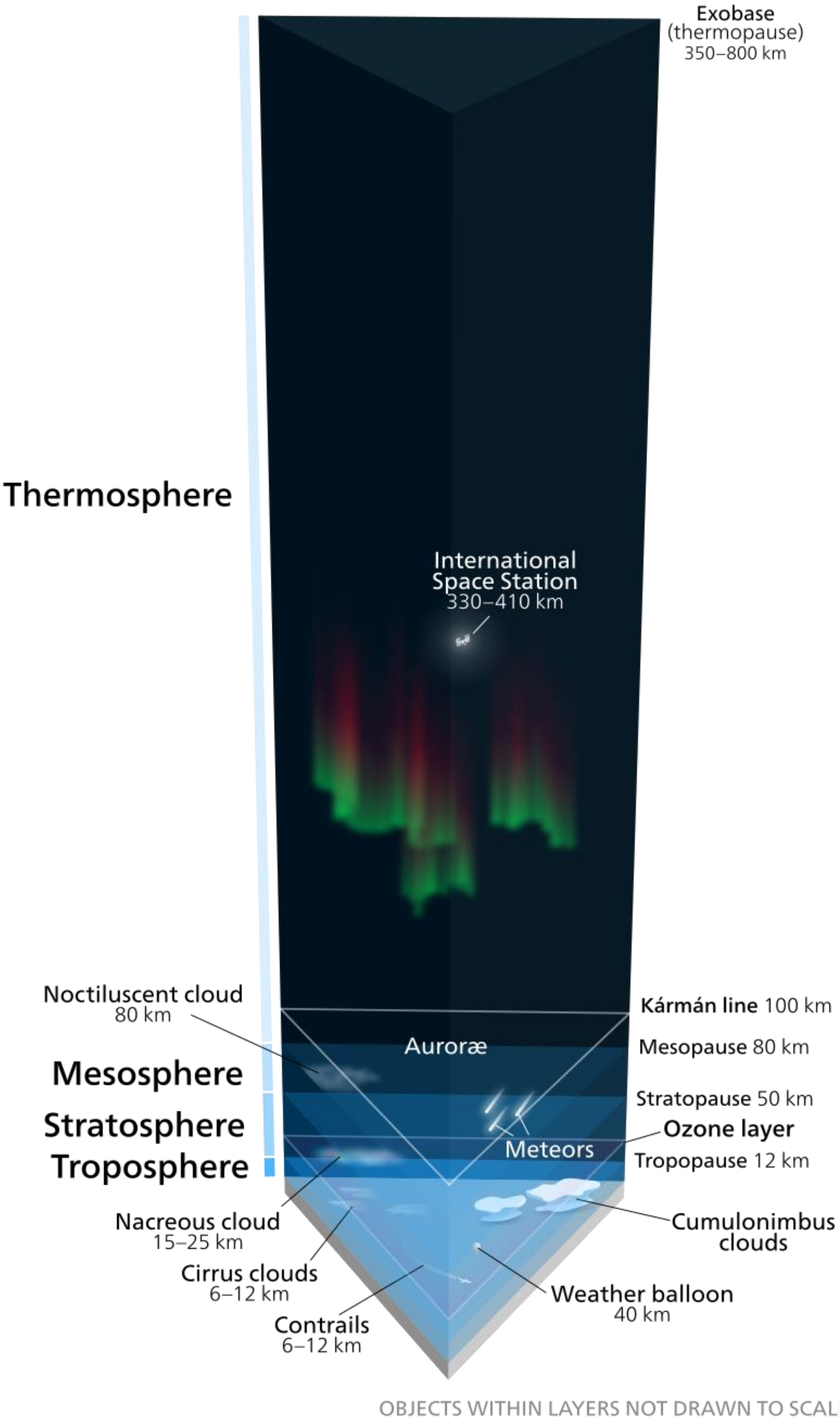

Figure 5.2 - Atmosphere structure

5.1.1 Exosphere

The exosphere is the outermost layer of Earth's atmosphere, i.e. the upper limit of the atmosphere. It extends from the exobase, which is located at the top of the thermosphere at an altitude of about 700 km above sea level, to about 10,000 km where it merges into the solar wind. This layer is mainly composed of extremely low densities of hydrogen, helium and several heavier molecules including nitrogen, oxygen and carbon dioxide closer to the exobase. The atoms and molecules are so far apart that they can travel hundreds of kilometres without colliding with one another. Thus, the exosphere no longer behaves like a gas, and the particles constantly escape into space. These free-moving particles follow ballistic trajectories and may migrate in and out of the magnetosphere or the solar wind.

5.1.2 Thermosphere

The thermosphere is the second-highest layer of Earth's atmosphere. It extends from the mesopause (which separates it from the mesosphere) at an altitude of about 80 km up to the thermopause at an altitude range of 500–1000 km. The height of the thermopause varies considerably due to changes in solar activity. Because the thermopause lies at the lower boundary of the exosphere, it is also referred to as the exobase. The lower part of the thermosphere, from 80 to 550 km above Earth's surface, contains the ionosphere. The temperature of the thermosphere gradually increases with height. Unlike the stratosphere beneath it, wherein a temperature inversion is due to the absorption of radiation by ozone, the inversion in the thermosphere occurs due to the extremely low density of its molecules. The temperature of this layer can rise as high as 1500 °C (2700 °F), though the gas molecules are so far apart that its temperature in the usual sense is not very meaningful. The air is so rarefied that an individual molecule (of oxygen, for example) travels an average of 1 km between collisions with other molecules. Although the thermosphere has a high proportion of molecules with high energy, it would not feel hot to a human in direct contact, because its density is too low to conduct a significant amount of energy to or from the skin.

This layer is completely cloudless and free of water vapour. Moreover, for information, the International Space Station orbits in this layer, between 350 and 420 km.

5.1.3 Mesosphere

The mesosphere is the third highest layer of Earth's atmosphere, occupying the region above the stratosphere and below the thermosphere. The exact upper and lower boundaries of the mesosphere vary with latitude and with season (higher in winter and at the tropics, lower in summer and at the poles), but the lower boundary (stratopause) is usually located at heights from 50 to 65 km above the Earth's surface and the upper boundary (mesopause) is usually around 85 to 100 km. Temperatures drop with increasing altitude to the mesopause that marks the top of this middle layer of the atmosphere. It is the coldest place on Earth and has an average temperature around −85 °C (−120 °F; 190 K); temperatures in the upper mesosphere fall as low as −101 °C (172 K; −150 °F), varying according to latitude and season. The mesosphere is the layer where most meteors burn up upon atmospheric entrance.

5.1.4 Stratosphere

The stratosphere is the second-lowest layer of Earth's atmosphere. It lies above the troposphere and is separated from it by the tropopause. This layer extends from the top of the troposphere at roughly 12 km above Earth's surface to the stratopause at an altitude of about 50 to 55 km. The atmospheric pressure at the top of the stratosphere is roughly 1/1000 the pressure at sea level. It contains the ozone layer, which is the part of Earth's atmosphere that contains relatively high concentrations of that gas. The stratosphere defines a layer in which temperatures rise with increasing altitude. This rise in temperature is caused by the absorption of ultraviolet radiation (UV) radiation from the Sun by the ozone layer, which restricts turbulence and mixing. Although the temperature may be −60 °C (−76 °F; 210 K) at the tropopause, the top of the stratosphere is much warmer, and may be near 0 °C.

5.1.5 Troposphere

The troposphere is the lowest layer of Earth's atmosphere. It extends from Earth's surface to an average height of about 12 km, although this altitude varies from about 9 km at the geographic poles to 17 km at the Equator, with some variation due to weather. The troposphere is bounded above by the tropopause, a boundary marked in most places by a temperature inversion (i.e. a layer of relatively warm air above a colder one), and in others by a zone which is isothermal with height. Although variations do occur, the temperature usually declines with increasing altitude in the troposphere because the troposphere is mostly heated through energy transfer from the surface. Thus, the lowest part of the troposphere (i.e. Earth's surface) is typically the warmest section of the troposphere. This promotes vertical mixing (hence, the origin of its name in the Greek word τρόπος, tropos, meaning "turn"). The troposphere contains roughly 80% of the mass of Earth's atmosphere. The troposphere is denser than all its overlying atmospheric layers because a larger atmospheric weight sits on top of the troposphere and causes it to be most severely compressed. Fifty percent of the total mass of the atmosphere is located in the lower 5.6 km of the troposphere.

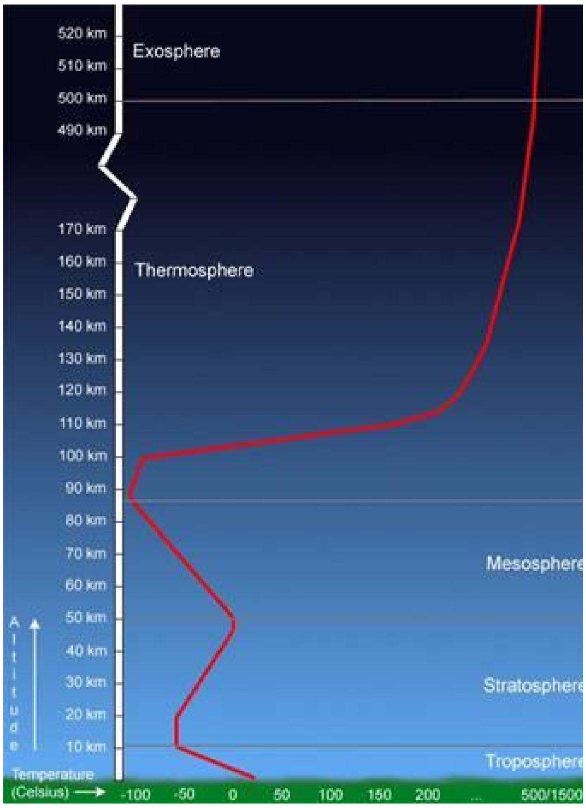

Figure 5.3 - Temperature profile in atmosphere's layers

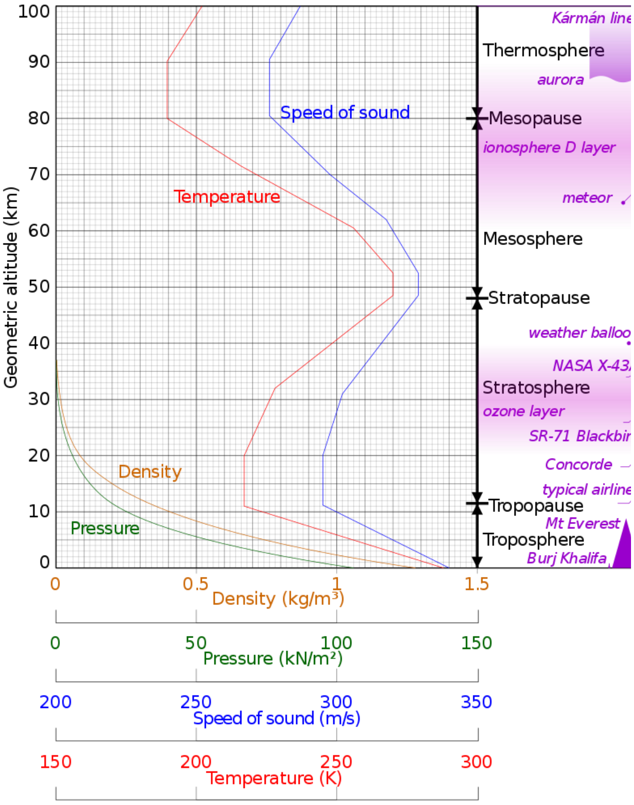

Figure 5.4 - Temperature, density, pressure and speed of sound profiles in atmosphere's layers

5.1.6 Other layers

Within the five principal layers above, that are largely determined by temperature, several secondary layers may be distinguished by other properties:

The *ozone layer* is contained within the stratosphere. In this layer, ozone concentrations are about 2 to 8 parts per million, which is much higher than in the lower atmosphere but still very small compared to the main components of the atmosphere. It is mainly located in the lower portion of the stratosphere from about 15–35 km, though the thickness varies seasonally and geographically. About 90% of the ozone in Earth's atmosphere is contained in the stratosphere.

The *ionosphere* is a region of the atmosphere that is ionized by solar radiation. It is responsible for auroras. During daytime hours, it stretches from 50 to 1000 km and includes the mesosphere, thermosphere, and parts of the exosphere. However, ionization in the mesosphere largely ceases during the night, so auroras are normally seen only in the thermosphere and lower exosphere. The ionosphere forms the inner edge of the magnetosphere. It has a peculiar importance because it influences, for example, radio propagation on Earth.

The *homosphere* and *heterosphere* are defined by whether the atmospheric gases are well mixed. The surface-based *homosphere* includes the troposphere, stratosphere, mesosphere, and the lowest part of the thermosphere, where the chemical composition of the atmosphere does not depend on molecular weight because the gases are mixed by turbulence. This relatively homogeneous layer ends at the turbopause found at about 100 km, the very edge of space itself as accepted by the FAI (Fédération Aéronautique Internationale), which places it about 20 km above the mesopause.

Above this altitude lies the *heterosphere*, which includes the exosphere and most of the thermosphere. Here, the chemical composition varies with altitude. This is because the distance that particles can move without colliding with one another is large compared with the size of motions that cause mixing. This allows the gases to stratify by molecular weight, with the heavier ones, such as oxygen and nitrogen, present only near the bottom of the heterosphere. The upper part of the heterosphere is composed almost completely of hydrogen, the lightest element.

The *planetary boundary layer* is the part of the troposphere that is closest to Earth's surface and is directly affected by it, mainly through turbulent diffusion. During the day the planetary boundary layer usually is well-mixed, whereas at night it becomes stably stratified. The depth of the planetary boundary layer ranges from as little as about 100 metres on clear, calm nights to 3000 m or more during the afternoon in dry regions.

The average temperature of the atmosphere at Earth's surface is 14 °C (57 °F; 287 K) or 15 °C (59 °F; 288 K), depending on the reference, but the last one seems to be the most accepted. [W2] [W3]

5.2 Description of atmosphere’s models and their solar indices

Aerodynamic drag is the major perturbation source of the LEO orbits and it is the largest uncertainty in determining orbits of satellites which operate in Earth’s upper atmosphere below about 600 km. Critical precision orbit determination and tracking operations include collision avoidance warnings for the International Space Station, satellite lifetime estimates, laser communication and re-entry prediction. Orbital drag accelerations (a_D) for a satellite in the Earth's atmosphere are related to neutral density by:

$$a_D = -\frac{1}{2}\rho V^2 c_D \frac{S}{m}$$

where ρ is the atmospheric total mass density and S, m, C_D and V are the satellite's cross section area, mass, drag coefficient and velocity respectively.

Meanwhile the thermospheric neutral density model’s error is the major error for computing satellite drag. Density models have been studied continuously since the first satellite was launched. In 1964, Jacchia brought forward his Jacchia64 (J64) model, which was represented by diffuse analytic equations, and its revised version is Jacchia71 and Jacchia77. The major density variations such as diurnal, seasonal, semi-annual, solar activity and geomagnetic activity were first incorporated into the model, laying the foundation for the models still used today. Other institutions also presented their own famous models, such as NASA MET (Marshall Engineering Thermosphere), DTM (Drag Temperature Model)78, DTM94, MSIS (Mass Spectrometer Incoherent scatter)90, NRLMSISE (Naval Research Laboratory MSIS)00, JB (Jacchia-Bowman)2006, JB2008, etc. Because the variation of the upper atmosphere is very complex, and the accuracy of the data used to build the model is limited, in the past 40 years, all of the models had similar one-sigma errors of about 15% for a given data set since J64 was published. Though the scientists continue using more and more accurate data to improve the model coefficients, the error of “15%” seemed to be the limit of the accuracy of empirical models.

In this paper, two quantities will be used to analyse the models: the data-to-model ratio and standard deviation.

The quantity statistically analysed is the ratio, $R = \frac{\rho_{measured}}{\rho_{model}}$, between measured density and model density, but the main focus is on analysing the mean ratios

$$\bar{R} = \sum_{i=1}^{N} \frac{R_i}{N}$$

where R_i is the ratio of the ith density measurement to the model and N is the total number of data points.

The standard deviation is given by

$$\sigma = \left[\sum_{i=1}^{N} \frac{(R_i - \bar{R})^2}{N-1} \right]^{1/2}$$

We are going to describe each model of atmosphere, their accuracies, the differences among them and the forecasting processes of solar indices.

5.2.1 Jacchia-Bowman 2006 (JB2006)

A new empirical atmospheric density model is developed using the CIRA72 (Jacchia 71) model as the basis for the diffusion equations. New solar indices based on orbit-based sensor data are used for the solar irradiances in the extreme and far ultraviolet wavelengths. New exospheric temperature and semi-annual density equations are employed to represent the major thermospheric density variations. Temperature correction equations are also developed for diurnal and latitudinal effects, and finally density correction factors are used for model corrections required at high altitude (1500–4000 km). The new model, Jacchia–Bowman 2006, is validated through comparisons of accurate daily density drag data previously computed for numerous satellites. For 400km altitude the standard deviation of 16% for the standard Jacchia model is reduced to 10% for the new JB2006 model for periods of low geomagnetic storm activity.

The basis of the new Jacchia–Bowman JB2006 model, as previously mentioned, is the CIRA72 (COSPAR International Reference Atmosphere, 1972) model atmosphere. The CIRA72 model integrates the diffusion equations using the Jacchia (1971) temperature formulation to compute density values for an input geographical location and solar conditions. The CIRA72 model was first converted to a CIRA ''70'' model by replacing the CIRA72 equations with equations from the Jacchia 70 model. This was done because the model corrections, for altitudes below 1000km, obtained for temperature and density are based on the Jacchia (1970) model, not the Jacchia (1971) model used in CIRA72. New semi-annual density equations (Bowman, 2004) were developed to replace the Jacchia formulation. New global night-time minimum exospheric temperature equations, using new solar indices, replaced Jacchia's T_c equation. In addition, several other equations to correct errors in the diurnal (local solar time) modelling were also incorporated. Finally, new density factors were incorporated to correct model errors at altitudes from 1000 to 4000 km.

5.2.1.1 Data source

The density data used to develop the new model equations are very accurate daily values obtained from drag analysis of numerous satellites with perigee altitudes of 175– 1100km. Daily temperature corrections to the US Air Force High Accuracy Satellite Drag Model's (HASDM) modified Jacchia (1970) atmospheric model were obtained on the satellites throughout the period 1978–2004. Approximately 120,000 daily temperature values were computed using a special energy dissipation rate (EDR) method, where radar and optical observations are fit with special orbit perturbations. For each satellite tracked from 1978 through 2004 approximately 100,000 radar and optical observations were available for the special perturbation orbit fitting. A differential orbit correction program was used to fit the observations to obtain the standard 6 Keplerian elements plus the ballistic coefficient. ''True'' ballistic coefficients were then used with the observed daily temperature corrections to obtain daily density values. The daily density computation was validated by comparing historical daily density values computed for the last 30 years for over 30 satellites. The accuracy of the density values was determined from comparisons of geographically overlapping perigee location data, with over 8500 pairs of density values used in the comparisons. The density errors were found to be less than 4% overall, with errors on the order of 2% for values covering the latest solar maximum.

5.2.1.2 Global night-time minimum exospheric temperature

5.2.1.2.1 Solar indices

Regarding solar irradiance indices and proxies, which are surrogates for solar irradiances, the usages of the terms are still evolving. In this way, an explanation is needed. A common usage is that a solar irradiance *proxy* is a measured or modelled data type that is used as a substitute for solar spectral irradiances. A solar irradiance *index*, on the other hand, is a measured or modelled data type that is an indicator of solar spectral irradiance activity level. The daily indices selected for this model include F_{10}, S_{10} and Mg_{10}.

$F_{10.7}$: The 10.7-cm solar radio flux, $F_{10.7}$ or F_{10}, was first observed by Covington on a daily basis beginning on February 14, 1947 and is now produced daily by the Canadian National Research Council's Herzberg Institute of Astrophysics at its ground-based Dominion Radio Astrophysical Observatory located in Penticton, British Columbia. Observations of the $F_{10.7}$ flux density values are made at 18, 20 and 22 UT each day and made available through the DRAO website http://hia-iha.nrc-cnrc.gc.ca/drao/icarus_e.html. The 20 UT values are archived at the World Data Centre and were used in this study. The physical units of $F_{10.7}$ are $\times 10^{-22}$ W m^{-2} Hz^{-1} and the numerical value without the multiplier is used as it is customarily done and expressed as solar flux units (sfu). In other words, a 10.7-cm radio emission of 150×10^{-22} W m^{-2} Hz^{-1} is simply referred to as $F_{10.7} = 150$ sfu. A running 81-day Centred smoothed set of values were created using the moving box-car method and these data are referred to as either F_{81} or F_{BAR} or $\bar{F}_{10}$. In this analysis, it is used a linear regression with daily $F_{10.7}$ to scale and report all other solar indices in units of sfu. Missing data values are not included in the regressions. $F_{10.7}$ is the traditional solar energy proxy that has been used since Jacchia developed empirical exospheric temperature equations for atmospheric density models, e.g. CIRA72. Its formation is physically dominated by non-thermal processes in the solar transition region and cool corona and, while it is a non-effective solar emission relative to the Earth's atmosphere, it is a useful proxy for the broad combination of chromospheric, transition region, and coronal solar EUV emissions modulated by bright solar active regions whose energy, at Earth, is deposited in the thermosphere. It is used the observed archival daily values, with a 1-day lag, over the common time frame.

As observed in the Figure 5.5, the $F_{10.7}$ solar radio flux has a period of 11 years which is equal to a solar cycle; the first cycle is Cycle 23, the second is Cycle 24 that is going to finish in

2019. The minimum before Cycle 23 was in 1997 and the minimum after was in 2008, but Cycle 23 has two maximums, the second one higher than the first one. Cycle 24 is weaker than the 23, which is weaker than Cycle 22; for this reason, Cycle 23 is chosen as a reference solar cycle.

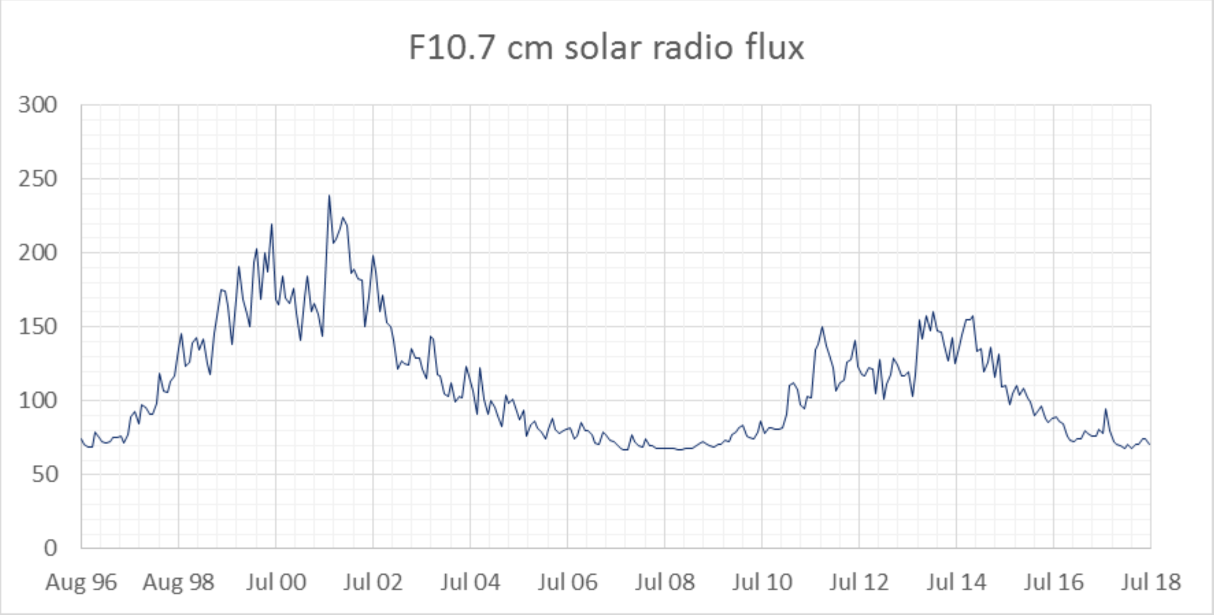

Figure 5.5 - F10.7 cm solar radio flux of Solar Cycle 23 and 24

The $F_{10.7}$ solar flux is strictly correlated to the sunspot number R by the formulation:

$$F_{10.7} = 63.7 + 0.728\,R + 8.9 * 10^{-4}\,R^2$$

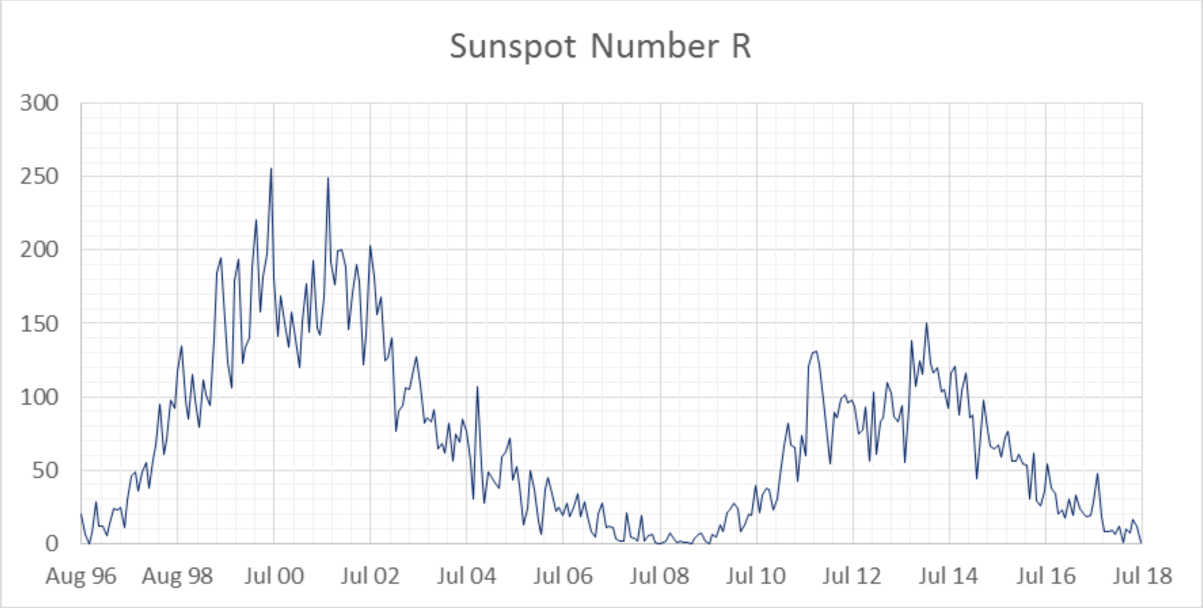

Figure 5.6 - Sunspot number R of Solar Cycle 23 and 24

The connection between them can also be seen in the picture by NASA below. The resemblance with the Figure 5.5 is noticeable.

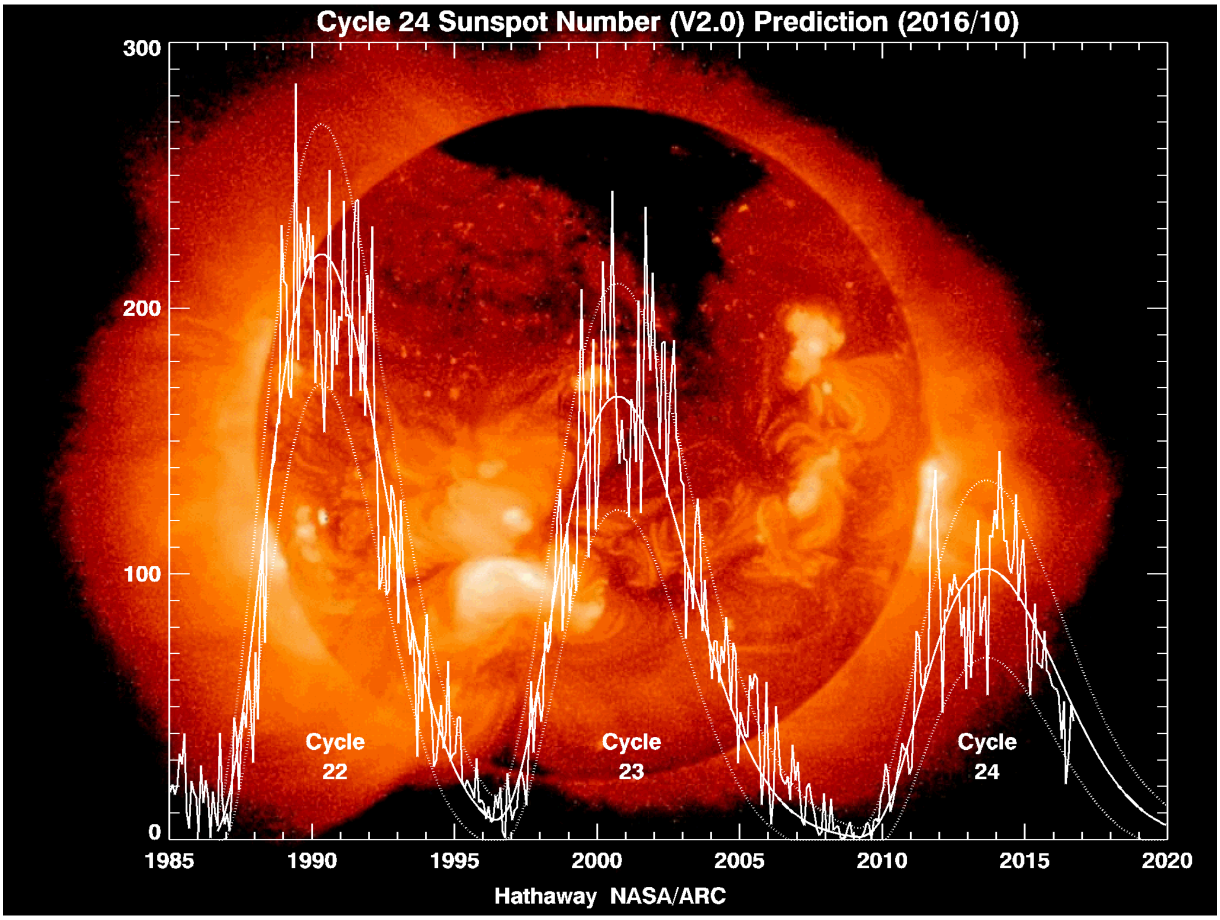

Figure 5.7 - Sunspot number R of Solar Cycle 22, 23 and 24

$S_{10.7}$: The NASA/ESA Solar and Heliospheric Observatory (SOHO) research satellite operates in a halo orbit at the Lagrange Point 1 (L1) on the Earth-Sun line, approximately 1.5 million km from the Earth, and has an uninterrupted view of the Sun. One of the instruments on SOHO is the Solar Extreme-ultraviolet Monitor (SEM) that was built and is operated by the University of Southern California's (USC) Space Science Centre (SSC). SOHO was launched on December 2, 1995 and SEM has been making observations since December 16, 1995. As part of its continuous solar observations, the SEM instrument measures the 26–34 nm solar EUV emission with 15-second time resolution in its first order broadband wavelength range. The orbit and solar data are both retrieved daily by USC SSC for processing in order to create daily solar irradiances with a latency of up to 24 hours. Integrated 26–34 nm emission ($SOHO\_SEM_{26\text{-}34}$) is used and it is normalized by dividing the daily value by the common time frame mean value. The $SOHO\_SEM_{26\text{-}34mean}$ mean value is 1.9955×10^{10} photons cm^{-2} s^{-1}. The normalized value is converted to sfu through linear regression with $F_{10.7}$ over the common time frame and the resulting index is called S_{EUV} or $S_{10.7}$ or S_{10}. The following equation is the formulation to derive the SOHO EUV, S_{EUV}.

$$S_{EUV} = S_{10.7} = -12.01 + 141.23 * (SOHO\_SEM_{26-34}/SOHO\_SEM_{26-34mean})$$

The broadband (wavelength integrated) SEM 26-34 nm irradiances, represented by the $S_{10.7}$ index, are EUV line emissions dominated by the chromospheric He II line at 30.4 nm with contributions from other chromospheric and coronal lines. This energy principally comes from solar active regions. Once the photons reach the Earth, they are deposited (absorbed) in the terrestrial thermosphere mostly by atomic oxygen above 200 km. The daily index, with a 1-day lag, is used over the common time frame.

$M_{10.7}$: The NOAA series operational satellites, e.g., NOAA 16 and NOAA 17, host the Solar Backscatter Ultraviolet (SBUV) spectrometer that has the objective of monitoring ozone in the Earth's lower atmosphere. In its discrete operating mode, a diffuser screen is placed in front of the instrument's aperture in order to scatter solar MUV radiation near 280 nm into the instrument. This solar spectral region contains both photospheric continuum and chromospheric line emissions. The chromospheric Mg II h and k lines at 279.56 and 280.27 nm, respectively, and the weakly varying photospheric wings or continuum long ward and short ward of the core line emission, are operationally observed by the instrument. On the ground, the Mg II core-to-wing ratio is calculated between the variable lines and nearly non-varying wings. The result is a measure of chromospheric and some photospheric solar active region activity independent of instrument sensitivity change through time, is referred to as the Mg II core-to-wing ratio (cwr), and is provided daily by NOAA Space Environment Centre (SEC). The ratio is an especially good proxy for some solar FUV and EUV emissions. The analysis has found that it can represent very well the photospheric and lower chromospheric solar FUV Schumann-Runge Continuum emission. It has been taken the Mg II cwr and performed a linear regression with $F_{10.7}$ for the common time frame to derive the $M_{10.7}$ index that is the Mg II cwr reported in $F_{10.7}$ units, i.e. sfu. The following equation provides the calculation of $M_{10.7}$ based on the NOAA 16 SBUV Mg II cwr data. The daily index, with a 5-day lag over the common time frame is used as a proxy for E_{SRC} since the latter is not operationally available.

$$M_{10.7} = Mg_{10} = -1943.85 + 7606.56 * Mg_{II_{NOAA16}}$$

In the first version of JB2006, dated second half of 2007, these were the only indices that were taken into account by Bowman and Tobiska. In the following revision – March 2008 – of the same atmosphere model, the authors updated the list of solar indices by considering four more: E_{SRC}, E_{HRT}, $E_{10.7}$ and $XL_{10.7}$.

E_{SRC}: The solar FUV Schumann-Runge Continuum (SRC) contains emission between 125–175 nm from the photosphere and lower chromosphere. This solar energy is deposited in the terrestrial mesosphere and lower thermosphere (80–125 km) primarily through the energy released from the dissociation of molecular oxygen. The SRC has been observed with the SOLSTICE instruments on UARS by Rottman and Woods and on SORCE by McClintok. These are NASA research satellites as is the TIMED satellite that hosts the SEE instrument; all three are conducting long-term investigations of solar spectral irradiances. After a comparison of three bands in the SRC (144–145, 151–152, 145–165 nm), it is selected the 145–165 nm band as a representative wavelength range for the remainder of the SRC. The emission in this band is mostly deposited in the 110–125 altitude region. In order to conduct the analysis, the daily SOLSTICE 145–165 nm emission from UARS and SORCE, was integrated, it was created a normalized index by dividing the daily value by the common time frame mean value, $SOLSTICE_{145\text{-}165\text{-mean}}$, which has a value of 2.1105×10^{11} photons cm^{-2} s^{-1}. Next, it is performed a linear regression with $F_{10.7}$ to report the index in sfu. E_{SRC}, as shown in the following equation, is the result and this index with a 5-day lag is used.

$$E_{SRC} = -784.03 + 909.34 * (SOLSTICE_{145-165}/SOLSTICE_{145-165mean})$$

E_{HRT}: The solar MUV Hartley Band (HB) contains emission between 245–254 nm from the photosphere. This solar energy is deposited in the terrestrial stratosphere (30–40 km) primarily through the energy released from the dissociation of ozone. The solar HB emissions have been observed daily by the SOLSTICE instrument on the UARS and SORCE NASA research satellites. For this analysis, the daily SOLSTICE 245–254 nm emission is integrated and it is created a normalized index by dividing the daily value by the common time frame mean value, $SOLSTICE_{245\text{-}254\text{-mean}}$, which has a value of 3.1496×10^{13} photons cm^{-2} s^{-1}. Next, it is performed a linear regression with $F_{10.7}$ to report the index in sfu. E_{HRT}, as shown in the following equation, is the result and it is used this index with multiple-day lags, but with no apparent effect upon reducing the JB2006 modelled residuals with respect to the satellite-derived density data.

$$E_{HRT} = -726.27 + 851.57 * (HB_{245-254}/HB_{245-254mean})$$

$E_{10.7}$: this solar index represents the 1-105 nm solar radiation flux and was brought out by Tobiska in 2000; he said that the daily altitude decay for the Solar Mesosphere Explorer (SME) satellite in 1982 was well represented by models using $E_{10.7}$ instead of $F_{10.7}$. In fact, in 2000, Space Environment Technologies (SpaceWX, USA) released "Solar Irradiance Model 2000" which produces variable EUV irradiances, including the $E_{10.7}$ time-dependent solar EUV proxy. Because the wavelength of the radiation which may heat the thermosphere was involved in the range, it was reported that $E_{10.7}$ is better than $F_{10.7}$ to represent solar emission, and can be used in any application requiring $F_{10.7}$ without modification.

$XL_{10.7}$: The X-ray Spectrometer (XRS) instrument is part of the instrument package on the GOES series operational spacecraft. The XRS on GOES 10 and GOES 12 provide the 0.1–0.8 nm solar X-ray emission with 1-minute cadence and 5-minute latency. These data, used for flare detection, are continuously reported by NOAA SEC at the website of http://www.sec.noaa.gov/. X-rays in the 0.1–0.8 nm range come from the cool and hot corona and are typically a combination of both very bright solar active region background that varies slowly (days to months) plus flares that vary rapidly (minutes to hours), respectively. The photons arriving at Earth are primarily absorbed in the mesosphere and lower thermosphere (80–90 km) by molecular oxygen and nitrogen where they ionize those neutral constituents to create the ionospheric D-region. An index of the solar X-ray active region background, without the flare component, has been developed. This is called the X_{b10} index and it is used to represent the daily energy that is deposited into the mesosphere and lower thermosphere. The 0.1-0.8 nm X-rays are a major energy source in these atmospheric regions during high solar activity but relinquish their dominance to the competing hydrogen (H) Lyman-α emission during moderate and low solar activity. Lyman-α is also deposited in the same atmospheric regions, is created in the solar upper chromosphere and transition region and demarcates the EUV from the FUV spectral regions. It is formed primarily in solar active regions; the photons, arriving at Earth, are absorbed in the mesosphere and lower thermosphere where they dissociate nitric oxide (NO) and participate in water (H_2O) chemistry. Lyman-α has been observed by the SOLSTICE instrument on the UARS and SORCE NASA research satellites as well as by the SEE instrument on NASA TIMED research satellite. Since these two solar emissions are competing drivers to the mesosphere and lower thermosphere, it has been developed a mixed solar index $XL_{10.7}$ of X_{b10} and Lyman-α. It is weighted to represent mostly X_{b10} during solar maximum and to represent mostly Lyman-α during moderate and low solar activity. The independent, normalized $\bar{F}_{10}$, is used as the weighting function and multiplied with the X_{b10} and Lyman-α as fractions to their solar maximum values. $XL_{10.7}$ index is measured in sfu. This daily index with an 8-day lag is tested over the common time frame and it was found that it provides a few percent improvement in reducing the JB2006 modelled residuals versus the derived satellite densities. However, due to the operational complexity of producing this index, Bowman and Tobiska decided not to include it in the final formulation of JB2006 but it will be added in the JB2008 (Jacchia-Bowman 2008 model).

5.2.1.2.2 Geomagnetic index

JB2006 uses only one geomagnetic index, i.e. a_p. The A_p-index provides a daily average level for the amplitude of planetary geomagnetic activity, and thus also that of the Earth. As just said, it is a geomagnetic activity index where days with high levels of geomagnetic activity have a higher daily A_p-value. a_p-index instead is a 3-hourly value of geomagnetic index and is measured in units of 2 nT. The average from 8 daily a_p-values gives us the A_p-index of a certain day. To get these a_p-values you first need to convert the 3-hour K_p-values to a_p-values. K_p is the same as the a_p value, but in another scale and it is measured by GeoForschungsZentrum Potsdam Adolf-Schmidt-Observatory for Geomagnetism in Potsdam, Germany. K_p is derived from geomagnetic field measurements made at several locations around the world. To make it a bit more clear on how you can determine the A_p for a certain day, an example has been given: it is considered one day with the following measured K_p-values: 0+, 2-, 2o, 3o, 7-, 8o, 9- and 9o. The next step would be to convert these K_p-values to a_p-values. The table below will help with this. When conversion is done, eight a_p-values are obtained: 2, 6, 7, 15, 111, 207, 300 and 400. The average of these eight values will give the A_p for that day. The day that it is used in this example day would have an A_p-value of 131.

Table 5.1 - Convertion table from K_p to a_p

K_p	0	0+	1-	1o	1+	2-	2o	2+	3	3o	3+	4-	4o	4+
a_p	0	2	3	4	5	6	7	9	12	15	18	22	27	32
K_p	5-	5o	5+	6-	6o	6+	7-	7o	7+	8-	8o	8+	9-	9o
a_p	39	48	56	67	80	94	111	132	154	179	207	236	300	400

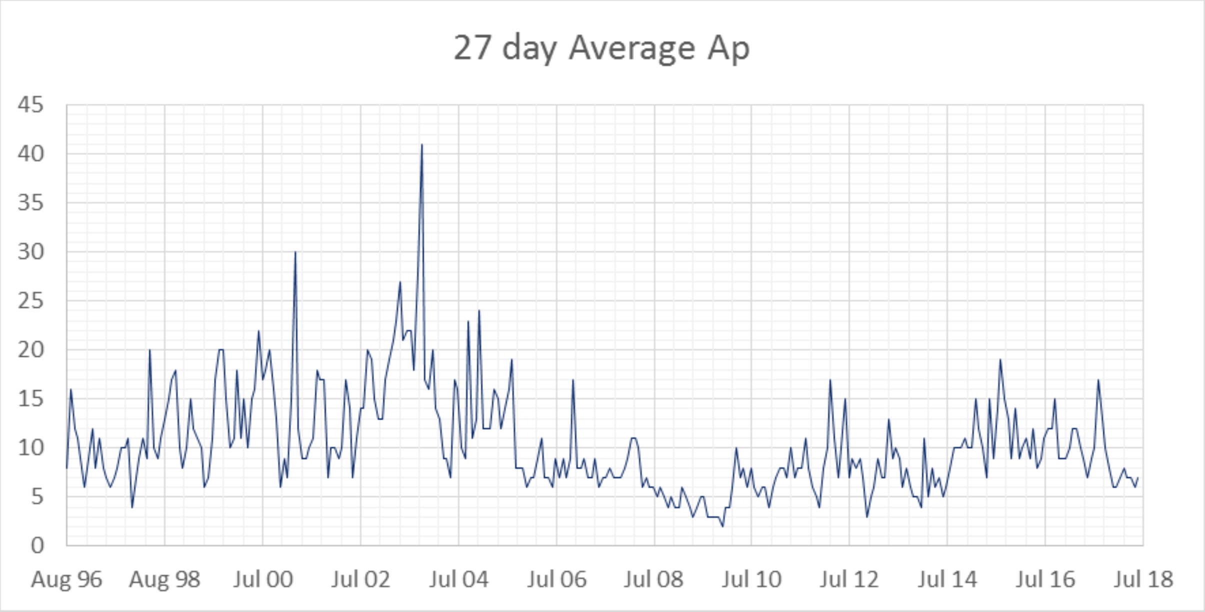

Figure 5.8 - Trend of 27 day average Ap value

5.2.1.2.3 T_c temperature equation

The solution of the best Tc equation was obtained using numerous satellites for the years from 1996 through 2004 when all new solar indices were available. The resulting equation is

$$T_c = 379.0 + 3.353\,\bar{F}_{10} + 0.358\,\Delta F_{10} + 2.094\,\Delta S_{10} + 0.343\,\Delta Mg_{10}$$

The delta values represent the difference of the daily and 81-day Centred average value of each index. The 81-day (3-solar rotation period) Centred value was determined to be the best long-term average to use. To avoid increases in T_c due to geomagnetic storms, all daily data with the geomagnetic index $a_p > 25$ were rejected. This meant that if a solar index required a lag time of 5 days, each of the 5 days prior to the current time had to have $a_p < 25$ for the current daily density data to be used. It was determined that a lag time of 1 day was the best to use for the F_{10} and S_{10} indices. However, for using the Mg_{10} index the analysis initially Centred on using an index E_{SRC} representing the FUV solar radiation from the Schumann–Runge continuum. From the analysis it was determined that the Mg_{10} index could be used as an excellent proxy for the real FUV E_{SRC} index. The best time lag determined for both E_{SRC} and Mg_{10} corresponded to a 5-day lag, which was used in determining the new T_c equation above.

The testing of the new T_c equation was done by placing the new equation into the Jacchia 70 atmospheric model, along with the real observed yearly semi-annual variations. The new diurnal and latitudinal corrections, lately explained, were also included.

5.2.1.3 Semi-annual density variation

The semi-annual density variation was first discovered by Paetzold and Zschorner (1961). They observed a global density variation from analysis of satellite drag data, which showed 6-month periodicity maximum occurring in April and October, and minimum occurring in January and July. For the new JB2006 model the semi-annual variations were computed first by differencing the real daily density values with density values obtained from the Jacchia model without applying Jacchia’s semi-annual equations. For a perfect model the resulting differences would only contain the observed semi-annual variation. Figure 5.9 shows examples of the individual density differences obtained from the data. Also shown are Jacchia’s semi-annual density variation and a Fourier series fitted to smoothed density difference values. This Fourier function is discussed in detail below. As can be observed in the figure, there is a very large unmodelled 27-day variation in the difference values. Therefore, it was decided to smooth the values with a 28-day moving filter. The resulting values would then produce a smoother fit with the Fourier series. It is interesting to note how the semi-annual variation changes with height and time. Figure 5.9 shows the variation during a year near solar maximum (2002). The semi-annual amplitude is measured from the yearly minimum, normally occurring in July, to the yearly maximum, normally in October. During solar maximum, the semi-annual variation can be as small as 30% at 220 km, and as large as 250% near 800km. During solar minimum, the maximum variation near 800km is only 60%. Thus, there is a major difference in amplitudes of the yearly variation from solar minimum to solar maximum, unlike Jacchia’s model, which maintains constant amplitude from year to year.

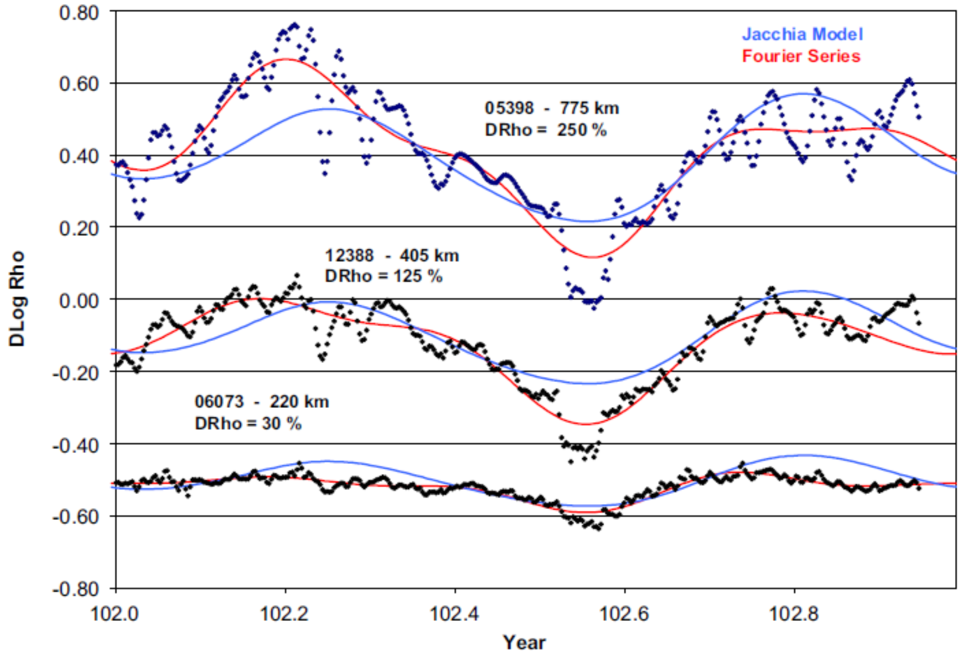

Figure 5.9 - Semiannual density variation for selected satellites in 2002

5.2.1.3.1 Semi-annual density variation function

Jacchia (1971) represented the semi-annual density variation in the form

$$\Delta_{SA} \log_{10} \rho = F(z)\, G(t)$$

where F(z) represents the variation amplitude (i.e. the difference in log10 density between the principal minimum normally in July and the principle maximum normally in October) as a function of altitude and G(t) represents the average density variation as a function of time in which the amplitude has been normalized to 1.

It was previously determined that a Fourier series could accurately represent Jacchia’s G(t) equation structure and simplify the solution of the coefficients. It was determined that a 9-coefficient series, including frequencies up to 4 cycles per year, was sufficient to capture all the variability in G(t) that had been previously observed. It was also determined that a simplified quadratic polynomial equation in z could sufficiently capture Jacchia’s F(z) equation and not lose any fidelity in the observed F(z) values. The resulting equations used for modelling the observed yearly variations were

$$F(z) = B_1 + B_2 z + B_3 z^2 \quad (z\ in\ km)$$
$$G(t) = C_1 + C_2 \sin(\omega) + C_3 \cos(\omega) + C_4 \sin(2\omega) + C_5 \cos(2\omega) +$$
$$+C_6 \sin(3\omega) + C_7 \cos(3\omega) + C_8 \sin(4\omega) + C_9 \cos(4\omega)$$

where $\omega = 2\pi\theta$, $\theta = (t - 1.0)/365$ and t = day of year.

5.2.1.3.2 Semi-annual F(z) height function

The amplitude, F(z), of the semi-annual variation was determined on a year-by-year and satellite-by-satellite basis. The smoothed density difference data was fit each year for each satellite using the 9 term Fourier series. The F(z) value was then computed from each fit as the difference between the minimum and maximum values for the year.

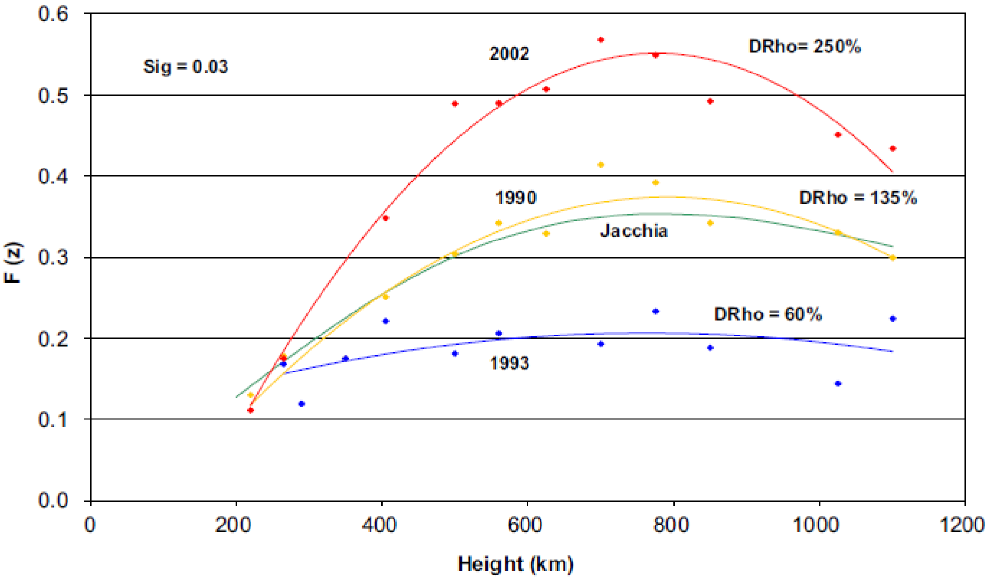

Figure 5.10 - The amplitude function F(z) for 3 different years (1990, 1993, 2002)

Figure 5.10 shows the results of three different years of data with semiannual amplitudes plotted for each satellite for each year, along with the plot of the constant Jacchia's F(z) function. For each year, the F(z) values were fit with a quadratic polynomial in height. The smoothed curves shown in Figure 5.10 represent the least squares quadratic fit obtained for three different years. The F(z) $\Delta\log_{10}\rho$ data for all satellites are very consistent within each year, producing a standard deviation of only 0.03. The most notable feature in Figure 5.10 is the very large difference in maximum amplitude among the years displayed. The 2002 data shows a maximum density variation of 250% near 800km, while the 1993 data shows only a 60% maximum variation. Jacchia's F(z) function only gives a constant 130% maximum variation for all years. To obtain a global fit, covering all years and all heights, all F(z) values for all satellites and all years were fitted to obtain the F(z) global function using the following equation:

$$F(z) = B_1 + B_2\bar{F}_{10} + B_3\bar{F}_{10}z + B_4\bar{F}_{10}z^2 + B_5\bar{F}_{10}^2z + B_6\bar{F}_{10}^2z^2$$

where z = (height (km) / 1000), and $\bar{F}_{10}$ is the 81-day Centred average of F_{10} Centred at the July minimum time. Figure 5.11 shows the observed yearly F(z) values at 500 km and the fitted F(z) global values at 500 km plotted as a function of year. Also shown are the average $\bar{F}_{10}$ values. The strong correlation of the yearly F(z) values with $\bar{F}_{10}$ is readily apparent. Also apparent are the occasional large deviations in the observed values from the global model values. These deviations are mostly the result of large variations in the 27-day F_{10} flux occurring during the July semi-annual minimum time.

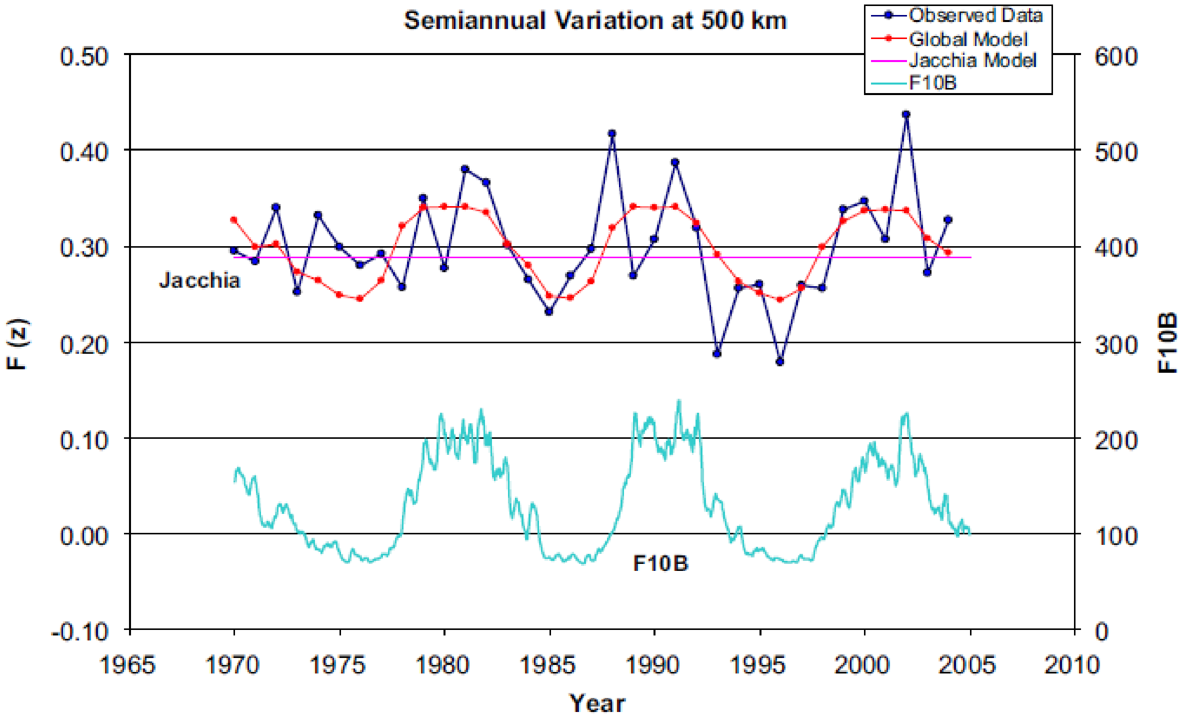

Figure 5.11 - The observed F(z) value at 500 km height for each year plotted by year

5.2.1.3.3 Semi-annual G(t) yearly periodic function

The G(t) yearly function, as previously discussed, consists of a Fourier series with 9 coefficients. The 28-day smoothed density difference data for each satellite was fitted with the Fourier series for each year. The density difference data is the accurate observed daily density values minus the Jacchia values without Jacchia's semi-annual variation. The G(t) function was then obtained by normalizing to a value of 1 the difference between the minimum and maximum values for the year. The F(z) value for each satellite by year was used for the normalization. Figure 5.12 shows the results obtained for the year 1990 for the majority of the satellites. Worth of note is the tight consistency of the curves for all heights, covering over 800 km in altitude. A yearly G(t) function was then fit using the data for all the satellites for each year. Figure 5.12 also shows the yearly G(t) equation values, with a standard deviation of 0.11 in $\Delta \log_{10} \rho$. A small sigma was obtained for every year's fit, especially during solar maximum years. Figure 5.13 shows the yearly G(t) fits for 1999 through 2001; each set of curves for 1999 and 2001 has been offset by +1.00 and -1.00 respectively for clarity. It is readily apparent that the series changes dramatically from year to year. During solar maximum the July minimum date can vary by as much as 80 days. The variability is especially large for defining the time of the July minimum during solar maximum, while the solar minimum July minimum times are much more consistency from year to year.

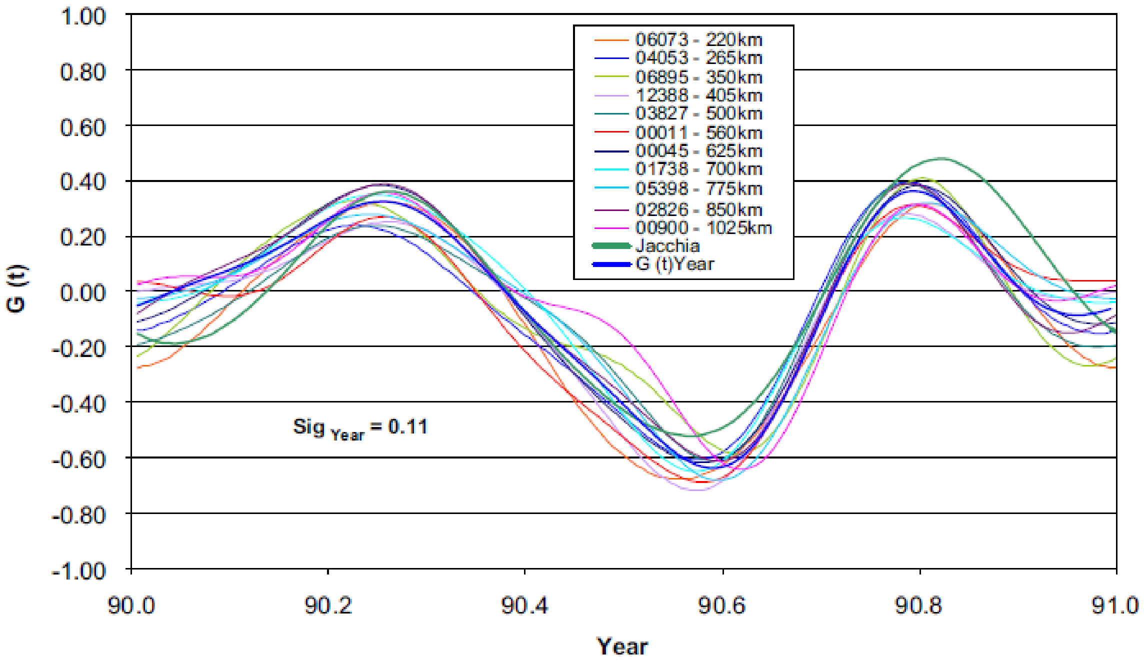

Figure 5.12 - The individual satellite G(t) fits plotted for 1990 with Jacchia model and yearly fit equation values

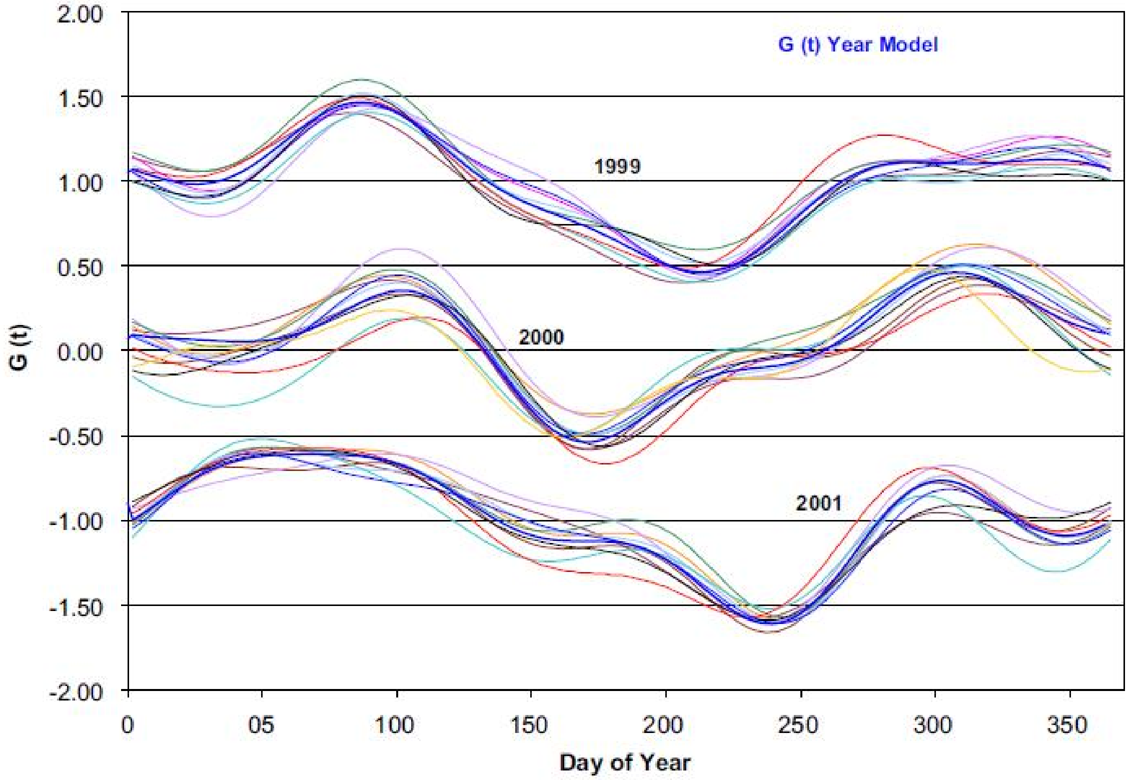

Figure 5.13 - The individual satellite fits for 3 different years with G(t) highlighted

5.2.1.3.4 Semi-annual G(t) global function

A global G(t) function was obtained using all satellite data for all years. Since the yearly G(t) functions demonstrated a dependence on solar activity it was decided to expand the series as a function of the average $\bar{F}_{10}$. The following equation was finally adopted for the global G(t) function:

Equation 1 - Semi-annual G(t) global function

$$\begin{aligned} G(t) = {} & C_1 + C_2 \sin(\omega) + C_3 \cos(\omega) + C_4 \sin(2\omega) + C_5 \cos(2\omega) \\ & + C_6 \sin(3\omega) + C_7 \cos(3\omega) + C_8 \sin(4\omega) + C_9 \cos(4\omega) \\ & + \overline{F}_{10}\{C_{10} + C_{11} \sin(\omega) + C_{12} \cos(\omega) + C_{13} \sin(2\omega) + C_{14} \cos(2\omega) \\ & + C_{15} \sin(3\omega) + C_{16} \cos(3\omega) + C_{17} \sin(4\omega) + C_{18} \cos(4\omega)\} \\ & + \overline{F}_{10}^2\{C_{19} + C_{20} \sin(\omega) + C_{21} \cos(\omega) + C_{22} \sin(2\omega) + C_{23} \cos(2\omega)\} \end{aligned}$$

where $\omega = 2\pi\vartheta$ $\quad \vartheta = (t - 1.0)/365$ $\quad$ t = day of year

Figure 5.14 is a plot of the global G(t) equation as fitted with all the satellite data. Jacchia's equation for G(t) is also shown. It is interesting to note that the solar minimum and solar maximum plots are significantly different except near the October maximum, which appears to have only a slight phase shift among the different curves. The April maximum variation is much larger in amplitude, though not in phase. Jacchia's function overestimates the October maximum for all solar activity, and only correctly estimates the April maximum during average solar activity. The curves once again demonstrate the need for solar activity to be included in the semi-annual G(t) function. The resulting new semi-annual equation for $\Delta_{SA} \log_{10} \rho$ used in the JB2006 model is obtained using the previous F(z) semi-annual height function and the last G(t) equation – semi-annual global function – in the standard semi-annual density variation equation.

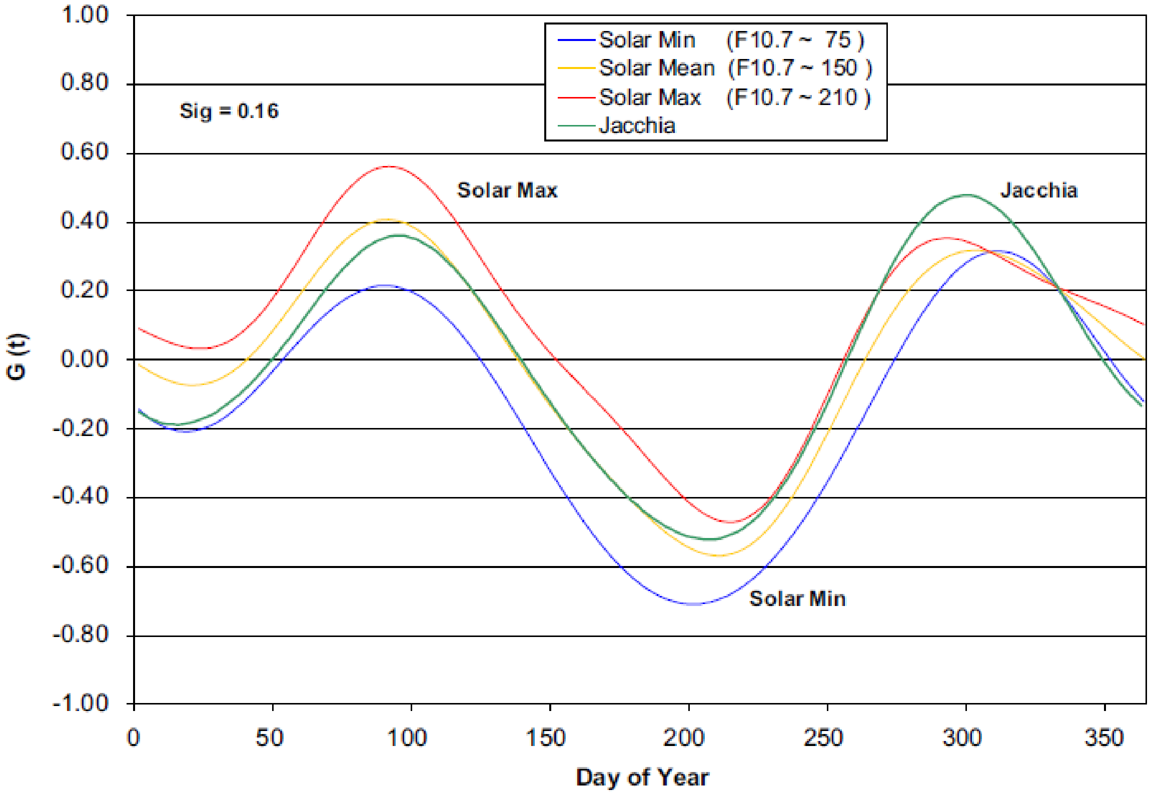

Figure 5.14 - G(t) curves for different solar activities

5.2.1.4 Diurnal density correction

Daily temperature corrections, dT_c, to the Jacchia 1970 atmospheric model were obtained on 79 calibration satellites for the period 1994 through 2003, and 35 calibration satellites for the solar maximum period 1989 through 1990. All the "calibration" satellites have moderate to high eccentricity orbits, with perigee heights ranging from 150 to 500 km. This means that the daily dT_c correction value obtained for a satellite represents the temperature correction needed for a specific local solar time, latitude, and height corresponding to the perigee location. Corrections to the diurnal (local solar time) and latitude equations were then obtained in the following manner. The dT_c values on all the calibration satellites were least squares fit daily as a function of height. These daily fits represented the global dT_c correction on a day-by-day basis. The daily fit values of dT_c were then removed from the original dT_c temperature corrections obtained for each satellite. The resulting ΔT_c corrections could then be attributed to model errors in local solar time and latitude. The original approach to correcting the observed model errors was to obtain, using the new ΔT_c values, new coefficients to Jacchia's original diurnal equations. However, this proved unfruitful because of the complexity of the errors, so a polynomial approach was adopted. Since the observed errors showed variations as a function of local solar time, latitude, height, and F_{10}, the objective was to obtain polynomial fits with the least number of trigonometry functions to facilitate computer computation time. These daily ΔT_c values were all lumped together, and equations were least squares fit as a function of local solar time, latitude, height, and solar flux. Figure 5.15 shows the ΔT_c values at 200-300 km altitude along with the fitted equation as a function of local solar time. The ΔT_c values are for solar minimum conditions. Figure 5.16 shows the ΔT_c values with the fitted equation for solar maximum conditions at an altitude of 400-500 km. Finally, Figure 5.17 shows the fitted equations in ΔT_x for a range of altitudes below 200 km for moderate solar conditions. The correction in T_x, the inflection point temperature at $z_x = 125$ km, was used for heights below 200 km because it better represented density variations than T_c for these very low altitudes. As can be seen in the figures the ΔT_c correction equations vary significantly with respect to local solar time, height, and solar flux. The resulting ΔT_c equations are divided into heights above 250 km and between 200 km and 250 km. Below 200 km a ΔT_x correction was obtained. The intermediate altitude Equation 3 was obtained from spline fitting Equation 2 with the boundary conditions in ΔT_c obtained from Equation 4, where the boundary value and slope of Equation 3 agrees with the values of Equation 2 and the ΔT_c values computed from Equation 4 at the respective boundary altitudes. Finally, either the ΔT_c or the ΔT_x values computed from Equation 2, Equation 3, or Equation 4 are added to the T_c or T_x values from Jacchia 1970 and put in the JB2006 model to obtain the T_c and T_x values used for the density computations.

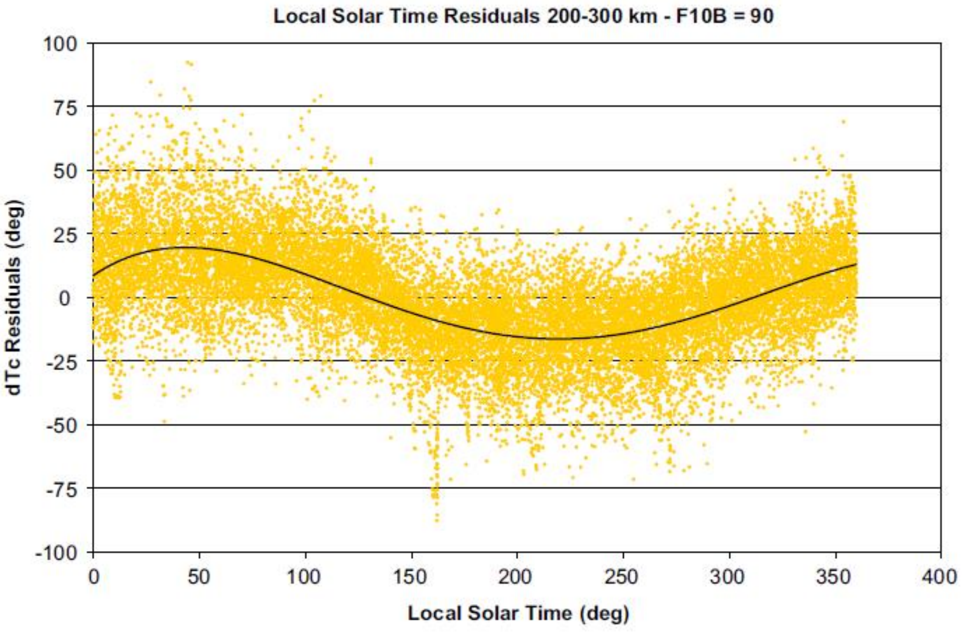

Figure 5.15 - ΔT_c values for solar minimum conditions as a function of local solar time

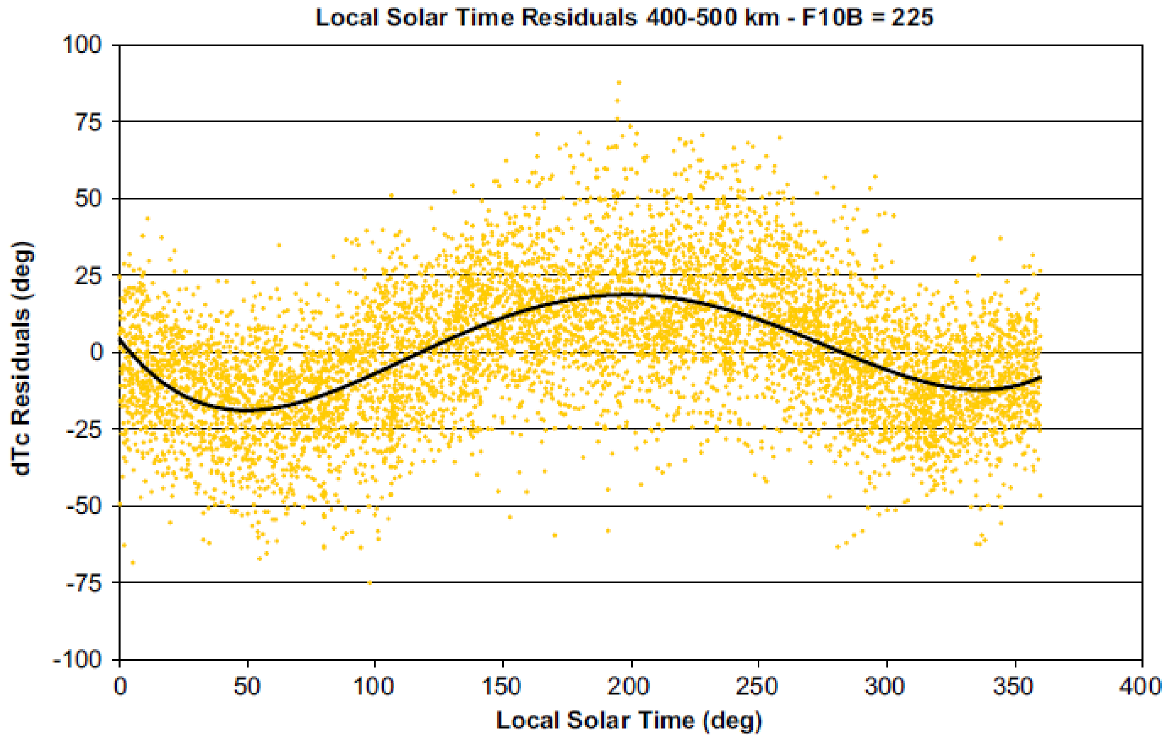

Figure 5.16 – ΔT_c values for solar maximum conditions as a function of local solar time

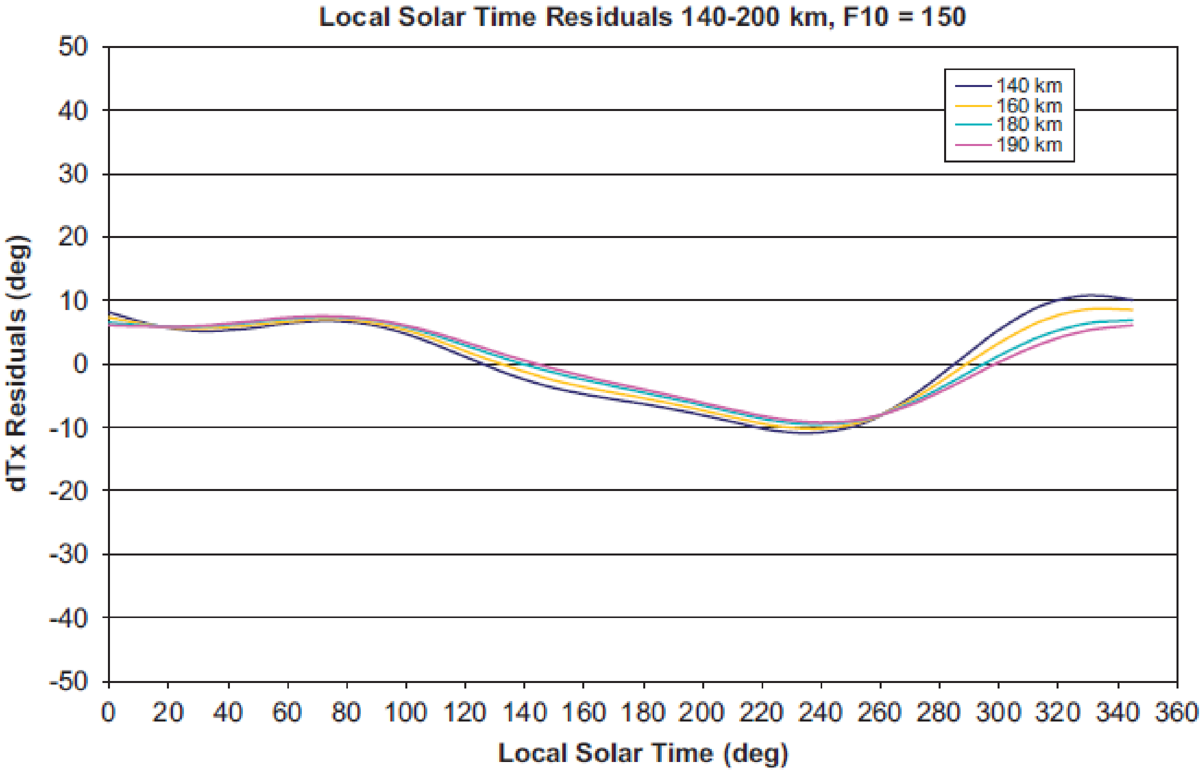

Figure 5.17 - ΔT_x values for solar moderate conditions as a function of local solar time and altitude

$F = (F_{10} - 100)/100$
$\theta = (\text{local solar time(hr)})/24$
$\varphi = \cos(\text{latitude})$
$z = \text{height (km)}$

Equation 2 - ΔT_c for 250 km < z < 700 km

```
For 700 km > z >= 250 km   :    H = z/100
```

$$\begin{aligned}\Delta Tc = {} & B_1 + F\left(B_2 + B_3\theta + B_4\theta^2 + B_5\theta^3 + B_6\theta^4 + B_7\theta^5\right)\\ & + \varphi\left(B_8\theta + B_9\theta^2 + B_{10}\theta^3 + B_{11}\theta^4 + B_{12}\theta^5\right)\\ & + \varphi H\left(B_{13} + B_{14}\theta + B_{15}\theta^2 + B_{16}\theta^3 + B_{17}\theta^4 + B_{18}\theta^5\right) + B_{19}\varphi\end{aligned}$$

Equation 3 - ΔT_c for 200 km < z < 250 km

```
For 250 km >= z >= 200    :    H = (z - 200)/50
```

$$\begin{aligned}\Delta Tc = {} & HC_1 + HF\left(C_2 + C_3\theta + C_4\theta^2 + C_5\theta^3 + C_6\theta^4 + C_7\theta^5\right)\\ & + H\varphi\left(C_8\theta + C_9\theta^2 + C_{10}\theta^3 + C_{11}\theta^4 + C_{12}\theta^5 + C_{13} + C_{14}F + C_{15}F\theta + C_{16}F\theta^2\right)\\ & + C_{17} + \varphi\left(C_{18}\theta + C_{19}\theta^2 + C_{20}\theta^3 + C_{21}F + C_{22}F\theta + C_{23}F\theta^2\right)\end{aligned}$$

Equation 4 - ΔT_x for 140 km < z < 200 km

```
For 200 km >= z > 140     :     H = z/100
```

$$\begin{aligned}\Delta Tx = {} & D_1 + \left(D_2\theta + D_3\theta^2 + D_4\theta^3 + D_5\theta^4\right)\\ & + H\left(D_6 + D_7\theta + D_8\theta^2 + D_9\theta^3\right) + F\left(D_{10} + D_{11}\theta + D_{12}\theta^2\right)\end{aligned}$$

For sake of completeness, the formulation of T_x from Jacchia model of atmosphere of 1970 is reported.

All temperature profiles start from a constant value $T_0 = 183\ K$ at the height $z_0 = 90\ km$, rise to an inflection point at a fixed altitude $z_x = 125\ km$ and become asymptotic to a temperature $T_\infty\ or\ T_c$, referred to as the "exospheric" temperature. The temperature equation T_x is

$$T_x = 444.3807 + 0.02385\ T_c - 392.8292\exp(-0.0021357\ T_c) \quad @\ z_x$$

with the constraint that $T_x = T_0$ when $T_c = T_0$ (i.e. for the hypothetical case in which the exospheric temperature is the same as the temperature at 90 km, namely 183 K, there is no variation of temperature with height). [4]

5.2.1.5 High-altitude density correction

All atmospheric models developed to date have only been able to incorporate small amounts of neutral density values above 1000 km due to lack of data at these higher altitudes. The models developed by Jacchia only used a few satellites to correlate long-term density variations with the 11-year variation of the $\bar{F}_{10}$ index, and those satellites were all below 800 km altitude. Later work by Hedin in developing the MSIS models still used only density data below 1000 km. Only a handful of density analyses have been done for satellites in the 1500 km to 4000 km height range. A number of papers were published in the 1970s based on analyses of the orbital decay of the Pageos 1 and Dash-2 balloons. Prior studies found hydrogen concentrations about 3 times that of the U.S. Standard 1966 Atmosphere Supplement for both Pageos and Dash-2 during 1967 when they were at approximately 3500 km altitude. Rousseau analysed Dash-2 data in the height range of 1500 to 3000 km and found that the Jacchia 70 model underestimated the density values by about a factor of 3. Slowey reduced Dash-2 data for selected time spans between 1964 and 1971, and found the Jacchia 70 model again underestimated the density by about a factor of 3. From the previously analyses it appeared that the Jacchia 70 model underestimated the densities at 1500 km to 3500 km by up to a factor of 3, which prompted a more complete analysis of this underestimated high-altitude variation.

The above-mentioned analyses for the height range of 1500 km to 4000 km covered only a short time span relative to the solar 11-year sunspot cycle, and thus no correlation was obtained between density variations and the $\bar{F}_{10}$ solar index. The current JB2006 model uses a recent analysis of over 30 years of density data, in the height range of 1500 km to 4000 km obtained from 25 satellite orbits, to formulate density variations with respect to altitude and the $\bar{F}_{10}$ index.

The atmospheric drag equations required modification for the variation of the drag coefficient. For a circular satellite below 600 km height, the C_D value remains almost constant at 2.2 throughout the 11-year solar cycle. However, C_D is a function of the mass and velocity of the atmospheric constituents, which means that it will increase with altitude as the abundance of the lighter elements increases with altitude. As the height increases, the lighter atomic and molecular species become predominant, depending upon the level of solar activity present. At 3500 km the C_D value can be higher than 4.0, where atomic hydrogen is the dominant species during solar minimum. Figure 5.18 shows three regions representing the log densities of the different high-altitude species as a function of solar activity, each of them separated from the other for clarity. During high solar activity, atomic oxygen is dominant at altitudes from 500 km up to 1200 km, while during solar minimum conditions it loses dominance just above 500 km. During solar minimum the lightest element hydrogen becomes dominant above 800 km, while during solar maximum it does not start showing an effective presence until altitudes over 4000 km have been reached. Therefore, the C_D value changes greatly depending upon altitude and solar conditions.

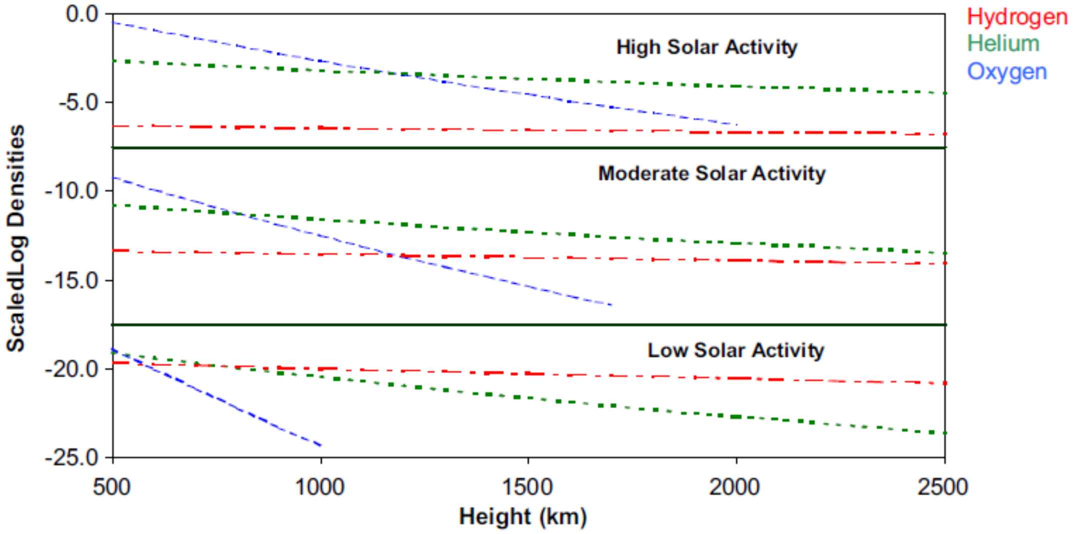

Figure 5.18 - Species abundances as a function of altitude and solar conditions.

Following determination of the 1–2 year average density factors for each satellite, the data were plotted with respect to time and the 81-day average $\bar{F}_{10}$ solar index. Figure 5.19 shows an example of the data obtained for the needle cluster 02530 over the 30-year period of analysis for this satellite. The factors can be separated into periods when hydrogen was dominant ($\rho_{He}/\rho_H < 0.3$), when helium was dominant ($\rho_{He}/\rho_H > 3$), and when an approximately even mixture of hydrogen and helium occurred. The CIRA72 model was used to determine the concentration of each species. Satellite 02530 remained in the height range of 3000–3600km during the entire 30-year span. Figure 5.19 shows that hydrogen was dominant during periods of low solar activity ($\bar{F}_{10} < 90$), while helium was dominant during periods of high solar activity ($\bar{F}_{10} > 150$).

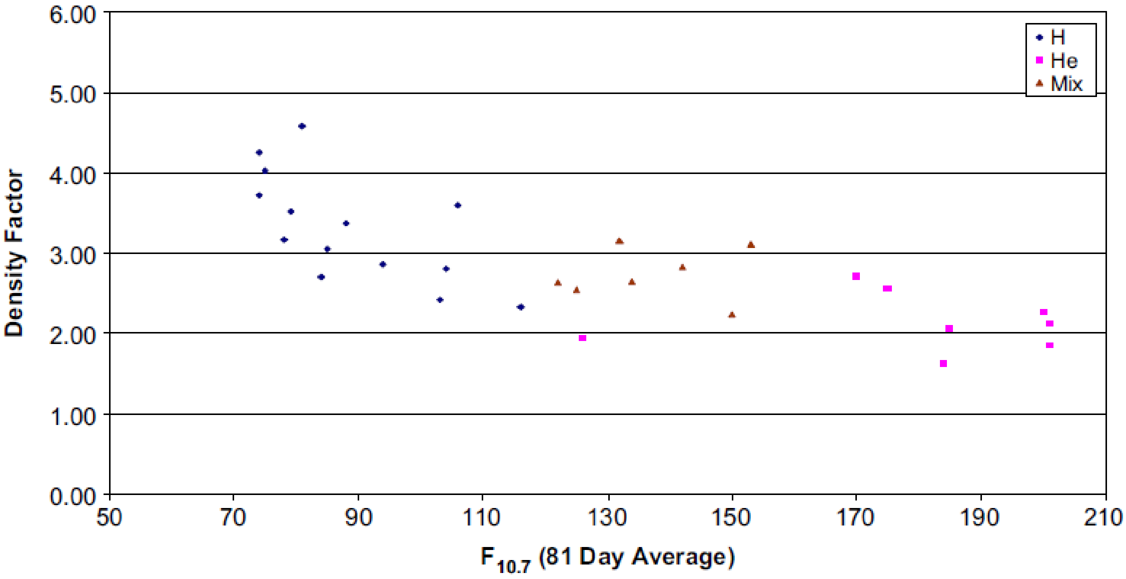

Figure 5.19 - Density factors obtained for satellite 02530 from 1970 to 2000 as a function of F_{10}.

5.2.1.5.1 High-altitude density equations

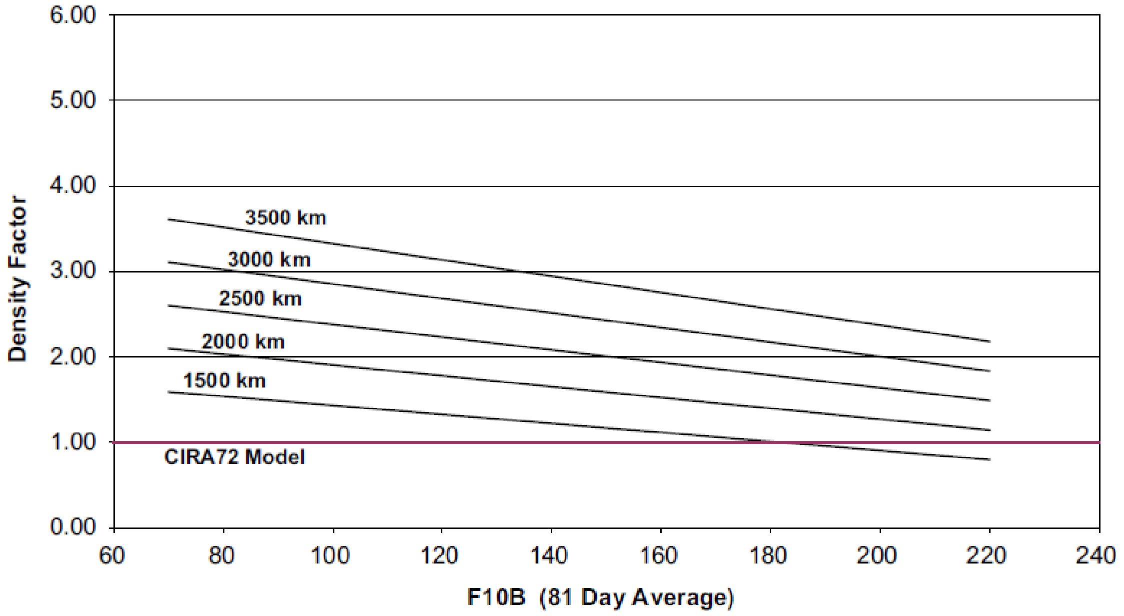

Figure 5.20 - Density factors for CIRA72 (Jacchia 71) model as a function of altitude and F_{10} for attitude from 1000 to 3500 km

The new JB2006 equation plots are shown in Figure 5.20 as a function of height and $\bar{F}_{10}$ values. The least-squares model obtained from fitting the factor data for z > 1500 km is

$$F_\rho = C_1 + C_2\bar{F}_{10} + C_3 z + C_4 z\bar{F}_{10}$$

Where z is the height in km and $\bar{F}_{10}$ is the 81-day F_{10} average.

Between 1000 km (factor = 1.0) and 1500km the factor equation was obtained as a spline fit (factor value and slope equal at boundary values of 1000 and 1500km). For 1500 km > z > 1000km the spline-fit equation is

Equation 5 - Density factor equation

$$F_\rho(H) = \text{density factor}, \quad H = (z-1000)/500$$

$$F_{1500} = \text{density factor at } 1500 \text{ km}$$

$$\frac{\partial F_{1500}}{\partial z} = 500(C_3 + C_4\bar{F}_{10}), \quad \text{partial of density factor at 1500 km}$$

$$F_\rho(H) = 1 + \left\{3F_{1500} - 500\frac{\partial F_{1500}}{\partial z} - 3\right\}H^2 + \left\{500\frac{\partial F_{1500}}{\partial z} - 2F_{1500} + 2\right\}H^3$$

where F_ρ is the density factor applied to the JB2006 high-altitude density computations. The plots in Figure 5.20 agree very well with other authors' previous results mentioned earlier, with the Jacchia models underestimating the densities in the 1500–3500 km altitude range by up to a factor of 3.5, depending upon solar conditions.

5.2.1.6 Model density errors

The new equations described above were incorporated into the JB2006 model, and differential orbit corrections were obtained on different satellites using this new model. Figure 5.21 shows a plot of delta ballistic coefficient values (corrections to the 30-year average value) for one of the satellites during 2001. A value of 0% indicates that the atmospheric model correctly modelled the density during the orbit fit. The JB2006 curve uses the full JB2006 model, the Jacchia 70 curve uses the unmodified Jacchia 70 model, and the intermediate curve uses the JB2006 model, but with the original Jacchia semi-annual equations in place of the new JB2006 semi-annual equations. The delta B values can be attributed strictly to density variations since this satellite is a sphere at a near constant perigee height of 400 km. The standard deviation has decreased from approximately 17% for the Jacchia model to just under 10% using the complete new JB2006 model. The intermediate curve shows that half of this decrease is due to the new semi-annual equations. Additional orbit corrections showed that the new diurnal and latitudinal corrections accounted for approximately 0.5% reduction in the standard deviation. Therefore, the remaining (almost half of the) decrease in the standard deviation can be attributed to using the new T_c equation with the new solar indices. A_p is shown in red, F_{10} and S_{10} are in blue and yellow respectively.

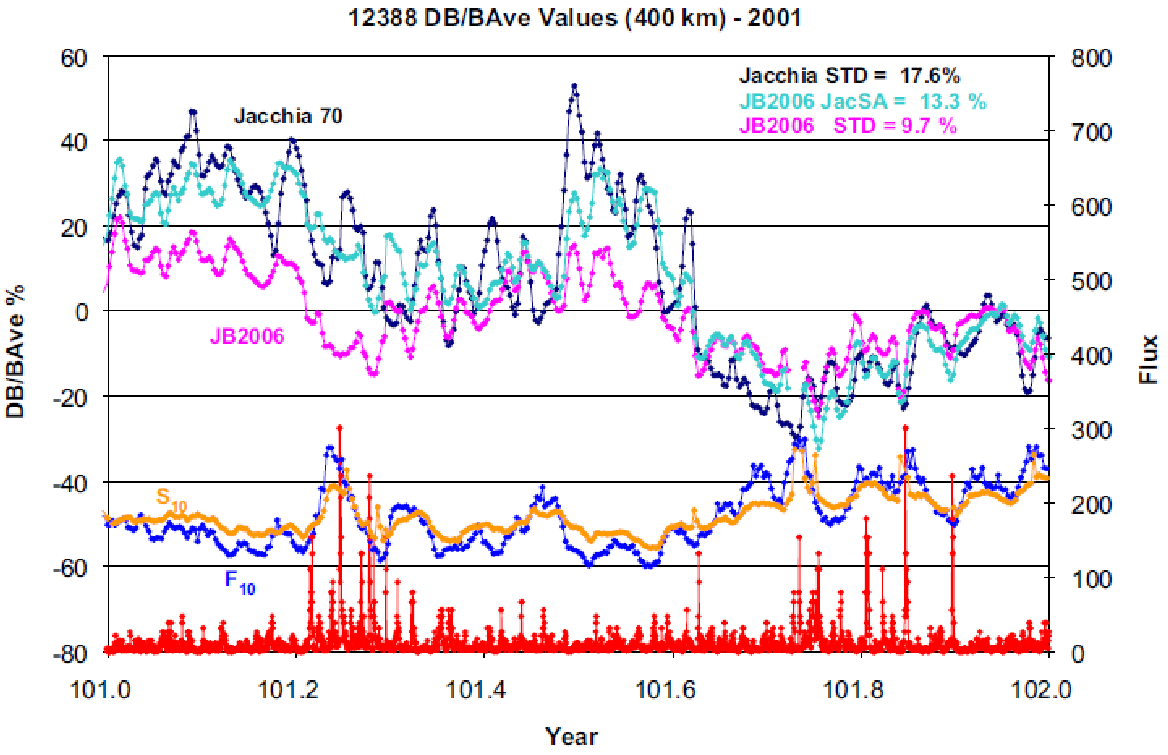

Figure 5.21 - Ballistic coefficient variation for satellite 12388 during 2001

The primary objective was to evaluate density model performance in the 200–1100 km altitude region where satellite drag is the dominant source of tracking errors. It is available an extensive representative set of data capable of evaluating models in the region of maximum importance, with densities from 37 satellites for the period from 1997 through 2004. The data were derived using the method of Bowman (2004) to obtain densities with 1-day temporal resolution for the first time from satellite tracking observations. The density errors are estimated to be less than 5%. Approximately 75,000 daily density values were obtained for the period 1997–2004 throughout the altitude region from about 200 to 1100km. The scope of the current database allows an unambiguous determination of model errors as a function of altitude. These errors for the JB2006, J70 (Jacchia70), NRLMSIS, MET, and DTM models were examined by plotting standard deviation for each individual satellite based on daily data-to-model ratios covering the 1997–2004 period. While the statistics are determined using the actual satellite altitude, the data for each satellite are plotted at their average perigee altitude. Standard deviations are examined in Figure 5.22. The data show a definite increase in model errors with altitude. The marked feature of Figure 5.22 is that standard deviations for JB2006 are systematically lower than those for the other models at all altitudes. This advantage varies from about 2% (vs. J70 and MET) to 6.5% (vs. DTM) near 218km to about 6% vs. all models near 600 km. The NRLMSIS, J70, and MET model errors all agree closely with altitude. The J70 values fall on those of MET up to about 550 km. Therefore, the precision of the JB2006 model represents a significant improvement over all other empirical models. [5]

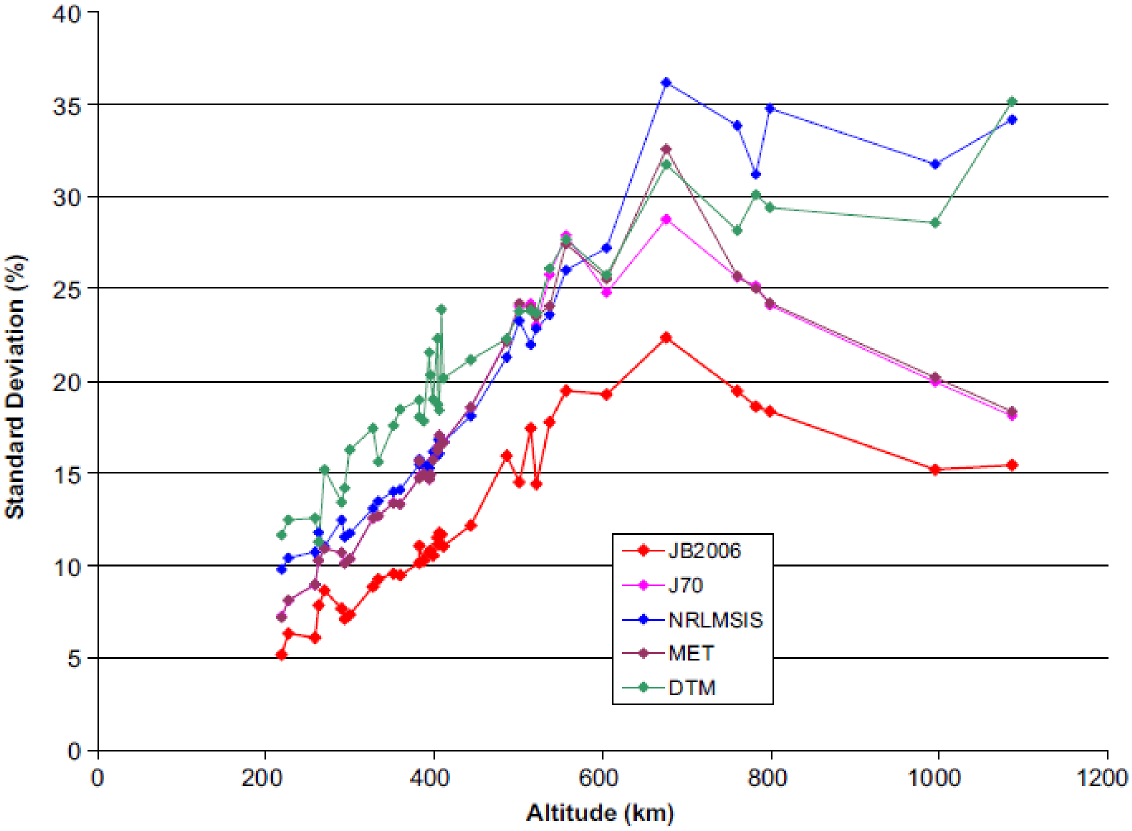

Figure 5.22 - Standard deviation of data-to-model ratios using 1997-2004 daily density data for JB2006, J70, NRLMSIS, MET and DTM models vs altitude

For sake of completeness, hereunder inputs and outputs of the MATLAB code for JB2006 are reported together with the MATLAB function formulation.

```
[T, rho] = jb2006(MJD, SUN, SAT, GEO, S10, S10B, XM10, XM10B)
```

Table 5.2 - JB2006: inputs and outputs

Inputs		**Outputs**	
`MJD`	Modified Julian date	`T`	Exospheric temperature above the input position
`SUN`	Right Ascension of the Sun		
	Declination of the Sun		
`SAT`	Right Ascension of the satellite		Temperature at input position
	Geocentric latitude of the satellite		
	Geodetic altitude of the satellite		
`GEO`	10.7-cm solar flux		
	10.7-cm solar flux, average, 81-day Centred on the input time	`rho`	Total mass density at input position
	Geomagnetic planetary 3-hour index Ap		
`S10`	EUV index (26-34 nm) scaled to F10		
`S10B`	EUV 81-day average Centred index		
`XM10`	MG2 index scaled to F10		
`XM10B`	MG2 81-day average Centred index		

5.2.2 Jacchia-Bowman 2008 (JB2008)

A new empirical atmospheric density model, Jacchia-Bowman 2008, is developed as an improved revision to the Jacchia-Bowman 2006 model which is based on Jacchia’s diffusion equations. Driving solar indices are computed from on-orbit sensor, data are used for the solar irradiances in the extreme through far ultraviolet, including X-ray and Lyman-α wavelengths. New exospheric temperature equations are developed to represent the thermospheric EUV and FUV heating. New semi-annual density equations based on multiple 81-day average solar indices are used to represent the variations in the semi-annual density cycle that result from EUV heating. Geomagnetic storm effects are modelled using the Dst index as the driver of global density changes. The model is validated through comparisons with accurate daily density drag data previously computed for numerous satellites in the altitude range of 175 to 1000 km. Model comparisons are computed for the JB2008, JB2006, Jacchia 1970, and NRLMSIS 2000 models. Accelerometer measurements from the CHAMP and GRACE satellites are also used to validate the new geomagnetic storm equations.

5.2.2.1 Introduction

Until development of the Jacchia-Bowman 2006 (JB2006) model, typical density model errors on the order of 15%-20% one standard deviation were recognized for all empirical models developed since the mid-1960s. These large density standard deviations correspond to maximum density errors of approximately 40-60% as observed in satellite drag data. There are two main reasons for these consistently large values. One is the result of not modelling the semi-annual density variation as a function of solar activity, and the other results from not modelling the full thermospheric heating from solar ultraviolet radiation. Geomagnetic storms provide episodic, and overall smaller, contributions to the standard deviation. All models prior to JB2006 have used the F_{10} and 81-day centred average $\bar{F}_{10}$ proxies as representative of the solar ultraviolet (UV) heating. However, the unmodeled errors derived from satellite drag data all show very large density errors with approximately 27-day periods, representing one solar rotation cycle. These errors are the result of not fully modelling the ultraviolet radiation effects on the thermosphere, which have a one solar rotation periodicity. JB2008 extends the methodology of JB2006 and includes an additional thermospheric layer, i.e., the 85-100 km mesopause and lower thermosphere. In the description below, it is explained the further development of the Jacchia-Bowman models that incorporate new solar indices, a new semi-annual density model, and a new geomagnetic index model.

5.2.2.2 Density data sources

Four different density data sources were used in the development of the JB2008 model. These sources included:

- Air Force daily density values from 1997 through 2007: these values consist of very accurate daily evaluations obtained from drag analysis of numerous satellites with perigee altitudes of 175 km to 1000 km.; the accuracy of the density values was determined from comparisons of geographically overlapping perigee location data, with over 8500 pairs of density values used in the comparisons. The density errors were found to be less than 4% overall, with errors on the order of 2% for values covering the latest solar maximum.
- Air Force HASDM densities values from 2001 through 2005: the Air Force Space Command's High Accuracy Satellite Drag Model (HASDM) processes drag information from the trajectories of 75 to 80 inactive payloads and debris (*calibration satellites*) to solve for a dynamically changing global correction to the thermosphere. This correction covers the altitude range of ~200 to 800 km.; for JB2008 model development densities were computed every 10 seconds along the CHAMP and GRACE orbits using the HASDM temperature coefficients obtained for the 2001 through 2005 time period.
- CHAMP accelerometer densities from 2001 through 2005: another density data source came from the CHAMP (CHAllenging Minisatellite Payload) satellite, a German small satellite mission for geoscientific and atmospheric research and applications, managed by GFZ, Potsdam. CHAMP was launched on July 15, 2000 into an almost circular, near-polar orbit (inclination 87.2°) with an initial average altitude of 450 km. CHAMP carries a very sensitive STAR accelerometer, the data of which can be used

to derive neutral densities. This instrument can measure the non-conservative forces acting on the satellite accurately, including atmosphere drag, sun radiation pressure, and earth albedo, etc. Densities every 10 seconds were available for the 2001 through 2005 time period.

Table 5.3 - CHAMP orbital parameters

CHAMP orbital parameters		
Reference system	Geocentric	
Type of orbit	Low Earth Orbit (LEO)	
Semi-major axis	6823.28	km
Eccentricity	0.0007115	
Inclination	87.18	deg
Period	93.55	min
RAAN	124.21	deg
Epoch	July 15, 2000 @ 12:00:00 UTC	

- GRACE accelerometer densities from 2002 through 2005: a fourth density data source used in this model development came from the GRACE satellite mission (Gravity Recovery and Climate Experiment), the mission objective being to map the global gravity field with unprecedented accuracy. GRACE is a twin satellite configuration, which was launched on March 17, 2002 into an almost circular, near-polar orbit (inclination 89.0°) with an initial altitude of 500 km. GRACE carries extremely sensitive SuperSTAR accelerometers which are an order of magnitude more precise than STAR. Densities every 5 seconds were available for the 2002 through 2005 time period.

Table 5.4 - GRACE orbital parameters

GRACE orbital parameters		
Reference system	Geocentric	
Type of orbit	Low Earth Orbit (LEO) Sun-synchronous	
Semi-major axis	6873.5	km
Eccentricity	0.00182	
Inclination	89	deg
Period	94.5	min
Epoch	March 17, 2002 @ 04:21:00 UTC	

5.2.2.3 Global night-time minimum exospheric temperature

The variations in the ultraviolet solar radiation that heats the earth's thermosphere consists of two components, one related to solar rotational modulation of active region emission, and the other long-term evolution of the main solar magnetic field. The passage of active regions across the disk during a solar rotation period produces irradiance variations of approximately 27 days, while the main solar magnetic field evolution produces irradiance variations over approximately 11 years. The 10.7-cm solar flux, F_{10}, has in the past been used to represent these effects. However, new solar indices have been recently used to compute better density variation correlations with ultraviolet radiation covering the entire Far UV as well as the EUV wavelengths.

In determining a new global night-time minimum exospheric temperature T_c equation with the new solar indices, the density values were converted into daily T_c temperature values using the Jacchia 70 empirical atmospheric density model. To obtain accurate T_c values the large semi-annual density variations had to be correctly modelled. A major density variation, aside from the 11-year and 27-day solar heating effect, is the semi-annual change. This can be as large as 250% from a July minimum to an October maximum during solar maximum years, and as small as 60% from July to October during solar minimum years (at 600 km). The semi-annual variation was computed on a yearly basis from the previously derived density data. Jacchia's 70 semi-annual density model equation was then replaced using these observed semi-annual yearly variations. A smaller correction to Jacchia's model was also made for the observed errors in the latitude and local solar time density variations. From these different model corrections an accurate T_c value, due almost entirely to solar heating, was obtained.

5.2.2.3.1 Solar indices

The solar UV absorption spectrum in the thermosphere was analysed to determine the new solar indices required for the new temperature equation development. The solar index F_{10} is really a proxy index because it is measured at a 10.7-cm wavelength, which is not a direct measure of any ultraviolet radiation and is not absorbed by the atmosphere. Direct ultraviolet heating indices were recently developed that represent the extreme (EUV), far (FUV), and mid (MUV) solar UV radiation. Previous analyses suggested that EUV and FUV indices were required to capture most of the thermospheric heating, and an additional improvement could be obtained by using an index representing UV energy absorption at lower thermospheric altitudes than by using previous EUV and FUV indices. The daily indices selected for this model development include F_{10}, S_{10}, M_{10}, and Y_{10}.

F_{10}: It has the same features as that previously described in JB2006, but, moreover, a running 81-day centred smoothed set of values using the moving boxcar method was created, and these data are referred to as $\bar{F}_{10}$. Both are used with 1-day lag. F_{10} was used by Jacchia to represent all solar energy available for thermospheric heating. Although thermospheric heating is dominated by the solar chromospheric EUV energy, it also comes from coronal soft X-ray, Lyman-α, and photospheric FUV wavelengths.

S_{10}: It has the same features as that previously described in JB2006 but, moreover, a running 81-day centred smoothed set of values using the moving boxcar method was created, and these data are referred to as $\bar{S}_{10}$. Both S_{10} and $\bar{S}_{10}$ are used with a 1-day lag. The new formulation varies very little compared to the previous, at the order of < 0.5%.

$$S_{10} = -2.90193 + 118.512 \; * \; (SOHO\_SEM_{26-34}/SOHO\_SEM_{26-34mean})$$

M_{10}: Also this index has mainly the same features as before but with the addition of a running 81-day centred smoothed set of values using the moving boxcar method was created, and these data are referred to as $\bar{M}_{10}$. However, some considerations must be done. The new formulation can reveal slight differences of up to 1% compared to earlier versions of M_{10}.

$$
\begin{aligned}
M_{10} = -2107.6186 + 8203.0537 * MgII_{cwr} + M_{10}^{*} \\
* (1.2890589 - (8.3777235 * 10^{-5})x - 1)
\end{aligned}
$$

where x = 0,1,2,… is the day number with x = 0 equivalent to starting on 2448542.0 JD (October 12, 1991 12:00 UT) near the peak of solar cycle 22 and M_{10}^{*} is the result of a relationship between the long-term daily $MgII_{cwr}$ and F_{10}, which can translate the M_{10} index into sfu.

Moreover, both M_{10} and M_{81}, its 81-day running Centre-smoothed values, are used with a 2-day lag in JB2008 as a proxy for the Schumann-Runge continuum FUV emission. JB2006 used the same indices, but with a lag time of 5 days since the index was incorporating a combination of lag times from several energy transfer processes in the lower thermosphere to the mesopause. Now, with the addition of the lower altitude (85–100 km) relevant Y_{10} index, a shorter lag time was appropriate for M_{10}, which represents O_2 photodissociation, recombination, conduction, and transport processes at the 95–110 km level.

Y_{10}: it has the same features as the $XL_{10.7}$ described in JB2006, but now the formulation is explained, in sfu:

$$
\begin{aligned}
Y_{10} &= F_{81norm} * X_{10} + (1 - F_{81norm}) * L_{10} \\
L_{10} &= -88.3926 + 3.35891 * 10^{-10} * Lya + 2.40481 * 10^{-22} * Lya^{2} \\
X_{10} &= -42.5991 + 0.533669 * X_{b_{10}}
\end{aligned}
$$

where X_{b10} is the solar X-ray index, Lya represents the hydrogen (H) Lyman-α emission and F_{81norm} consists of the 81-day centred smoothed $F_{10.7}$ (F_{81}) divided by its mean value for the common time frame. X_{10} has a minimum threshold value of 40. Moreover, both Y_{10} and Y_{81}, its 81-day running Centre-smoothed value, are used with the 5-day lag.

The $F_{10.7}$, $S_{10.7}$, $M_{10.7}$, and $Y_{10.7}$ solar indices are formed using the JB2006 methodology and they were created to map energy from specific solar irradiance sources to major thermospheric layers that are dominated by unique atmospheric neutral constituents. Energy that is deposited to the lower thermosphere and mesopause (85-100 km) is now provided.

5.2.2.3.2 T_c temperature equation

Previous analyses of different density model errors have shown that using the $\bar{F}_{10}$ index to capture the 11-year solar cycle variation does not fully represent the entire thermospheric heating, especially during solar minimum conditions. It has been shown that real density-to-model ratios have drops of 30-40% at solar minimum. The $\bar{F}_{10}$ index has long been known to "flatten-out" around solar minimum, while the real EUV heating continues to show variability. However, previous analyses demonstrated that the $\bar{F}_{10}$ index was still better at representing the full 11-year cycle changes than either the $\bar{S}_{10}$ or $\bar{M}_{10}$ index. Therefore, it was decided to use the $\bar{F}_{10}$ index for the great majority of the time, but supplementing it with the EUV $\bar{S}_{10}$ during solar minimum times. With this approach a new 11-year solar index was developed with the following weighting scheme:

$$\bar{F}_s = \bar{F}_{10} \cdot W_T + \bar{S}_{10} \cdot (1 - W_T) \quad where \;\; W_T = \sqrt[4]{\frac{\bar{F}_{10}}{240}}$$

With this new index the solution of the best night-time minimum exospheric T_c equation was obtained using numerous satellites for the years from 1997 through 2007 when all new solar indices were available. The resulting equation is:

$$T_c = 392.4 + 3.227\bar{F}_s + 0.298\Delta F_{10} + 2.259\Delta S_{10} + 0.312\Delta M_{10} + 0.178\Delta Y_{10}$$

The delta values (ΔF10, ΔS10, ΔM10, ΔY10) represent the difference of the daily and 81-day centred average value of each index. The 81-day (3-solar rotation period) centred value was determined to be the best long-term average to use. In the solution, the 2007 solar minimum data was heavily weighted to help better define the density variations during solar minimum times. To avoid increases in T_c due to geomagnetic storms all daily data with the geomagnetic index $a_p \geq 30$ were rejected. This meant that if a solar index required a lag time of 5 days, each of the 5 days prior to the current time had to have $a_p < 30$ for the current daily density data to be used.

It was determined that a lag time of 1 day was the best to use for the F_{10} and S_{10} indices. For using the M_{10} index an analysis determined that the best (least squares minimum) lag time was 2 days, and for Y_{10} a best lag time of 5 days was obtained.

Initially for the JB2006 model, which did not use Y_{10}, the lag time for M_{10} was determined to be 5 days. The M_{10} index was previously accounting for the longer lag times in the lower thermosphere. However, with the addition of the low altitude Y_{10} index, the M_{10} lag time became shorter, and the low altitude longer absorption lag time was captured by Y_{10} combining absorption of X-Rays and Lyman-α at altitudes around 80-90 km.

In order to evaluate the new T_c equation, the “observed” density-to-model ratios were computed for both the JB2006 and new JB2008 models, the Jacchia 70 model, and the NRLMSIS model at 400 km of altitude. The new JB2008 semi-annual equations, discussed in the following sections, were used in the JB2008 evaluation. The “observed” densities were obtained by using the computed 3-hour spherical harmonic HASDM temperature correction coefficients, and computing density values at 10-minute steps along the CHAMP reference orbits obtained for 2001 through 2007. These HASDM-to-Model ratios were then binned by $\bar{F}_{10}$ and plotted in Figure 5.23. It can be readily seen that all the previous models using just $\bar{F}_{10}$ for the 11-year cycle variations show a significant decrease in the ratios at solar minimum conditions. The JB2008 model does much better at representing the solar minimum density decrease, although it still does not completely capture the density variation. Figure 5.24 shows the density model standard deviations binned again by $\bar{F}_{10}$. The much larger sigma at solar minimum (very low $\bar{F}_{10}$) are a direct result of the model ratio errors at low $\bar{F}_{10}$.

The new JB2008 T_c equation is a significant improvement over all other models in representing the solar thermospheric heating.

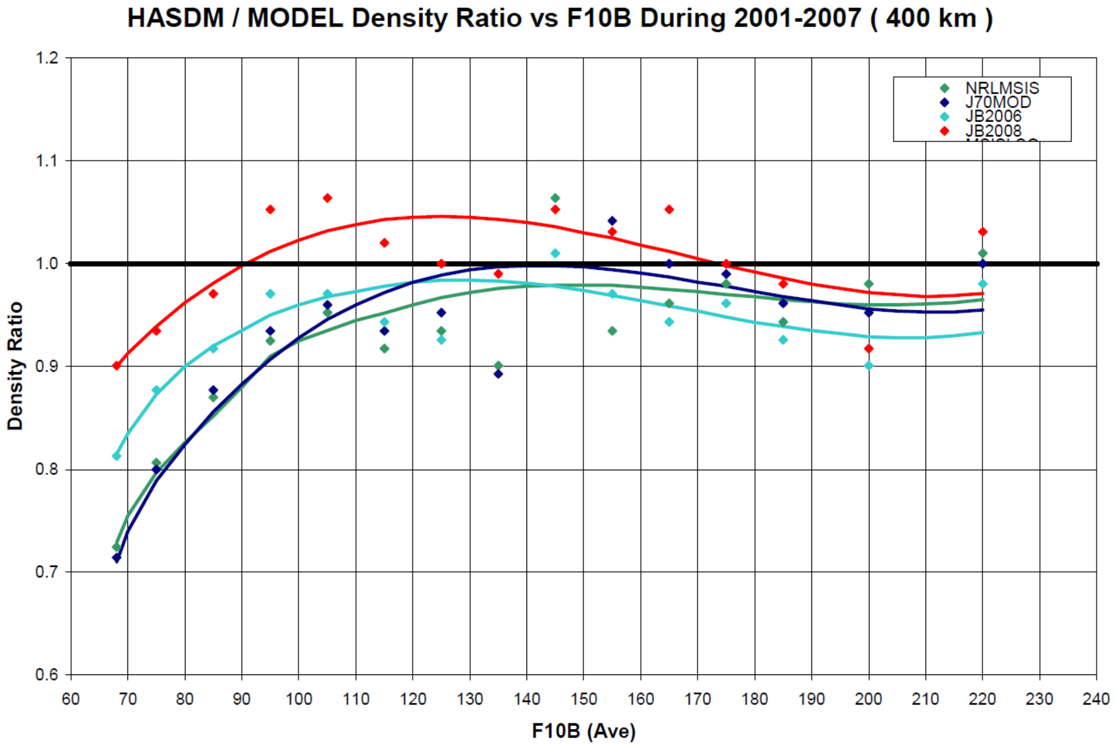

Figure 5.23 - HASDM-to-Model density ratios at 400 km altitude as a function of $F_{10}B$

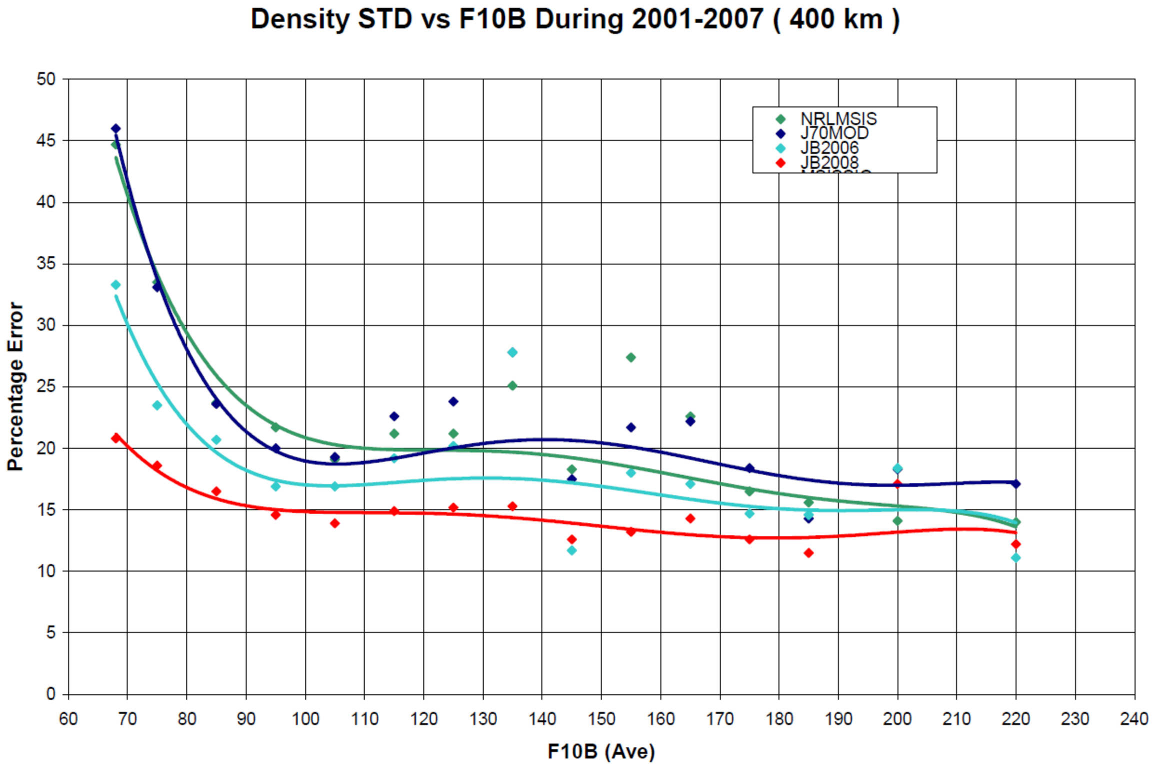

Figure 5.24 - Density percentage errors (1 standard deviation) from model density values at 400 km altitude compared to HASDM density values

5.2.2.4 Semi-annual density variation

The semi-annual density variation was first discovered in 1961. Paetzold and Zschorner observed a global density variation from analysis of satellite drag data, which showed a 6-month periodicity maximum occurring in April and October, and minimum occurring in January and July. Many authors analysed the semi-annual effect from satellite drag during the 1960s and early 1970s. They found that the semi-annual variation was a worldwide effect with the times of the yearly maximum and minimum occurring independent of height. However, the semi-annual period was found to be only approximate, as the times of occurrence of the minima and maxima seemed to vary from year to year. Generally, the October maximum exceeded that in April and the July minimum was deeper than that in January. The main driving mechanism for the observed variability in the semi-annual effect remained a mystery. Jacchia first modelled the effect as a temperature variation which included a function of the 81-day solar flux $\bar{F}_{10}$ index. However, he soon discovered difficulties with the temperature model, and eventually modelled the semi-annual variation as a density variation. He also dropped the $\bar{F}_{10}$ dependence, suggesting that he did not have enough data to support this solar flux relationship. He found that the amplitude of the semi-annual density variation was strongly height-dependent and variable from year to year. However, he could not show a definitive correlation of the variation with solar activity.

5.2.2.4.1 Semi-annual density variation function

Jacchia obtained the following equations from analysis of 12 years of satellite drag data. He represented the semi-annual density variation in the form:

$$\Delta_{SA} \log_{10} \rho = F(z)\, G(t)$$

G(t) represents the average density variation as a function of time in which the amplitude (i.e. the difference in $\log_{10}$ density between the principal minimum in July and the principle maximum in October) is normalized to 1, and F(z) is the relation between the amplitude and the height z, in fact F(z) is the strongly related to the amplitude of the semi-annual variation.

From previous analysis it was determined that a Fourier series could accurately represent Jacchia's G(t) equation structure. A 9-term coefficient series, including frequencies up to 4 cycles per year, was sufficient to capture all the yearly variability in G(t) that had been previously observed by Jacchia. It was also determined that a simplified quadratic polynomial equation in z could sufficiently capture Jacchia's F(z) equation and not lose any fidelity in the observed F(z) values.

5.2.2.4.2 Semi-annual F(z) height function

For the Jacchia-Bowman model developments, the amplitude F(z) of the semi-annual variation was determined on a year-by-year and satellite-by-satellite basis. The smoothed density difference data was fit each year for each satellite using a 9 term Fourier series. The F(z) value was then computed from each fit as the difference between the minimum and maximum values for the year.

Figure 5.25 shows the results of three different years of data, along with the plot of Jacchia's constant F(z) function. For each year, the F(z) values were fit with a quadratic polynomial in height. The smoothed curves shown in Figure 5.25 represent the least squares quadratic fit obtained for three different years. The $\Delta_{SA}\log_{10}\rho$ data of F(z) for all satellites are very consistent within each year. The most notable feature in Figure 5.25 is the very large difference in maximum amplitude among the years displayed. The 2002 data shows a maximum density variation of 250% near 800km, while the 1993 data shows only a 60% maximum variation. Jacchia's F(z) function only gives a constant 130% maximum variation for all years.

Previous development of the JB2006 model showed that solar EUV and FUV heating played an important part in thermospheric density variations. Bowman extended the previous semi-annual work to include additional solar EUV indices in an attempt to capture the remaining semi-annual variations not modelled by the JB2006 model.

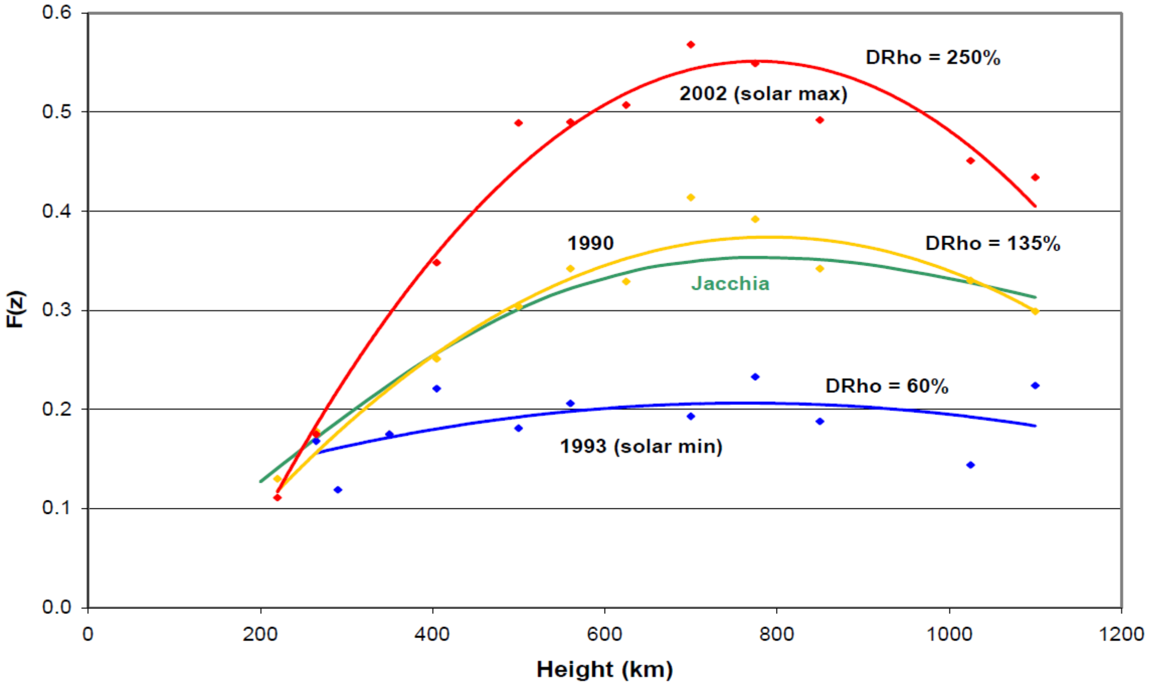

Figure 5.25 - The amplitude function F(z) for three different years (1990, 1993, 2002)

Roble computed the thermospheric temperature response to solar EUV heating using his coupled thermosphere and ionosphere global average model. He found that removing the He II 30.4 nm emission produced the largest (by a factor of 2) temperature change. Therefore, it was very important to select an EUV index that captured the emission of this He II irradiance line. These results together with previous analysis of thermospheric response to new solar indices suggested a new set of solar indices to use for the semi-annual variation. New 81-day centred $\bar{S}_{10}$ and $\bar{M}_{10}$ indices were computed for use along with the previous $\bar{F}_{10}$ index.

Previous work determined the new solar index for F(z) to be

Equation 6 – New solar index F_{SMJ}

$$\bar{F}_{SMJ} = 1.00\,\bar{F}_J - 0.70\bar{S}_J - 0.04\bar{M}_J$$

where the $\bar{F}_J$, $\bar{F}_J$, and $\bar{F}_J$ indices represent the July averages of the $\bar{F}_{10}$, $\bar{S}_{10}$, and $\bar{M}_{10}$ indices respectively. This $\bar{F}_{SMJ}$ index was then used to determine which terms were significant in defining a new F(z) equation. The resultant new F(z) equation, with z = height/1000, using the new index was determined to be

Equation 7 - Resultant new F(z) equation

$$F(z) = B_1 + B_2\bar{F}_{SMJ} + B_3 z\bar{F}_{SMJ} + B_4 z^2\bar{F}_{SMJ} + B_5 z\bar{F}_{SMJ}^2$$

Table 5.5 lists the resulting B coefficient values with their standard deviations obtained from using Equation 6 for the solar index required in Equation 7. The standard deviations of all the coefficients are an order of magnitude less than the coefficient values, indicating that all five coefficients have been well determined.

Equation 7 using $\bar{F}_{SMJ}$ represents a global equation in F(z) using data from yearly semi-annual amplitudes observed from 1997 through 2006. For incorporation into JB2008 the 81-day centred July average values are replaced by daily 81-day centred values of $\bar{F}_{10}$, $\bar{S}_{10}$, and $\bar{M}_{10}$. This is an approximation to the best fit equation. Using the daily 81-day Centred values in Equation 6 and Equation 7 result in an increase in the density error standard deviation of less than 1%.

Table 5.5 - F(z) coefficient values with standard deviations from best fit results

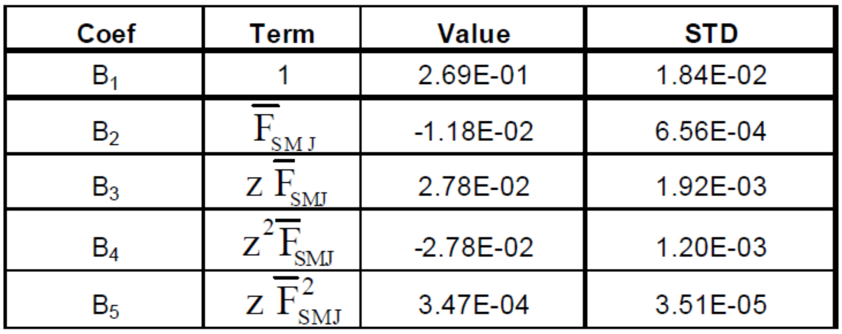

Coef	Term	Value	STD
B_1	1	2.69E-01	1.84E-02
B_2	$\bar{F}_{SMJ}$	-1.18E-02	6.56E-04
B_3	$z\bar{F}_{SMJ}$	2.78E-02	1.92E-03
B_4	$z^2\bar{F}_{SMJ}$	-2.78E-02	1.20E-03
B_5	$z\bar{F}_{SMJ}^2$	3.47E-04	3.51E-05

5.2.2.4.3 Semi-annual G(t) yearly periodic function

The yearly observed G(t) function, as previously discussed, consists of a Fourier series with 9 coefficients representing a quadannual variation. 28-day smoothed density difference data for each satellite was fitted with this Fourier series for each year. The density difference data is the accurate observed daily density values minus the Jacchia values without Jacchia’s semi-annual variation. The G(t) function was then obtained by normalizing to a value of 1.0 the difference between the minimum and maximum values for the year. The F(z) value for each satellite by year was used for the normalization. Figure 5.26 shows the results obtained for the year 1990 for the majority of the satellites. Note the tight consistency of the curves for all heights, covering over 800 km in altitude, which demonstrates the validity of using one G(t) function per year to represent the yearly semi-annual phase for all altitudes. This tight consistency of the G(t) phase for all satellites also indicates that there is no significant latitude or local solar time effects with the semi-annual density variation. This conclusion can be made because the majority of the satellites have moderate to high eccentricity orbits. This means that the great majority of the density sampling on each revolution occurs very close to the perigee location, and the daily density values computed from the orbit decays can be assigned to the argument of perigee latitude and local solar time, which is different for each satellite. The precession of the argument of perigee can be very slow (from zero to a few degrees per day), so if there is a latitude or local solar time semi-annual effect the G(t) phase curves in Figure 5.26 should show significant differences because of the random nature of the argument of perigee locations. This is definitely not observed when comparing all of the individual satellite G(t) phase curves.

The next step in the study was to fit a yearly 9-term G(t) function for each year using the data for all the satellites for the year. Figure 5.26 also shows the yearly fit G(t) value for the year 1990. A small standard deviation was obtained for every year's fit, especially during solar maximum years. Figure 5.27 shows the yearly G(t) fits for 1999 through 2001, again showing the consistency of the semi-annual phase at all altitudes for a given year. Each set of curves of 1999 and 2001 has been offset by +1.00 and -1.00 respectively for clarity. Moreover, it is readily apparent that the series changes dramatically from year to year. It was determined that during solar maximum the July minimum date can vary by as much as 80 days. During solar minimum, the semi-annual July minimum time variation is much smaller and appears to be flattened out in time.

As was done for the F(z) analysis it was decided to combine the new 81-day average indices in a linear function since each index is expressed in terms of F_{10} units and this approach worked very well for the F(z) analysis. A new solar index, representing long term EUV and FUV heating, was determined to be

Equation 8 - New solar index F_{SM}

$$\bar{F}_{SM} = 1.00\,\bar{F}_{10} - 0.75\bar{S}_{10} - 0.37\bar{M}_{10}$$

It was decided to start out using only annual and semi-annual terms, instead of the JB2006 quadannual terms previously used, to try to represent the yearly semi-annual phase variations. The yearly observed values had been fit with terms up to quadannual, but it was hoped that only terms up to semi-annual needed to be included for a global model. The resulting equation was

Equation 9 - Resulting G(t) equation

$$\begin{aligned} G(t) = {} & C_1 + C_2\sin(\omega) + C_3\cos(\omega) + C_4\sin(2\omega) + C_5\cos(2\omega) + \\ & + \bar{F}_{SM}\{C_6 + C_7\sin(\omega) + C_8\cos(\omega) + C_9\sin(2\omega) + C_{10}\cos(2\omega)\} \end{aligned}$$

The coefficients in Equation 8 are better defined than those for the F(z) index function specified by Equation 6 . This is because density (G(t)) data and $\bar{F}_{SM}$ values were available throughout the entire year as opposed to using one July averaged value per year to derive Equation 6.

Table 5.6 lists the resulting C coefficient values with their standard deviations obtained from using Equation 8 for the solar index used in Equation 9. The standard deviations of the coefficients are all an order of magnitude smaller than the coefficient values except for the C_7 and C_8 $\bar{F}_{SM}$ annual terms, indicating a well determined set of coefficients.

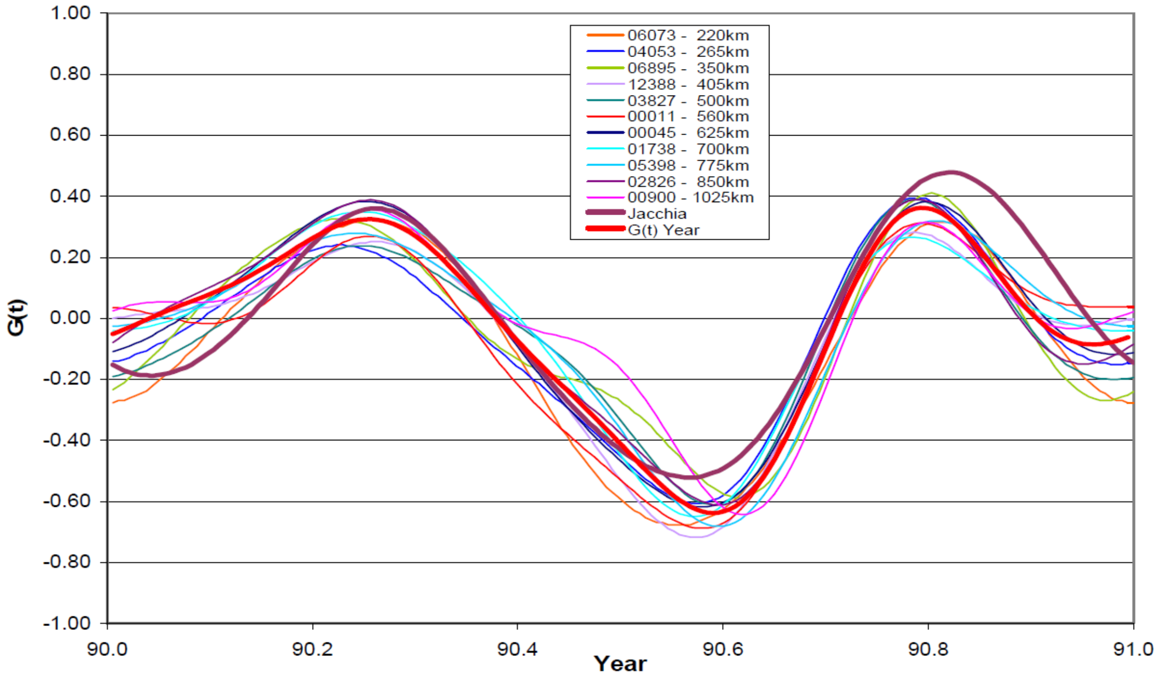

Figure 5.26 - The individual satellite G(t) fits plotted for 1990 together with Jacchia model and yearly fit model

Table 5.6 - G(t) coefficient values with standard deviations from best fit results

Coef	Term	Value	STD
C_1	1	-3.63E-01	6.33E-03
C_2	$\sin(\omega)$	8.51E-02	9.23E-03
C_3	$\cos(\omega)$	2.40E-01	8.60E-03
C_4	$\sin(2\omega)$	-1.90E-01	8.61E-03
C_5	$\cos(2\omega)$	-2.55E-01	8.79E-03
C_6	$\bar{F}_{SM}$	-1.79E-02	3.63E-04
C_7	$\bar{F}_{SM}\sin(\omega)$	5.65E-04	5.39E-04
C_8	$\bar{F}_{SM}\cos(\omega)$	-6.41E-04	4.77E-04
C_9	$\bar{F}_{SM}\sin(2\omega)$	-3.42E-03	4.91E-04
C_{10}	$\bar{F}_{SM}\cos(2\omega)$	-1.25E-03	5.07E-04

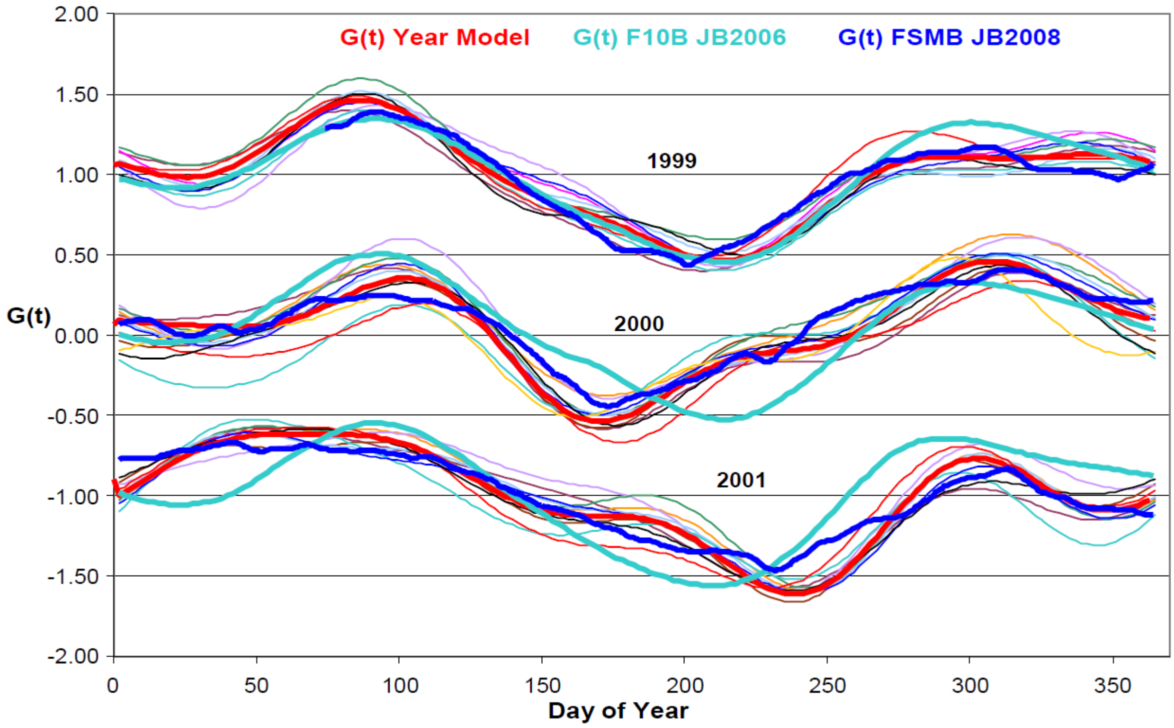

Figure 5.27 - The individual satellite fits for three different years with Year G(t) model highlighted

The results of the new global model from Equation 8 and Equation 9 are plotted in Figure 5.27 as the FSMB model. Also plotted are the yearly observed values for each year, and the original JB2006 $\bar{F}_{10}$ global model values. The 10-term new model results are impressive. Even with only annual and semi-annual terms the new model accounts almost completely for the July minimum phase shifting which could not be captured in the $\bar{F}_{10}$ global model using even quadannual terms. This clearly demonstrates that the large majority of the variations observed in the semi-annual density variation can be attributed to direct solar heating responses.

5.2.2.5 Geomagnetic storm modelling

JB2008 uses two geomagnetic indices, a_p and Dst. a_p is essentially the same as that described in JB2006 model but there is a new one, Dst, that adds a strong contribution to the atmosphere's modelling. Dst in an index of the strength of the geomagnetic storms of the Sun. The a_p geomagnetic and Dst ring current indices are used in a two-index formulation that captures both low/unsettled activity and substorms/storms to represent changes to the neutral thermospheric densities as a result of high-latitude Joule heating and charged particle precipitation. These processes result in the interaction with the dynamics of, and the photoabsorbtion energy process in, the neutral atmosphere and lead to increased densities during geomagnetic storms. Moreover, the storm effects change the rate of exospheric temperature change, dT_c, which affects satellite orbits.

5.2.2.5.1 Dst index description

A ring current is an electric current carried by charged particles trapped in a planet's magnetosphere. It is caused by the longitudinal drift of energetic (10–200 keV) particles. Earth's ring current is responsible for shielding the lower latitudes of the Earth from magnetospheric electric fields. It therefore has a large effect on the electrodynamics of geomagnetic storms. The ring current system consists of a band, at a distance of 3 to 8 R_E, which lies in the equatorial plane and circulates clockwise around the Earth (when viewed from the north). The particles of this region produce a magnetic field in opposition to the Earth's magnetic field and so an Earthly observer would observe a decrease in the magnetic field in this area. The negative deflection of the Earth's magnetic field due to the ring current is measured by the Dst index. The ring current energy is mainly carried around by the ions, most of which are protons. However, one also sees alpha particles in the ring current, a type of ion that is plentiful in the solar wind. In addition, there is a certain percentage of O+ oxygen ions, similar to those in the ionosphere of Earth, though much more energetic.

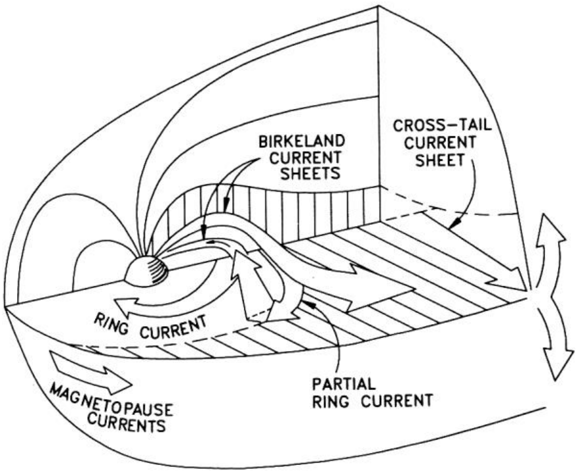

Figure 5.28 - Schematic view of the different current systems which shape the Earth's magnetosphere

The Disturbance Storm Time (Dst, Kyoto Dst) index is a measure in the context of space weather. It is primarily used to indicate the strength of the storm-time ring current around the Earth in the inner magnetosphere caused by solar protons and electrons.

During the main phase of magnetic storms, the ring current around the Earth becomes highly energized, as the number of particles increases, and produces a southward-directed magnetic field perturbation at low latitudes on the Earth’s surface. This is opposite to the normal northward-directed main field. Moreover, if the difference between solar electrons and protons gets higher, then Earth's magnetic field becomes weaker, so a negative Dst value means that Earth's magnetic field is weakened and this only occurs during solar storms.

The index is determined from hourly measurements of the magnetic field made at four stations around the Earth’s equator (Hermanus (HER), South Africa; Kakioka (KAK), Japan; Honolulu (HON), Hawaii; and San Juan (SJG), Puerto Rico) and is released by World Data Centre (WDC) in Kyoto, Japan.

After initial explanations, the treatment is moved to a practical example.

Most magnetic storms begin with sharp rises in Dst, called the storm sudden commencement, in response to increased solar wind pressure. Following a southward turning of the interplanetary magnetic field, Dst decreases as ring current energy increases during the storm's main phase. During the recovery phase the ring current energy decreases and Dst increases until the storm's end. Traces of Dst show a transition from the early to late recovery phase characterized by significant changes in slope as the distribution of the ring current becomes symmetric in local-time. However, a significant fraction of magnetic storms manifests more complex structuring, with multiple main and partial recovery phases. Figure 5.29 is useful for an example of the Dst events during a complex storm.

Use of Dst as a parameter of the energy deposited in the thermosphere during magnetic storms is more accurate than the use of the a_p index. The 3-hour a_p is an indicator of general magnetic activity over the Earth and responds primarily to currents flowing in the ionosphere and only secondarily to magnetospheric variations. The a_p index is determined by observatories at high latitudes which can be blind to energy input during large storms and thus underestimate the effects of storms on the thermosphere.

As described below the thermosphere acts during storm periods as a driven-but-dissipative system whose dynamics is represented by a differential equation, with the changes in exospheric temperature change given as a function of Dst. To determine the exospheric temperature, and thereby the thermospheric density distribution at any time in a storm, it is necessary to integrate the differential equation for dT_c starting at the storm commencement and proceeding throughout the entire storm period. Therefore, it is necessary to recognize where Dst measurements come in a particular storm's development.

An algorithm for determine the storm events was developed for locating in time the start, Dst minimum, recovery slope change, and final end of the storm. For practical reasons a magnetic disturbance is defined as a storm only if the minimum Dst < -75 nT. It was selected this value because disturbances with minimum Dst > -75 nT often lack identifiable storm profiles. Once the starting point of the storm is determined the algorithm steps forward in time until the minimum Dst value is obtained. This is defined as the end of the storm main phase. Because individual Dst traces may exhibit several local minima before reaching the deepest minimum, the algorithm specifies the real storm minimum point. Once the minimum is identified the algorithm continues stepping forward through the recovery phase until a major slope change is detected. From this point to the end of the storm the Dst slope is relatively shallow. It has been found that Dst takes much longer to recover than does the thermosphere. To determine a "real" density recovery time more than 80 storms were analysed. A linear fit of storm duration verse storm magnitude was obtained to give an equation for the approximate end time of the storm. The algorithm determines if the storm ends before this by examining when the Dst values are above the -75 nT limit. The lesser in time of the Dst limit or linear fit time is used for the end time. For complex storms (a second disturbance starts before the previous one ends) the algorithm determines the start, minimum, recovery slope change, and end point events of each storm. For a multiple storm the starting time of the second storm will be at the same time as the ending point of the first storm. Figure 5.29 shows the events for a complex storm. Even if the temperature and density are required at some point during the second storm it is important to start the temperature integration at the commencement of the first storm and carry it through into the second storm, since the thermosphere would already be heightened when the second disturbance began.

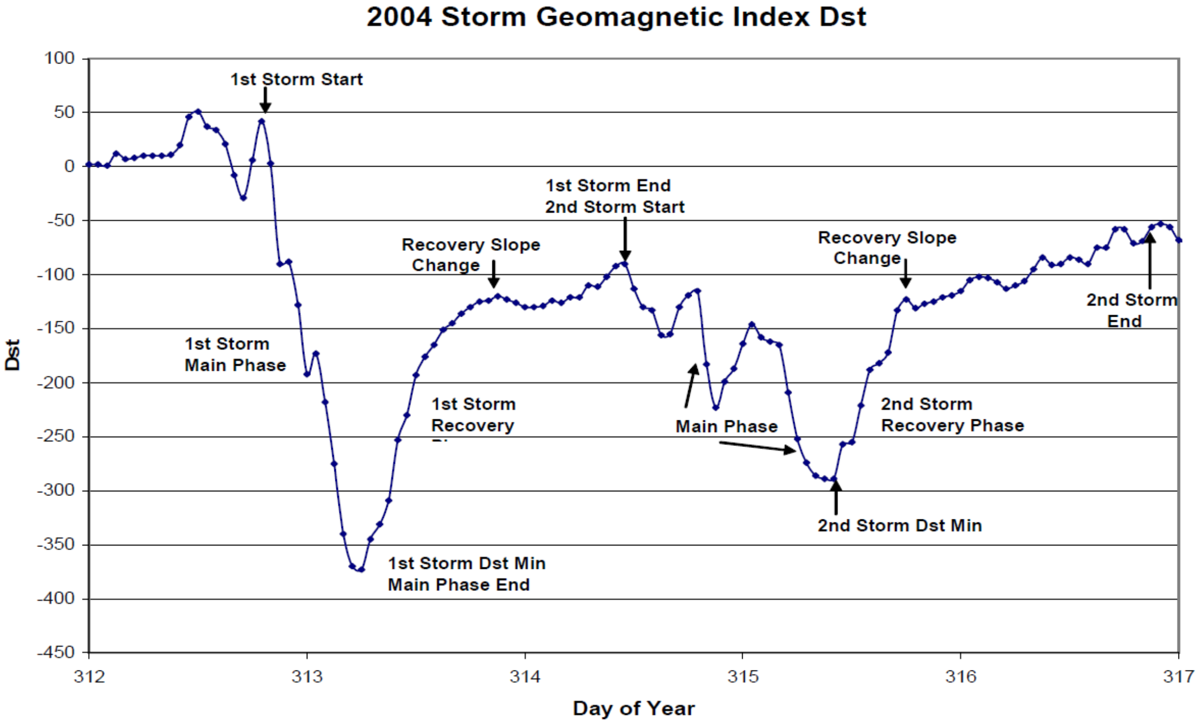

Figure 5.29 - Example of multiple storm during 2004, showing the different storm events

The geomagnetic indices used in JB2008 incorporate existing as well as expanded empirical modelling formulations compared to previous Jacchia and MSIS-type models. A two-index formulation now captures low, unsettled, and substorm/storm related geomagnetic activity. When the a_p value is 40 and below (unsettled to quiet activity), the a_p value is used. Above that threshold the code assumes that there is a storm/substorm in progress and Dst is used.

5.2.2.5.2 Dst temperature equation

Wilson suggested that on a global scale the storm-time thermosphere acts like a large thermodynamic system that never strays far from equilibrium. From an analysis of GRACE density measurements, Burke further argued that the energy input to the thermosphere can be treated as a large driven-but-dissipative thermodynamic system, which can be described by differential equations similar to that of a resistor-inductor circuit. The driver is the magnetospheric electric field. They also demonstrated that Dst and storm-time changes of the exospheric temperature dTc share the same driver but have different relaxation time constants. By eliminating the electric field term from the two equations Burke established the following relation to determine exospheric temperature responses as a function of Dst.

$$dT_{c_1} = \left(1 - \frac{1}{\tau_1}\right) dT_{c_0} + S\left[Dst_1 - \left(1 - \frac{1}{\tau_2}\right) Dst_0\right]$$

where τ_1 and τ_2 represent the temperature and Dst relaxation times. From an analysis of the GRACE data during 2004 storms Burke obtained values of τ_1 = 6.5 hours and τ_2 = 7.7 hours; the slope S ≈ 1.58. dTc is the rate of exospheric temperature change and it affects satellite orbits.

The previous equation was integrated from storm commencement time until storm end time, producing exospheric temperature change values every hour throughout the storm period. These temperature change values were input into the JB2008 model to represent the geomagnetic storm effects at all points throughout the storm.

Comparisons of orbit averaged density values were obtained using results from the previous equation and the CHAMP and GRACE accelerometer densities. Since it had been shown that the Dst index was proportional to “global” thermospheric variations, it was decided to use orbit averaged values for all the comparisons. Using that equation, it produced good correlations of the JB2008 model density with the accelerometer data, but it was noticed that the model and data deviations became greater as the maximum storm magnitude decreased among all storms. It was decided to re-determine the value of the slope S while accepting Burke’s values of both the relaxation parameters. An optimization study during the JB2008 development determined that these τ_1 and τ_2 values were the best to use. This was done for several storms varying from minor to major. The slope value for each storm was optimized by minimizing the differences of the JB2008 model orbit averaged density ratios using the equation above with the orbit averaged accelerometer ratios during the main phase region. The newly determined slope for each storm was then plotted as a function of the storm Dst minimum value, and also plotted as a function of the ΔDst (minimum-maximum) value. The Dst minimum values produced the least scatter of the data.

The following equation represents the new quadratic function for S as a function of the Dst minimum (Dst_{MIN}) value. If Dst_{MIN} < -450 then S = -1.40.

$$S = -1.5050 \cdot 10^{-5}(Dst_{MIN})^2 - 1.0604 \cdot 10^{-2} Dst_{MIN} - 3.20 \quad [S] = \frac{deg}{Dst}$$

Using this new slope quadratic equation produced very consistent results for storms of all magnitudes. However, a few additional adjustments had to be made to produce even better results. It was discovered that starting the dTc integration at dTc = 0 for the storm commencement time sometimes resulted in large negative temperature changes at storm start. This was due to the fact that the thermosphere was already at a slightly heightened temperature state. Therefore, it was decided to start the dTc integration with a value equal to a temperature change obtained from Jacchia’s 1970 geomagnetic storm equation using the 3-hour a_p value (with a 6.7-hour lag time) at the start time. Further analysis of all the storms showed that this produced better results than using an initial zero value. A second adjustment during this main phase analysis occurred during sub-storms when the Dst variations became positive. The density values did not drop as expected. In fact, the accelerometer and HASDM density changes during these time periods continued to increase even though the Dst value was increasing during these short main phase time periods. Additional equations were developed for these time periods:

$$dT_{c_1} = dT_{c_0} + S_{FAC}S(Dst_1 - Dst_0)$$

where the best factor S_{FAC} was found to be 0.3 for all storms. Since S is negative and ΔDst is positive during these time periods, this equation has the effect of continuing to increase the temperature change (and therefore the density) even though Dst is increasing during these times. Using this equation in the JB2008 model produced better correlations with the accelerometer data. Finally, it was noticed that a small lag time was needed to better represent the main phase density increase, especially during small storm events. It was determined that for large storms (Dst < -350), moderate storms (-350 < Dst < -250), and minor storms (-250 < Dst) lag times of 0, 1, and 2 hours respectively better represented the main phase density changes.

The recovery phase was addressed after the main phase equations had been developed. The first dTc_1 equation and the S equation were initially used to represent the recovery phase changes. This did work well except for a few outstanding cases. Each storm was re-optimized for the recovery phase by optimizing the slope for this phase only. However, the recovery phase of the large 2003 multiple storm did not fit the accelerometer density data even with optimizing first dTc_1 equation just for the recovery phase. It was decided to optimize τ_1 and τ_2 for this phase. After many trials the best fit for the 2003 multiple storm was and $\tau_1=\infty$ and $\tau_2=1$. A new slope was then obtained for this storm, and the resulting equation for this large storm was:

$$dT_{c_1} = 1.00dT_{c_0} + 0.13Dst_1$$

The next step was to determine the varying slopes for storms of other magnitudes. Surprisingly this last equation was found to be the best representation for all the other storms representing all magnitudes. This single slope value was excellent for the entire recovery phase up to the recovery slope change.

The final equation fitting was for the period covering the recovery slope change to the end of the storm. It was decided to use the simpler equation below since it was supposed that for this time period the ring current had disconnected from the ionosphere, which meant that the function representing the ring current energy release was unknown.

$$dT_{c_1} = dT_{c_0} + S(Dst_1 - Dst_0)$$

The resulting slope S was found to be a constant -2.5 to best fit all the storms. It was found sometimes that dTc became negative towards the "end" time of the storm because the end time was not defined correctly. To make sure this didn't occur, the algorithm sets dTc = 0 when the integration step produces a negative dTc. Finally, for Dst "non-storm" periods (Dst>-75), JB2008 uses Jacchia's 1970 dTc equation as a function of the 3-hour a_p value. When the JB2008 storm computation algorithm has determined that no Dst storm is present, then if $a_p > 50$, a value of 50 is used for the dTc. This avoids large spurious density increases due to high a_p values when no storm really exists.

5.2.2.5.3 Dst modelling results

Using these equations for each of the 3 different storm phases results in very good comparisons of the JB2008 density values with the accelerometer and HASDM values. Figure 5.30 and Figure 5.31 below are examples of plots of model density ratios during two major storm periods. Yearly average density values were obtained for the CHAMP and GRACE data. The displayed CHAMP density ratios are orbit averaged values/yearly average, and then multiplied by 1.17 to adjust to the HASDM values. The 17% factor is based on averaging the CHAMP/HASDM ratios over the 2001-2005 time period. A factor of 0.74 was obtained for the GRACE/HASDM ratios based on all data from 2002 through 2005. The HASDM values plus other model values are orbit averaged (along the CHAMP or GRACE orbit), with all ratios based on each year's CHAMP (or GRACE) average density value. Figure 5.30 shows the 2004 major storm period when the GRACE accelerometer data was available, and Figure 5.31 shows the 2003 major storm period when the CHAMP accelerometer data was available. The HASDM ratios agree extremely well with the accelerometer data following the single calibration for each data set. The JB2008 model also is very consistent with the density changes throughout each storm, indicating that the JB2008 model temperature equations are working extremely well for these orbit altitudes of 400 to 500 km. The MSIS (NRLMSIS) density values are mostly low at storm peak times during the largest storms, which is consistent with the results previously reported by Burke. The Jacchia 70 (J70) values are extremely high at peak storm times because they are based on single a_p values which are maxed out at a value of 400 when the magnetometers are saturated. For the 2003 storms in Figure 5.31 both the MSIS and J70 values before and after the storm periods are much too high, a result of not correctly modelling the solar EUV during this period when the 27-day F_{10} values were exceptionally high.

Finally, Figure 5.32 shows 1-standard deviation model density errors as a function of storm magnitude. The values were obtained as percent density differences from the calibrated orbit averaged accelerometer data, from both CHAMP and GRACE, and the different model orbit averaged values. The results show that the JB2008 model is a major improvement over modelling density changes during large geomagnetic storms. The HASDM modelling is the best at under a 10% sigma, which is expected since it accounts for real time density changes. The J70 modelling is the worst since it is based on computing a density from a single 3-hour a_p value, while the MSIS model uses a history of a_p values for 57 hours prior to the time of interest.

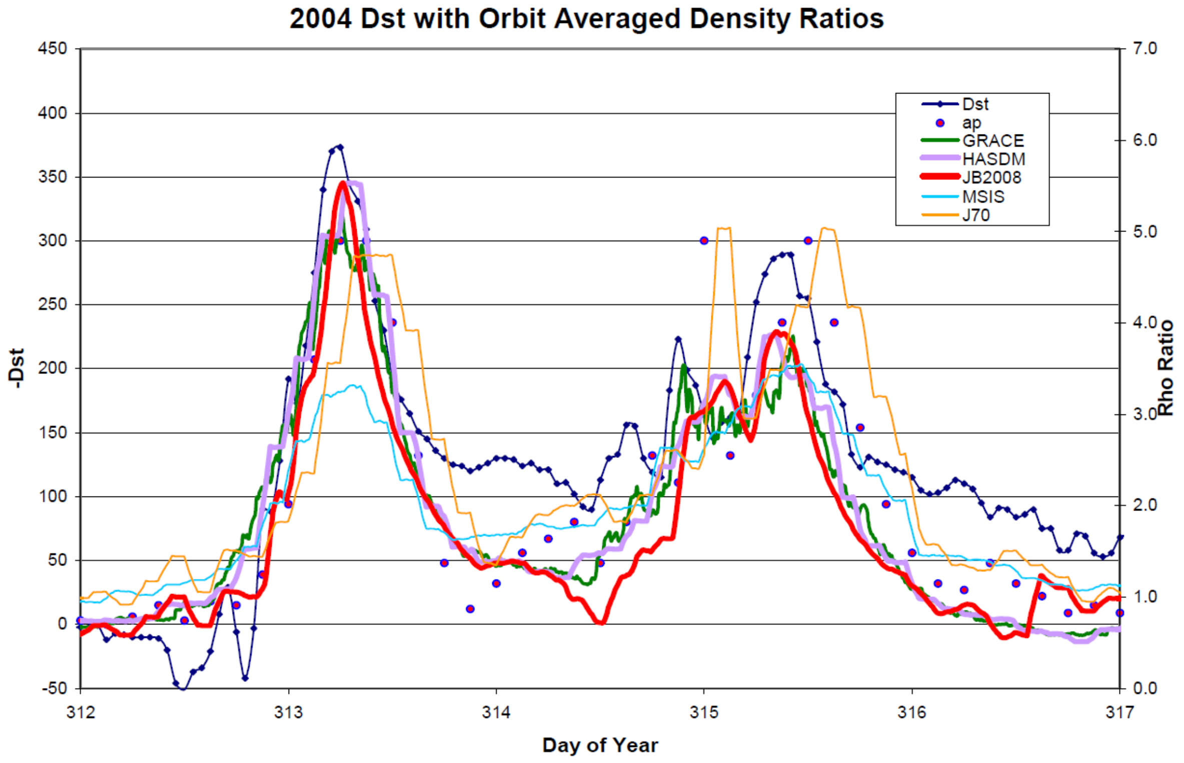

Figure 5.30 - Major 2004 storms with Dst, a_p (left scale) and density ratios

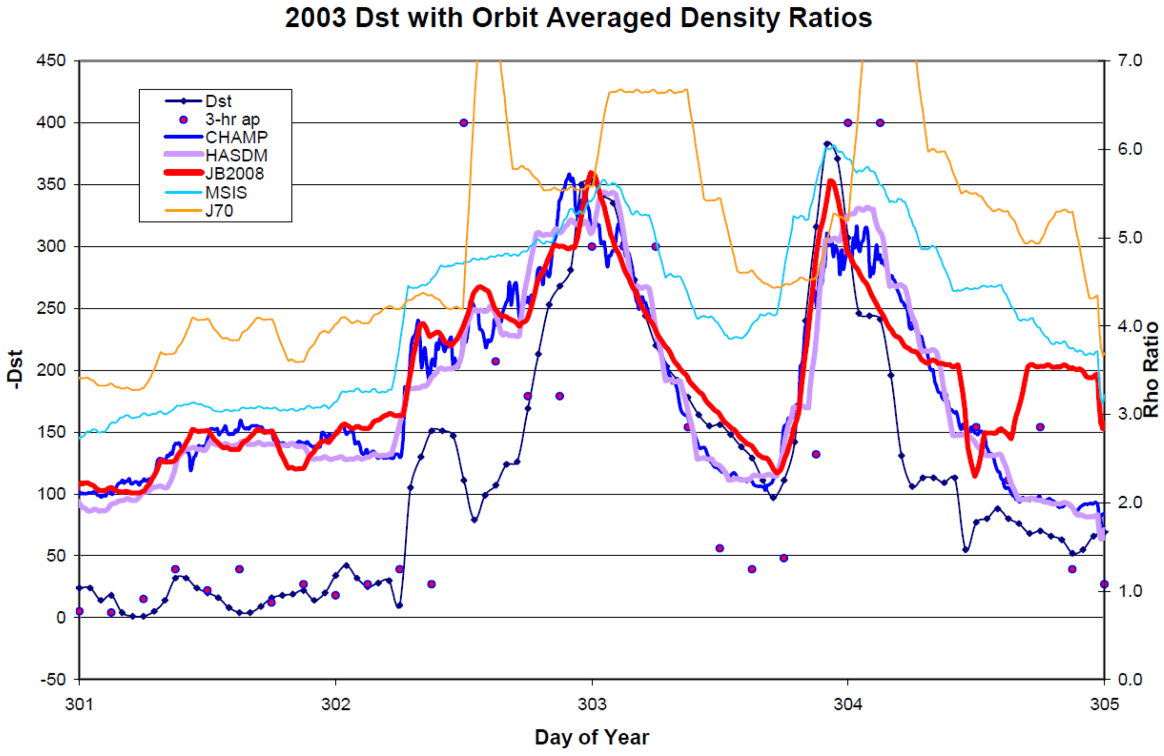

Figure 5.31 - Major 2003 storms with Dst, a_p (left scale) and density ratios

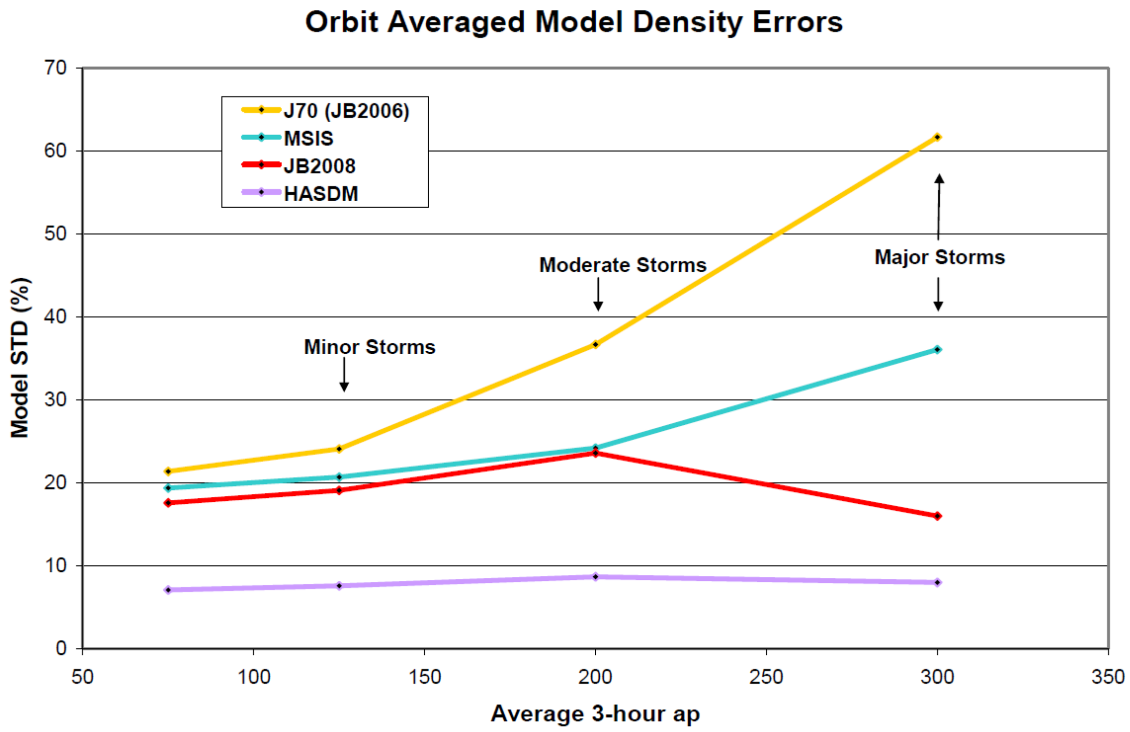

Figure 5.32 - Model density 1-standard deviation errors as a function of a_p ranges representing storm magnitudes

The geomagnetic storm temperature index used by JB2008 reflects the change in the exospheric temperature. This temperature change is computed from the change in the Dst index during a storm. Outside of storm periods this index is computed from Jacchia's 1970 equation using the 3-hour a_p value. Since the temperature change is global, in nature it only needs to be computed once independent of any geography (latitude, longitude, altitude) when new Dst values are obtained. The web site will provide the continuously updated temperature index on a daily basis as new Dst values are obtained and added to the Dst file. The temperature index file is then used as an input to the JB2008 model. To run this program requires the Dst file and the 3-hour a_p file, both of which are also found on the web site. [6]

For sake of completeness, hereunder inputs and outputs of the MATLAB code for JB2008 are reported together with the MATLAB function formulation.

```
[T, rho] = jb2008(MJD, SUN, SAT, F10, F10B, S10, S10B, XM10,
XM10B, Y10, Y10B, DSTDTC)
```

Table 5.7 - JB2008: inputs and outputs

Inputs		**Outputs**	
MJD	Modified Julian date	**T**	Exospheric temperature above the input position
SUN	Right Ascension of the Sun		
	Declination of the Sun		
SAT	Right Ascension of the satellite		Temperature at input position
	Geocentric latitude of the satellite		
	Geodetic altitude of the satellite		
F10	10.7-cm solar flux		
F10B	10.7-cm solar flux, average, 81-day Centred on the input time	**rho**	Total mass density at input position
S10	EUV index (26-34 nm) scaled to F10		
S10B	EUV 81-day average Centred index		
XM10	MG2 index scaled to F10		
XM10B	MG2 81-day average Centred index		
Y10	Solar X-Ray & Lya index scaled to F10		
Y10B	Solar X-Ray & Lya 81-day average Centred index		
DSTDTC	Temperature change computed from DST index		

The tables below summarize the characteristics of all the solar indices explained before with a special focus on indices used in Jacchia-Bowman models. In particular, the first two are linked to JB2006 and the second two to JB2008.

Table 5.8 - Solar indices studied for atmospheric heating

Index	ISO 21348[1] Spectral category	ISO 21348 Spectral sub-category	Wavelength range (nm)	Solar source temperature region	Solar source feature	Atmosphere absorption (unit optical depth, km)	Terrestrial atmosphere absorption (thermal region)
X_{hf}	X-rays	X-rays	0.1-0.8	Hot corona	Flare	70-90	Mesosphere
X_{b10}	X-rays	X-rays	0.1-0.8	Corona	Active region background	70-90	Mesosphere
$XE_{10.7}$	X-rays and UV	XUV+EUV	1-40	Chromosphere, corona	Active region, plage	90-200	Lower, mid thermosphere
$E_{10.7}$	X-rays and ultraviolet	XUV+EUV	1-105	Chromosphere, corona	Active region, plage, network	90-500	Thermosphere
*$F_{10.7}$	Radio	Radio	10.7E7	Transition region, cool corona	Active region	90-500	Thermosphere
*$S_{10.7}$	UV	EUV	26-34	Chromosphere, corona	Active region, plage, network	200-300	Thermosphere
$XL_{10.7}$	X-rays and UV	X-rays+H Lyman-α	0.1-0.8, 121	Chromosphere, transition region, corona	Active region, plage, network	70-90	Mesosphere
H Lya	UV	H Lyman-α	121	Transition region, chromosphere	Active region, plage, network	70-90	Mesosphere
E_{SRC0}	UV	FUV	125-175	Photosphere, chromosphere	Plage and network	90-125	Mesosphere, lower thermosphere
E_{SRC1}	UV	FUV	151-152	Chromosphere	Plage and network	125	Lower thermosphere
E_{SRC2}	UV	FUV	144-145	Chromosphere	Plage and network	125	Lower thermosphere
$E_{SRC3} = E_{SRC}$	UV	FUV	145-165	Photosphere, chromosphere	Plage and network	125	Lower thermosphere
*$M_{10.7}$	UV	MUV	280	Chromosphere	Active region	20	Stratosphere
E_{SRB}	UV	FUV+MUV	175-205	Photosphere	Plage and network	50-70	Mesosphere
E_{HRT}	UV	MUV	245-254	Photosphere	Network, background	25	Stratosphere

*Index or proxy is used in the JB2006[3] model exospheric temperature equation.

Table 5.9 - Characteristics of daily reported JB2006 solar indices

Index or proxy	Observing facility	Instrument	Observation time frame	Measurement cadence	Measurement latency	Operational availability
$F_{10.7}$	Penticton ground observatory	Radio telescope	1947-2006	3 times/day	Up to 24 hours	yes
$S_{10.7}$	SOHO	SEM	1996-2006	15-second	Up to 24 hours	(a)
$XL_{10.7}$	GOES-12, UARS, SORCE, TIMED	XRS, SOLSTICE (2), SEE	1991-2006	1-minute, 16 times/day	Up to 10 minutes, up to 48 hours	(b)
E_{SRC}	UARS, SORCE	SOLSTICE (2)	1991-2006	16 times/day	Up to 48i hours	(c)
$M_{10.7}$	NOAA-16,17	SBUV	1991-2006	2 times/day	Up to 24 hours	yes
E_{HRT}	UARS, SORCE	SOLSTICE (2)	1991-2006	16 times/day	Up to 48 hours	(c)

(a) SOHO/SEM is a NASA research instrument but provides daily irradiances on an operational measurement cadence.

(b) GOES XRS is a NOAA operational instrument whereas TIMED/SEE and SORCE/SOLSTICE are NASA research instruments providing daily irradiances on an operational measurement cadence.

(c) UARS/SOLSTICE stopped in 2005; SORCE/SOLSTICE intends to provide data for several years.

Table 5.10 - Solar indices related to atmospheric heating

Index	IS 21348 Spectral category	IS 21348 Spectral sub-category	Wavelength range (nm)	Solar source temperature region[1]	Solar source feature[1]	Atmosphere absorption (unit optical depth, km)[2]	Terrestrial atmosphere absorption (thermal region)[2]
*$F_{10.7}$	Radio	Radio	10.7E7	Transition region, cool corona	Active region	90-500	Thermosphere with 1-day lag; 9.8% daily variability contribution
*$S_{10.7}$	UV	EUV	26-34	Chromosphere, corona	Active region, plage, network	200-300	Thermosphere with 1-day lag; 74.1% daily variability contribution
*$M_{10.7}$	UV	FUV	160	Photosphere-lower chromosphere	SRC	95-110	Lower thermosphere with 2-day lag; 10.3% daily variability contribution
$MgII_{cwr}$	UV	MUV	280[3]	Chromosphere	Active region, plage, network	200-300	Thermosphere
*$Y_{10.7}$	X-rays and UV	X-rays+H Lyman-α	0.1-0.8, 121	Chromosphere, transition region, hot corona	Active region, plage, network	85-100	Mesopause-lower thermosphere with 5-day lag; 5.8% daily variability contribution
H Lya	UV	H Lyman-α	121	Transition region, chromosphere	Active region, plage, network	85-100	Mesopause-lower thermosphere
X_{b10}	X-rays	X-rays	0.1-0.8	Hot corona	Active region background	85-100	Mesopause-lower thermosphere

*Index or proxy is used in the JB2008 model exospheric temperature equation.

Table 5.11 - Characteristics of daily JB2008 solar indices

Index or proxy	Observing facility	Instrument	Observation time frame	Measurement cadence	Measurement latency	Operational availability
$F_{10.7}$	Penticton ground observatory	Radio telescope	1947-2009	3 times/day	Up to 24 hours	yes
$S_{10.7}$	SOHO, GOES	SEM, EUVS	1996-2009	15-second	Up to 24 hours	(a)
$M_{10.7}$	NOAA-16,17,18, SORCE, ERS-2	SBUV, SOLSTICE, GOME	1991-2009	2 times/day	Up to 24 hours	yes
$Y_{10.7}$	GOES-12, UARS, SORCE, TIMED	XRS, SOLSTICE (2), SEE	1991-2009	1-minute, 16 times/day	Up to 10 minutes, up to 48 hours	(b)

(a) SOHO/SEM is a NASA research instrument but provides daily irradiances on an operational cadence; GOES 13 EUVS B channel makes measurements in the same bandpass as SOHO SEM.

(b) GOES XRS is a NOAA operational instrument whereas TIMED/SEE and SORCE/SOLSTICE are NASA research instruments providing daily irradiances on an operational measurement cadence.

(c) UARS/SOLSTICE stopped in 2005; SORCE/SOLSTICE intends to provide data for several years.

5.2.3 NRLMSISE-00

NRLMSISE-00 is an empirical, global reference atmospheric model of the Earth from ground to space that models the temperatures and densities of the atmosphere's components. A primary use of this model is to aid predictions of satellite orbital decay due to atmospheric drag. The model, developed by Mike Picone, Alan Hedin, and Doug Drob, is based on the earlier models MSIS-86, which ranges upward from 90 km, and MSISE-90, which extends from the ground to the exobase, but updated with actual satellite drag data.

NRL stands for the US Naval Research Laboratory; MSIS stands for Mass Spectrometer and Incoherent Scatter Radar, the two primary data sources for development of earlier versions of the model; E indicates that the model extends from the ground through exosphere and 00 is the year of release (i.e. year 2000).

The new NRLMSISE-00 empirical atmospheric model is a major upgrade of the MSISE-90 model in the thermosphere. The new model and the associated NRLMSIS database now include the following data:

1) total mass density from satellite accelerometers and from orbit determination;
2) temperature from incoherent scatter radar covering 1981–1997;
3) molecular oxygen number density, [O_2], from solar ultraviolet occultation aboard the Solar Maximum Mission.

A new component, ‘‘anomalous oxygen,’’ allows for appreciable O+ and hot atomic oxygen contributions to the total mass density at high altitudes and applies primarily to drag estimation above 500 km. Noteworthy is the solar activity dependence of the Jacchia data, with which it was studied a large O+ contribution to the total mass density under the combination of summer, low solar activity, high latitude, and high altitude. Under these conditions, except at very low solar activity, the Jacchia data and the Jacchia-70 model indeed show a significantly higher total mass density than does MSISE-90. However, under the corresponding winter conditions, the MSIS-class models represent a noticeable improvement relative to Jacchia-70 over a wide range of $F_{10.7}$. Therefore, NRLMSISE-00 achieves an improvement over both MSISE-90 and Jacchia-70 by incorporating advantages of each.

This upgrade is important because the MSIS and Jacchia models do not depend on calendar year and do not explicitly account for any gradual changes in the atmosphere due to solar influences. The only way in which empirical models can reflect the recent state of the atmosphere is by continually adding recent data to their databases and then modifying their parameter sets. In addition, instrumentation and data processing methods have improved and have become more diverse, potentially allowing the addition of higher-order terms and reducing the uncertainty of model coefficients. To accommodate new data, the formulation of the model and the methodology for generating it have become more robust.

One change is particularly worthy of mention. The inclusion of drag data in the neutral atmospheric model has required to account explicitly for an additional high altitude drag component which is appreciable under some conditions and which is not in equilibrium at the thermospheric temperature. Limited studies have indicated that O+ and hot atomic oxygen can contribute appreciably to drag for the combination of summer, high latitude, and high altitude. As a result, the NRLMSIS formulation now explicitly includes a component called ‘‘anomalous oxygen’’ to account for the contribution of non-thermospheric species to satellite drag at high altitudes and permits the user to compute both the ‘‘thermospheric mass density’’ (or total neutral mass density) provided by past generations of MSIS and an ‘‘effective’’ mass density, which denotes the sum of the thermospheric mass density and the anomalous oxygen contribution at altitudes near the exobase.

5.2.3.1 Data sources

Recent data sets and new categories of data now augment the NRLMSIS database and model:

1) Satellite drag, orbit determination;
2) Accelerometer (Atmosphere Explorer MESA, Air Force SETA, CACTUS, San Marco 5);
3) Incoherent scatter radar – Exospheric temperature (Millstone Hill, Arecibo);
4) Incoherent scatter radar – Lower thermosphere temperature (Millstone Hill);
5) Solar Maximum Mission (SMM) O_2 density data derived from occultation of solar UV emissions.

With the inclusion of the Jacchia data, the more extensive and well-documented NRLMSIS database should equal or improve the statistical predictions of ρ and of drag over those of the Jacchia models. The Incoherent Scatter Radar (ISR) data directly influence the model temperature, which is the core of the MSIS formulation. Because the new data are recent and cover an appreciable fraction of a solar cycle or more, these data are vital for both testing the existing models and producing new versions. The methods of processing ISR data have also undergone significant improvements over the last decade, increasing the quality of the inferred ionospheric properties. This imparts high value to the new data sets.

The Millstone Hill data on lower thermospheric temperature (T_{low}) cover 100 km $\leq z \leq$ 130 km. In this atmospheric region, the neutral temperature is approximately equal to the ion temperature, so that extraction of the information is easy. These high-quality data permit us to check and reinforce MSIS temperature model key parameters. The data are also important in defining the model near the mesopause.

The SMM mission provided data on the molecular oxygen number density [O_2] over the altitude range 140–220 km and over a wide range of solar activity. Prior to SMM, direct measurements of [O_2] above 150 km were not available at high solar activity. The SMM occultation measurements suggest that dissociation may increase sufficiently to keep this density nearly constant at 200 km as solar activity increases. These data are now part of the NRLMSIS database and are important in determining dependence on the solar extreme ultraviolet (EUV) flux and on magnetic activity. As a result, the data should be particularly useful in future analysis of EUV proxies developed recently. On the other hand, a longstanding conflict between mass spectrometer and solar UV occultation measurements of thermospheric [O_2] has had a profound effect on NRLMSIS because the occultation data do not follow diffusive equilibrium, corresponding to the thermospheric temperature T(z), in the altitude range 140–220 km. The SMM data set has therefore required alterations in the formulation of NRLMSIS and has significantly influenced the dependence of $[O_2]$ estimates on $F_{10.7}$. It was found that the new SMM data have caused a shift in the mean value of $[O_2]$ in the lower thermosphere.

5.2.3.2 Statistical comparison of models to data

The NRLMSIS database consists of two components: the complete data sets acquired from the various sources and the subset of data ‘‘selected’’ to generate the model. For a data set and the corresponding model estimates, two factors are computed: the weighted mean β of the residuals and the corresponding standard deviation σ. The mean residual β indicates the magnitude of systematic differences between a data set and corresponding model estimates. Positive β indicates that a model underestimates the measured values on average. A negative mean residual signifies overestimation. The standard deviation measures the agreement between the geophysical variability contained in the model and the geophysical variability implicit in the NRLMSIS database. When multiple models are compared with identical data sets, the relative values of σ should indicate relative agreement of respective models with measured timescales and the associated phases inherent in the data.

The most obvious differences among the models involve the standard deviation of data-model residuals. The most important observation is that NRLMSISE-00 is somewhat better than Jacchia-70 and MSISE-90 overall. For the data on total mass density, σ is comparable among the models, confirming the internal consistency of the drag/accelerometer data and the non-drag (composition and temperature) data. The latter conclusion was reached because the total mass density in MSISE-90 derives almost entirely from composition and temperature data, while Jacchia-70 derives entirely from drag and NRLMSISE-00 includes both data classes. As expected, NRLMSISE-00 and MSISE-90 show better results for composition than does Jacchia-70, especially as altitude increases. The comparable performance of NRLMSISE-00 and MSISE-90 for composition (except for $[O_2]$) also verifies that the extensive new data on total mass density have been added in a manner consistent with the prior MSIS representation of composition.

The two MSIS models also agree better (than Jacchia-70 does) with incoherent scatter radar measurements of exospheric temperature, which showed lower standard deviation values than satellite data did. For Jacchia-70, the best temperature results relative to the MSIS-class models occurred for the combination of lower altitudes and satellite-based observations, for which the three models had similar values of σ. At high geomagnetic activity, comparisons of all models with the data generally showed higher σ values than did the low geomagnetic activity cases. Also at high geomagnetic activity, the MSIS models showed lower s values than did Jacchia-70. Table 5.12 compares the Jacchia data set to the three models. The table shows that the mean residuals (denoted ‘‘Mean’’) and standard deviations (‘‘SD’’) of the three models are comparable in magnitude at low to moderate geomagnetic activity. However, two additional, secondary features appear. First, the Jacchia model shows a consistent negative mean residual (β), on average overestimating the Jacchia data at all altitudes, while

NRLMSIS and MSISE-90 show a positive mean residual at high altitude and negative mean values at lower altitudes. This difference at high altitudes is likely attributable to a non-optimal match of Jacchia-70 with the $F_{10.7}$ variability of the data. Second, at high geomagnetic activity, the standard deviations of the MSISE-90 and Jacchia-70 models are consistently higher than that of NRLMSIS. This suggests that the new model handles spatial and temporal variability somewhat better than the other models at elevated geomagnetic activity. In addition, at high geomagnetic activity, the mean residual of the Jacchia-70 model is noticeably larger than the residuals of the MSIS models, indicating that the former systematically overestimates the data.

Table 5.12 - Statistical comparison of empirical models to Jacchia data

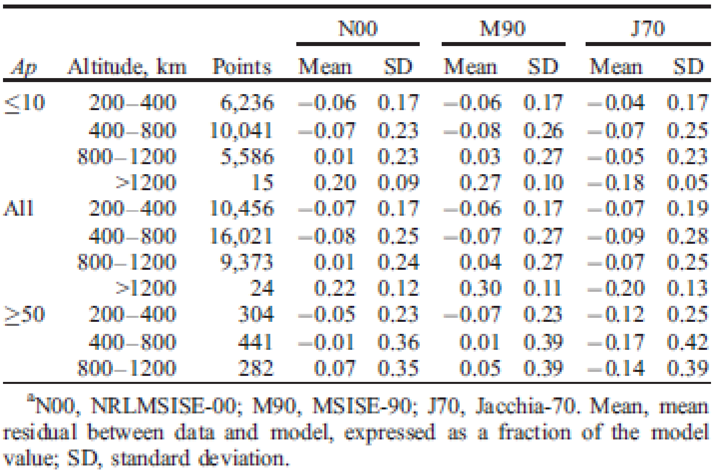

			N00		M90		J70	
Ap	Altitude, km	Points	Mean	SD	Mean	SD	Mean	SD
≤10	200–400	6,236	−0.06	0.17	−0.06	0.17	−0.04	0.17
	400–800	10,041	−0.07	0.23	−0.08	0.26	−0.07	0.25
	800–1200	5,586	0.01	0.23	0.03	0.27	−0.05	0.23
	>1200	15	0.20	0.09	0.27	0.10	−0.18	0.05
All	200–400	10,456	−0.07	0.17	−0.06	0.17	−0.07	0.19
	400–800	16,021	−0.08	0.25	−0.07	0.27	−0.09	0.28
	800–1200	9,373	0.01	0.24	0.04	0.27	−0.07	0.25
	>1200	24	0.22	0.12	0.30	0.11	−0.20	0.13
≥50	200–400	304	−0.05	0.23	−0.07	0.23	−0.12	0.25
	400–800	441	−0.01	0.36	0.01	0.39	−0.17	0.42
	800–1200	282	0.07	0.35	0.05	0.39	−0.14	0.39

[a] N00, NRLMSISE-00; M90, MSISE-90; J70, Jacchia-70. Mean, mean residual between data and model, expressed as a fraction of the model value; SD, standard deviation.

5.2.3.3 Scientific and technical issues

An important addition to the NRLMSIS model is an ‘‘anomalous oxygen’’ component to high-altitude drag and total mass density at the summer high latitudes. At high altitude (>500 km), this component augments the ‘‘thermospheric’’ total mass density attributable to the neutral species in diffusive equilibrium at the thermospheric temperature T, including atomic hydrogen and helium. The anomalous oxygen component accounts for the presence of appreciable hot atomic oxygen (O_h) or atomic oxygen ions (O+) near the exobase under some conditions but does not explicitly distinguish contributions by the two species. As described below, observational evidence is sufficient to warrant this additional component to drag.

Keating in 1998 demonstrates that an appreciable O+ component to high-altitude drag can exist. He also analysed neutral and ion mass spectrometer measurements aboard the Midcourse Space Experiment (MSX). MSX flew in a Sun-synchronous (near-polar) circular orbit at approximately 900 km during the most recent solar minimum. He then found that the O+ density measured by MSX accounted for the higher mass density implied by Jacchia-70 near the summer pole at 900 km under solar minimum conditions and also found that the mass density attributable to other iconic species (e.g. H+, He+) was minor in relation to O+ under studied conditions. Hedin found that an appreciable hot atomic oxygen population could be present under the combination of high latitude and high altitude (>600 km) in the summer hemisphere. For this region of the atmosphere, during high solar activity, Hedin observed an elevated atomic oxygen population by comparing the MSIS-86 model to high-altitude data from the neutral mass spectrometer aboard Dynamics Explorer 2 (DE 2). Recent analyses of ISR data from Millstone Hill by Oliver showed that the hot oxygen component would be especially important at night, at the solstice and during solar minimum. In response to these developments, the NRLMSIS model now includes an ‘‘anomalous oxygen’’ (AO) component, which represents any appreciable, persistent non-thermal species (thought to be O+ or hot O populations) at higher altitudes (>500 km). The functional form of the anomalous oxygen model profile is similar to that of an isothermal Chapman layer, with an adjustable magnitude and scale height or temperature. The data used to evaluate these parameters were the drag data sets of Jacchia and Barlier (JB) above 600 km. At the same time, the summer JB data above 600 km have been excluded from the data sets used to determine the He and ‘‘thermospheric’’ O components of the model. The term ‘‘thermospheric’’ O represents the atomic oxygen population in equilibrium at the thermospheric temperature T. While the winter JB data above 600 km have been used to generate coefficients for He, thermospheric O, and anomalous O, comparisons of NRLMSISE-00 and MSISE-90 to these data have shown only small differences. To conclude, the anomalous oxygen component has influenced the new model far less during winter at high altitudes. Surprisingly, the Jacchia-70 model agrees less well with the Jacchia data than do the MSIS models under such conditions.

In this model, UV occultation observations of [O_2] from the Solar Maximum Mission were included. The SMM UV data show much weaker solar activity dependence than do the mass spectrometer data. As a result of these differences, the parameterization of the lower thermospheric altitude profiles of O_2 and O have been modified to allow more flexibility in NRLMSISE-00. The model now accounts for solar activity dependent departures from diffusive equilibrium in the lower thermosphere. Figure 5.33 shows that the new model is a statistical compromise between the two data sources in the altitude region 125–225 km covered by the SMM data. Above this region the NRLMSIS [O_2] profile approaches diffusive equilibrium.

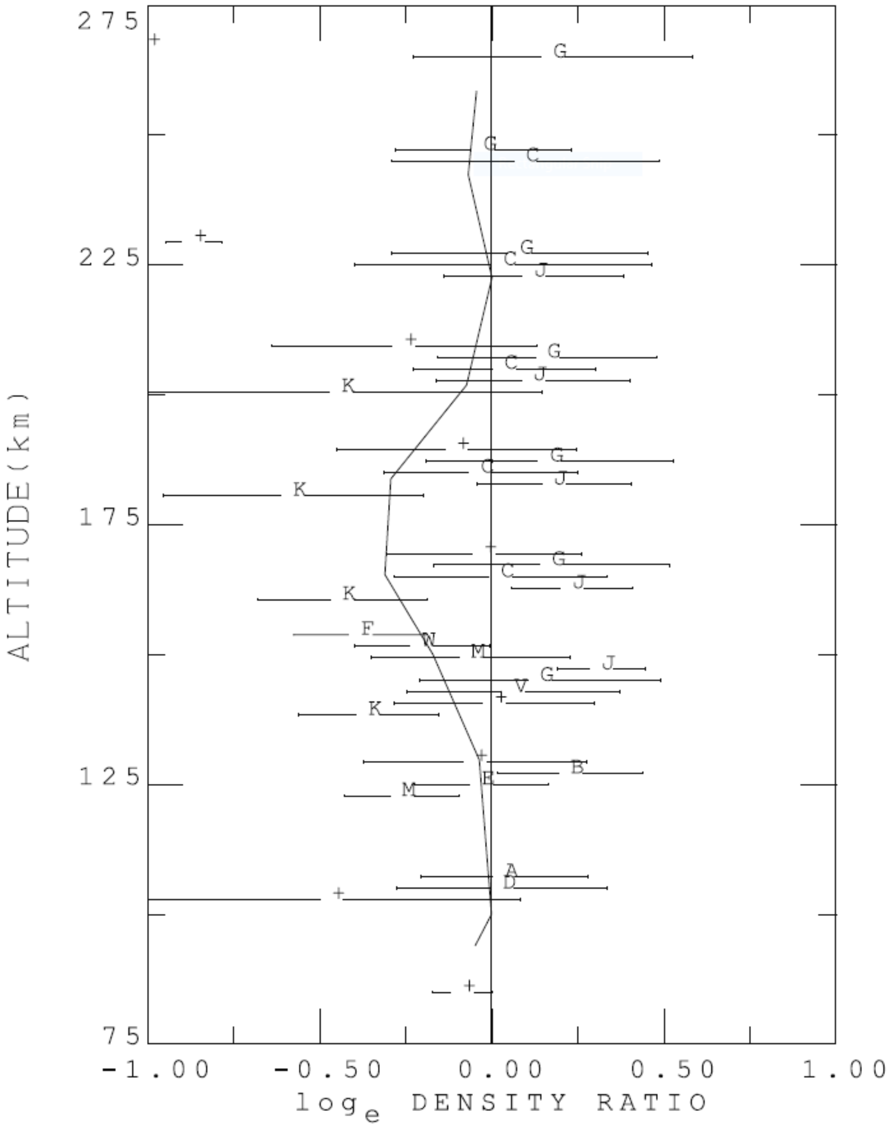

Figure 5.33 - Lower thermospheric profile of [O_2]: log$_e$ of ratio to MSISE-90 values

The accuracy of both mass spectrometry and solar UV occultation remains an open question. Further improvement of the NRLMSIS model of [O_2] in the lower thermosphere awaits a resolution of the differences between the two major data classes (i.e., observational techniques). This also affects the model atomic oxygen ([O]) profile in the lower thermosphere, where the primary source of information on [O] is mass spectrometer data on total oxygen number density, [O] + 2[O_2]. Comparison of the new model with the total oxygen data shows some evidence of slight improvements, for example, in variation with mean $F_{10.7}$. On the more limited basis of statistical measures (mean residual and standard deviation), the new model is quite similar to MSISE-90 compared with data on total oxygen content in the thermosphere. On the other hand, the molecular oxygen number density, [O_2], is noticeably lower in NRLMSISE-00 throughout the thermosphere and over a broad range of $F_{10.7}$ values. This has consequences also for the model’s O_2 mixing ratio in the mesosphere, as compared with that of MSISE-90.

5.2.3.4 Exospheric temperature

The Millstone Hill and Arecibo incoherent scatter radar data on exospheric temperature (T_{ex}) are of high quality and extend the NRLMSIS database well into the 1990s. These data result from fitting a model of ion heat balance and chemistry to the ion temperature profile ($T_i(z)$), using ISR observables and parameterized models of neutral oxygen and temperature. The retrieval of T_{ex} from the ISR data did not include a hot oxygen component. The newly added Millstone Hill data cover the period 1981–1997. Interestingly, MSISE-90 provides a somewhat better fit at high solar activity (≥240) than does NRLMSISE-00, suggesting that the response to solar forcing might vary with latitude.

Most importantly, the new ISR and total mass density data, when combined with the previous MSIS data sets, have changed the solar activity dependence of the temperature in NRLMSISE-00 relative to that of MSISE-90 (and MSIS-86), especially at higher altitudes. The NRLMSISE-00 T_{ex} is above that of MSISE-90 only at low latitudes and for moderate to low $F_{10.7}$ and then by only a few degrees. As solar activity increases above moderate values, the NRLMSISE-00 value of T_{ex} falls below that of MSISE-90 by a steadily increasing amount, reaching -40 K at $F_{10.7} > 220$ and high latitudes, $\theta > 45°$. This difference is less pronounced at lower latitudes. The mean total mass density behaves similarly to the temperature. Inspection of the individual NRLMSISE-00 data sets on composition, temperature, and density have generally confirmed this behaviour.

5.2.3.5 Formulation

The MSIS-class model formulation consists of parametric analytic approximations to physical theory for the vertical structure of the atmosphere as a function of location, time, solar activity (10.7-cm solar radio flux), and geomagnetic activity. Extending from the ground to the exobase, the NRLMSISE-00 model provides altitude profiles of temperature T(z), number densities of species (He, O, N_2, O_2, Ar, H, N) in equilibrium at the temperature T(z), total mass density $\rho(z)$, and the number density of a high-altitude ''anomalous oxygen'' component of total mass density that is not in thermal equilibrium at T(z). For the thermosphere, the value of the total mass density at high altitude is the sum of two factors. The standard model subroutine (GTD7) always computes the ''thermospheric'' mass density by explicitly summing the masses of the species in equilibrium at the thermospheric temperature T(z). A separate subroutine (GTD7D) computes the ''effective'' mass density by summing the thermospheric mass density and the mass density of the anomalous oxygen component. Below 500 km, the effective mass density is equivalent to the thermospheric mass density.

The model accounts for the approximate spheroidal symmetry of the Earth and the atmosphere by incorporating a gravity field and an effective Earth radius which are both latitude-dependent and by using spherical harmonics to represent spatial variability of the key parameters that define temperature and species number density profiles. Parameterized correction factors account for deviations of the profiles from the basic approximations in the lower thermosphere. Constraints on mixing ratio, hydrostatic equilibrium, and profile smoothness govern the transition between the thermosphere and the mesosphere.

5.2.3.6 Thermosphere

In the thermosphere, the Bates-Walker equations represent the basic profiles of the temperature and of species number density as analytic functions of altitude. These equations are an exact solution for thermal and diffusive equilibrium and include thermal diffusion. Below a species-dependent altitude in the range 160–450 km, the profiles differ from diffusive equilibrium by progressively greater amounts as z decreases, transitioning to a fully mixed state at a turbopause $z_h \approx 100$ km. In this transition region, MSIS-class models modify the density profile due to the effects of chemistry, dynamics, and ''loss/flow'' processes.

5.2.3.7 Mesosphere

The NRLMSIS database contains primarily data on total mass density and temperature in the upper mesosphere. For composition, the model primarily provides a smooth connection between the lower thermosphere and the region below 62.5 km, where ground-level mixing ratios are maintained.

5.2.3.8 Molecular oxygen O2 in the Mesosphere

The SMM O_2 data have driven the NRLMSISE-00 thermospheric O_2 number density significantly lower than that of MSISE-90. Depending on the value of $F_{10.7}$, this causes the increase of the NRLMSIS O_2 mixing ratio from the lower thermospheric value to the constant value (below 62.5 km) to be more gradual than that of MSISE-90, causing a lower O_2 mixing ratio by up to a few percent in the mesosphere. Since the total mass density (ρ) in the mesosphere is credible, it is suggested that users apply their mixing ratios of choice to ρ in order to estimate total oxygen content or O_2 mixing ratio in that region. Moreover, the NRLMSIS formulation is sufficiently robust (or can be modified) to fit any data or constraints considered appropriate by the mesospheric research community.

5.2.3.9 Constraints

For altitudes $0 \leq z < 120$ km, the fundamental variables define nodes and gradients of the temperature profile, while pressure and density are defined by hydrostatic equilibrium and the ideal gas law. As was mentioned above, diffusive equilibrium no longer holds for the MSIS-class models below altitudes of ~300 km. Because the code fits the temperature and individual species separately (different coefficient sets), the MSIS-class models do not maintain hydrostatic equilibrium a priori below 300 km. For this reason, the model generation process imposes an approximate hydrostatic equilibrium constraint in the region 80–300 km. This couples the lower and upper atmospheric regions, modifying some details of previous MSIS versions. Finally, since all of the new data relate to the thermosphere, NRLMSISE-00 retained the MSISE-90 coefficients below 72.5 km while constraining coefficient values in the range 72.5–110 km to give a total mass density at the ground in agreement with MSISE-90. [7]

For sake of completeness, hereunder inputs and outputs of the MATLAB code for NRLMSISE-00 are reported together with the MATLAB function formulation.

```
[T, rho] = nrlmsise00(h, lat, lon, year, doy, sec, lst, f107a,
f107, aph, flags, itype, otype, action)
```

Table 5.13 - NRLMSISE-00: inputs and outputs

Inputs		Outputs	
`h`	Geodetic altitude	**`T`**	Exospheric temperature
`lat`	Geodetic latitude		Temperature at altitude
`lon`	Longitude	**`rho`**	Helium (He) number density
`year`	Year		Oxygen (O) number density
`doy`	Day of year		Nitrogen (N2) number density
`sec`	Seconds		Oxygen (O2) number density
`lst`	Local Solar Time		Argon (Ar) number density
`f107a`	81-day average of F10.7 solar flux		Total mass density
`f107`	Daily F10.7 solar flux for previous day		Hydrogen (H) number density
`aph`	Daily magnetic index		Nitrogen (N) number density
`flags`	*‘settings’*		Anomalous oxygen number density
`otype`	Yes/No anomalous Oxygen		
`action`	*‘settings’*		

5.3 Comparison and accuracy of the three models

5.3.1 Effects of solar indices on models

5.3.1.1 $E_{10.7}$ and $F_{10.7}$

In Figure 5.34, it will be found that all of the models’ errors are about -30% using $F_{10.7}$, which means these models underestimate the real density. If $E_{10.7}$ was input to models instead of $F_{10.7}$, the models’ error would reduce about 15% immediately. However, the errors near 2002 increase quickly and reach 80% for CIRA72 and DTM94, 60% for NRLMSISE-00 and JB2006. Considering it is under the active solar condition near 2002, it implies that $E_{10.7}$ might cause the model error augment oppressively during acute solar radiation.

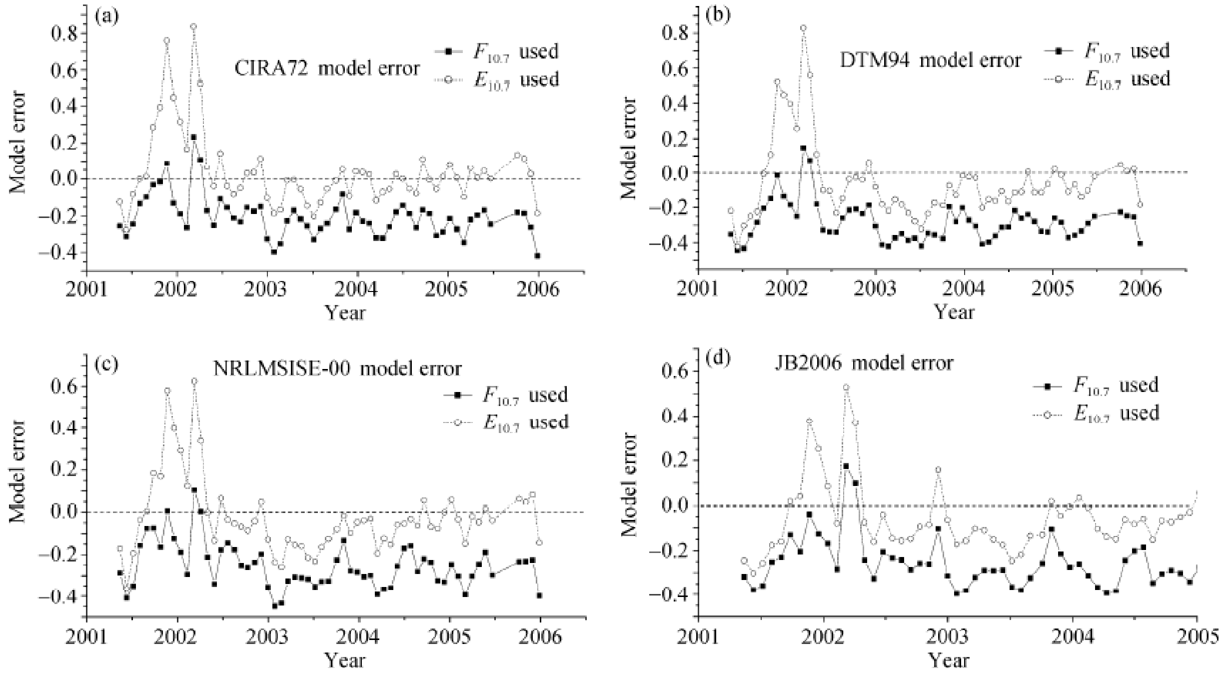

Figure 5.34 - Average model errors of 27-a period using $E_{10.7}$ and $F_{10.7}$

Figure 5.35 only shows NRLMSISE-00 result because other models’ results are similar to it. When the solar flux is less than 200, the average error of the model using $E_{10.7}$ is obviously less than that using $F_{10.7}$. However, if the solar flux is greater than 200, the error using $E_{10.7}$ increases quickly and switches from negative to positive, implying that $E_{10.7}$ will make models overestimate the density. Under this condition, the error using $E_{10.7}$ is about 15% greater than that using $F_{10.7}$. According to standard deviation, when the solar flux is less than 160, σ using both indices are under 20%, and that using $E_{10.7}$ is about 5% greater than that of $F_{10.7}$. When the flux exceeds 160, the standard deviation of $E_{10.7}$ increases fast and reaches its maximum at 200, which is about 10%-20% greater than that of $F_{10.7}$. When evaluating models, there are two factors to be taken into account: the first is the average of relative error $(\bar{R}-1)$ and the second is error standard deviation σ. It is well known that $(\bar{R}-1)$ means model relative errors’ level, while σ means model errors’ dispersion. In Figure 5.35, when the solar flux exceeds 160, error dispersion of $E_{10.7}$ is greater than that of $F_{10.7}$ obviously, that is to say, $E_{10.7}$ makes the model error unstable under the active solar condition. But if the solar flux is below 160, $E_{10.7}$ makes the average model error reduce about 15%, and at the same time its dispersion only increases about 5%. Under this special condition, the accuracies of models are improved effectively by using $E_{10.7}$ instead of $F_{10.7}$. A possible reason of the fast increase of the standard deviation when the solar flux exceeds 160 is that these models were all constructed based on $F_{10.7}$ originally, which are not well consistent with $E_{10.7}$. [8]

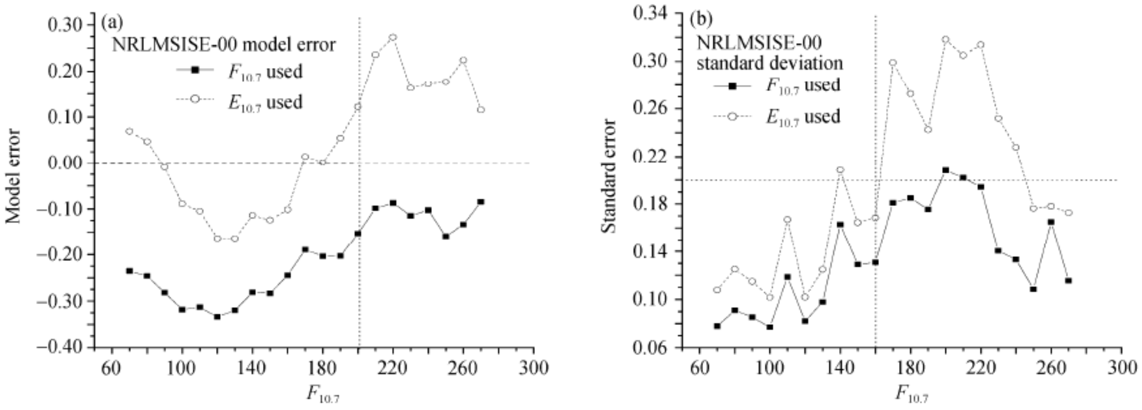

Figure 5.35 - NRLMSISE-00 model error and standard deviation via $F_{10.7}$ using both indices

5.3.1.2 S_{10} and Mg_{10}

JB2006 model is based on CIRA72, whose major change uses three kinds of indices such as $F_{10.7}$, S_{10} and Mg_{10} instead of single index $F_{10.7}$ to compute temperature at 120 km. So it was detected the effect of S_{10} and Mg_{10} by comparing JB2006 with CIRA72. Figure 5.36 shows the two models' errors using $F_{10.7}$, while Figure 5.37 shows both errors using $E_{10.7}$. In Figure 5.36, CIRA72's average error is less than JB2006, but in the high solar activity ($F_{10.7} > 200$) JB2006's error dispersion is much less than CIRA72's. JB2006 is more stable than CIRA72 in the high solar activity using $F_{10.7}$. In Figure 5.37, JB2006's error is about 10%, which reduces about 20%, compared with CIRA72's, meanwhile the error dispersion is obviously lower than CIRA72's. That is to say, new indices S_{10} and Mg_{10} may make the model error more stable in the high solar activity and improve the model accuracy about 20% in combination with $E_{10.7}$. [8]

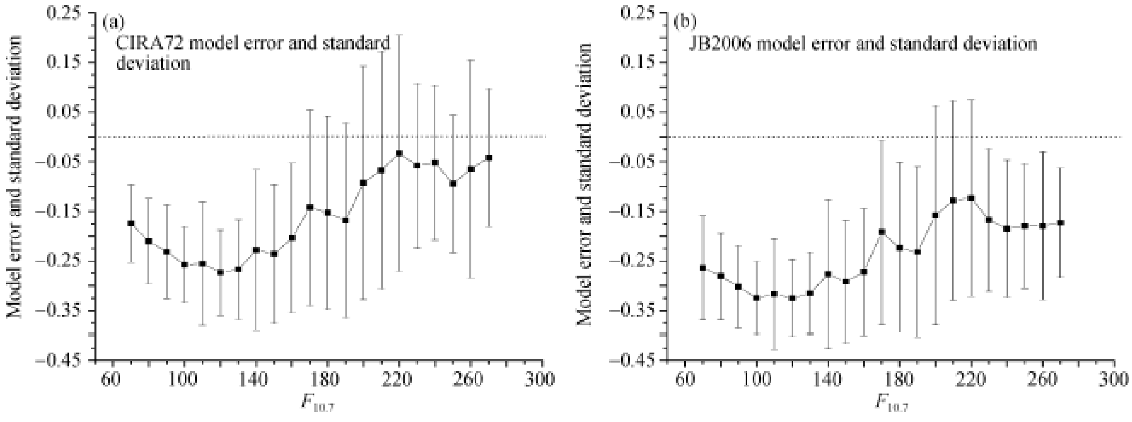

Figure 5.36 - Errors and standard deviation of CIRA72 and JB2006 using $F_{10.7}$

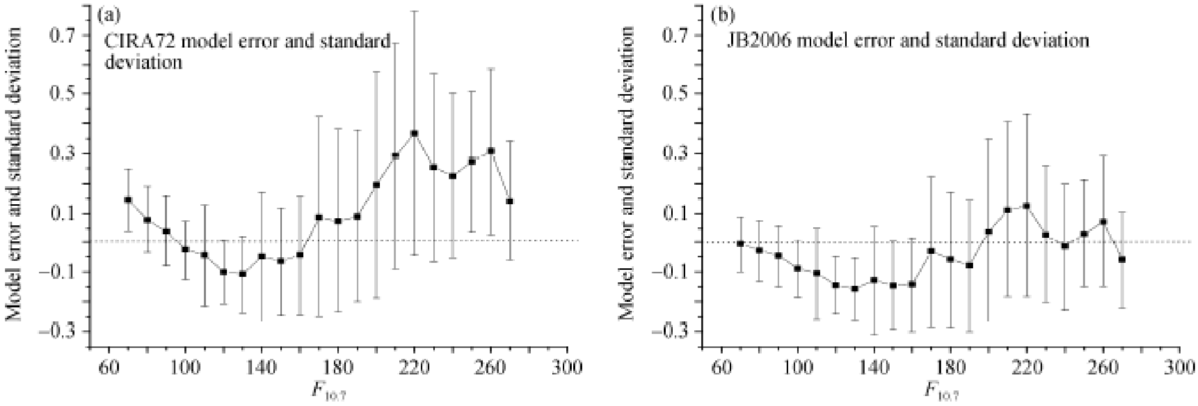

Figure 5.37 - Errors and standard deviation of CIRA72 and JB2006 using $E_{10.7}$

5.3.2 Comparison of JB2006 with NRLMSISE-00 and DTM94

DTM94 and NRLMSISE-00 are proved to be preferable model nowadays and play an important role in satellite orbit prediction and determination. As said before, they are set up by single index, $F_{10.7}$. JB2006 is the first atmosphere model built with three kinds of solar indices. It has been chosen to compare the models results with true observations of CHAMP because if they match perfectly in the past, they are supposed to be perfect for future estimates and for a good representation of the atmosphere. Besides the comparison, the accuracy of models during the solar long-term activity and short-term burst event is analysed. [8]

5.3.2.1 *Short-term burst event accuracy*

It has been brought as an example the strong solar burst that lasted for 25 days from October 17th to November 10th, 2003. During this period $F_{10.7}$ increased from 90 to 280 and reduced back (Figure 5.38). Other indices also fluctuated. The maximum value of $E_{10.7}$ is 215, while S_{10} is 162 and Mg_{10} is 197. Especially, the time that the maximum Mg_{10} occurred at lagged 5 days behind other indices. In this event, several strong geomagnetic storms were driven with the maximum a_p reaching 400.

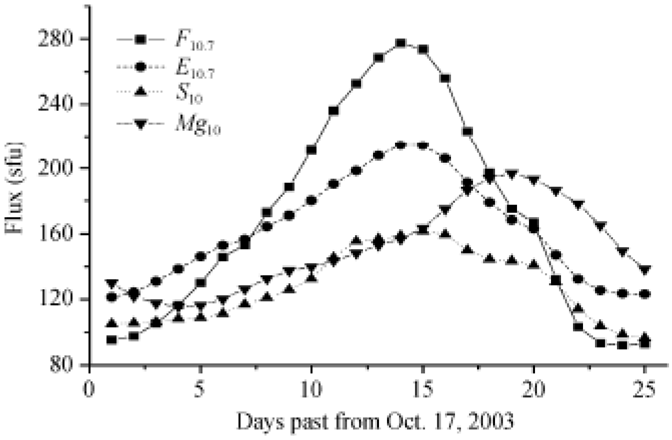

Figure 5.38 - Variation of indices in the sun burst event in October, 2003

The figures below show the average model densities of every day, which were calculated by models using $F_{10.7}$ and $E_{10.7}$, respectively. Compared with CHAMP observation, JB2006 is the closest to CHAMP among three models. Especially after the burst time, JB2006's result using $E_{10.7}$ inosculates with CHAMP very well. With regard to the detailed variation, JB2006 is closer with CHAMP than the others. By analysing the small-scale variation signal in CHAMP measurement during the solar and magnetic storms, the distinct difference between models and observation was found. For example:

1. JB2006 model's response to magnetic storms is delayed for 4—6h, while the NRLMSISE-00 model almost has no response to those short-term events;

2. the models underestimate the maximum densities. Especially, the NRLMSISE-00 model's maximum value is only half of the observation.

All of these differences imply that the models have difficulty in depicting the small-scale variation of local atmosphere, because they are restricted by the model mechanism and its sample distribution. [8]

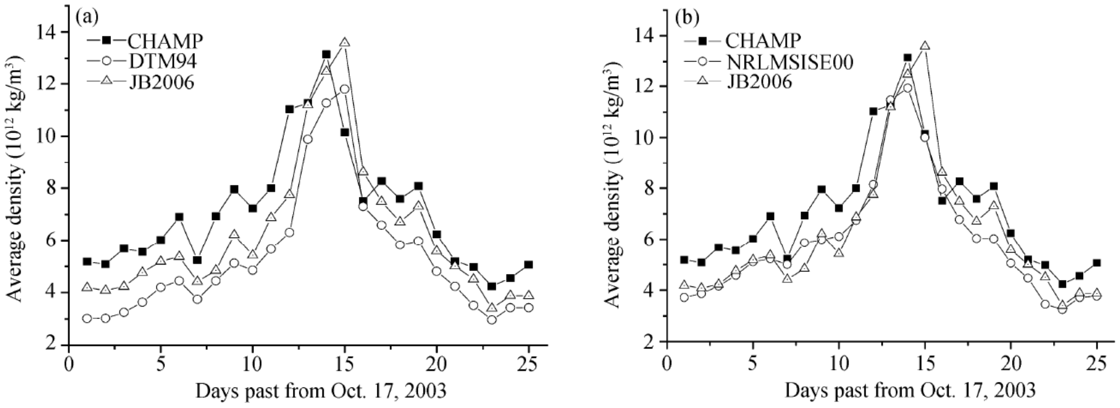

Figure 5.39 - Everyday average models densities using $F_{10.7}$, compared with CHAMP observation

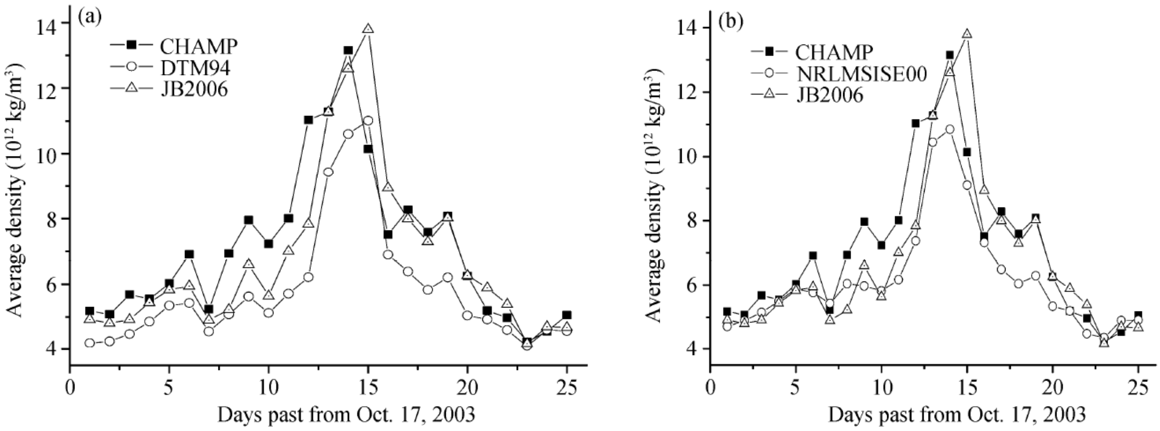

Figure 5.40 - Everyday average densities of models using $E_{10.7}$, compared with CHAMP observation

5.3.2.2 Long-term event accuracy

To evaluate the accuracy of models during solar long-term variation, their relative error and standard deviation were compared with CHAMP density from 2001 to 2005. Figure 5.41 shows the average relative error. JB2006’s error is between DTM94 and NRLMSISE-00 when $F_{10.7}$ is used. When in the high solar activity, JB2006’s error using $E_{10.7}$ is less than the others. Figure 5.42 shows the standard deviations of models. It seemed that DTM94 is the greatest while JB2006 and NRLMSISE-00 are close to each other. All in all, it can be concluded that:

1. the accuracy of JB2006 is slightly better than that of DTM94;
2. in quiet and moderate solar activity JB2006 is close to NRLMSISE-00.

When using $E_{10.7}$ instead of $F_{10.7}$, JB2006’s accuracy under the high active condition is obviously better than NRLMSISE-00, implying that the multi-solar-indices $E_{10.7}$, S_{10}, Mg_{10} can effectively improve models’ accuracy. [8]

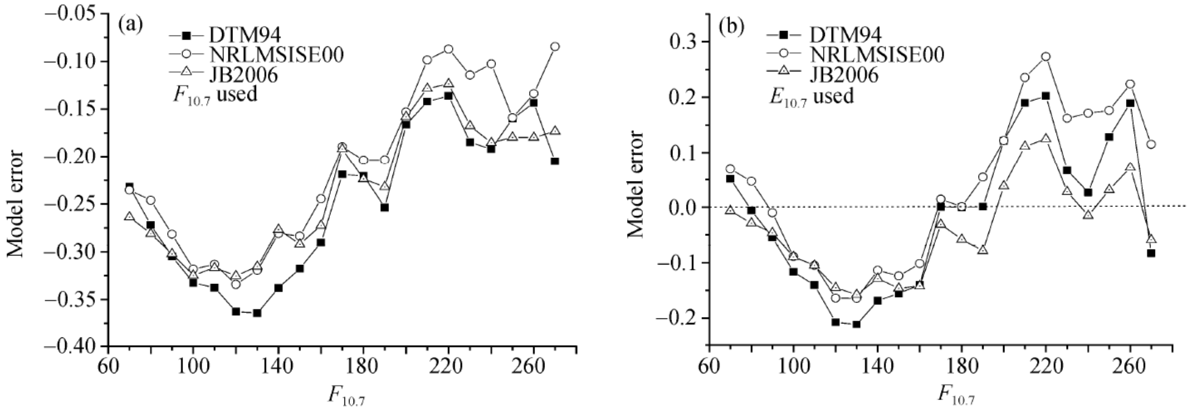

Figure 5.41 - Average relative errors of JB2006, DTM94, NRLMSISE-00 using $F_{10.7}$ and $E_{10.7}$ respectively

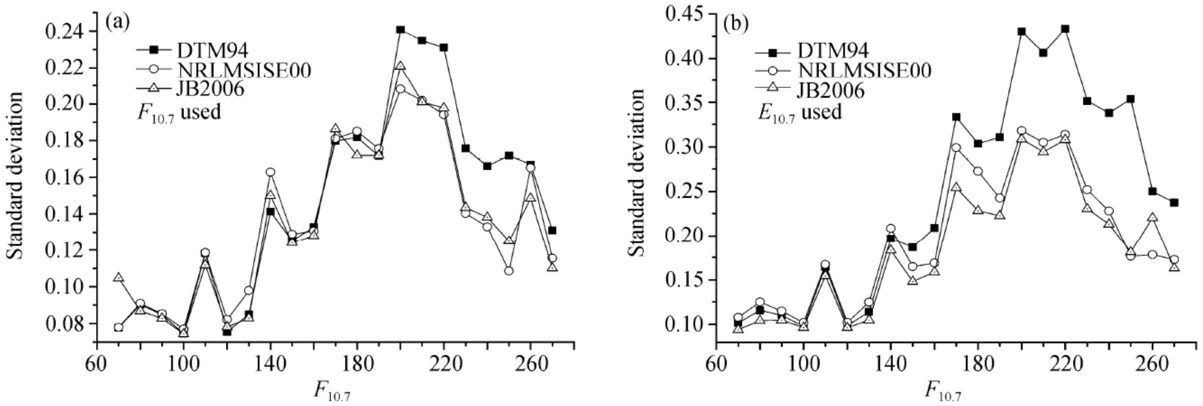

Figure 5.42 - Standard deviations of JB2006, DTM94, NRLMSISE-00 using $F_{10.7}$ and $E_{10.7}$ respectively

5.3.3 Comparison among models and accuracy

5.3.3.1 Data-to-model ratio vs altitude

To make further evaluations about the accuracy of the models, the following list of satellites was taken into account, whose measurements are used for the analyses. While the statistics are determined using the actual satellite altitude, the data for each satellite are plotted at their average perigee altitude. The models are in excellent climatological agreement.

Table 5.14 - Satellites used in model evaluation, sorted by perigee height

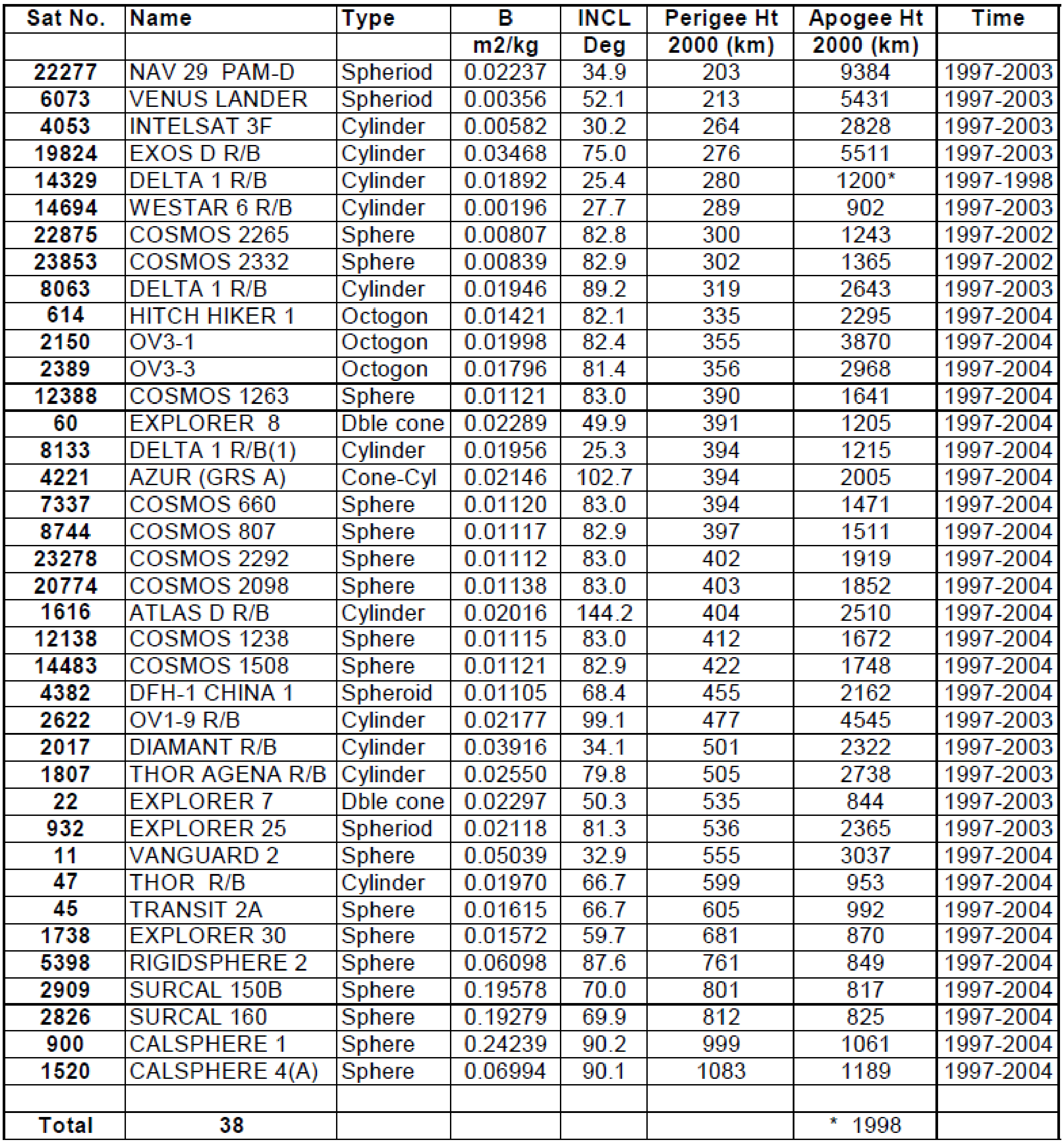

Sat No.	Name	Type	B	INCL	Perigee Ht	Apogee Ht	Time
			m2/kg	Deg	2000 (km)	2000 (km)	
22277	NAV 29 PAM-D	Spheriod	0.02237	34.9	203	9384	1997-2003
6073	VENUS LANDER	Spheriod	0.00356	52.1	213	5431	1997-2003
4053	INTELSAT 3F	Cylinder	0.00582	30.2	264	2828	1997-2003
19824	EXOS D R/B	Cylinder	0.03468	75.0	276	5511	1997-2003
14329	DELTA 1 R/B	Cylinder	0.01892	25.4	280	1200*	1997-1998
14694	WESTAR 6 R/B	Cylinder	0.00196	27.7	289	902	1997-2003
22875	COSMOS 2265	Sphere	0.00807	82.8	300	1243	1997-2002
23853	COSMOS 2332	Sphere	0.00839	82.9	302	1365	1997-2002
8063	DELTA 1 R/B	Cylinder	0.01946	89.2	319	2643	1997-2003
614	HITCH HIKER 1	Octogon	0.01421	82.1	335	2295	1997-2004
2150	OV3-1	Octogon	0.01998	82.4	355	3870	1997-2004
2389	OV3-3	Octogon	0.01796	81.4	356	2968	1997-2004
12388	COSMOS 1263	Sphere	0.01121	83.0	390	1641	1997-2004
60	EXPLORER 8	Dble cone	0.02289	49.9	391	1205	1997-2004
8133	DELTA 1 R/B(1)	Cylinder	0.01956	25.3	394	1215	1997-2004
4221	AZUR (GRS A)	Cone-Cyl	0.02146	102.7	394	2005	1997-2004
7337	COSMOS 660	Sphere	0.01120	83.0	394	1471	1997-2004
8744	COSMOS 807	Sphere	0.01117	82.9	397	1511	1997-2004
23278	COSMOS 2292	Sphere	0.01112	83.0	402	1919	1997-2004
20774	COSMOS 2098	Sphere	0.01138	83.0	403	1852	1997-2004
1616	ATLAS D R/B	Cylinder	0.02016	144.2	404	2510	1997-2004
12138	COSMOS 1238	Sphere	0.01115	83.0	412	1672	1997-2004
14483	COSMOS 1508	Sphere	0.01121	82.9	422	1748	1997-2004
4382	DFH-1 CHINA 1	Spheroid	0.01105	68.4	455	2162	1997-2004
2622	OV1-9 R/B	Cylinder	0.02177	99.1	477	4545	1997-2003
2017	DIAMANT R/B	Cylinder	0.03916	34.1	501	2322	1997-2003
1807	THOR AGENA R/B	Cylinder	0.02550	79.8	505	2738	1997-2003
22	EXPLORER 7	Dble cone	0.02297	50.3	535	844	1997-2003
932	EXPLORER 25	Spheriod	0.02118	81.3	536	2365	1997-2003
11	VANGUARD 2	Sphere	0.05039	32.9	555	3037	1997-2004
47	THOR R/B	Cylinder	0.01970	66.7	599	953	1997-2004
45	TRANSIT 2A	Sphere	0.01615	66.7	605	992	1997-2004
1738	EXPLORER 30	Sphere	0.01572	59.7	681	870	1997-2004
5398	RIGIDSPHERE 2	Sphere	0.06098	87.6	761	849	1997-2004
2909	SURCAL 150B	Sphere	0.19578	70.0	801	817	1997-2004
2826	SURCAL 160	Sphere	0.19279	69.9	812	825	1997-2004
900	CALSPHERE 1	Sphere	0.24239	90.2	999	1061	1997-2004
1520	CALSPHERE 4(A)	Sphere	0.06994	90.1	1083	1189	1997-2004
Total	**38**					* 1998	

Figure 5.43 represents data coming from the 32 satellites in the altitude region 200-600 km; it shows that all mean ratios are within 1 +/- 0.05 except for one DTM point at 515 km. The average values over all altitudes are 0.978, 0.996. 1.009, 1.012 and 0.994 for JB2006, NRLMSIS, MET, J70 and DTM respectively.

High altitude evaluations shown in Figure 5.44 use data from the last 6 satellites; they are all in polar, near-circular orbits in the altitude region 680-1100 km. Data from two satellites between 550-650 km was added to facilitate comparisons with data in Figure 5.43. The mean ratios are again close to one for all models except NRLMSIS. The NRLMSIS mean ratios increase from about 6% higher than JB2006 at 680 km to about 25% higher at 1080 km. Picone found good agreement between NRLMSIS and J70 data for the combination of summer, high latitude and high altitude (600 to >900 km) data. This comparison was made because the NRLMSIS contains an "anomalous oxygen" during these conditions. Assuming that the drag coefficient theory used did not apply in this regime, and a value of 2.2 was applicable these densities at 900 km would be increased by an average of about 14%. Further examination is required to evaluate the differences between model density predictions in this altitude regime. [9]

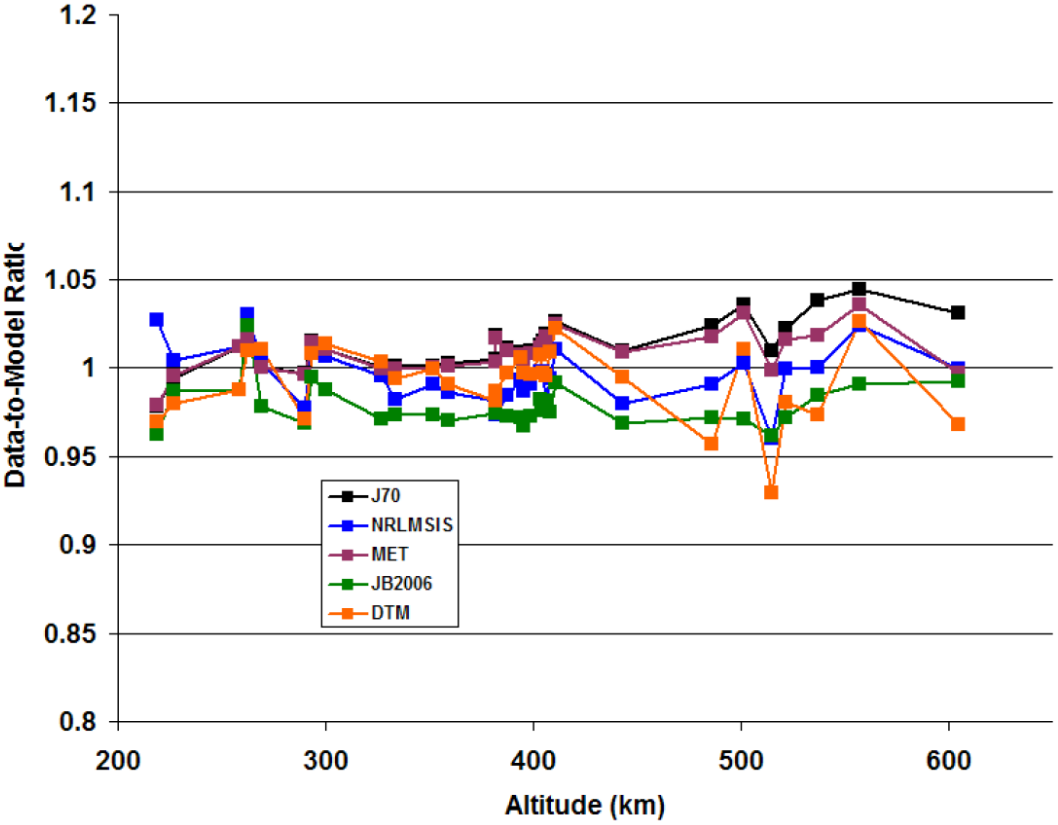

Figure 5.43 - Mean data-to-model ratios for JB2006, Jacchia70, NRLMSISE-00, MET and DTM models vs altitude

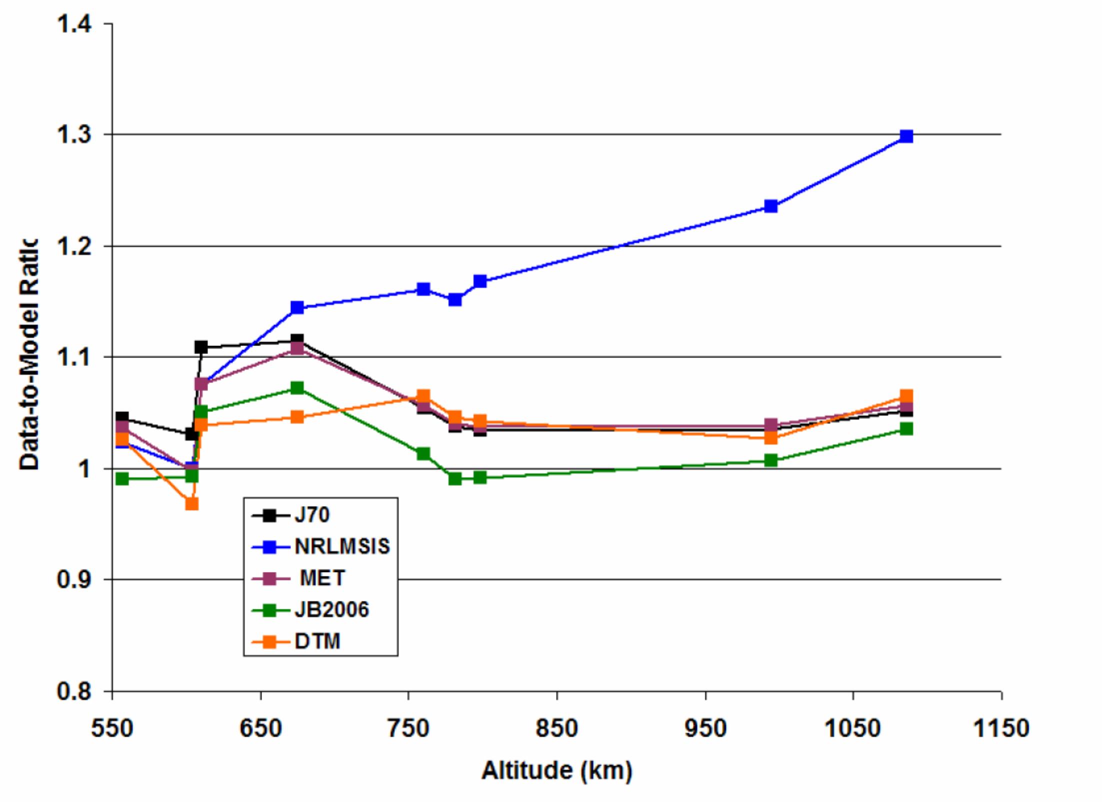

Figure 5.44 - Mean data-to-model ratios for JB2006, Jacchia70, NRLMSISE-00, MET and DTM models vs high altitude data

5.3.3.2 Standard deviation vs altitude

Standard deviations relative to previous satellites' measurements are examined in Figure 5.45. The data, obtained below 600 km, show a definite increase in model errors with altitude. The marked feature of Figure 5.45 is that standard deviations for JB2006 are systematically lower than those for the other models at all altitudes. This advantage varies from about 2% (vs J70 and MET) to 6.5% (s DTM) near 218 km to about 6% vs all models near 600 km. The NRLMSIS, J70 and MET model errors all agree closely with altitude. The J70 values fall on those of MET up to about 550 km. Therefore, while all models agree on climatology, the precision of the JB2006 model represents a significant improvement over all other empirical models.

Figure 5.46 shows standard deviations over 600 km decreasing with altitude, in contrast to the increase below about 600 km shown in Figure 5.46. Again, JB2006 values are lowest, being generally about 5% less than J70 (and MET). [9]

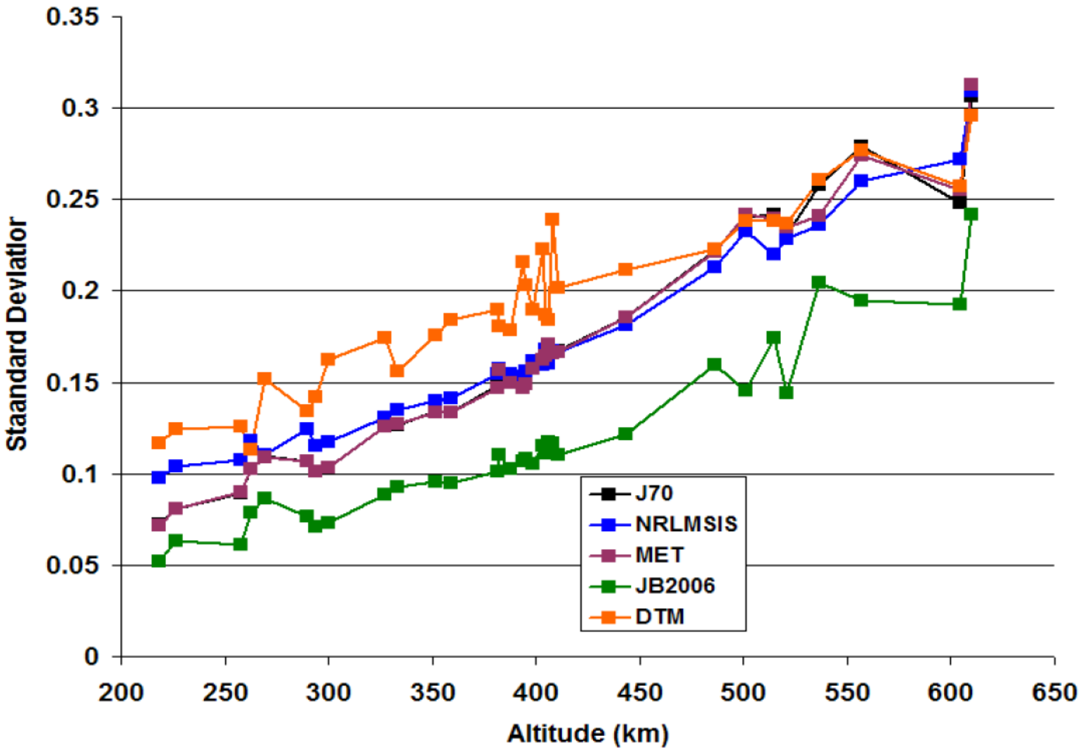

Figure 5.45 - Standard deviations of data-to-model ratios for JB2006, Jacchia70, NRLMSISE-00, MET and DTM models vs altitude

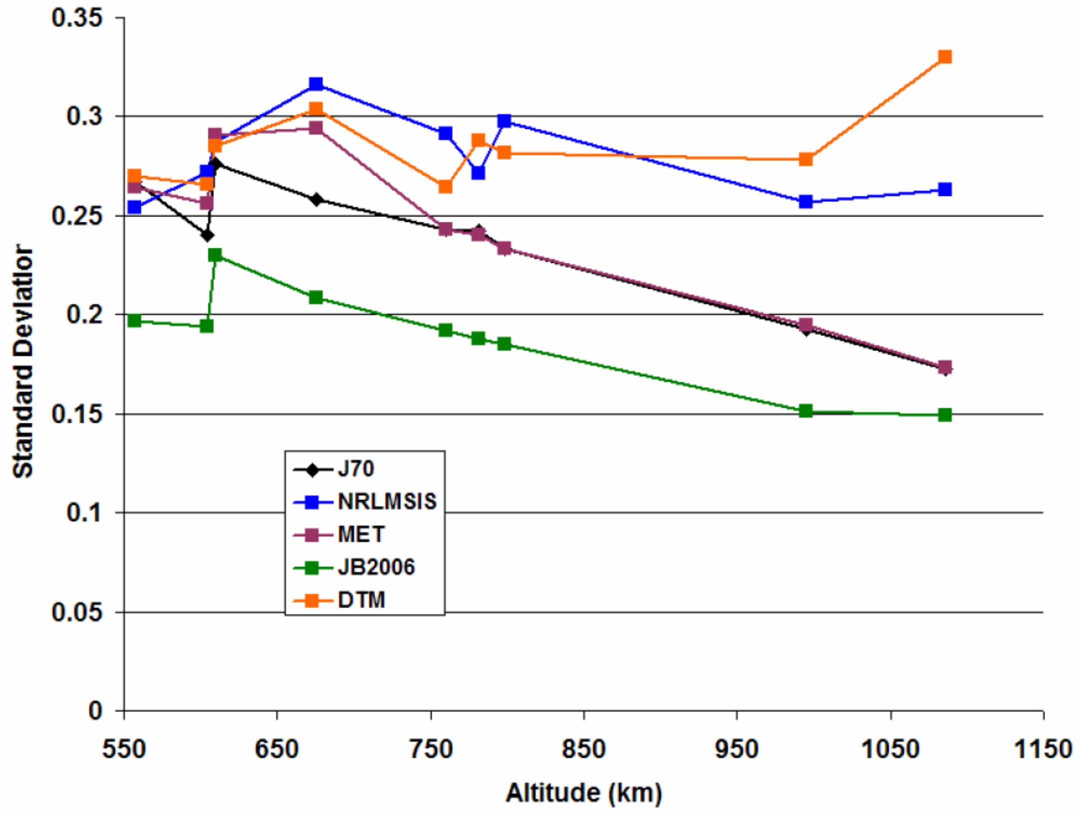

Figure 5.46 - Standard deviations of data-to-model ratios for JB2006, Jacchia70, NRLMSISE-00, MET and DTM models vs high altitude data

6 SOLAR INDICES FORECAST

6.1 Forecast method of Jacchia-Bowman 2006 (JB2006)

The new solar indices are provided in forecast on the website of the Space Environment Technologies (SET) (http://SpaceWx.com) through the model SOLAR2000 (S2K) as well as real-time and historical time frames on the website (http://sol.spacenvironment.net/~jb2006/) which does not exist anymore, due to the new model JB2008. The $F_{10.7}$, $S_{10.7}$, and $M_{10.7}$ proxies and indices, along with their 81-day Centred smoothed values, are used as the solar inputs for the JB2006 empirical thermospheric density model. An additional motivation has been to provide real-time and forecast solar indices for thermospheric density and ionospheric applications. The foundation for the empirical forecasting in SET's Forecast Generation 2 (FGen2/D3.5) of S2K is persistence and recurrence, and this is achieved using linear prediction for $F_{10.7}$, $S_{10.7}$, and $M_{10.7}$. A generic formulation of a linear predictive technique was developed, that was proved to be the most successful in the 0-72 hours' time frame:

$$x_t = \varphi_1 x_{t-1} + \varphi_2 x_{t-2} + \cdots + \varphi_P x_{t-P} + w_t$$

Where x is the solar index value at a forecast time 't', P is most recent values to be used, φ are linear coefficients, and w is a residual error term.

Out to 48 hours prediction it is used the 3 most recent days of index values.

Between 48–96 hours it is used the last 5 solar rotations (137 days) as the most recent values.

The predictive results for high solar activity between January 20 and July 15, 2001 are shown in figure below and can be created for $F_{10.7}$, $S_{10.7}$, and $M_{10.7}$ indices and proxies.

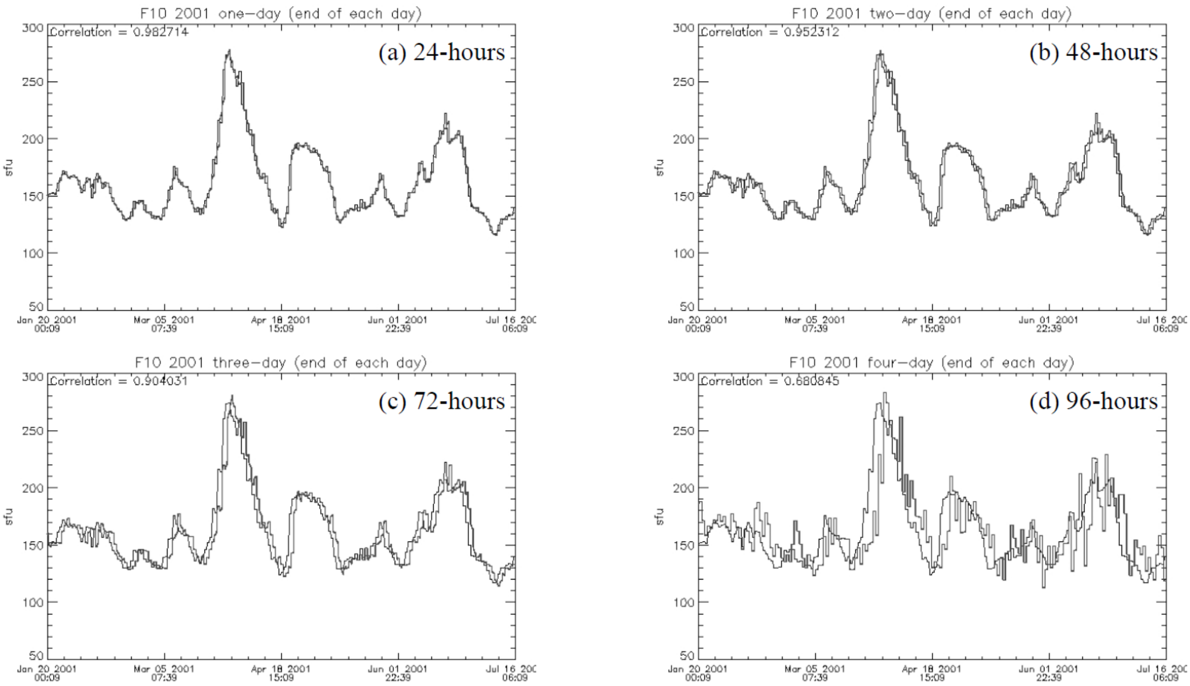

Figure 6.1 - Predicted (dark grey) and actual (black) $F_{10.7}$ for January 20 - July 15, 2001

The results for low solar activity between April 1 and October 1, 2005 are show below for $F_{10.7}$, $S_{10.7}$, and $M_{10.7}$ indices and proxies.

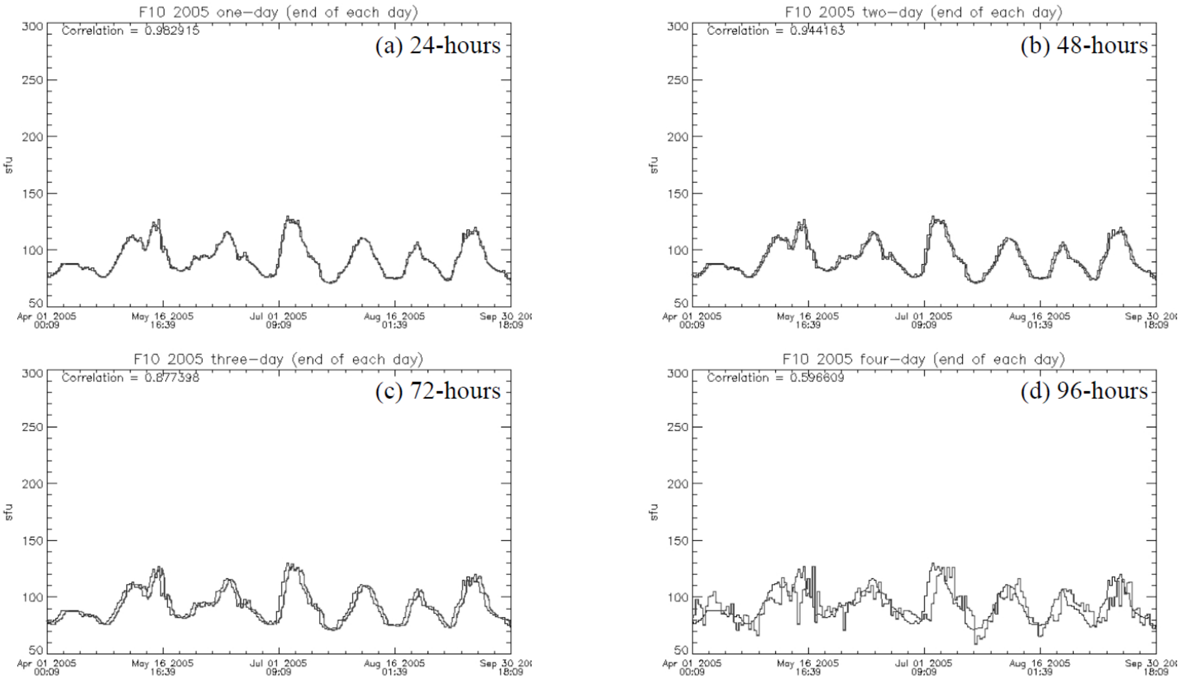

Figure 6.2 - Predicted (dark grey) and actual (black) $F_{10.7}$ for April 1 - September 30, 2005

The table below summarizes the regression coefficients from the forecasts for both high (2001) and low (2005) solar activity. The forecasts were generated every 6 hours throughout the six-month duration of each solar activity period, that is the time of forecast. There is a 3-hour time granularity at each forecast epoch. Since solar indices that are produced operationally are derived from multiple data sets, there is a time lag between the most recent values driving the forecast and the current epoch. In some cases, there may be a 24-hour lag between the current epoch nowcast and the most recent data used to create it.

Table 6.1 - Correlation coefficients (R) of forecast solar indices and proxies

Index or proxy	**2001 nowcast**	**2001 24-hour**	**2001 48-hour**	**2001 72-hour**	**2001 96-hour**	**2005 nowcast**	**2005 24-hour**	**2005 48-hour**	**2005 72-hour**	**2005 96-hour**
$F_{10.7}$	0.989090	0.982714	0.952312	0.904031	0.680845	0.983788	0.982915	0.944163	0.877398	0.596609
$S_{10.7}$	0.991434	0.986761	0.962630	0.911422	0.683100	0.981661	0.982107	0.945225	0.867663	0.626203
$M_{10.7}$	0.990299	0.987867	0.953183	0.894666	0.626743	0.988092	0.989048	0.955103	0.895198	0.727505

The FGen2 linked data and model system is at TRL 7, i.e., a system prototype has been demonstrated in a relevant operational environment; the system is at or near the scale of an operational system with most functions available for demonstration and test; it is well integrated with collateral and ancillary systems and there is limited documentation available.

The capabilities combine real-time solar irradiance data streams with operational models to produce current epoch and forecast geoeffective integrated solar irradiances in the form of $F_{10.7}$, $S_{10.7}$, and $M_{10.7}$ indices and proxies. The $F_{10.7}$ proxy has existed for many years and, with a 1-day lag, continues to be a useful surrogate for cool corona and transition region XUV–EUV solar irradiances depositing their energy throughout the thermosphere. The new $S_{10.7}$

index of chromospheric EUV solar irradiances, with a 1-day lag, significantly improves the estimation of the solar energy that heats atomic oxygen in the terrestrial thermosphere. The revised $M_{10.7}$ proxy for photosphere/lower chromosphere FUV solar irradiances, based on the Mg II and with a 5-day lag, significantly improves the estimation of the solar energy that dissociates molecular oxygen in the terrestrial lower thermosphere. One-sigma forecast uncertainties out to 72-hours are 1–10% for all three proxies/indices in high as well as low solar activity conditions. These three indices and proxies are designed for use in the new JB2006 thermospheric density model. They provide a significantly improved 72-hour thermospheric density forecast for operational satellite users and make available the information to interpret irradiance-related space weather events quickly and to react appropriately. [10]

Table 6.2 - 1-sigma percentage uncertainty at selected forecast epochs

Hours from current epoch	+00	+24	+48	+72	+96
NOAA SEC/AFWA	3.6	6.3	9.0	11.7	–
FGen1X	2.7	5.6	8.2	11.4	–
FGen2	0.0	1.3	3.9	8.4	32.5

6.2 Forecast method of Jacchia-Bowman 2008 (JB2008)

The indices previously described for input into the JB2008 model, as well as the model Fortran source code, are provided by Space Environment Technologies at the JB2008 menu link on the website http://spacewx.com. The Solar Irradiance Platform (SIP) – also known as SOLAR2000 (S2K) provides historical, current epoch, and forecast daily JB2008 indices and proxies updated hourly with daily time granularity, as well as full spectral irradiances and real-time solar activity monitoring for satellite and communication system operations. SIP can be downloaded at the http://spacewx.com SIP menu link. Hereunder the process to determine the solar and geomagnetic indices is described. These reference values can be used to test model scenarios under standardized conditions of solar and geomagnetic activity if forecasts are not available. [11]

6.2.1 Intermediate-term and short-term solar variability reference values

Reference index values are provided in Table 6.3 for intermediate-term variability that includes more than one solar rotation (>27 days), but for not more than a half solar cycle (<6 years). The 81-day smoothed minimum, mean, and maximum values rounded to the nearest unit of 5 for solar cycle 23 (year 1997-2008) are used for reference low, moderate, and high intermediate-term examples, respectively. Solar cycle 23 is considered a moderate cycle by recent historical standards. Daily (short-term) solar variability reference values for less than a solar rotation (27 days) are also provided in Table 6.3 as rounded numbers to the nearest unit of 5.

The period of October 14 to November 9, 2003 in solar cycle 23 is used as a reference period when highly variable activity occurred; these are conditions appropriate to the rise of a solar cycle or large events that occur during the decline of a solar cycle. A second period is provided from January 7 to February 2, 2005 when lower variable activity occurred; these are conditions appropriate approaching or leaving the minimum of a solar cycle. In short-term periods, higher values have been measured than those given in Table 6.3, e.g., $F_{10.7} = 380$ over a day. However, empirical atmosphere density models are not developed for such high index values and their use will lead to large and unknown errors.

In Table 6.3, the example Cases 1, 2, and 3 should use the low, moderate, and high solar activity levels for that Case only as one complete set of inputs into JB2008. The 81-day value should be set to the moderate Case value for each proxy or index. Values from different Case examples should not be mixed. If a single daily value from one Case and one solar activity level is desired, the 81-day index should be set to the moderate value for each index. [11]

Table 6.3 - Reference values for intermediate-term and short-term solar variability

	Case 1: Intermediate-term (81 days)			Case 2: Short-term (27 days high activity)			Case 3: Short-term (27 days low activity)		
Daily	Low	Moderate	High	Low	Moderate	High	Low	Moderate	High
$F_{10.7}$	65	120	225	90	165	280	80	105	145
$S_{10.7}$	60	120	215	105	135	185	85	100	120
$M_{10.7}$	60	115	215	95	135	185	80	95	115
$Y_{10.7}$	50	115	180	110	150	185	90	110	135

6.2.2 Long-term solar cycle variability

Table 6.4 and Table 6.5 are provided for estimating solar cycle variability in the four solar indices. The example of solar cycle 23, a moderate cycle, is used. In these tables, the actual monthly minimum, mean, and maximum value of each index or proxy is given for a period of time of 143 months that is a solar cycle (~11-12 years). Table 6.4 reports monthly values for the $F_{10.7}$, F_{81} proxy and the $S_{10.7}$, S_{81} index. Table 6.5 reports monthly values for the $M_{10.7}$, M_{81} proxy and the $Y_{10.7}$, Y_{81} index. The table values should be used as provided for periods of up to a solar cycle if no forecasts are available. If daily values are required, the monthly values can be interpolated to daily resolution.

Monthly $F_{10.7}$ forecasts that include confidence bounds are provided by the NASA Marshall Space Flight Centre (http://solarscience.msfc.nasa.gov/) and by the NOAA SWPC (http://www.swpc.noaa.gov/). Daily forecasts for $F_{10.7}$, F_{81}, $S_{10.7}$, S_{81}, $M_{10.7}$, M_{81}, $Y_{10.7}$, and Y_{81} out to 5 solar rotations (137 days) are provided by Space Environment Technologies (http://spacewx.com "Innovations: SET Space Weather Forecasts" menu link). [11]

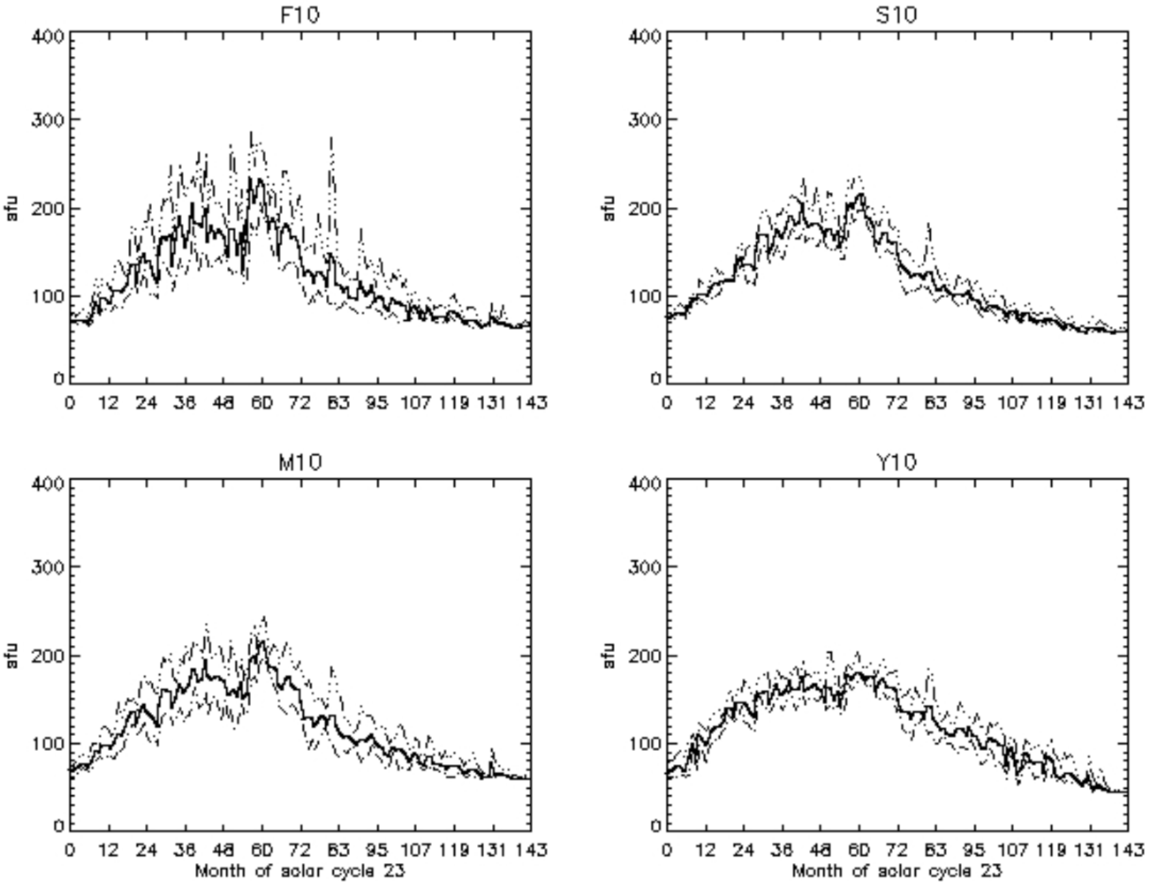

Figure 6.3 - Solar indices: monthly minimum, mean and maximum values for use by the JB2008 model from January 1, 1997 to January 1, 2009

Table 6.4 - Reference values for long-term solar cycle variability in the $F_{10.7}$, F_{81} proxy and $S_{10.7}$, S_{81} index

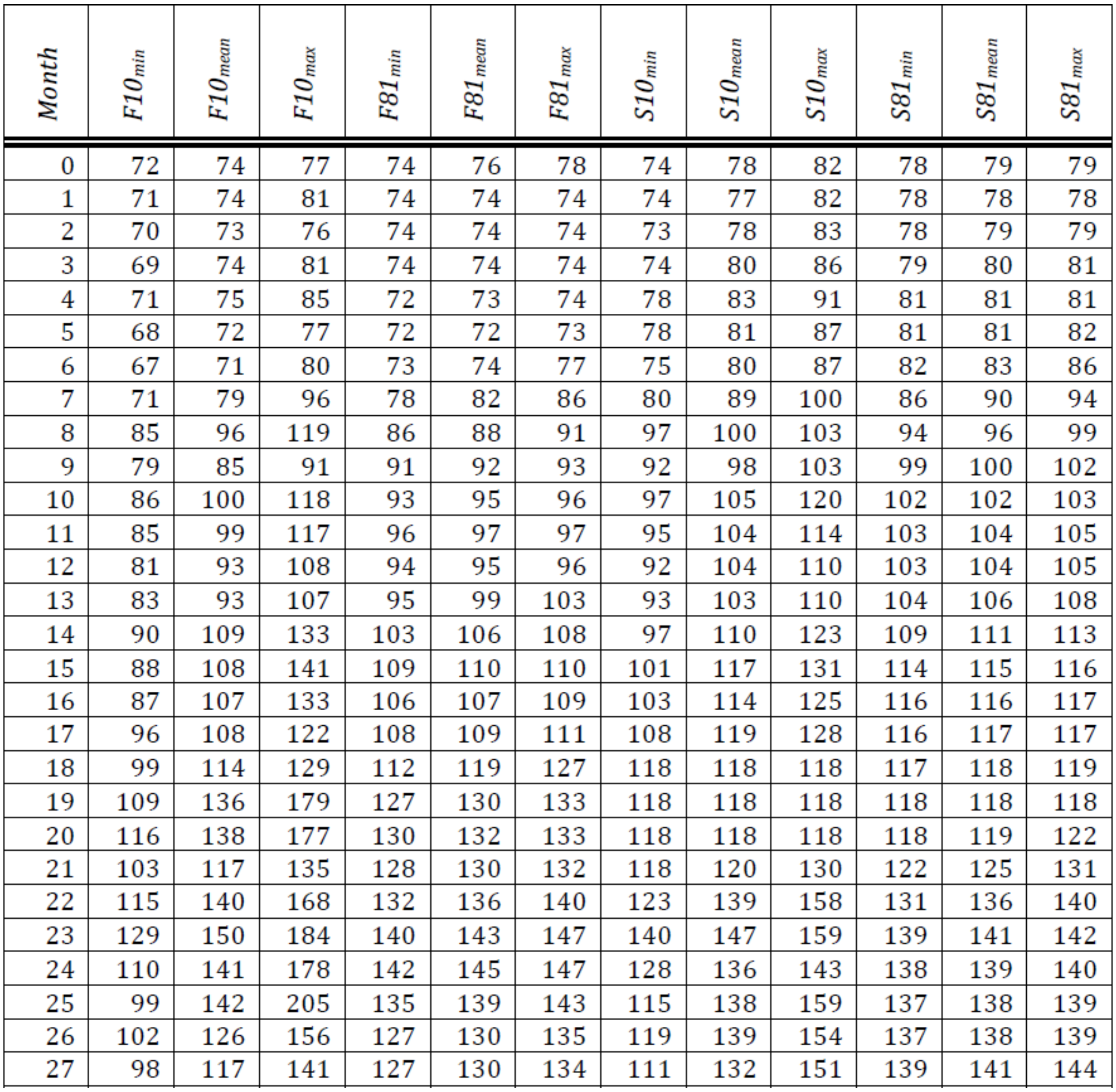

Month	$F10_{min}$	$F10_{mean}$	$F10_{max}$	$F81_{min}$	$F81_{mean}$	$F81_{max}$	$S10_{min}$	$S10_{mean}$	$S10_{max}$	$S81_{min}$	$S81_{mean}$	$S81_{max}$
0	72	74	77	74	76	78	74	78	82	78	79	79
1	71	74	81	74	74	74	74	77	82	78	78	78
2	70	73	76	74	74	74	73	78	83	78	79	79
3	69	74	81	74	74	74	74	80	86	79	80	81
4	71	75	85	72	73	74	78	83	91	81	81	81
5	68	72	77	72	72	73	78	81	87	81	81	82
6	67	71	80	73	74	77	75	80	87	82	83	86
7	71	79	96	78	82	86	80	89	100	86	90	94
8	85	96	119	86	88	91	97	100	103	94	96	99
9	79	85	91	91	92	93	92	98	103	99	100	102
10	86	100	118	93	95	96	97	105	120	102	102	103
11	85	99	117	96	97	97	95	104	114	103	104	105
12	81	93	108	94	95	96	92	104	110	103	104	105
13	83	93	107	95	99	103	93	103	110	104	106	108
14	90	109	133	103	106	108	97	110	123	109	111	113
15	88	108	141	109	110	110	101	117	131	114	115	116
16	87	107	133	106	107	109	103	114	125	116	116	117
17	96	108	122	108	109	111	108	119	128	116	117	117
18	99	114	129	112	119	127	118	118	118	117	118	119
19	109	136	179	127	130	133	118	118	118	118	118	118
20	116	138	177	130	132	133	118	118	118	118	119	122
21	103	117	135	128	130	132	118	120	130	122	125	131
22	115	140	168	132	136	140	123	139	158	131	136	140
23	129	150	184	140	143	147	140	147	159	139	141	142
24	110	141	178	142	145	147	128	136	143	138	139	140
25	99	142	205	135	139	143	115	138	159	137	138	139
26	102	126	156	127	130	135	119	139	154	137	138	139
27	98	117	141	127	130	134	111	132	151	139	141	144

Table 6.5 - Reference values for long-term solar cycle variability in the $M_{10.7}$, M_{81} proxy and $Y_{10.7}$, Y_{81} index

Month	$M10_{min}$	$M10_{mean}$	$M10_{max}$	$M81_{min}$	$M81_{mean}$	$M81_{max}$	$Y10_{min}$	$Y10_{mean}$	$Y10_{max}$	$Y81_{min}$	$Y81_{mean}$	$Y81_{max}$
0	65	72	76	72	73	74	62	66	73	69	71	74
1	62	71	75	72	72	73	63	70	84	69	69	71
2	66	73	80	73	73	74	61	71	80	71	72	72
3	67	75	86	74	75	76	63	74	87	72	73	74
4	72	78	87	76	76	77	64	76	92	72	73	75
5	70	76	86	76	76	77	65	71	86	72	72	73
6	68	75	85	76	77	80	63	70	91	73	75	80
7	73	82	99	80	84	88	65	85	104	81	87	92
8	81	94	101	88	90	92	96	103	110	92	94	98
9	85	91	98	92	93	95	68	90	100	98	100	102
10	84	98	121	95	96	97	98	112	125	101	103	104
11	84	100	120	97	98	99	91	106	120	104	105	106
12	85	99	114	97	98	99	77	101	114	102	103	104
13	85	96	107	98	99	102	91	102	116	103	106	111
14	83	103	117	103	106	109	102	115	131	111	114	118
15	94	113	147	109	111	112	105	120	136	118	120	121
16	90	110	129	112	113	114	107	122	138	120	121	122
17	99	115	139	115	117	119	113	122	129	122	123	125
18	111	128	150	119	125	130	117	127	137	125	130	134
19	122	135	148	130	132	134	132	142	162	135	136	138
20	121	137	151	132	134	135	130	140	154	138	139	139
21	109	126	137	131	133	135	123	132	138	138	139	141
22	116	137	169	134	136	138	129	148	162	141	143	145
23	126	146	175	137	139	140	142	149	158	145	148	149
24	109	138	166	137	138	140	126	149	171	146	147	148
25	102	134	172	134	135	138	123	144	167	142	144	147
26	109	130	159	130	132	134	117	136	157	137	138	142
27	97	121	157	131	132	135	115	131	143	137	139	141

6.2.3 Long-term 25-year solar variability

In order to plan orbit lifetime of a satellite, it is often useful to have a 25-year estimate of atmosphere density variability that is driven by solar indices. The procedure, described hereunder, is useful to produce a consistent, repeatable estimate of long-term 25-year JB2008 thermospheric densities.

1. Determine the relative starting point in the solar cycle for the proxies and indices from Table 6.4 and Table 6.5; the most useful index for this is the F_{81} mean value in Table 6.4; the start may be at the beginning, rise, maximum, decline, or end of a cycle; for example, to plan a mission with a spacecraft launch in 2012 and to estimate its 25-year lifetime, the assumption would be made that the mission start is approximately at the maximum of cycle 24; an appropriate date in cycle 23 would be selected such as Month 60 where the F_{81} mean value is 223; the F_{81} mean value can be used a generalized indicator of solar cycle phases;

2. Form a consecutive set of monthly proxy and index values by concatenating onto Table 6.4 and Table 6.5 the Month 0 line of the tables starting in place of Month 124; although solar cycles are often thought of as 11-year cycles, there is actually a range of cycle periods and this method results in an acceptable solar cycle length of 124 months (10 years, 4 months) where the discontinuity between the end of one cycle and the start of another cycle is minimized; the cycle start in the table data set is Month 0, the peak is Month 60, and the cycle end is Month 123.

3. Repeat this process as many months, years, or solar cycles as are needed. [11]

6.2.4 a_p geomagnetic variability and Dst storm and substorm variability

Low, moderate or high values for a_p can occur at any time in the solar cycle. Table 6.6 shows the a_p high-latitude planetary geomagnetic index, the Dst ring current index, and the change in exospheric temperature dT_c for an example storm on November 20-21, 2003 over the course of 48 hours. Figure 6.4 and Figure 6.5 show the a_p, Dst, and dT_c indices for solar cycle 23 and for a storm period of November 19-22, 2003.

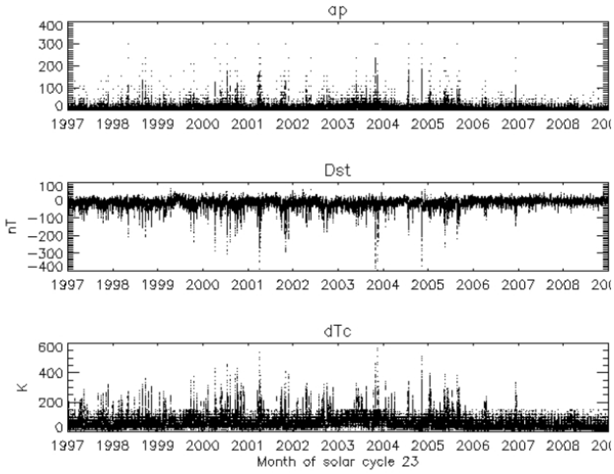

Figure 6.4 - The a_p, Dst and dT_c geomagnetic, ring current and delta temperature indices for use by the JB2008 model in solar cycle 23

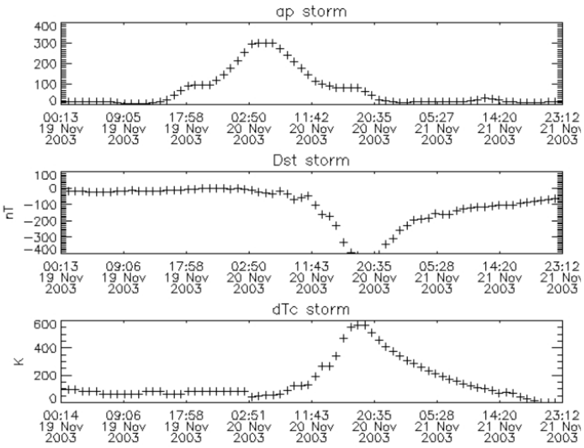

Figure 6.5 - The a_p, Dst and dT_c geomagnetic, ring current and delta temperature indices for use by the JB2008 model in a storm period between November 19-22, 2003

In short-term periods, higher values than those given in Table 6.6 have been measured, e.g. a_p= 400 for 3 hours. However, empirical atmosphere density models are not developed for such high index values and their use will lead to large and unknown errors. When JB2008 is run for long periods without consideration of storms, e.g. using Table 6.4 and Table 6.5 or the 25-year prediction method, a suitable low level constant a_p can be used such as the historical long-term mean value, a_p = 12. The long-term historical mean value of Dst is -15 and the historical long-term mean value of dT_c is 58. [11]

Table 6.6 - Example values for a_p, Dst and dTc storm variability

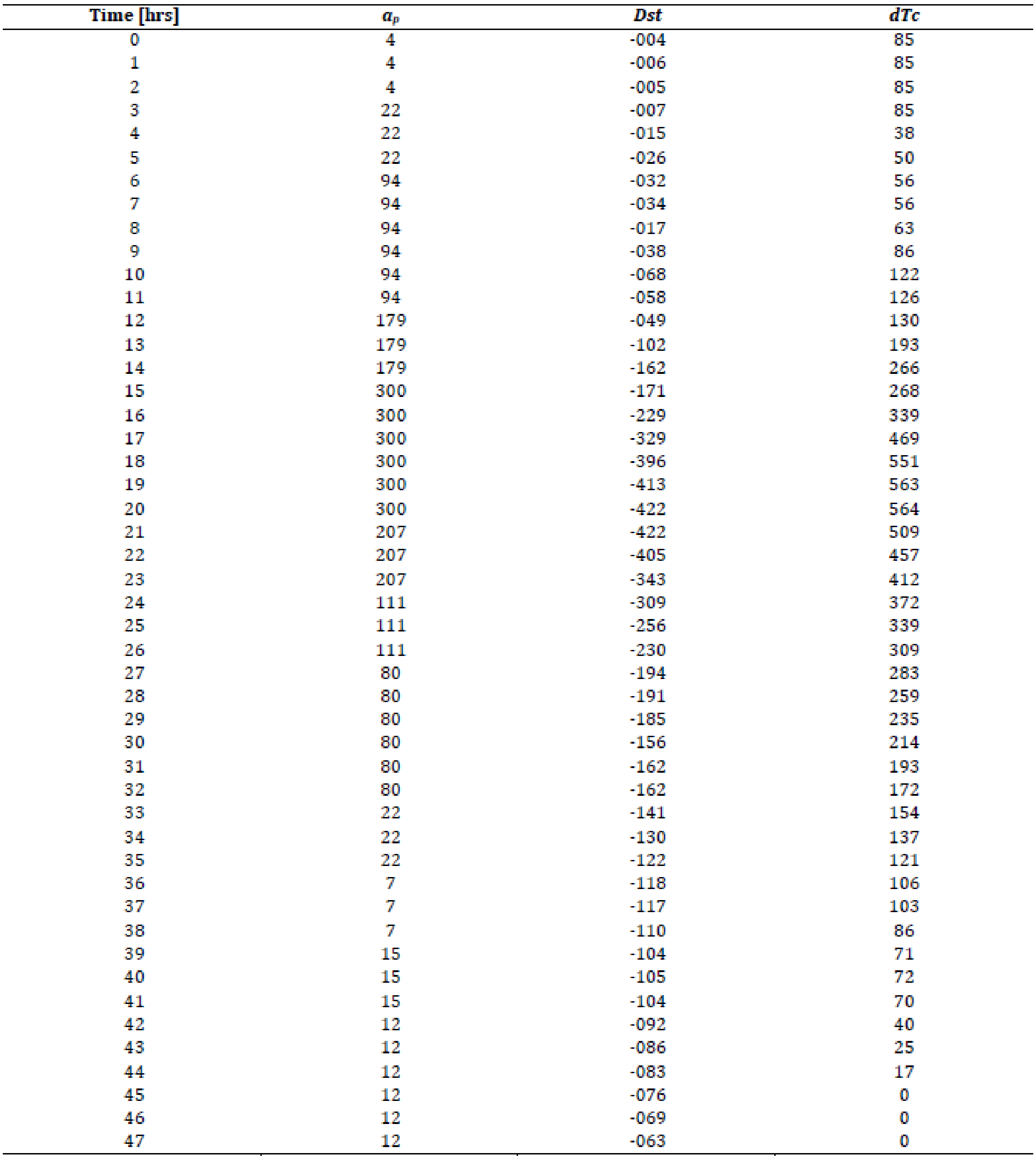

Time [hrs]	a_p	*Dst*	*dTc*
0	4	-004	85
1	4	-006	85
2	4	-005	85
3	22	-007	85
4	22	-015	38
5	22	-026	50
6	94	-032	56
7	94	-034	56
8	94	-017	63
9	94	-038	86
10	94	-068	122
11	94	-058	126
12	179	-049	130
13	179	-102	193
14	179	-162	266
15	300	-171	268
16	300	-229	339
17	300	-329	469
18	300	-396	551
19	300	-413	563
20	300	-422	564
21	207	-422	509
22	207	-405	457
23	207	-343	412
24	111	-309	372
25	111	-256	339
26	111	-230	309
27	80	-194	283
28	80	-191	259
29	80	-185	235
30	80	-156	214
31	80	-162	193
32	80	-162	172
33	22	-141	154
34	22	-130	137
35	22	-122	121
36	7	-118	106
37	7	-117	103
38	7	-110	86
39	15	-104	71
40	15	-105	72
41	15	-104	70
42	12	-092	40
43	12	-086	25
44	12	-083	17
45	12	-076	0
46	12	-069	0
47	12	-063	0

6.3 Forecast method of NRLMSISE-00

The forecast of solar index $F_{10.7}$ and of geomagnetic a_p for NRLMSISE-00 model is due to the reading of the bulletins from Marshall Space Flight Centre website that regularly updates those files. In those bulletins there is a list of the estimates of 13-month smooth future indices with a time step of 1 month. This method was created because no generally accepted solar physical model was available to accurately predict future solar activity, so Marshall Space Flight Centre (MSFC) developed a 13-month smoothed solar flux and geomagnetic index intermediate (months) and long-range (years) statistical estimation technique. The reason for issuing intermediate and long-range solar activity estimates is the need for updated inputs to the upper atmosphere density models used for satellite orbital lifetime predictions and performance requirement analyses. Mission analysis and planning for future spacecraft launches and on-orbit operations require estimates of orbital lifetime, altitudes, inclinations and eccentricities. In the following lines, it is reported the MSFC 13-month smoothed solar flux and geomagnetic index intermediate and long-range statistical estimation technique referred to as the "MSFC Lagrangian Linear Regression Technique" (MLLRT). It uses modified McNish-Lincoln linear regression method. This technique is contained in the NASA Technical Memorandum 4759 by K. O. Niehuss.

6.3.1 13-Month Smoothed Solar Flux ($\bar{F}_{10.7}$) Data Base

MLLRT for estimation of future $\bar{F}_{10.7}$ uses the observed data for all the observed cycles. The measured $\bar{F}_{10.7}$ data base was extended back to 1749 by using Wolf's relative sunspot values R and a $\bar{R}$ to $\bar{F}_{10.7}$ conversion equation. R is defined by the equation:

$$R = k(10g + f)$$

where R is the Wolf number, k is a correction factor to equalize counts from different observers, g is the number of groups visible on a given day and f is the number of a single spot observed on a given day. The R values were smoothed using the Zurich 13-month smoothing equation:

Equation 10 - Smoothed sunspot values R using Zurich 13-month smoothing equation

$$\bar{R}_i = \frac{1}{12}\left[\sum_{k=i-5}^{i+5} R_k + \frac{(R_{i-6} + R_{i+6})}{2}\right]$$

Where i indicates the month of interest. This smoothing technique was developed by the Swiss Federal Observatory, Zurich, Switzerland.

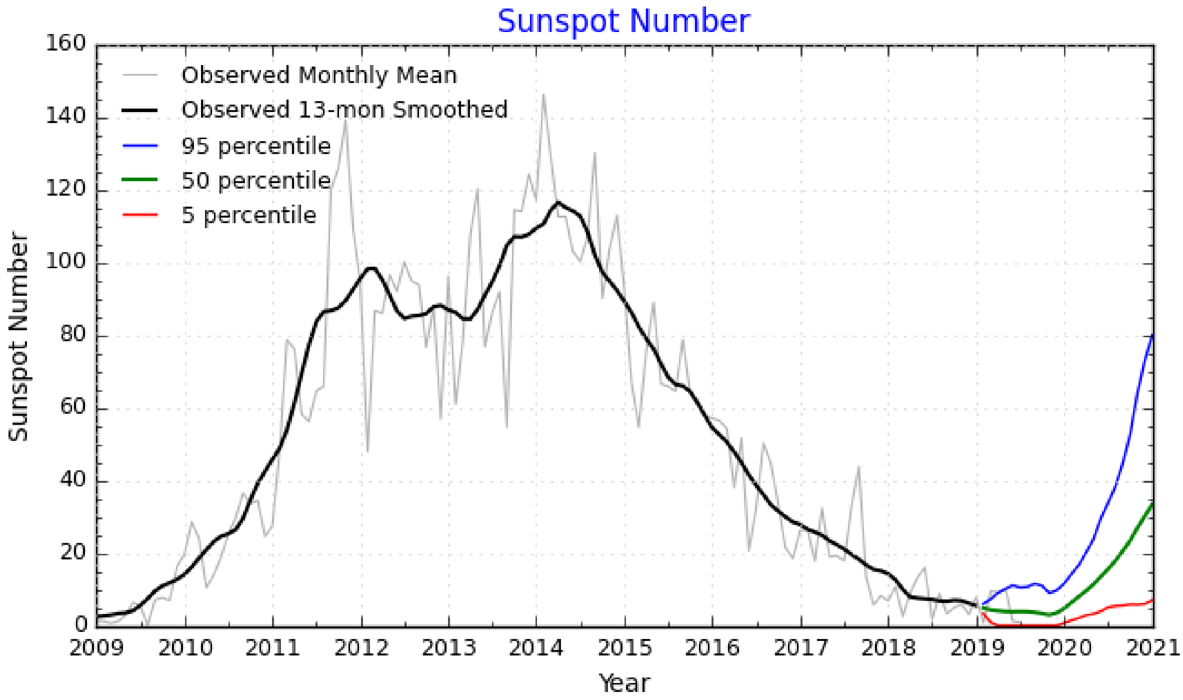

Figure 6.6 - Sunspot number trend for solar cycle 24

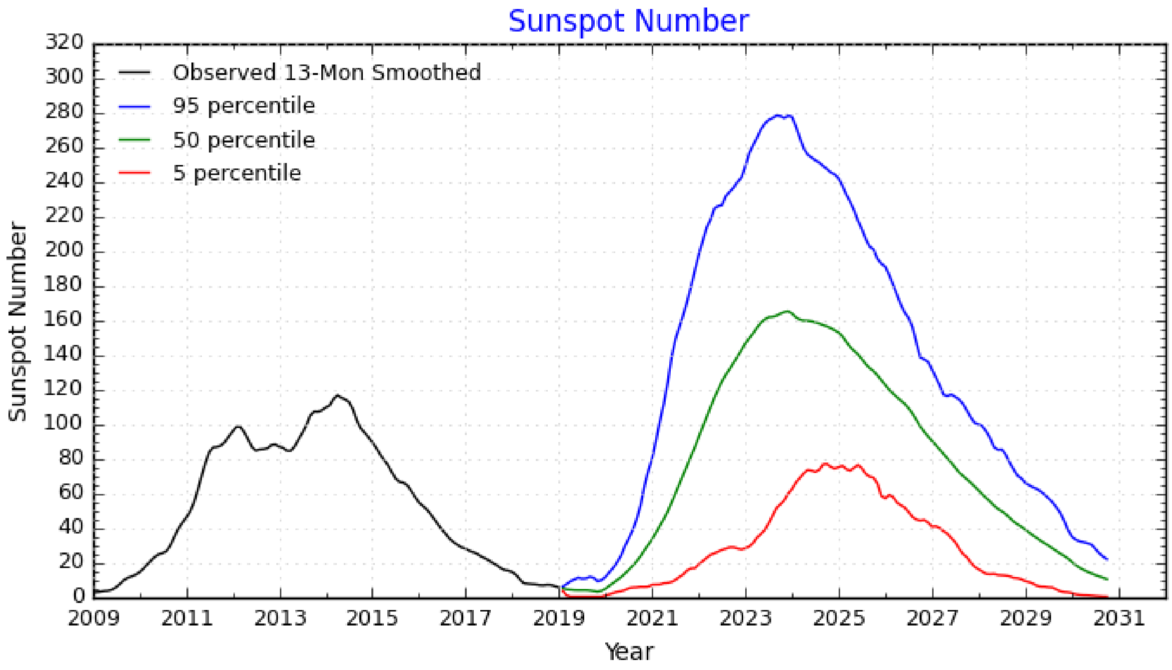

Figure 6.7 - Sunspot number forecast at 95, 50, 5 percentile for solar cycle 25

Once R values are smoothed to $\bar{R}$ values, the following equation converts recorded $\bar{R}$ data to $\bar{F}_{10.7}$ data:

$$\bar{F}_{10.7} = 49.4 + 0.97\bar{R} + 17.6e^{-0.035\bar{R}}$$

Since 1947, observed values of daily solar flux are used to directly compute mean monthly $F_{10.7}$ values. The Equation 10, replacing R with $F_{10.7}$, is used to calculate the $\bar{F}_{10.7}$. The data format in the tables is year with months in decimal form, i.e. January is 0.000 and December is 0.917. the equation to calculate the month is

$$month\ decimal\ value = \frac{month\ number - 1}{12}$$

The converted and observed $\bar{F}_{10.7}$ data are Lagrangian interpolated to normalize the data for the 132 months from the maximum of minimum cycle starting dates. The data are stored by month and cycle number to construct a database for use in the modified McNish-Lincoln linear regression method. [12]

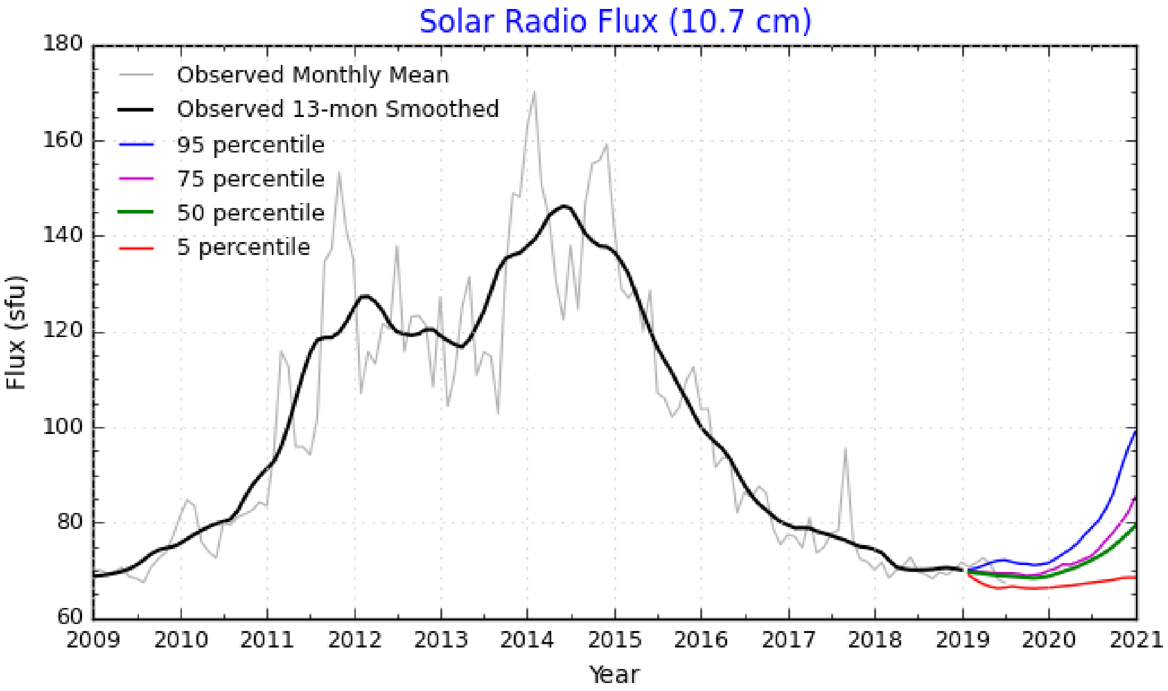

Figure 6.8 - Solar radio flux trend for solar cycle 24

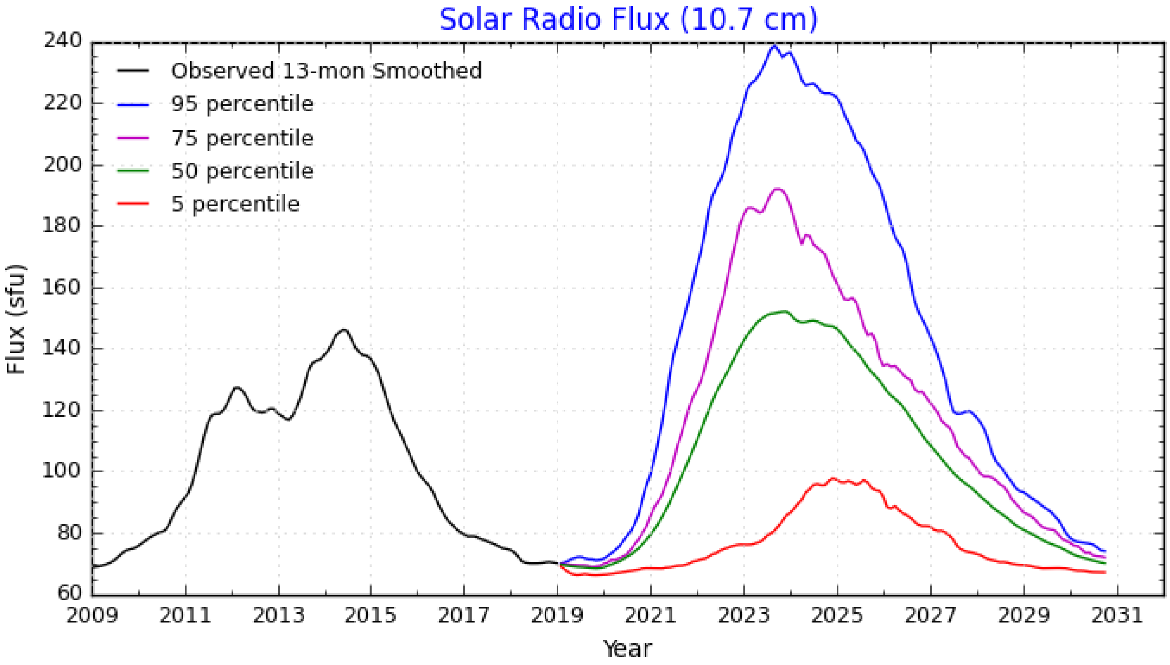

Figure 6.9 - Solar radio flux forecast at 95, 75, 50, 5 percentile for solar cycle 25

6.3.2 13-Month Smoothed Geomagnetic Index $(\bar{A}_p)$ Data Base

Because the measured geomagnetic index (A_p) data base is relatively short (1932 to 1996), it was extended back to 1884 using mean monthly magnetic character figure (C_i) data. This one is converted to 13-month smoothed data using Equation 10 and replacing R with C_i. Once it has been completed, use the following equation to convert the extended record of $\bar{C}_i$ data to $\bar{A}_p$ values.

$$\bar{A}_p = 2.8068\, e^{2.393\bar{C}_i}$$

After 1931, the measured values of daily A_p are used to compute the mean monthly value. Use Equation 10, replacing R with A_p to calculate $\bar{A}_p$. The converted and observed $\bar{A}_p$ data are Lagrangian interpolated to normalize the data for the 132 months from the maximum of minimum cycle starting dates. The data are stored by month and cycle number to construct a database for use in the modified McNish-Lincoln linear regression method. [12]

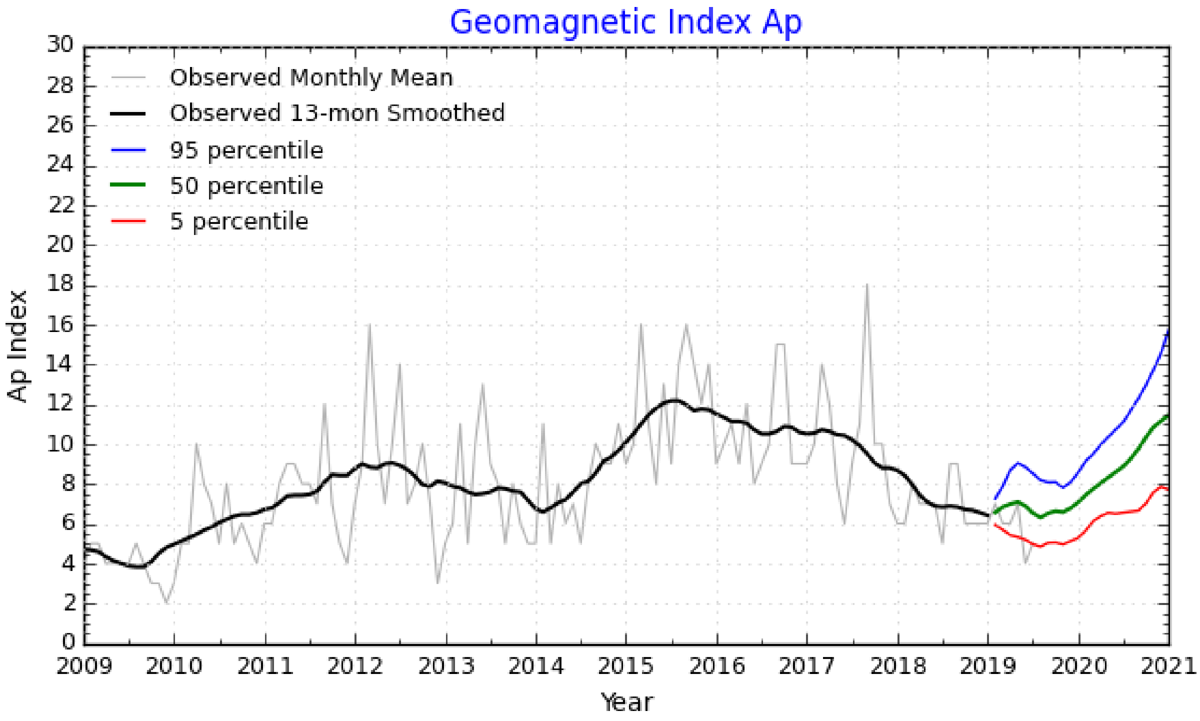

Figure 6.10 – Geomagnetic index A_p trend for solar cycle 24

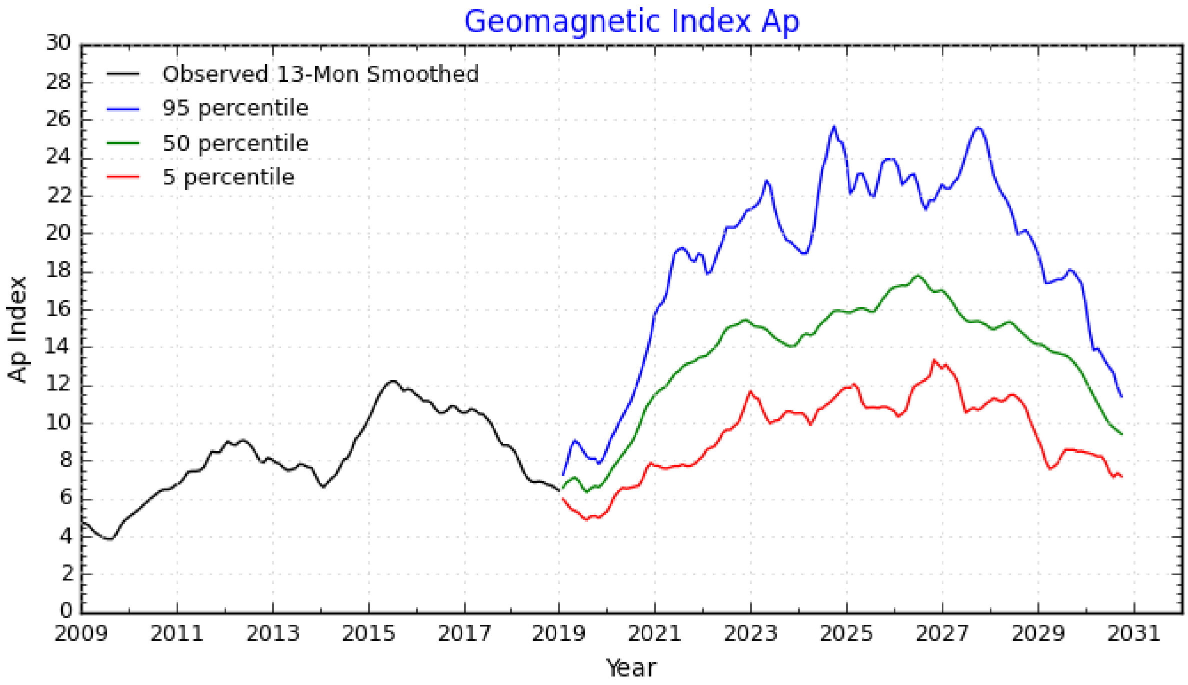

Figure 6.11 - Geomagnetic index A_p forecast at 95, 50, 5 percentile for solar cycle 25

6.3.3 Modified McNish-Lincoln Linear Regression Method

The MLLRT uses the Boykin and Richards modified McNish-Lincoln linear regression method (a kind of linear least square method) and an appropriately constructed data base that starts at the maximum or minimum to estimate the balance of the present cycle where the cycle is defined from the minimum to minimum or maximum to maximum. This method is summarized in the following steps:

1. Mean $\bar{F}_{10.7}$ or $\bar{A}_p$ is calculated from the completed cycles in the $\bar{F}_{10.7}$ or $\bar{A}_p$ data base constructed using the Lagrangian interpolated data points for use in the McNish-Lincoln linear regression method. This mean also estimates $\bar{F}_{10.7}$ or $\bar{A}_p$ for the nest cycle with $\bar{P}$.
2. McNish-Lincoln linear regression method produces a statistical estimate for the rest of the present cycle using one linear coefficient. The period for the present cycle, for which estimates of solar activity are being calculated, is the $\bar{P}$.
3. Since, for the present cycle, only 21 or 22 corresponding points are available for a linear regression fit of the estimated point to the last observed point, to justify calculating a standard deviation based on a normal distribution function is difficult. This non-normal distribution function produces upper and lower bounds that can and do go below the parameter physical limits. Despite being a non-normal distribution, the data are standardized to make calculations easier. The actual distribution of deviations from the smoothed linear regression line and mean line is divided by the standard deviation and used to determine the upper and lower bounds at predetermined percentile levels. Upper and lower bounds are calculated by Quantile method. The equation used is: $Q(x_i) = \frac{i}{n+1}$ where Q is quantile, i equals 1 through the total number of completed cycles, and n is equals to the total number of completed cycles. Once the quantile is calculated the percentile is: $Percentile(y) = 100.0\, Q(x)$. The percentiles are shown in the 6 pictures above by the coloured lines. They represent the upper limit of the future measurements: the percentage of future measures will certainly be under the relative lines. So for a future analysis, 50 percentile or 75 percentile lines – average values – are suitable to use.
4. Between the upper and the lower bounds discussed in step 3 is the “error space” on a two-dimensional plot of $\bar{F}_{10.7}$ or $\bar{A}_p$ versus time t. [12]

In the table below there is an example of the future estimate of $F_{10.7}$ and A_p values for three years at three percentile levels.

Table 6.7 - Estimates of 13-month smooth solar activity for balance of cycle 24 with a mean cycle given for cycle 25

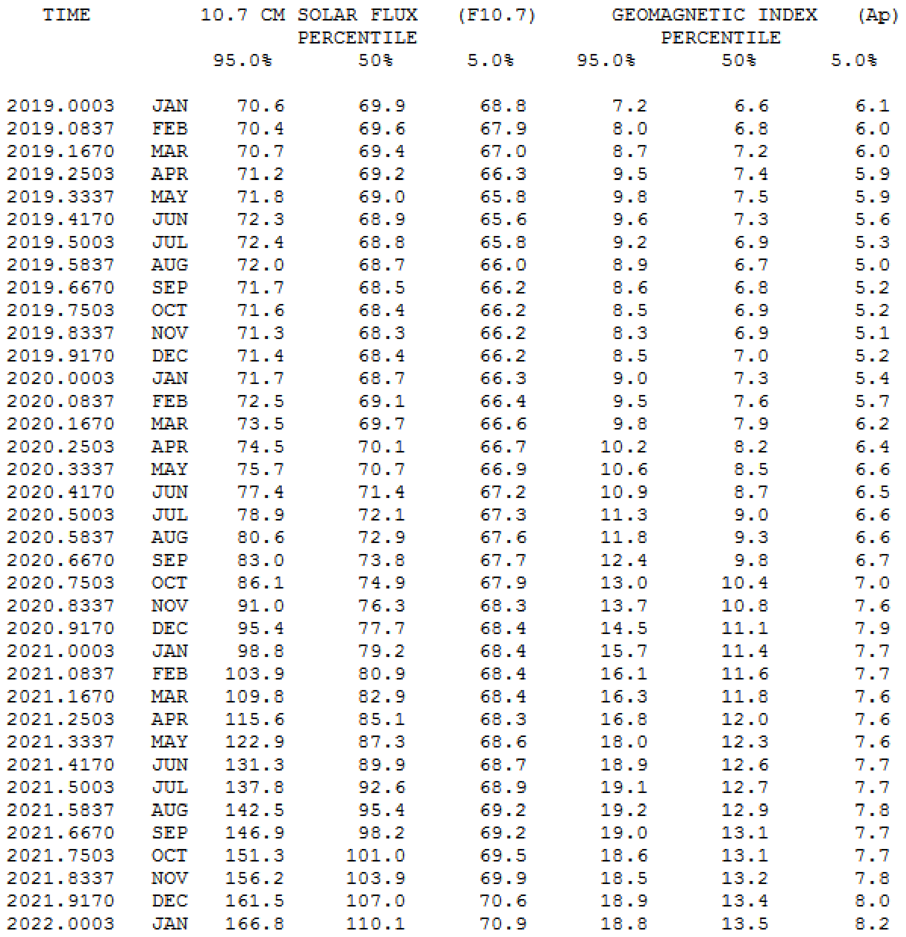

TIME		10.7 CM SOLAR FLUX PERCENTILE	(F10.7)		GEOMAGNETIC INDEX PERCENTILE	(Ap)	
		95.0%	50%	5.0%	95.0%	50%	5.0%
2019.0003	JAN	70.6	69.9	68.8	7.2	6.6	6.1
2019.0837	FEB	70.4	69.6	67.9	8.0	6.8	6.0
2019.1670	MAR	70.7	69.4	67.0	8.7	7.2	6.0
2019.2503	APR	71.2	69.2	66.3	9.5	7.4	5.9
2019.3337	MAY	71.8	69.0	65.8	9.8	7.5	5.9
2019.4170	JUN	72.3	68.9	65.6	9.6	7.3	5.6
2019.5003	JUL	72.4	68.8	65.8	9.2	6.9	5.3
2019.5837	AUG	72.0	68.7	66.0	8.9	6.7	5.0
2019.6670	SEP	71.7	68.5	66.2	8.6	6.8	5.2
2019.7503	OCT	71.6	68.4	66.2	8.5	6.9	5.2
2019.8337	NOV	71.3	68.3	66.2	8.3	6.9	5.1
2019.9170	DEC	71.4	68.4	66.2	8.5	7.0	5.2
2020.0003	JAN	71.7	68.7	66.3	9.0	7.3	5.4
2020.0837	FEB	72.5	69.1	66.4	9.5	7.6	5.7
2020.1670	MAR	73.5	69.7	66.6	9.8	7.9	6.2
2020.2503	APR	74.5	70.1	66.7	10.2	8.2	6.4
2020.3337	MAY	75.7	70.7	66.9	10.6	8.5	6.6
2020.4170	JUN	77.4	71.4	67.2	10.9	8.7	6.5
2020.5003	JUL	78.9	72.1	67.3	11.3	9.0	6.6
2020.5837	AUG	80.6	72.9	67.6	11.8	9.3	6.6
2020.6670	SEP	83.0	73.8	67.7	12.4	9.8	6.7
2020.7503	OCT	86.1	74.9	67.9	13.0	10.4	7.0
2020.8337	NOV	91.0	76.3	68.3	13.7	10.8	7.6
2020.9170	DEC	95.4	77.7	68.4	14.5	11.1	7.9
2021.0003	JAN	98.8	79.2	68.4	15.7	11.4	7.7
2021.0837	FEB	103.9	80.9	68.4	16.1	11.6	7.7
2021.1670	MAR	109.8	82.9	68.4	16.3	11.8	7.6
2021.2503	APR	115.6	85.1	68.3	16.8	12.0	7.6
2021.3337	MAY	122.9	87.3	68.6	18.0	12.3	7.6
2021.4170	JUN	131.3	89.9	68.7	18.9	12.6	7.7
2021.5003	JUL	137.8	92.6	68.9	19.1	12.7	7.7
2021.5837	AUG	142.5	95.4	69.2	19.2	12.9	7.8
2021.6670	SEP	146.9	98.2	69.2	19.0	13.1	7.7
2021.7503	OCT	151.3	101.0	69.5	18.6	13.1	7.7
2021.8337	NOV	156.2	103.9	69.9	18.5	13.2	7.8
2021.9170	DEC	161.5	107.0	70.6	18.9	13.4	8.0
2022.0003	JAN	166.8	110.1	70.9	18.8	13.5	8.2

In the MATLAB code scripts of each atmosphere model, there is already inside the forecast of solar indices or of magnetic index; besides the user should update, or download from the websites, bulletins manually to have the most recent values for analysis through the appropriate script.

7 OCCULTATIONS OF PLANETS AND STARS BY THE MOON

7.1 What is an occultation?

An occultation is an event that occurs when one celestial object is hidden by another celestial object that passes between the first one and the observer. In astronomy, the term occultation is most frequently used to describe those relatively frequent occasions when the Moon passes in front of a star or a planet during the course of its orbital motion around the Earth.

The Moon's orbit is inclined ±5°9’ with respect to the Ecliptic which is inclined 23°27’ with respect to the Earth Equator, thus the inclination of the Moon’s orbit with respect to the Earth’s Equator varies from a minimum of 18°18’ to a maximum of 28°36’ meaning that any stars with an ecliptic latitude comparable to the Moon’s may be occulted by it. Three first magnitude stars appear well within that band – Regulus, Spica and Antares - meaning they may be occulted by the Moon and/or by planets. Occultations of Aldebaran are possible by the Moon only in the present years, because the planets pass Aldebaran to the north. Neither planetary nor lunar occultations of Pollux are currently possible, however in several thousand years this will happen. Some notably close deep-sky objects, such as the Pleiades can be occulted by the Moon.

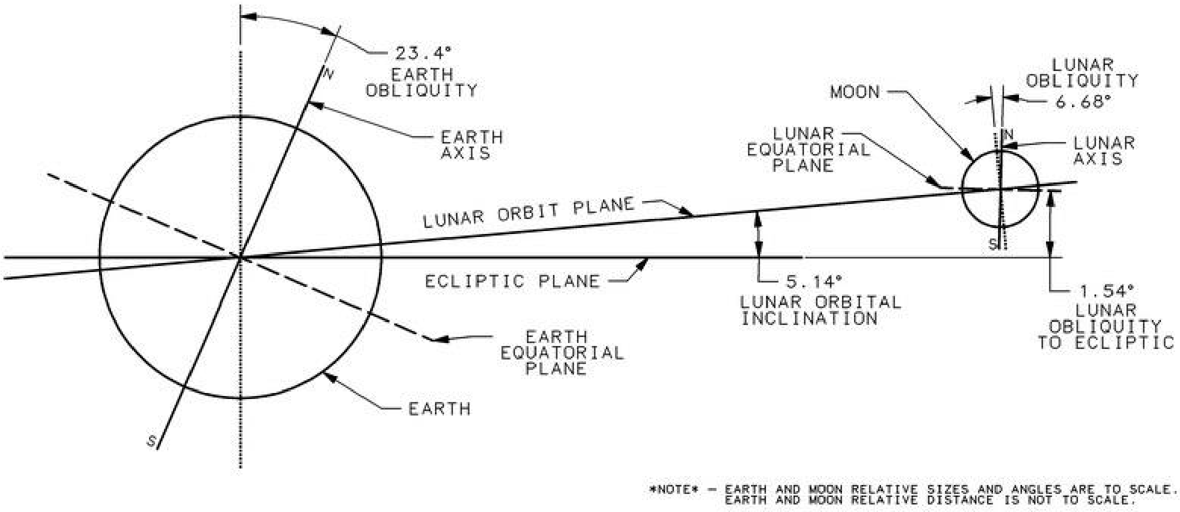

NOTE – EARTH AND MOON RELATIVE SIZES AND ANGLES ARE TO SCALE. EARTH AND MOON RELATIVE DISTANCE IS NOT TO SCALE.

Figure 7.1 – Inclination’s values of Earth and Moon

Several times during the year the Moon can be seen occulting a planet. Since planets, unlike stars, have significant angular sizes, lunar occultations of planets will create a narrow zone on Earth from which a partial occultation of the planet will occur. An observer located within that narrow zone could observe the planet's disk partly blocked by the slowly moving Moon. The same mechanic can be seen with the Sun, where observers on Earth will view it as a solar eclipse. Therefore, a total solar eclipse is effectively the same event as the Moon occulting the Sun.

A slightly difference is between the meanings of occultation and transit.

The transit is an astronomical phenomenon when a celestial body passes directly between a larger body and the observer. As viewed from a particular vantage point, the transiting body appears to move across the face of the larger body, covering a small portion of it. The word "transit" refers to cases where the nearer body appears smaller than the more distant body. Cases where the nearer body appears larger and hides completely the more distant body are known as occultations.

The typical example of a transit involves the motion of a planet between a terrestrial observer and the Sun. This can happen only with inferior planets, Mercury and Venus. However, because a transit is dependent on the point of observation, the Earth itself transits the Sun if observed from Mars, for example. The term can also be used to describe the motion of a satellite planet across its parent planet, for instance one of the Galilean satellites (Io, Europa, Ganymede, Callisto) across Jupiter, as seen from Earth. Although rare, cases where four bodies are lined up do happen. One of these events occurred on 27 June 1586, when Mercury transited the Sun as seen from Venus at the same time as a transit of Mercury from Saturn and a transit of Venus from Saturn. [W4]

For the aim of this thesis, the transits have not been taken into account because the Moon was considered the only occulting planet, and there are no planets between the Earth, where the spacecraft orbit, and the Moon.

For sake of clarity, a table with the main parameters and characteristics of the Moon is provided below.

Table 7.1 - Orbital parameters of the Moon

Property	Value
Semi-major axis	384748 km
Mean distance	385000 km
Perigee (i.e. min. distance from Earth)	362600 km (avg.) (356400–370400 km)
Apogee (i.e. max. distance from Earth)	405400 km (avg.) (404000–406700 km)
Mean eccentricity	0.0549006 (0.026–0.077)
Mean obliquity	6.687°
Mean inclination of orbit to ecliptic	5.15° (4.99–5.30)
Mean inclination of lunar equator to ecliptic	1.543°
Period of orbit around Earth (sidereal)	27.322 days
Period of orbit around Earth (synodic)	29.530 days
Period of precession of nodes	18.5996 years
Period of precession of line of apsides	8.8504 years

After this brief introduction about the event of the occultations, we are going to explain what was done for this part of the thesis.

Owning to the fact that the occultations are only related to the Moon, first of all it was studied the transit of the Moon in the Field of View of the telescopes installed on the spacecraft. Then, there are explained the two cases of the occultation of a planet and of a star, bringing also the examples of two events happened in the past. The chapter finishes with the explanation of two further cases, the observation of the sky and the future study. In connection with these routines, other scripts have been created with the only aim of writing in a .txt file the results of each study. However, these last processes are not explained here as they do not give any additional important results to the study, and thus concentrating only to the previous ones.

First of all, to be able to study the occultations, the user shall choose on which axes in the Local Orbital Reference Frame of the satellite (LORF) the instruments' FOV shall be installed. If the instruments are Star Tracker, it is advisable to put at least two of them in order to be able to determine the orientation of the satellite with reference to the stars along two directions, as star sensors do. Putting a FOV on Z_{LORF} axis, for example, means that its boresight direction coincides with the axis. In fact, it was assumed that the elevation angle from the orbital plane and the azimuth angle from one of the LORF axis, depending the chosen main direction of the FOV, are zero. For our scope, Y_{LORF} is not much used as it points towards the positive direction of the orbit angular momentum vector, i.e. perpendicular to the orbital plane and then in general with a slow motion. This choice was also strengthened by the fact that it was chosen an equatorial or slightly inclined prograde orbit as those used in the subsequent analysis. The reason is to be able to catch the Moon and the relative occultations. Therefore, Y_{LORF} telescope is not used as it will never have the Moon in its FOV. For this reason, it was chosen to set the FOV boresight only towards X_{LORF} and Z_{LORF}. It can be chosen only one telescope or both, the choice has been left to the user. To improve the code, the possibility of a Y_{LORF} telescope can be implemented in future, for other kinds of missions.

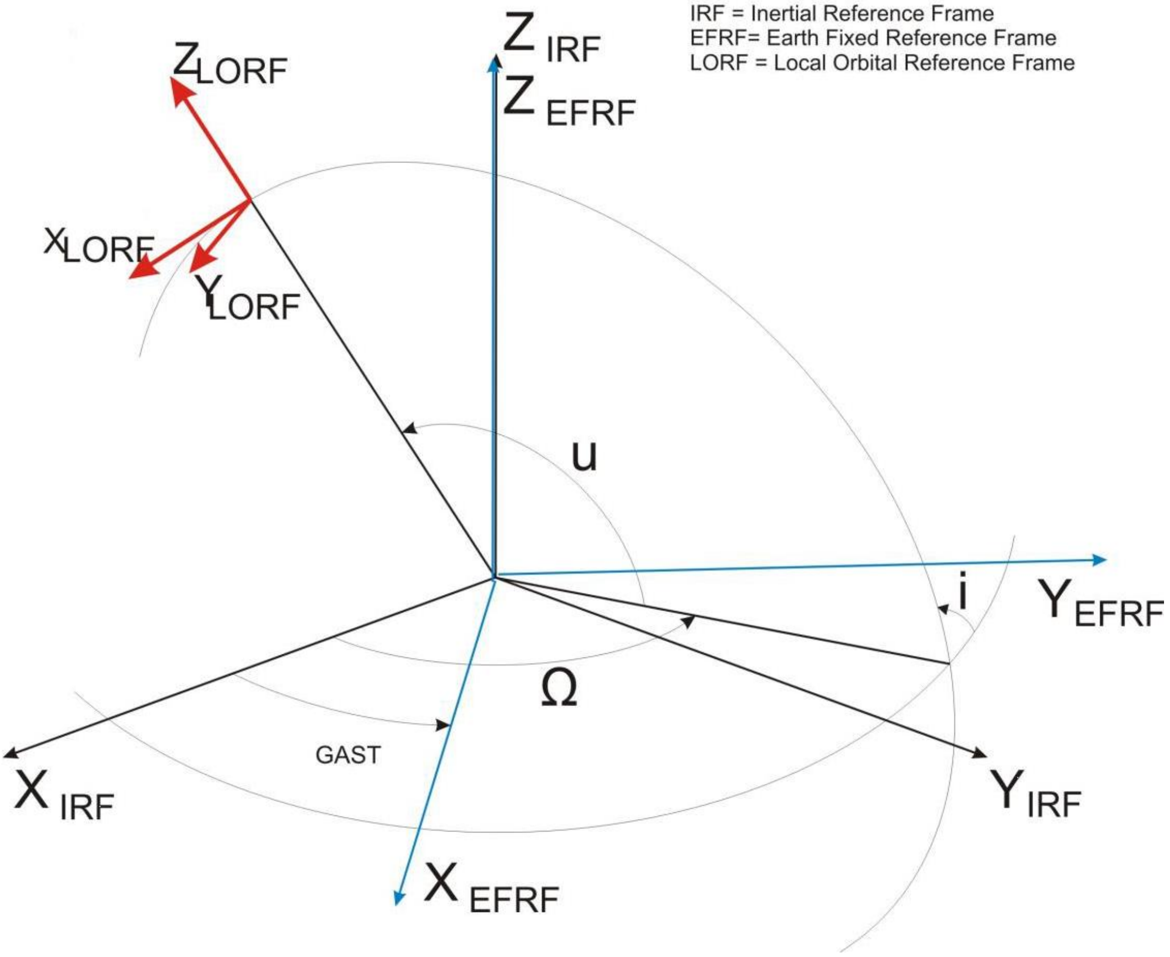

Figure 7.2 - LORF reference frame

X_{LORF} is directed towards the positive direction of the velocity, Z_{LORF} is directed as the vector connecting the Earth's centre to the satellite; the cross product of Z_{LORF} and X_{LORF} gives the Y_{LORF} as result. An explanation must be given to the reader: most of times, in this report, with the term of "telescope" and its plural form, it is meant every instrument with a Field of View, whether it is a telescope or a Star Tracker, depending on the purpose of the mission.

Once chosen the favourite positions for FOV, the angular dimensions of each Field of View (later FOV) shall be indicated. From a quick search on the net, it was found that most of star sensors have the FOV dimensions from few degrees up to 10°-15°. For initial evaluations of the scripts, it was chosen to put both dimensions of each telescope at 180° in order to be certain to catch each passage, whether it is of Moon or a planet or a star. After setting all these initial features, the Moon transitions in satellite FOVs have been studied.

7.2 Moon in Field of View of the satellite

To study the passages of the Moon in the FOV of the satellite, it is important to know the position of the satellite and the position of the Moon at each time step for the entire period of time of the simulation. The S/C's position is already known thanks to other previous parts of the code, which give as output the coordinates of the S/C in different reference systems, from TOD to GCRF to ITRF. Below a table comparing all the reference frames is provided.

Table 7.2 - Reference frames

Id.	Frame	Origin	X axis	Y axis	Z axis
GCRF	*Geocentric Celestial Reference Frame* inertial frame (SPICE: equivalent to J2000)	Centre of Earth	Intersection of the mean ecliptic plane with the mean equatorial plane at the date of 01/01/2000 noon and pointing positively towards the vernal equinox	Completes the right-handed orthogonal reference frame	Orthogonal to the mean equatorial plane at the date of 01/01/2000 noon and pointing positively towards the North
TOD	*True of Date* dynamic frame	Centre of Earth	On the true (instantaneous) Earth equatorial plane and pointing positively towards the true vernal equinox of date	Completes the right-handed orthogonal reference frame	Orthogonal to the true equatorial plane at the date and pointing positively towards the North
ITRF	*International Terrestrial Reference Frame* Earth-fixed frame (SPICE: ITRF93)	Centre of Earth	On the true equatorial plane at the epoch and pointing positively towards the Greenwich meridian	Completes the right-handed orthogonal reference frame	Orthogonal to the true equatorial plane at the epoch and pointing positively towards the North
LORF	*Local Orbital Reference Frame* satellite frame	Actual position of the satellite centre of mass	Parallel to the orbital plane and pointing positively along the velocity vector	Orthogonal to the orbital plane and pointing positively towards the same direction as the orbit angular momentum	In the orbital plane, directed as the vector connecting the Earth’s centre to the satellite

It was chosen to use TOD coordinates, which can be written as Cartesian or Keplerian: the former gives, for each time step, the Cartesian components of the position and the velocity, instead the latter has them transformed into the six orbital elements. For this use, the Cartesian components are preferred to the others. Then, it is necessary to know the position of the Moon; it can be easily found by using the NASA-JPL-NAIF SPICE routine, called *SPKEZR* (cspice_spkezr). [13] It generates the Moon's state vector (position and velocity) at time steps of the simulation as elapsed seconds since J2000.0, the reference system in which we want the output written to, i.e. TOD, and the observer, thus the Earth.

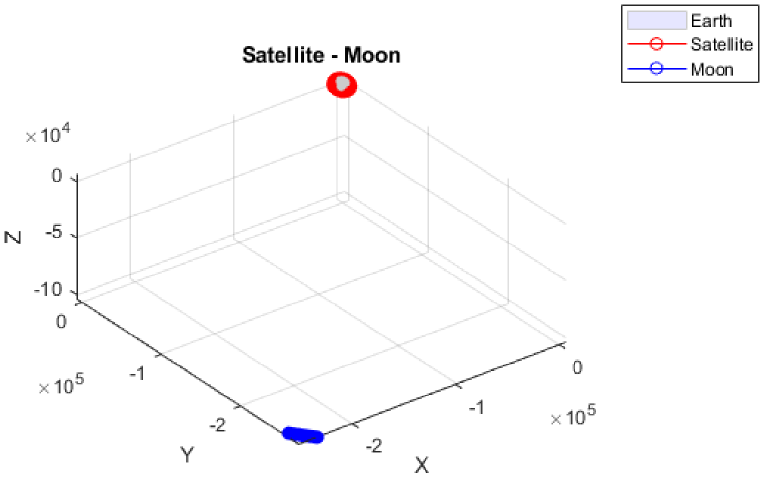

Figure 7.3 - Position of satellite and Moon in TOD (unit: km)

Once having the Cartesian coordinates of both objects, by subtracting the satellite's ones from the Moon's ones, the satellite-Moon vector is found in TOD that can be transformed into LORF by an already written routine. Now it is time to divide the process for each of the FOV mounted on X_{LORF} and Z_{LORF}.

7.2.1 ZLORF

Firstly, it is described the telescope mounted along the axis Z_{LORF} because it is the most important for our scope, i.e. the observation of the sky. As previously said, Z_{LORF} is the extension of the Earth's radius, or the Earth-satellite vector, pointing towards the celestial sphere.

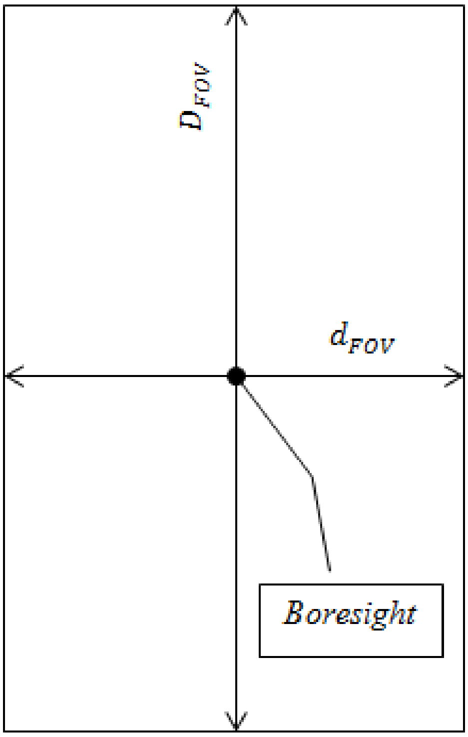

Figure 7.4 - Representation of FOV in 2D

What represented above is the FOV in two dimensions: the vertical extension is the major dimension instead the horizontal line is the minor dimension, but they can be reversed; the intersection of these two lines generates the boresight of the FOV. Another possible solution of defining the FOV dimensions to be implemented in the code is setting the half of the diagonal of a rectangular FOV as the main and comparative parameter. For this exercise, the boresight is placed along the positive Z_{LORF}, leading to have positive and negative Y_{LORF} respectively above and below the boresight along the D_{FOV} and positive and negative X_{LORF} respectively to the left and to the right of the boresight along the d_{FOV}. Moreover, the boresight divides each dimension of the FOV in two equal parts.

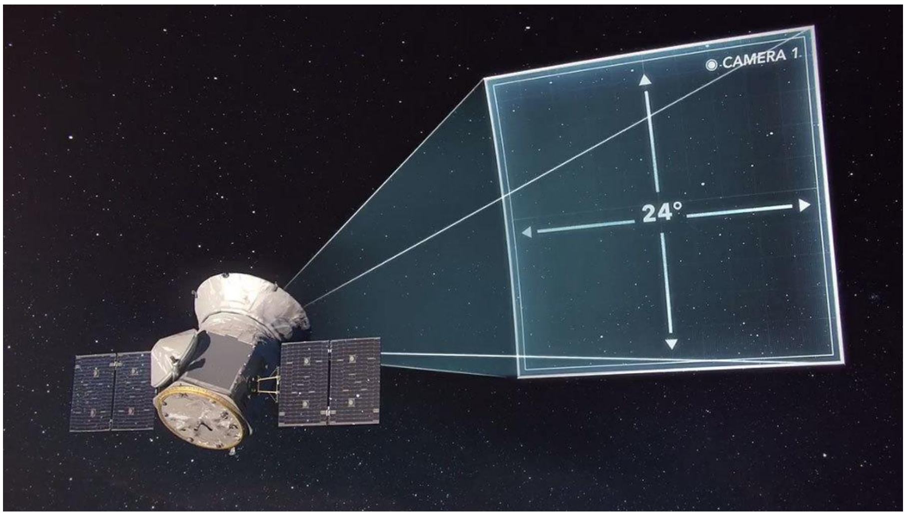

Figure 7.5 - Real example of FOV (NASA TESS)

Returning to the Moon, there are calculated the lunar angular radius β and the angle between the boresight direction and the satellite-Moon vector, both in LORF, called φ.

$$\beta = \arcsin\left(\frac{R_{Moon}}{|\vec{r}_{sat-Moon}|}\right) \qquad \varphi = \arccos\left(\frac{\left(\vec{r}_{sat-Moon} \cdot \hat{Z}_{LORF}\right)}{|\vec{r}_{sat-Moon}|\left|\hat{Z}_{LORF}\right|}\right)$$

where $R_{Moon} = 1738.1\ km \rightarrow\ Moon\ radius$

$|\vec{r}_{sat-Moon}| \rightarrow\ magnitude\ of\ the\ satellite - Moon\ vector\ \ [km]$

$\vec{r}_{sat-Moon} \rightarrow\ satellite - Moon\ vector\ in\ LORF$

$\hat{Z}_{LORF} = [0,0,1] \rightarrow boresight\ direction\ in\ LORF$

$\left|\hat{Z}_{LORF}\right| = 1 \rightarrow magnitude\ of\ unit\ vector$

$(\cdot) \rightarrow dot\ product$

Now what is important is the angle φ. For each time step, it is compared to the dimensions of the FOV: if it is less than the sum of half of one dimension with the lunar angular radius, the Moon is inside the FOV and it is followed and tracked up to its exit by recording its coordinates in LORF; the entrance and exit time are saved giving the total amount of time of its passage. At the end, the total number of occultations is determined. Moreover, for every passage, the percentage of FOV occultation is calculated by

$$Percentage = \frac{solidangle}{solidangle_{FOV}} \cdot 100$$

where $solidangle_{FOV}$ is the solid angle of the entire FOV calculated as

$$solidangle_{FOV} = 4 \arcsin\left(sin\left(\frac{d_{FOV}}{2}\right) sin\left(\frac{D_{FOV}}{2}\right)\right).$$

$solidangle$ is calculated in the following manner.

For each time step, when the Moon is in the FOV, i.e. when $\varphi \leq \frac{d_{FOV}}{2}$ or $\varphi \leq \frac{D_{FOV}}{2}$, there is a Δφ equal to the difference between the φ at the current time step and the φ at the previous time step. With this value, together with the angular radius β, the solid angle created between the two time step can be calculated as

$$\Delta solidangle = 4 \arcsin\left(sin\left(\frac{\Delta\varphi}{2}\right) sin(\beta)\right)$$

The sum of each $\Delta solidangle$ from the entrance to the exit of the Moon in FOV gives the $solidangle$.

Hereunder, there are shown two pictures representing the passages of the Moon in the FOVs. The time frame of both pictures is the same; what is different is the aperture of the FOV: the first spans all the hemisphere which has the $X_{LORF} - Y_{LORF}$ plane as its base, i.e. it has an aperture of 180° x 180°, the second, instead, is closer to the reality and has 3° x 4° FOV. The first case was done in order to be sure to be able to see the Moon during its passage; once this case was proved, the FOV dimensions were lowered to be compliant to the reality and also this test was successful. With a closer analysis, we can confirm that the two pictures represent the same passages seen with different FOVs. In each pictures, there are two graphics: the one on the left side is a 2D visualization of the FOV, i.e. what the telescope of the spacecraft sees, with the normal axis that enters the chart representing the Z_{LORF} axis; the X_{LORF} axis is growing positive as it goes from the right to the left because it is defined in this way, i.e. positive in the direction of the velocity vector; the chart on the right side is a 3D visualization of the previous 2D chart in fact, looking along the Z_{LORF} axis, we can find the same trend as the left chart. The blue circle represents the centre of the Moon and its position in all the figures below is always representative of the final step: in fact, for Figure 7.6 and Figure 7.7, the Moon moves rightward and from bottom up, like it transits in the FOV. The 2D charts of all the figures represent the traces that the Moon, and eventually also a celestial body, leaves on an ideal moving screen, that is the FOV.

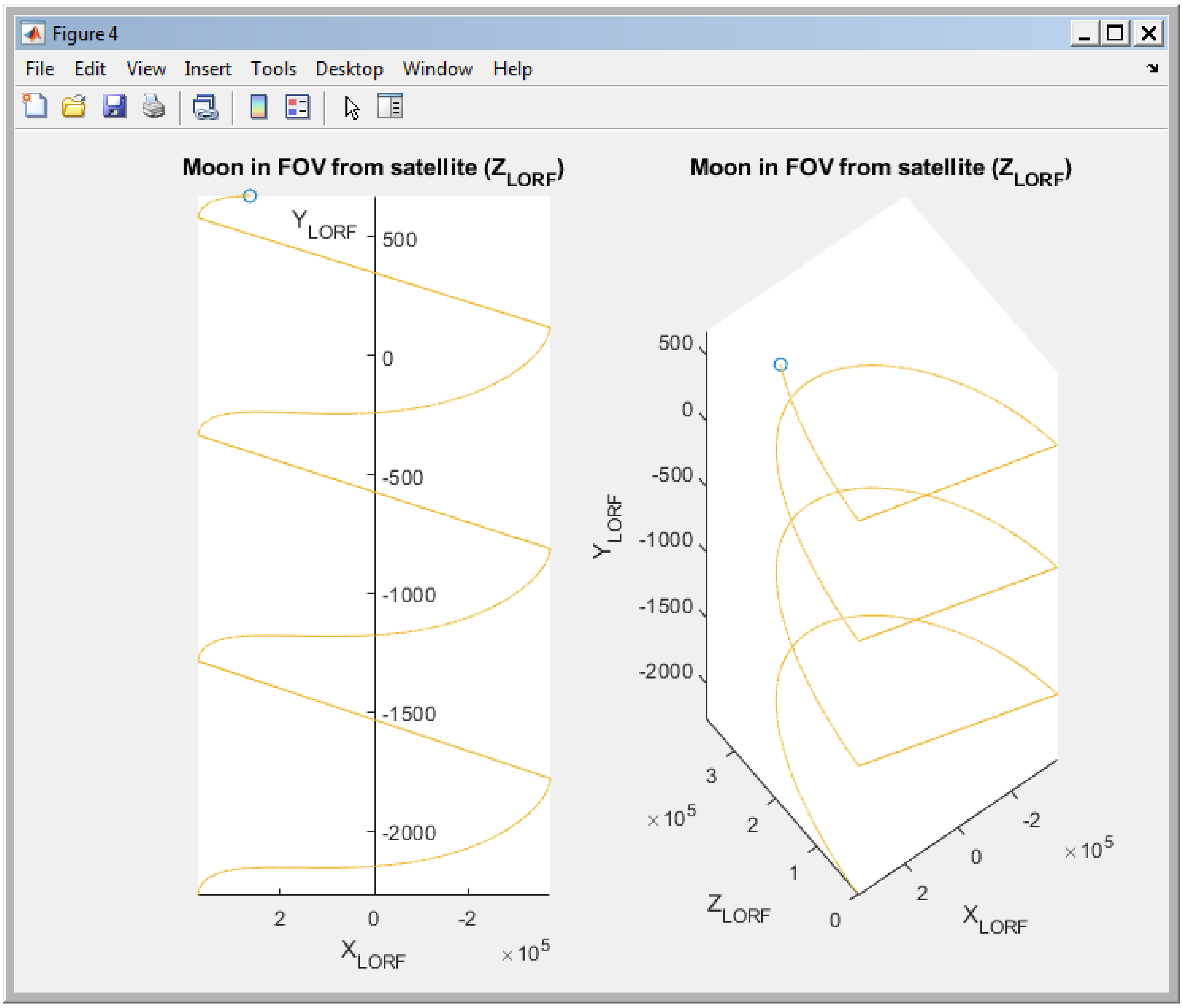

Figure 7.6 - 180° x 180° FOV on Z_{LORF} (unit: km)

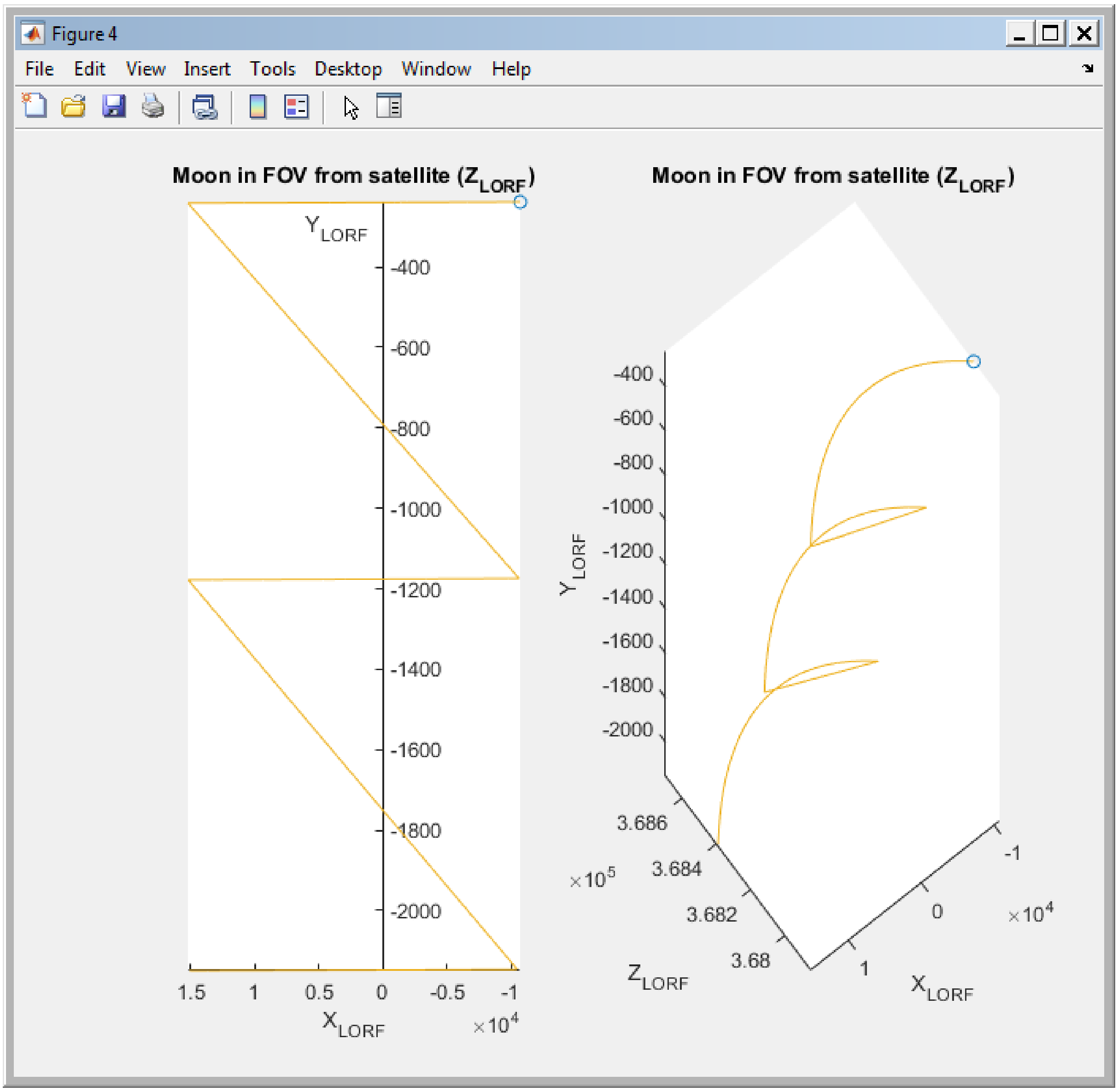

Figure 7.7 - 3° x 4° FOV on Z$_{LORF}$ (unit: km)

7.2.2 X$_{LORF}$

The second axis on which there was installed a telescope is the X_{LORF} due to the need of having a second telescope, or Star Tracker, to validate the position of the satellite given by the first telescope.

Whereas for Z_{LORF} telescope the FOV dimensions are not binding as the front view is clear, this is not valid for the X_{LORF} telescope; in fact, if the FOV is narrow – few degrees – it is very probable that the view of the telescope is not obstructed by anything instead, if the FOV is large, there is the possibility of an obstruction due to the Earth.

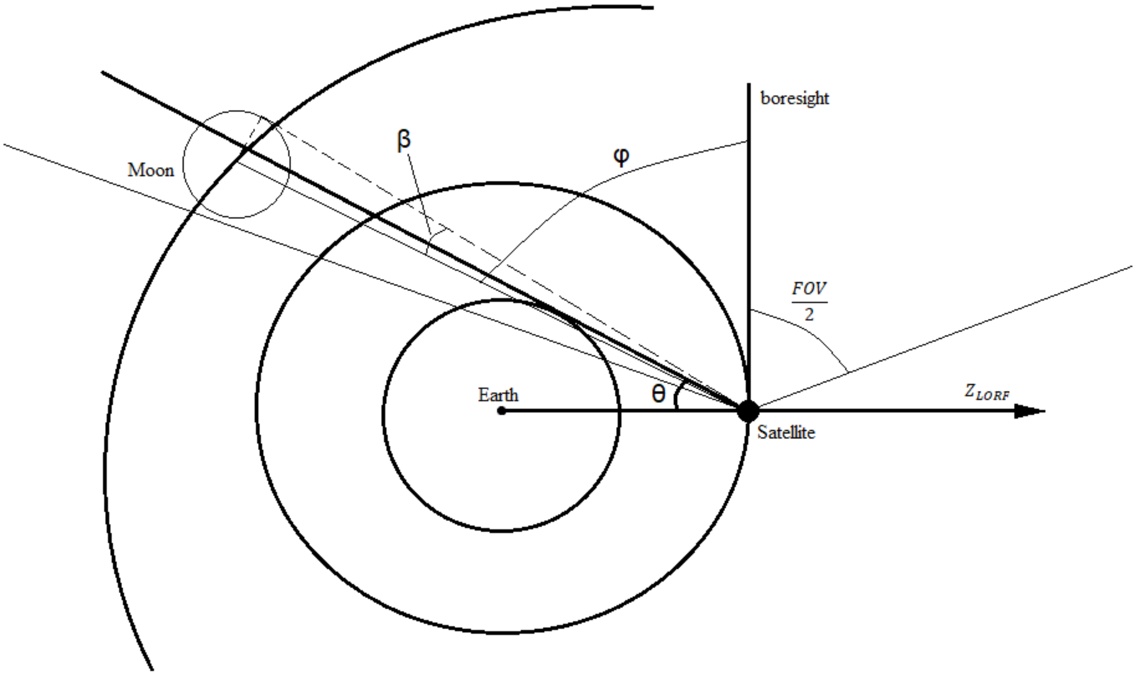

Figure 7.8 - Representation of angles for the Moon partially hidden by the Earth

The Earth can be an obstacle for Star Trackers having $\frac{d_{FOV}}{2} > 90° - \theta$, where $\theta = \arcsin\left(\frac{R_E + maa}{|\vec{r}|}\right)$ represents the angular radius of the Earth seen from the satellite taking into account the presence of the atmosphere, maa; R_E is the Earth radius and $|\vec{r}|$ is the magnitude of the Earth centre – satellite vector. The acronym maa stands for "minimum approach angle" and is highly considered in Mission Analysis calculations because it represents the thickness of the atmosphere's layers, also called "$limb$". To the Star Tracker, the limb represents a disturb because it causes problems in the detection of photons coming from the stars. The photonic disturb is given both by the limb and by the Earth illuminated by the Sun because the Earth reflects, refracts and absorbs photons and thus disturbs the photon counting. On the other hand, a planet without atmosphere, for example the Moon, has only the problem connected to the planet illumination and allows to have a clear and distinct occultation of stars and planets without any fading layer around the disk, as it happens for Earth. The maa could be set to 10 linear kilometres above the Earth's surface because the on-board instruments are getting more and more accurate and they are able to distinguish "clear" photons from the disturbing ones. This value of maa, if seen from 600 km of altitude, for example, measures 0.2024° but varies with the altitude of the satellite, and so does also θ. It must also be said that the analyses taken into consideration feature a prograde orbit, thus having the component of the angular momentum vector perpendicular to the Earth equator pointing towards the celestial North, and so the Earth is found to be always to the left of the spacecraft, i.e. for negative values of Z_{LORF}.

Once having defined, for each time step, the φ angle as the angle between the boresight direction, $\hat{X}_{LORF} = [1,0,0]$, and the satellite-Moon vector, in LORF,

$$\varphi = \arccos\left(\frac{\left(\vec{r}_{sat-Moon} \cdot \hat{X}_{LORF}\right)}{|\vec{r}_{sat-Moon}||\hat{X}_{LORF}|}\right)$$

it can be said that the Moon is completely occulted by the Earth if the following relation is satisfied:

$$\varphi - \beta > 90° - \theta;$$

in this case, no coordinates or time intervals are recorded as it is not a case of our interest; if it is not satisfied, i.e. for $\varphi - \beta \leq 90° - \theta$, the Moon starts to be visible by the satellite, exiting from the Earth limb. From this time step onwards, no other obstacle will be present between the satellite and the Moon and thus the computation of the Moon's passages can be done in the same way as previously done for Z_{LORF} up to the third component of satellite-Moon vector, i.e. the component along Z_{LORF}, is close to zero. Afterwards, for positive values this component, the Moon is free to pass through the entire $\frac{d_{FOV}}{2}$ without any interruption.

For $\frac{d_{FOV}}{2} \leq 90° - \theta$, there is no problem in visualizing the passages of the Moon and thus the process is exactly the same as that used in Z_{LORF}.

In both cases, the satellite-Moon vector coordinates in LORF when the Moon is in FOV, the entrance and exit times, the total number of occultations, the total solid angle of the entire passages and each percentage of the obscuration of the FOV by the Moon have been calculated.

The following two pictures represent the motion of the Moon in the field of view of the telescope mounted on X_{LORF}. The first picture shows the transit of the Moon in a FOV of *180° x 180°* dimensions. Taking into account what stated before about the obstruction of FOV by the Earth, we can see in each subchart that the FOV is not symmetrical with respect to the Y_{LORF} or that it lacks some values for negative Z_{LORF}. The reason is that the horizontal dimension of the field of view is higher than 90° – θ and thus the telescope catches also part of the Earth, that is not important for our study. In this way, the coordinates of the Moon behind the Earth are not considered in the charts, leaving an asymmetry in the X-axis values, linked to the missing part in the region of negative Z_{LORF} due to Earth.

The second picture is representative of a smaller FOV, *10° x 10°*, which is closer to the reality. What catches immediately our eye is the symmetry of the right-side chart with respect to the Y_{LORF}. This is possible owing to the fact that the FOV aperture is smaller than 90° – θ giving the change to the telescope to catch the entire transits of the Moon without being disturbed by the Earth. Moreover, if we compare 2D charts of both figures, we can state that, whereas the Y_{LORF} axis has the same scale, the Z_{LORF} axis of Figure 7.9 has an order or magnitude more than the same axis in Figure 7.10. This is normal, as a smaller FOV aperture leads to have a smaller range of lunar coordinates.

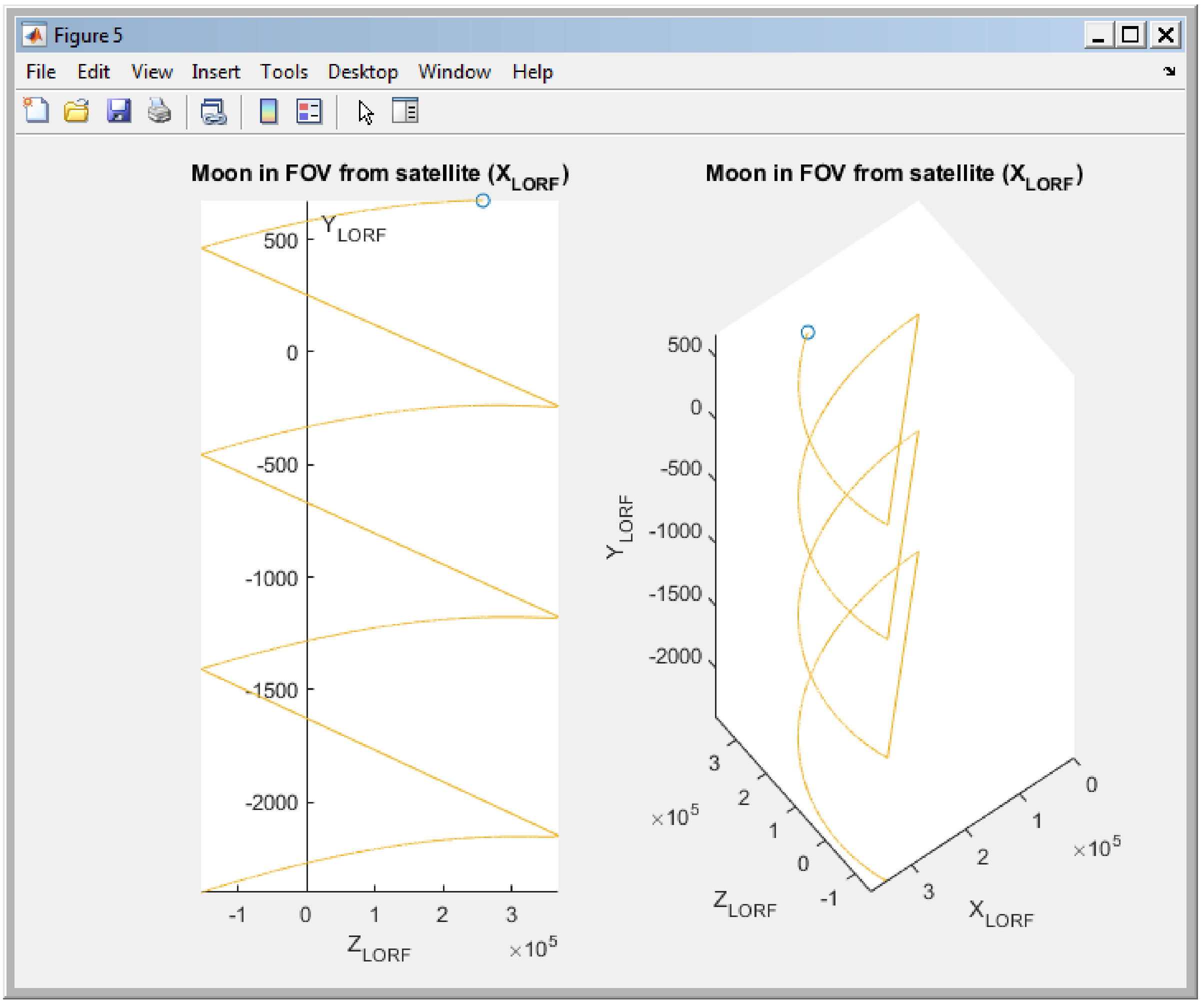

Figure 7.9 - 180° x 180° FOV on X_{LORF} (unit: km)

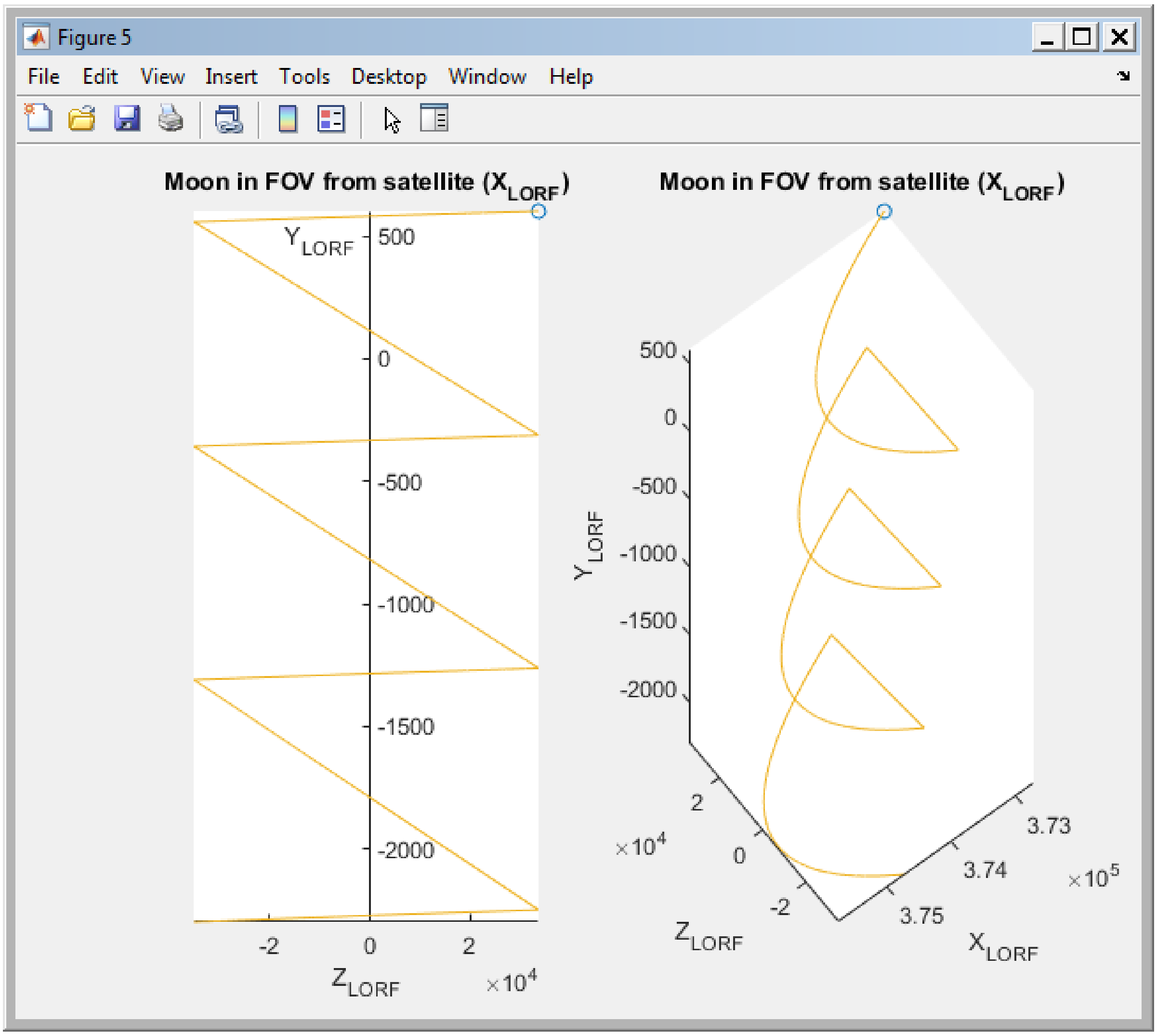

Figure 7.10 - 10° x 10° FOV on X_{LORF} (unit: km)

Because the Moon at the epoch time has negative TOD coordinates and the satellite is in its descending node orbit arc, the Moon is seen going from negative Y values to positive ones and from the left side to the right side of the charts, i.e. from negative X values to positive ones. This is valid for both Z_{LORF} and X_{LORF} telescopes.

Moreover, a clarification must be done. To be certain to see an occultation, whether it is of a planet or a star, for initial tests of the SW, the Moon's radius was put 10 times the real one; this was done because the angular radius of the Moon is half of a degree, so it is hard to see an occultation if we are not so precise in putting the satellite in the right position aligned with the other two bodies.

7.3 Occultation of a planet

Figure 7.11 - Occultation of Saturn

After studying the passages of the Moon in FOV of S/C, it is required to study if the Moon occults any celestial body when it transits in the FOVs of the satellite. In this way a new script was created to satisfy this requirement.

Initially, during the creation of the initial structure for the analysis, it is asked to insert the name of the planet you want to study. Once given the name, the process can start.

First of all, the state vector of the planet in TOD frame, as seen from Earth, for the entire period of the simulation, for each time step, is retrieved by the MATLAB routine of SPICE, called *spkezr*. From this vector, X-Y-Z coordinates are isolated. To find the satellite-planet vector in TOD, the coordinates of the satellite are subtracted from the coordinates of the planet; later, the transformation from TOD to LORF of the satellite-planet vector is done.

From this point onwards, the process is divided into two parts: one for the telescope pointing towards Z_{LORF} and one for telescope pointing towards X_{LORF}, obviously having already the coordinates of the Moon when it is in the respective FOVs of the satellite. Apart from the definition of the coordinates of the boresight direction, the procedures of the study are almost the same; therefore, the process is described only once, explaining the differences between the two parts.

After obtaining the satellite-planet vector in LORF frame, the boresight direction is determined. Talking about Z_{LORF}, it has the coordinates equal to [0,0,1]; talking about X_{LORF}, the coordinates are [1,0,0]. Now the discussion is focused on Z_{LORF}.

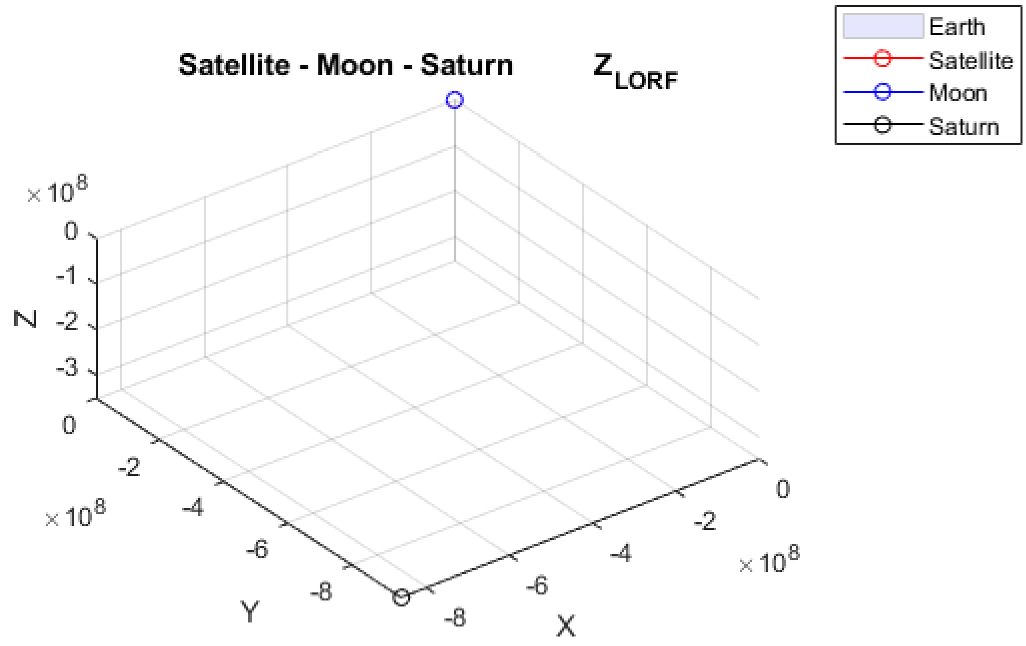

Figure 7.12 - Position of satellite, Moon and Saturn in TOD (unit: km)

In Figure 7.12, the satellite, the Earth and the Moon are concentrated in the blue circle, at the origin of the axes, as the great distance of Saturn from Earth does not allow to represent all the distances in scale and at the same time it does not allow all the celestial object to be clearly visible.

The angle between the boresight direction and the S/C-planet vector is defined as

$$\varphi_P = \arccos\left(\frac{(\vec{r}_{sat-planet} \cdot \hat{Z}_{LORF})}{|\vec{r}_{sat-planet}||\hat{Z}_{LORF}|}\right)$$

where $\vec{r}_{sat-planet} \rightarrow$ $satellite - planet\ vector\ in\ LORF$

$\hat{Z}_{LORF} = [0,0,1] \rightarrow boresight\ direction\ in\ LORF$

$|\vec{r}_{sat-planet}| \rightarrow magnitude\ of\ the\ satellite - planet\ vector\quad [km]$

$|\hat{Z}_{LORF}| = |\hat{X}_{LORF}| = 1 \rightarrow magnitude\ of\ unit\ vector$

$(\cdot) \rightarrow dot\ product$

However, this value is not much used as another parameter is revealed to be more complete. It is the case of the angle between the satellite-Moon vector and the satellite-planet vector, defined as

$$\psi_P = \arccos\left(\frac{\left(\vec{r}_{sat-Moon} \cdot \vec{r}_{sat-planet}\right)}{\left|\vec{r}_{sat-Moon}\right| \left|\vec{r}_{sat-planet}\right|}\right).$$

Talking about planets, it is necessary to state that they have a great angular radius for an Earth's observer, with respect to the stars, that are considered to have none, as a first approximation. It is defined as

$$\gamma = \arcsin\left(\frac{R_P}{\left|\vec{r}_{sat-planet}\right|}\right)$$

where $R_P \rightarrow \quad radius\ of\ the\ planet \quad [km]$.

Figure 7.13 gives a visible explanation on what stated before.

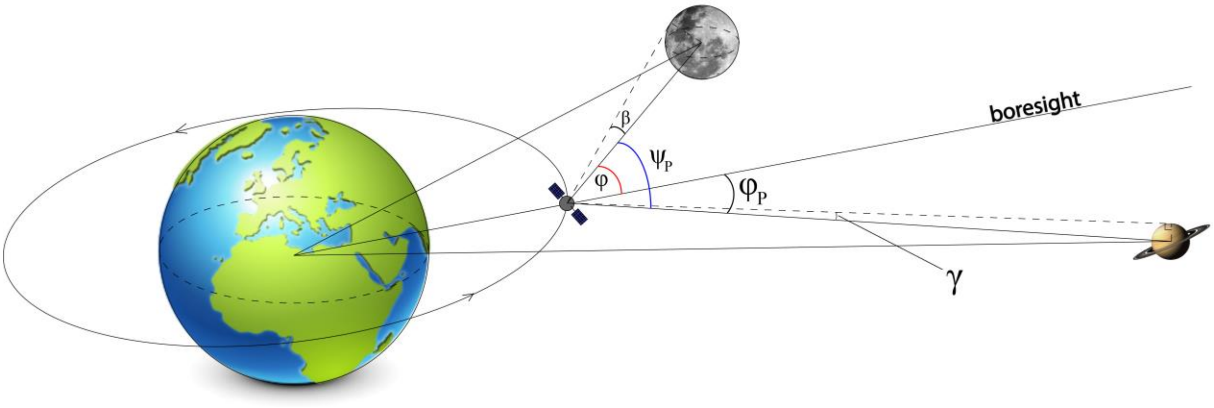

Figure 7.13 - Representation of angles for the case of the planet

For each time step, the flag vector reporting that the Moon is in the Z_{LORF} FOV of the satellite or not is inspected – 1 for inside and 0 for outside the FOV; in case of positive answer, the value of the angle ψ_P is checked: to be into an occultation, there should be:

$$\psi_P \leq \gamma + \beta$$

If this condition is accomplished, the LORF coordinates of satellite-Moon and satellite-planet vectors are saved to be plotted later. Moreover, the Moon coordinates in TOD and the planet coordinates in TOD for the beginning and final moment of occultation are saved, together with the entrance and exit time and date to determine how long the occultation lasts and how many occultations happened in the simulation's period of time.

7.3.1 Example of occultation of a planet: Saturn

After the explanation of the reasoning that stands behind the phenomenon, a real example of occultation of a planet was chosen to verify the study.

Looking on the internet, it was found that an occultation of Saturn occurred on May 14th, 2014, if seen from Australia and New Zealand when it is nighttime and the phenomenon can be seen clearly in the sky with naked eye.

The report from which this event's information comes states that the occultation begins when in Italy it is 12:00 p.m. that corresponds to 10:00 p.m. in, for example, Wellington time (lat: -41.2899° lon: 174.7758°). The relative UTC value is 10:00 a.m. and it is for this reason that it was set the simulation's initial epoch time at 9:00 a.m. UTC.

Table 7.3 - Saturn mission parameters

Quantity	Value	Unit of measure
Epoch date of the simulation	14 May 2014 @ 09:00:00 UTC	
Semi-major axis	7000	km
Eccentricity	0	
Inclination	21.0229	deg
RAAN	0	deg
Argument of the perigee	0	deg
True anomaly	6.1341	deg
Mission duration	21600 (6h)	s
Time step	0.1	s
Perturbation	Geopotential (EIGEN-GL04C)	
Order of expansion	30	

In this simulation, it was chosen to study both the telescopes, so they were put on Z_{LORF} and X_{LORF}; there have been decided to set both FOVs to 180° x 180° in order to have the maximum view area in the most important directions. Moreover, the radius of the Moon was set to be 10 times the real one to be able to catch the occultations even if we have not been so precise in setting the initial Keplerian elements of the satellite. This can be possible owing to the fact that this is meant to be an exercise to prove the correctness of the script: if it works with these parameters, it also works with more realistic angles and radii.

Now the process used to place the satellite in the right initial position is shown.

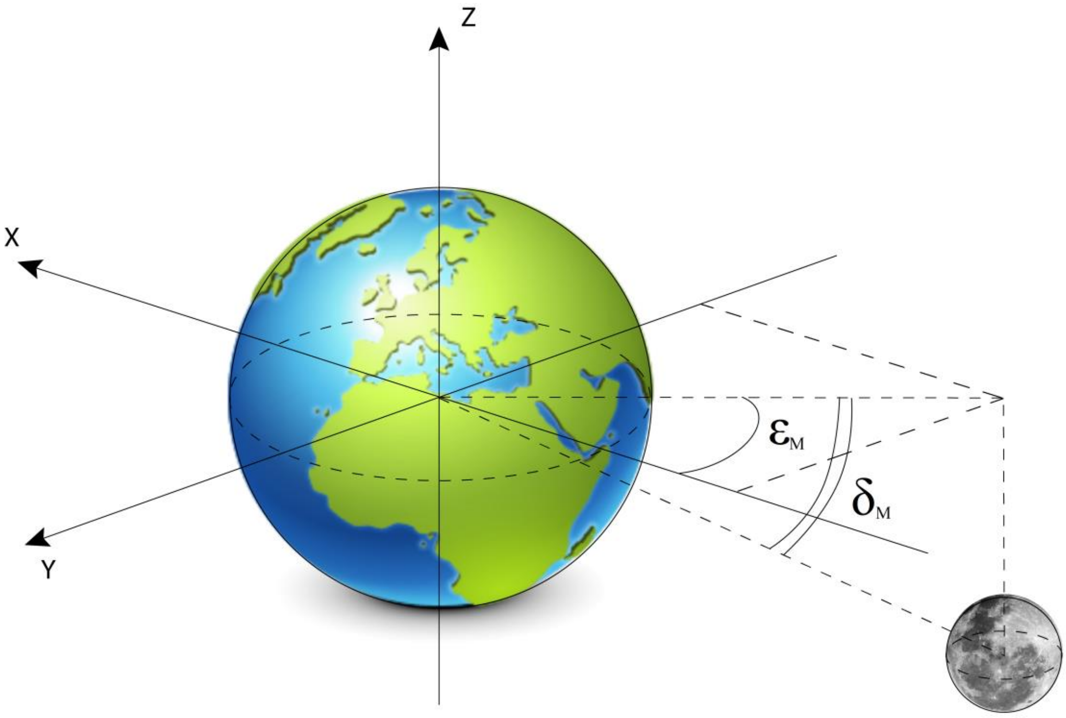

Figure 7.14 - Position of the Moon with respect to the fixed axes

The occultation occurs at 10:00 a.m. UTC, so the state vectors of the Moon and of Saturn seen by the Earth in TOD at that time are computed using the SPICE routine *spkezr*:

- Moon

$$state_{Moon} = [-2.4905 \cdot 10^5 \quad -2.6267 \cdot 10^5 \quad -1.0095 \cdot 10^5 \;\; 0.8162 \quad -0.6365 \quad -0.1797]$$

which can be divided into position and velocity:

$$position_{Moon} = [-2.4905 \cdot 10^5 \quad -2.6267 \cdot 10^5 \quad -1.0095 \cdot 10^5]\; km$$

$$velocity_{Moon} = [0.8162 \quad -0.6365 \quad -0.1797]\; km/s$$

- Saturn

$$state_{Saturn} = [-8.6057 \cdot 10^8 \quad -9.5395 \cdot 10^8 \quad -3.5070 \cdot 10^8 \quad -16.7500 \;\; 10.4795 \;\; 4.3633]$$

which can be divided into position and velocity:

$$position_{Saturn} = [-8.6057 \cdot 10^8 \quad -9.5395 \cdot 10^8 \quad -3.5070 \cdot 10^8]\; km$$

$$velocity_{Saturn} = [-16.7500 \;\; 10.4795 \;\; 4.3633]\; km/s$$

In Figure 7.14 there is the representation of the position of the Moon taking into consideration its state vector. Now the Right Ascension and the Declination of the Moon and of Saturn are calculated and later compared.

- Moon

$$Dec_M = \delta_M = \arccos\left(\frac{\sqrt{position_{Moon}(1)^2 + position_{Moon}(2)^2}}{d_{Earth-Moon}}\right) = 15.5833°$$

where

$$d_{Earth-Moon} = \sqrt{position_{Moon}(1)^2 + position_{Moon}(2)^2 + position_{Moon}(3)^2} \\ = 375787\ km$$

is the Earth – Moon distance. This value of Declination is negative due to the fact that the third component of the position vector of the Moon is negative.

$$\varepsilon_M = \arccos\left(\frac{|position_{Moon}(1)|}{\sqrt{position_{Moon}(1)^2 + position_{Moon}(2)^2}}\right) = 46.5246°$$

We have used the $position_{Moon}(1)$ because for this analysis the Moon has negative X and Y coordinates. To know the Right Ascension the calculus is:

$$RA_M = \alpha_M = 180° + \varepsilon_M = 226.5246°$$

- Saturn

$$Dec_S = \delta_S = \arccos\left(\frac{\sqrt{position_{Saturn}(1)^2 + position_{Saturn}(2)^2}}{d_{Earth-Saturn}}\right) = 15.2785°$$

where

$$d_{Earth-Saturn} = \sqrt{position_{Saturn}(1)^2 + position_{Saturn}(2)^2 + position_{Saturn}(3)^2} \\ = 1.331663107 \cdot 10^9\ km$$

is the Earth-Saturn distance. This value of Declination is negative due to the fact that the third component of the position vector of Saturn is negative.

$$\varepsilon_S = \arccos\left(\frac{|position_{Saturn}(1)|}{\sqrt{position_{Saturn}(1)^2 + position_{Saturn}(2)^2}}\right) = 47.9873°$$

We have used the $position_{Saturn}(1)$ because for this analysis Saturn has negative X and Y coordinates. To know the Right Ascension the calculus is:

$$RA_S = \alpha_S = 180° + \varepsilon_S = 227.9873°$$

We can see that the Right Ascensions and the Declinations of the two body are quite similar to each other, thus the phenomenon of the occultation can likely occur.

In order to allow the satellite to arrive at 10:00 a.m. in front of the Moon, in conjunction with it, on the vector that links the Earth's centre to the Moon's centre, some more calculations must be done. Looking to the figure below, we want to know the value of ω_1, that is the angle between the line of nodes and the Earth-Moon vector, on the orbital plane of the satellite.

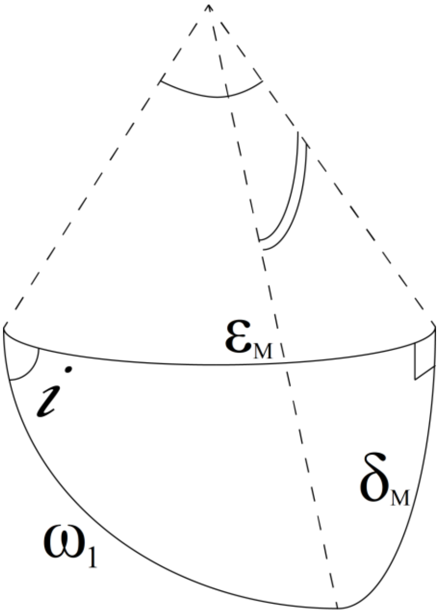

Figure 7.15 - Detail of the Earth's equator, satellite's orbit and declination of the Moon

The one equation for spherical triangles is:

$$\cos(\omega_1) = \cos(\varepsilon_M)\cos(\delta_M) + \cos(90°)\sin(\varepsilon_M)\sin(\delta_M)$$

$$\omega_1 = \arccos(\cos(\varepsilon_M)\cos(\delta_M)) = 48.4898°$$

Using another relation for spherical triangles, the value of the inclination is:

$$\frac{\sin(\omega_1)}{\sin(90)} = \frac{\sin(\delta_M)}{\sin(i)}$$

$$i = \arcsin\left(\frac{sin(\delta_M)}{sin(\omega_1)}\right) = 21.0229°$$

The period of the orbit for the satellite is:

$$\mathrm{T} = 2\pi\sqrt{\frac{a^3}{\mu}} = 5828.5\ s$$

where $a = 7000\ km \quad \rightarrow \quad semi - major\ axis$

$$\mu = 398600\frac{km^3}{s^2} \quad \rightarrow \quad Earth's\ gravitational\ parameter$$

Therefore, in 1 h (3600 s), the satellite travels for

$$\frac{3600\ s}{5828.5\,\frac{s}{orb}} = 0.6177\ orb$$

which means that it flies

$$0.6177\ orb \cdot 360\,\frac{deg}{orb} = 222.3557°\ .$$

Because it must have a $\omega_1 = 48.4898°$, it means that it should depart

$$222.3557° - 48.4898° = 173.8659°$$

before the line of nodes, in particular the descending node. This reflects into having an initial true anomaly of

$$\nu_0 = 180° - 173.8659° = 6.1341°$$

after the ascending node, having put the RAAN and the argument of the perigee both to zero. This reasoning can be done only with circular orbit, i.e. with eccentricity equal to zero, where the argument of the perigee is not defined. In Figure 7.16 it is shown what stated before.

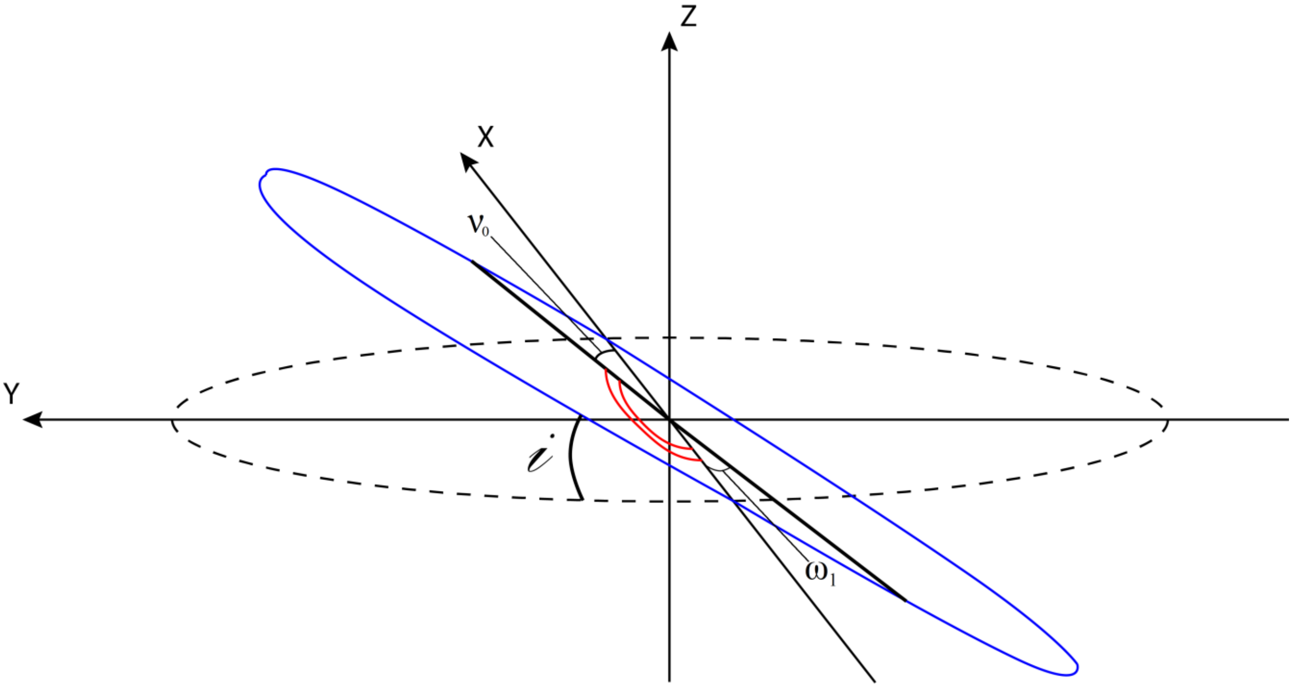

Figure 7.16 - Initial position of the satellite

The Chart 7.1 and Chart 7.2 show the passages of the Moon in the FOV of both the telescopes and the considerations made in the previous relative sections are still valid. The Moon, in fact, apparently goes from left to right and bottom up. Therefore, we must say that the satellite changes its inclination every orbit due to gravitational perturbations lowering it, and this is the reason why each passage of the Moon has Y coordinate higher and higher.

Chart 7.1 - Moon in 180° x 180° FOV on Z_{LORF} (unit: km)

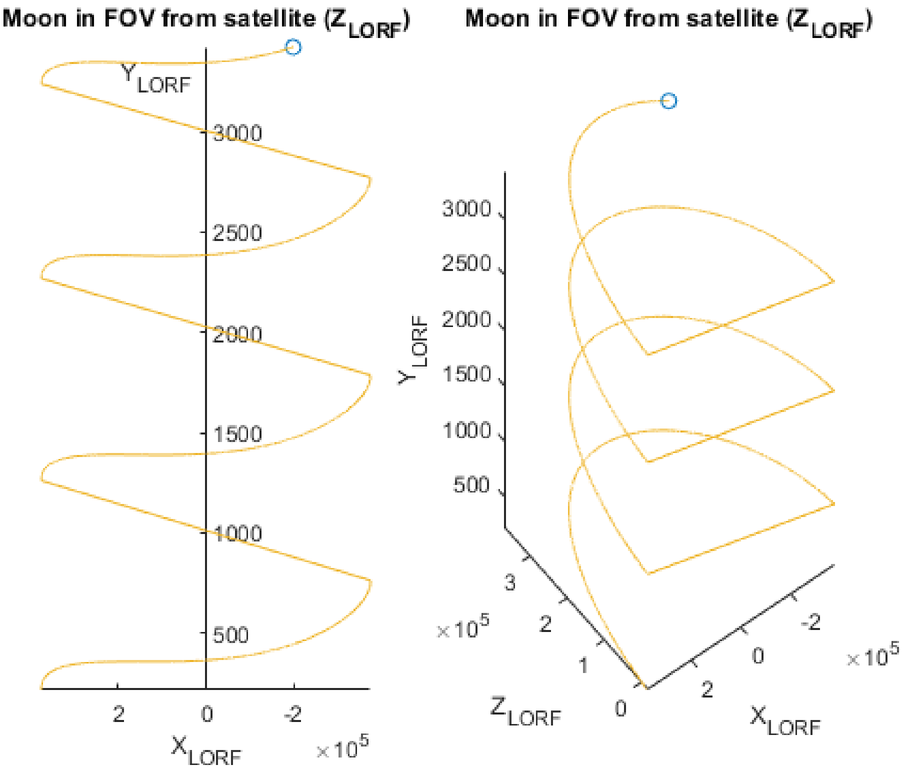

Chart 7.2 - Moon in 180° x 180° FOV on X_{LORF} (unit: km)

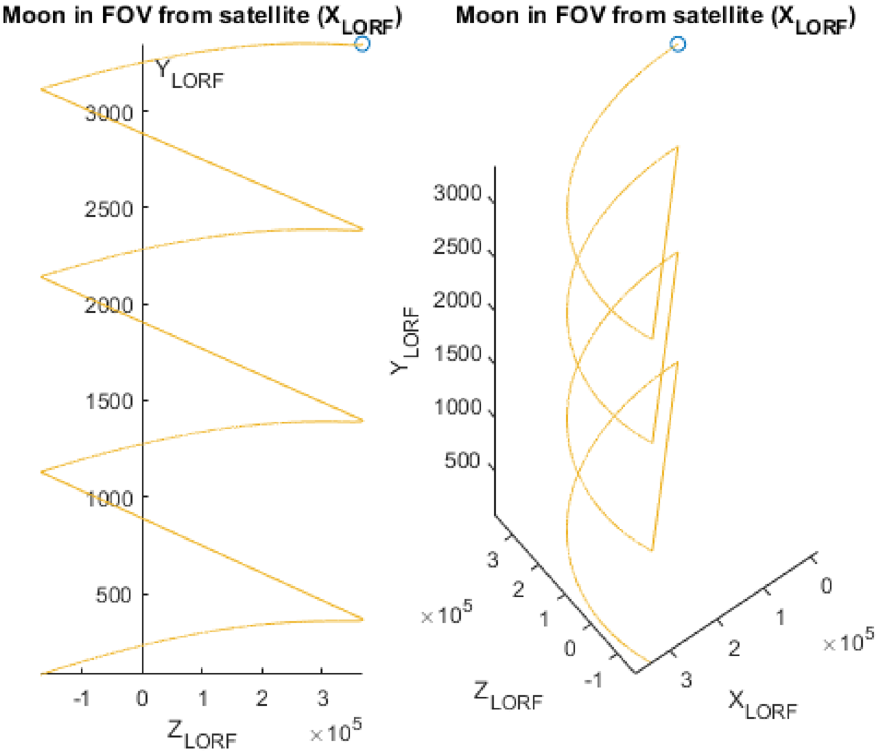

The Chart 7.3 and Chart 7.4 revel the occultation of Saturn by the Moon, both in 2D and in 3D for both the telescopes. Occultations start from the bottom going rightward and upward and the number of lines determines the number of occultations. The dots represent the centres of mass of the Moon (in blue) and of Saturn (in red); the lines go in pairs, the first red line is together the first blue line. For instance, if we check the two values of Moon and Saturn at the same time step, along the same occultation, in Chart 7.3 we can see that the X coordinate of the planet firstly follows, then comes closer and then exceeds the X coordinate of the Moon, thus revealing that Saturn moves across the lunar disk. Moreover, it was adopted a scale for Saturn's coordinates in order to bring them almost comparable with the order of magnitude of those of the Moon.

Chart 7.3 - 2D and 3D FOV of telescope set on Z_{LORF} with passages of the Moon and of Saturn (unit: km)

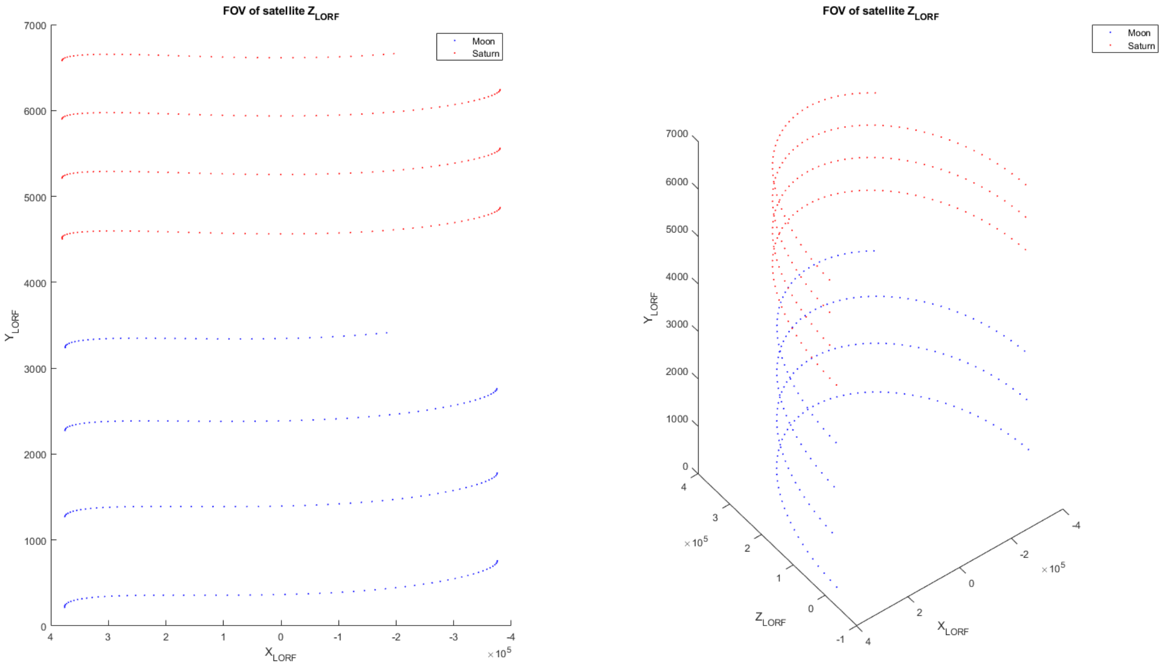

Chart 7.4 - 2D and 3D FOV of telescope set on X_{LORF} with passages of the Moon and of Saturn (unit: km)

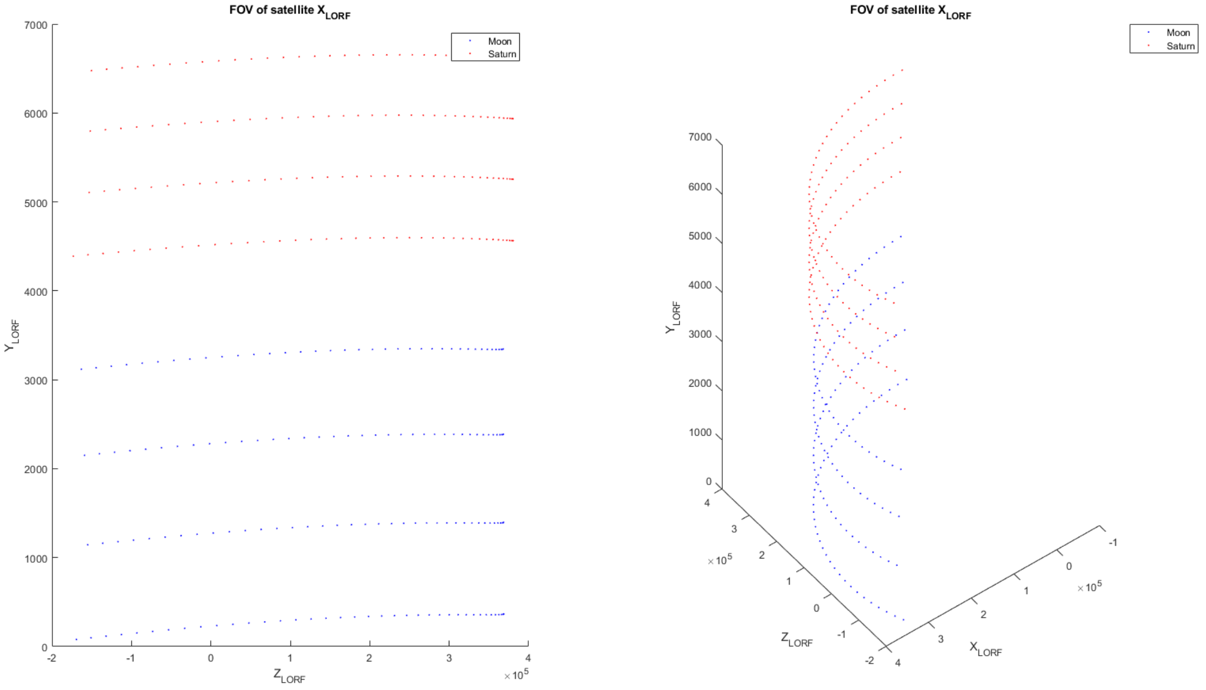

7.4 Occultation of a star

Figure 7.17 - Occultation of Aldebaran in 1347 A.D.

After verifying the phenomenon of the occultation for a planet, the target moves towards another celestial body: the stars. The question remains the same as before: does the Moon occult any star during its passages in the FOV of the S/C?

First of all, it is asked to define, during the input operations, the star you want to study the occultation of. You can type the name, if known, or you can search for it by an identification code: it is a number preceded by an identifier that can be HIP, HD or HR.

HIP is an abbreviation for Hipparcos Catalogue, probably one of the most accurate and complete existing star catalogue, together with Tycho Catalogue, that owes its name to the ESA mission in early 1990s – **Hi**gh **P**recision **Par**allax **Co**llecting **S**atellite. This mission was the first space experiment devoted to precision astrometry, the accurate measurement of the positions of celestial objects on the sky. This permitted the first high-precision measurements of the intrinsic brightness (compared to the less precise apparent brightness), proper motions and parallaxes of stars, enabling better calculations of their distance and tangential velocity. When combined with radial velocity measurements from spectroscopy, astrophysicists were able to finally measure all six quantities needed to determine the motion of stars. The results of this mission were thus the Hipparcos Catalogue, a high-precision catalogue of more than 118.200 stars with a resolution of 1 milliarcsec, that was published in 1997 together with the lower-precision Tycho Catalogue of more than a million stars with a resolution of 20-30 milliarcsec, while the enhanced Tycho-2 Catalogue of 2.5 million stars was published in 2000. [W14]

HD stands for Henry Draper Catalogue that is an astronomical star catalogue published between 1918 and 1924, giving spectroscopic classifications for 225.300 stars; it was later expanded by the Henry Draper Extension (HDE), published between 1925 and 1936, which gave classifications for 46.850 additional stars, and by the Henry Draper Extension Charts (HDEC), published from 1937 to 1949 in the form of charts, which gave classifications for 86.933 other stars. In all, 359.083 stars were classified as of August 2017. The HD catalogue is named after Henry Draper, an amateur astronomer, and covers the entire sky almost completely down to an apparent photographic magnitude of about 9; the extensions added fainter stars in certain areas of the sky. [W15]

HR is the Harvard Revised Photometry Catalogue, which has the same numbers as in the new Yale Bright Star Catalogue, because it is its predecessor. The HR or YBS is a star catalogue that lists all stars of stellar magnitude 6.5 or brighter, which is roughly every star visible to the naked eye from Earth. The catalogue lists 9.110 objects, of which 9.095 are stars, 11 are novae or supernovae and 4 are non-stellar objects. [W16]

This amount of stars with their characteristics are available thanks to an Excel sheet that puts together these stars and orders them according to the numbering of the Hipparcos Catalogue. This spreadsheet was downloaded from the web (http://www.astronexus.com/hyg) and transformed into a MATLAB data structure through an ad hoc script to be easily read and used by the SW. Some features – HIP code, Right Ascension, Declination, distance and magnitude – of the most known stars, as Vega, Betelgeuse, Polaris, Sirius, Rigil Kentaurus, Proxima Centauri, have been searched on other web pages to be sure that the values inside the database are correct. Therefore, returning to the occultations, the name or the identification code put at the beginning phase are necessary for the SW because, thanks to them, it looks for the star's characteristics in the database.

Because the stars can be searched by name or by code, the script related to this is duplicated: one is for stars with names, the other for stars with Catalogue's codes. The main process and the MATLAB instructions are exactly the same, what changes are little things related to plotting charts and inserting legends. To this reason, only one process is described considering to change where needed the word 'name' with 'type' and 'code'.

Once the name of the star is acquired, the process of study of the occultation can start, having already the coordinates of the Moon when it is in the FOV of the satellite, both for Z_{LORF} and for X_{LORF}.

First of all, the SW loads the just created star database to look for, through the star's name, some features it needs for the computation, i.e. the Right Ascension (RA) (see 9.5.1), the Declination (DEC) (see 9.5.2), the distance from Earth (DIST) and the Cartesian coordinates (X-Y-Z) in J2000.0 reference frame. However, the unit of measure of the distances in the database is the 'parsec', thus another script was created to transform it into IS unit, the kilometres (see 9.1.8.1).

When the target of the observation is a star, in order to position it on the celestial sphere, the Cartesian coordinates can be used for its unit vector, more rarely for the whole position vector, because the star distance is not always sufficiently known. The unit vector is equivalent to the spherical coordinates – Right Ascension and Declination – of the star.

The star radius, as well, is not always known, and each star is considered, at least in this context, as a point. The star selected for the present test, Aldebaran, has anyway a known distance. Moreover, its Cartesian coordinates are considered fixed due to the short period of time of the simulation. So its whole position vector has been used for the exercise.

Once having the coordinates of the star position in kilometres, by subtracting the coordinates of the satellite from these, the components of the satellite-star vector in TOD frame are found for each time step. Through a dedicated routine, these coordinates are transformed into LORF frame. From this point onwards, the process is split into two parts, relative to the telescopes pointing towards Z_{LORF} and towards X_{LORF}. For sake of briefness, only the part concerning the Z_{LORF} telescope is described, as previously done for the section about planets.

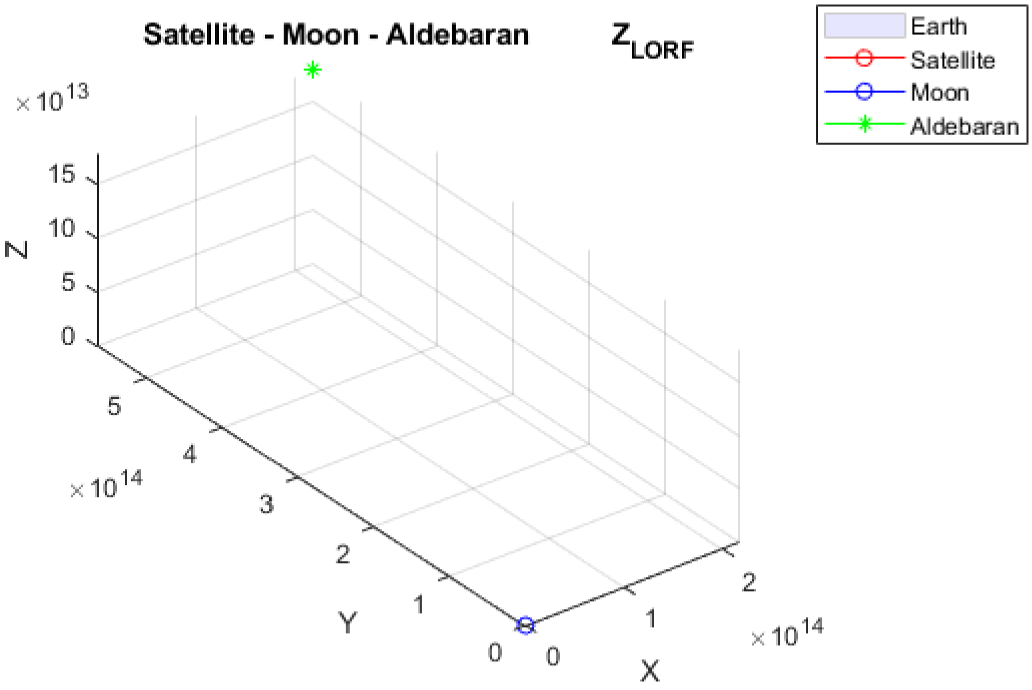

Figure 7.18 - Position of satellite, Moon and Aldebaran in TOD (unit: km)

In Figure 7.18, the satellite, the Earth and the Moon are concentrated in the blue circle, at the origin of the axes,, because the great distance of the star Aldebaran from Earth does not allow to represent all the distances in scale and at the same time it does not allow all the celestial object to be clearly visible.

It is defined the angle between the satellite-Moon vector and the satellite-star vector as:

$$\psi_S = \arccos\left(\frac{(\vec{r}_{sat-Moon} \cdot \vec{r}_{sat-star})}{|\vec{r}_{sat-Moon}|\,|\vec{r}_{sat-star}|}\right)$$

where $\vec{r}_{sat-star} \rightarrow satellite - star\ vector\ in\ LORF$

$|\vec{r}_{sat-star}| \rightarrow magnitude\ of\ the\ satellite - star\ vector\quad [km]$.

Unlike the planets of the Solar System, the stars do not have an angular radius owing to their great distance from the Earth and so they are considered like a point, as a first approximation for the moment.

Then, for each time step, it is checked if the Moon is in the FOV through a flag vector – 1 for inside and 0 for outside the FOV; in case of positive answer, the angle ψ is controlled: if

$$\psi_S \leq \beta$$

it means that the Moon hides the star, i.e. the occultation happens, and the coordinates in LORF of the star and the Moon as seen from the satellite are saved to plot them later. What is also saved are the coordinates of the Moon and the star in TOD for the beginning and ending time of occultation and the entrance and exit time in the Moon of the star, so the duration of each occultation and the total number of occultations can be calculated.

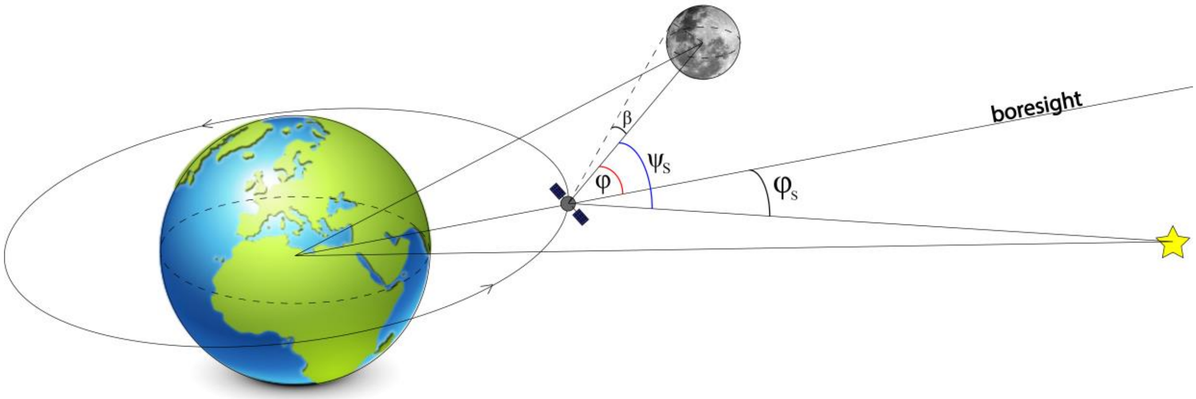

Figure 7.19 - Representation of angles for the case of the star

7.4.1 Example of occultation of a star: Aldebaran

The investigation is carried on with another example of the study of the occultation, now dealing with stars.

Some events of stars occultation were searched on the web and, in particular, it was found an occultation of the star, named Aldebaran, by the Moon happened on October 29th, 2015 in the period of time between 10:40 p.m. and 11:47 p.m. clearly visible from Rome (lat: 41.90°, lon: 12.49°) being the night sky. The relative UTC is between 9:40 p.m. and 10:47 p.m. but the start time of the mission was put to 5:00 p.m. in order to verify if other occultations happened in addition to the previous one.

Table 7.4 - Aldebaran mission parameters

Quantity	Value	Unit of measure
Epoch date of the simulation	29 Oct 2015 @ 17:00:00 UTC	
Semi-major axis	7000	km
Eccentricity	0	
Inclination	18.2514	deg
RAAN	0	deg
Argument of the perigee	0	deg
True anomaly	342.8780	deg
Mission duration	32400 (9h)	s
Time step	0.1	s
Perturbation	Geopotential (EIGEN-GL04C)	
Order of expansion	30	

In this simulation, it was chosen again to study both the telescopes, so they were put on Z_{LORF} and X_{LORF}; there have been decided to set again both FOVs to 180° x 180° in order to have the maximum view area in the most important directions. Moreover, the radius of the Moon was left 10 times the real one to be able to catch the occultations even if we have not been so precise in setting the initial Keplerian elements of the satellite. This can be possible owing to the fact that this is meant to be an exercise to prove the correctness of the script.

The Figure 7.18 shows the position of Earth, satellite, Moon and the star Aldebaran in scale; however, due to the fact that the star is very far from the Earth, the positions of satellite and Moon are zoomed in Figure 7.20 below.

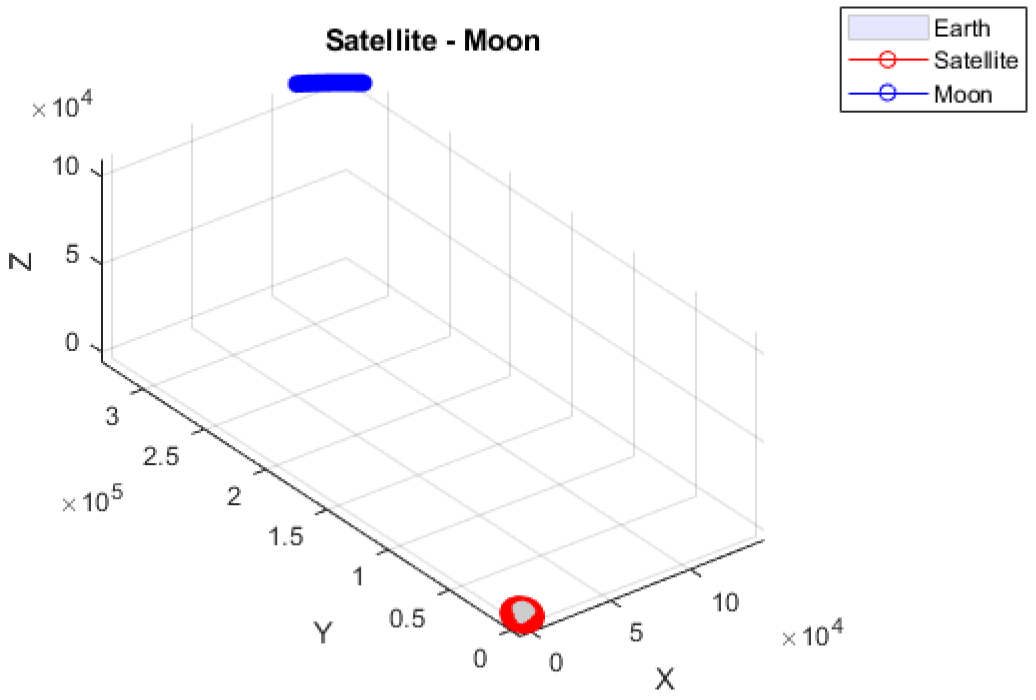

Figure 7.20 - Position of satellite and Moon in TOD (unit: km)

Now the process used to place the satellite in the right initial position is shown.

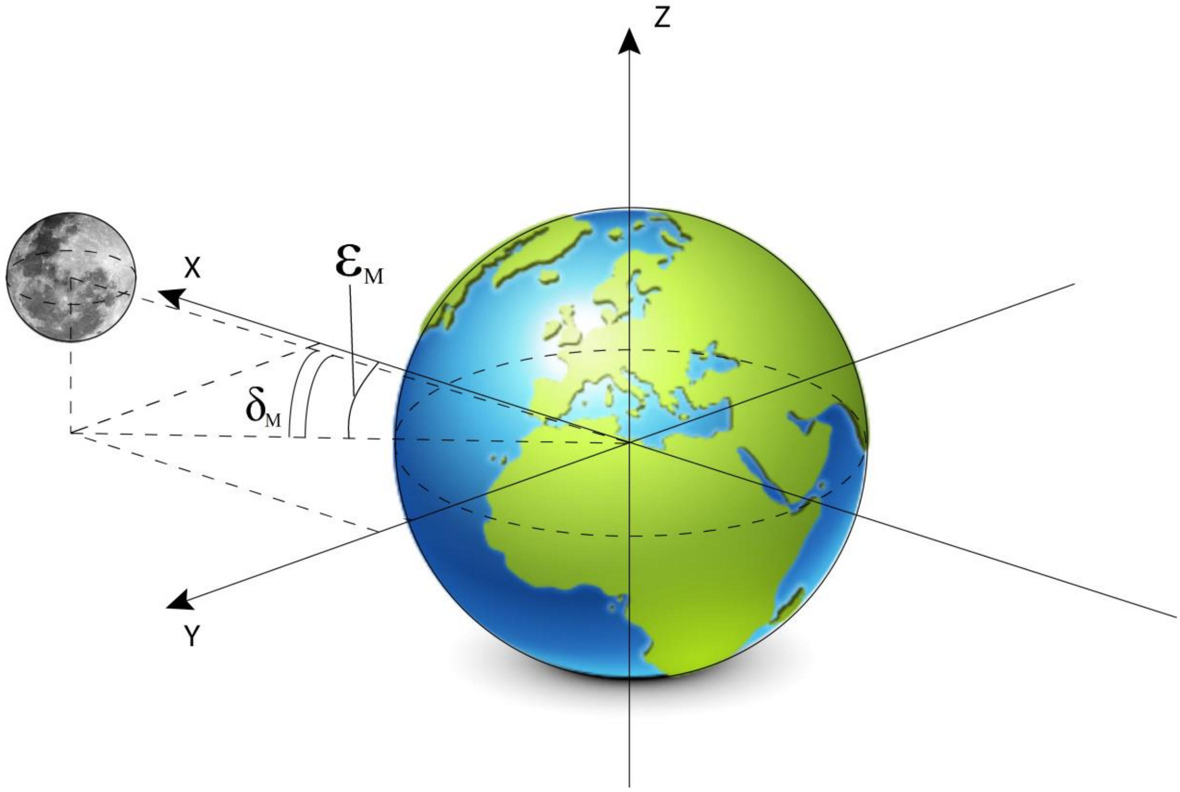

Figure 7.21 - Position of the Moon with respect to the fixed axes

The occultation occurs nearly at 10:15 p.m. UTC, that is 11:15 p.m. for Rome, so the state vector of the Moon seen by the Earth in TOD at that time is computed using the SPICE routine *spkezr*:

$$state_{Moon} = [1.2458 \cdot 10^5 \;\; 3.2952 \cdot 10^5 \;\; 1.0869 \cdot 10^5 \;\; -0.9817 \;\; 0.3983 \;\; 0.1304]$$

which can be divided into position and velocity:

$$position_{Moon} = [1.2458 \cdot 10^5 \;\; 3.2952 \cdot 10^5 \;\; 1.0869 \cdot 10^5]\; km$$

$$velocity_{Moon} = [-0.9817 \;\; 0.3983 \;\; 0.1304]\; km/s$$

The position of the star is not exactly fixed but it is considered moving slowly, at least for the short period of time of the simulation they can be considered fixed, and is given by the Star Catalogue, not in Cartesian coordinates, but in Right Ascension and Declination:

$$RA_A = \alpha_A = 4.598677\; h$$

$$Dec_A = \delta_A = 16.509301°$$

$$range = 20.4332\; pc$$

The *range* is the linear distance between the centre of Earth to the star in ‘parsec’. Some of them can be transformed into other units of measure to be more evident:

$$RA_A = \alpha_A = 68.9802°$$

$$Dec_A = \delta_A = 16.509301°$$

$$range = 6.3054 \cdot 10^{14}\; km$$

Now the Right Ascension and the Declination of the Moon are calculated and later compared to those of Aldebaran.

$$Dec_M = \delta_M = \arccos\left(\frac{\sqrt{position_{Moon}(1)^2 + position_{Moon}(2)^2}}{d_{Earth-Moon}}\right) = 17.1434°$$

where

$$\begin{aligned} d_{Earth-Moon} &= \sqrt{position_{Moon}(1)^2 + position_{Moon}(2)^2 + position_{Moon}(3)^2} \\ &= 368673\; km \end{aligned}$$

is the Earth – Moon distance.

$$RA_M = \alpha_M = \arccos\left(\frac{|position_{Moon}(1)|}{\sqrt{position_{Moon}(1)^2 + position_{Moon}(2)^2}}\right) = 69.2906°$$

We have used the $position_{Moon}(1)$ because for this analysis the Moon has positive X and Y coordinates and thus the Right Ascension is immediately obtained.

We can see that the Right Ascensions and the Declinations of the two body are quite similar to each other, thus the phenomenon of the occultation can likely occur.

In order to allow the satellite to arrive at 10:15 p.m. in front of the Moon, in conjunction with it, on the vector that links the Earth's centre to the Moon's centre, some more calculations must be done. Looking to the figure below, we want to know the value of ω_1, that is, as before, the angle between the line of nodes and the Earth-Moon vector, on the orbital plane of the satellite.

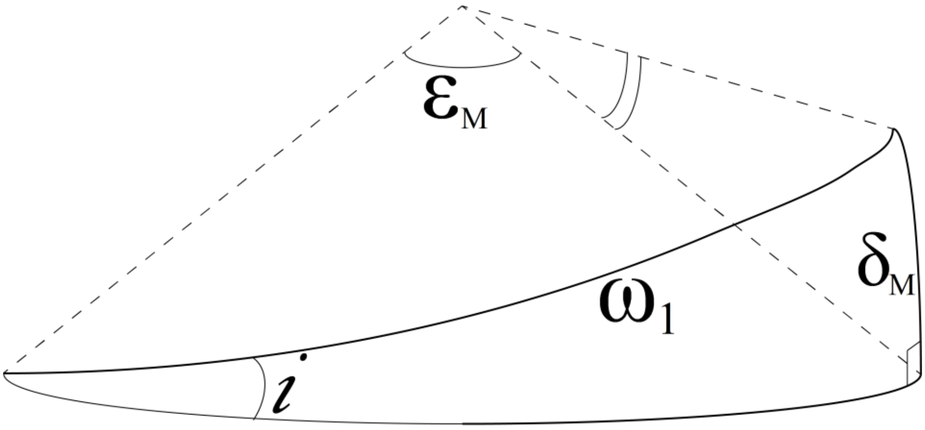

Figure 7.22 - Detail of the Earth's equator, satellite's orbit and declination of the Moon

The equation for spherical triangles is:

$$\cos(\omega_1) = \cos(\varepsilon_M)\cos(\delta_M) + \cos(90°)\sin(\varepsilon_M)\sin(\delta_M)$$

$$\omega_1 = \arccos(\cos(\varepsilon_M)\cos(\delta_M)) = 70.2500°$$

Using another relation for spherical triangles, the value of the inclination is:

$$\frac{\sin(\omega_1)}{\sin(90)} = \frac{\sin(\delta_M)}{\sin(i)}$$

$$i = \arcsin\left(\frac{sin(\delta_M)}{sin(\omega_1)}\right) = 18.2514°$$

The period of the orbit for the satellite is:

$$\mathrm{T} = 2\pi\sqrt{\frac{a^3}{\mu}} = 5828.5\ s$$

where $a = 7000\ km \rightarrow semi - major\ axis$

$\mu = 398600\frac{km^3}{s^2} \rightarrow Earth's gravitational\ parameter$

Therefore, in 5h 15min (18900 s), the satellite travels for

$$\frac{18900\ s}{5828.5\,\frac{s}{orb}} = 3.2427\ orb$$

which means that it flies for 3 entire orbits and

$$0.2427\ orb \cdot 360\,\frac{deg}{orb} = 87.3720°\,.$$

Because it must have a $\omega_1 = 70.2500°$, it means that it should depart

$$87.3720° - 70.2500° = 17.1220°$$

before the line of nodes, in particular the ascending node. This reflects into having an initial true anomaly of

$$\nu_0 = 360° - 17.1220° = 342.8780°$$

after the ascending node. This reasoning can be done only with circular orbit, i.e. with eccentricity equal to zero, where the argument of the perigee is not defined.

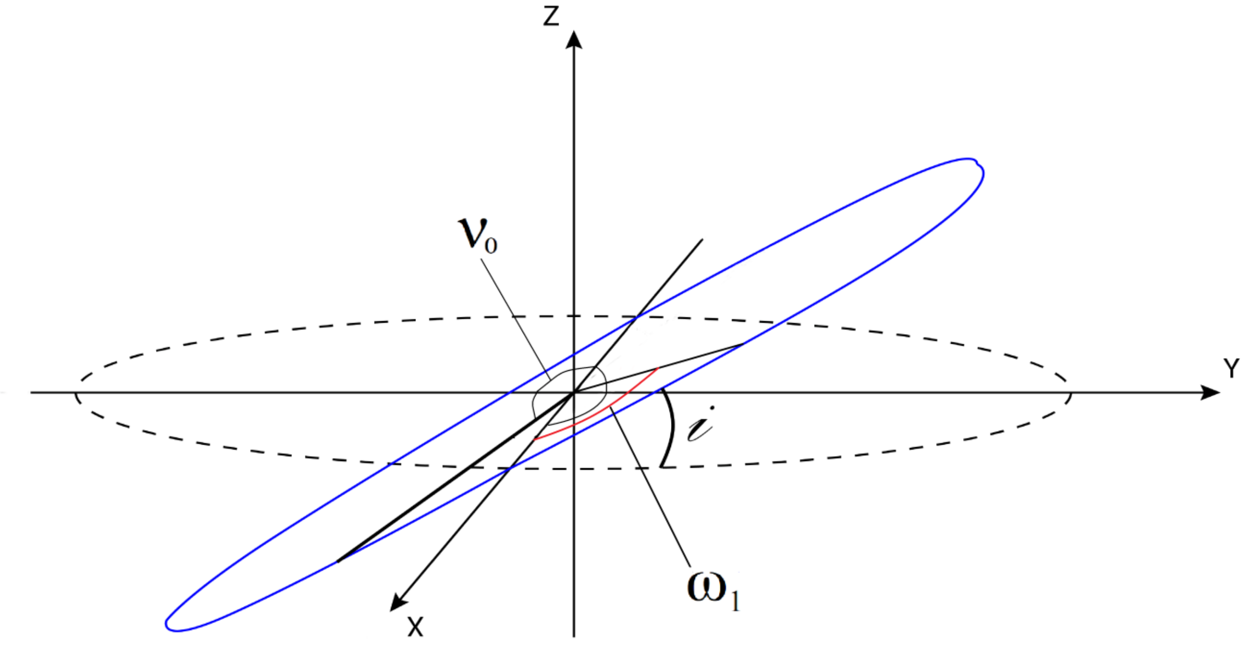

Figure 7.23 - Initial position of the satellite

The Chart 7.5and Chart 7.6 show the passages of the Moon in the FOV of both the telescopes and the considerations made in the previous relative sections are still valid. In contrast with the simulation of Saturn, the Moon path is always rightward but here it is downward, towards more negative Y coordinates, owing to a slight increase in the inclination of the S/C's orbital plane caused by gravitational perturbations.

Chart 7.5 – Moon in 180° x 180° FOV on Z_{LORF} (unit: km)

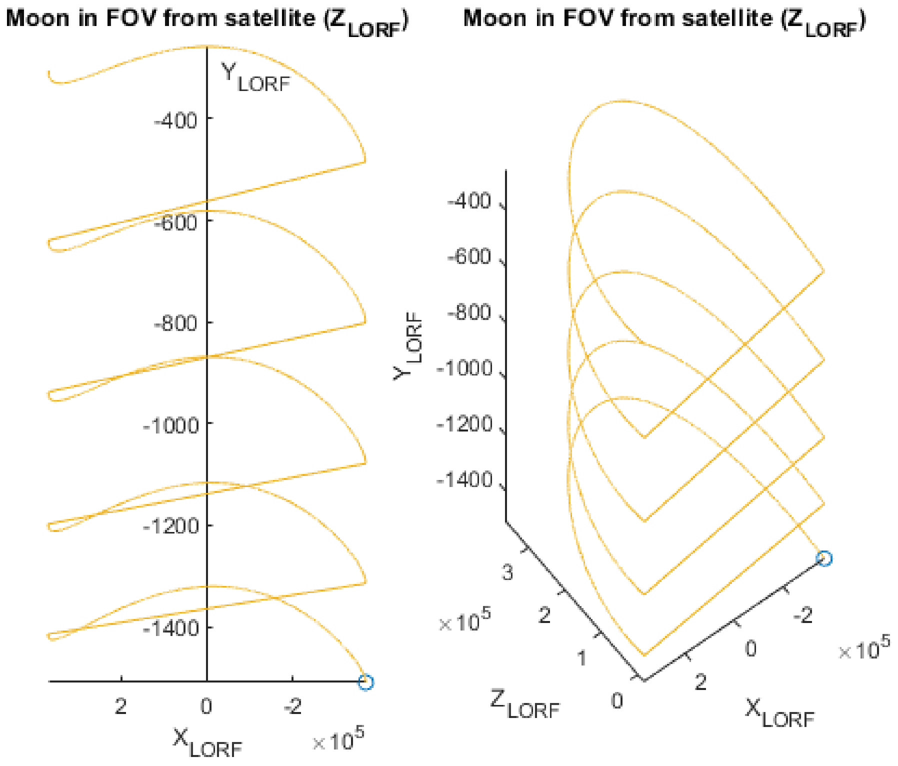

Chart 7.6 – Moon in 180° x 180° FOV on X_{LORF} (unit: km)

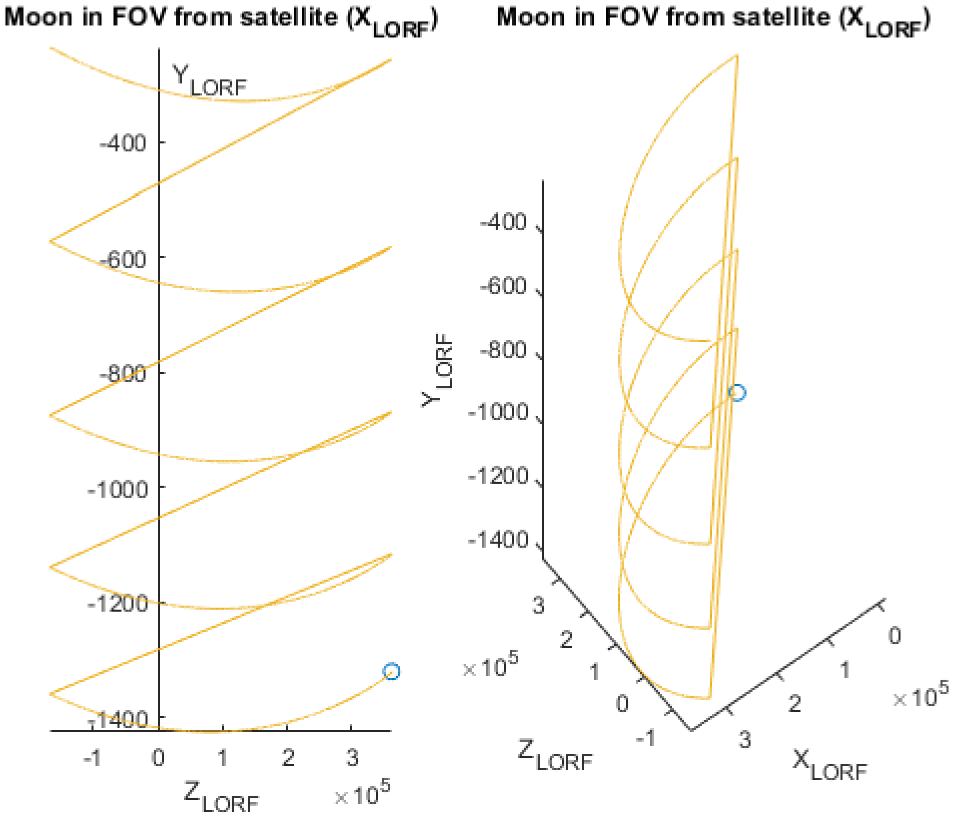

The occultation’s outlines in Chart 7.7 and Chart 7.8 have the same features as the passages of the Moon in FOV, rightward and downward; like the case of Saturn, these lines go in pairs: the first blue line with the first red line represent the first occultation and the number of lines are equal to the number of occultations. The red is the identifier of Aldebaran instead the blue represents the centre of the Moon. For example, if we check the two values of Moon and Aldebaran at the same time step, along the same occultation, in Chart 7.7 we can see that the X coordinate of the star firstly follows, then comes closer and then exceeds the X coordinate of the Moon, thus revealing that Aldebaran moves across the lunar disk. It must be said that to represent both the Moon and the star, it was adopted a scale for the star’s coordinates in order to bring them almost comparable with the order of magnitude of those of the Moon.

Chart 7.7 - 2D and 3D FOV of telescope set on Z_{LORF} with passages of the Moon and of Aldebaran (unit: km)

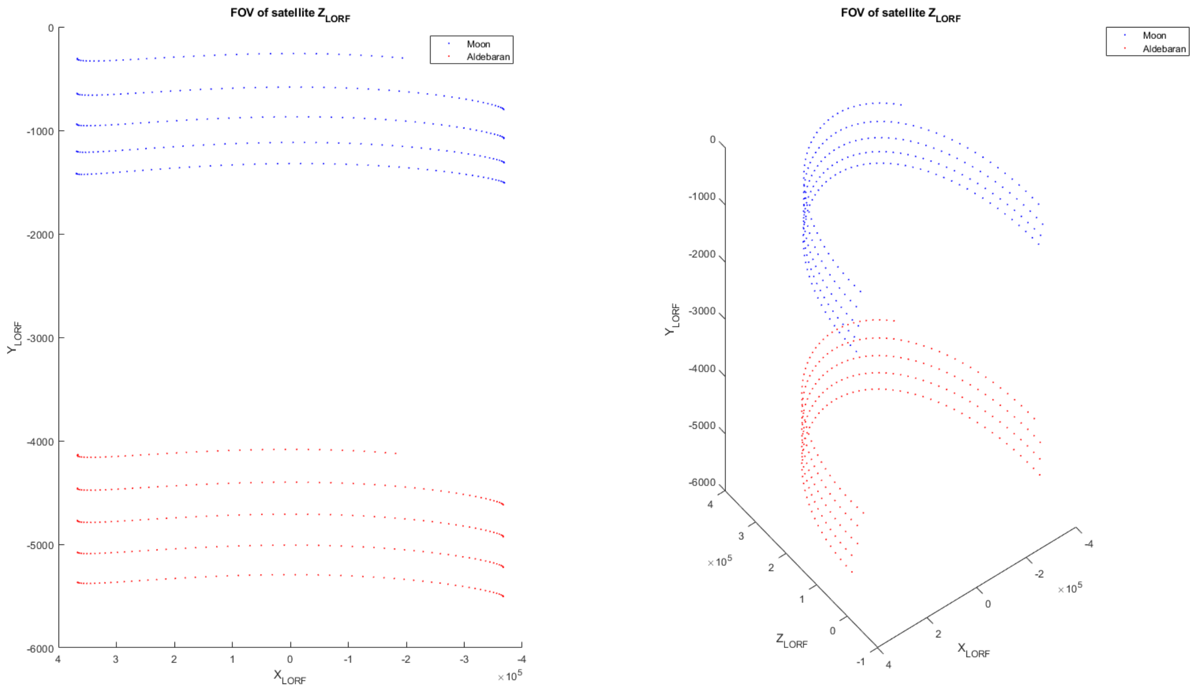

Chart 7.8 - 2D and 3D FOV of telescope set on X_{LORF} with passages of the Moon and of Aldebaran (unit: km)

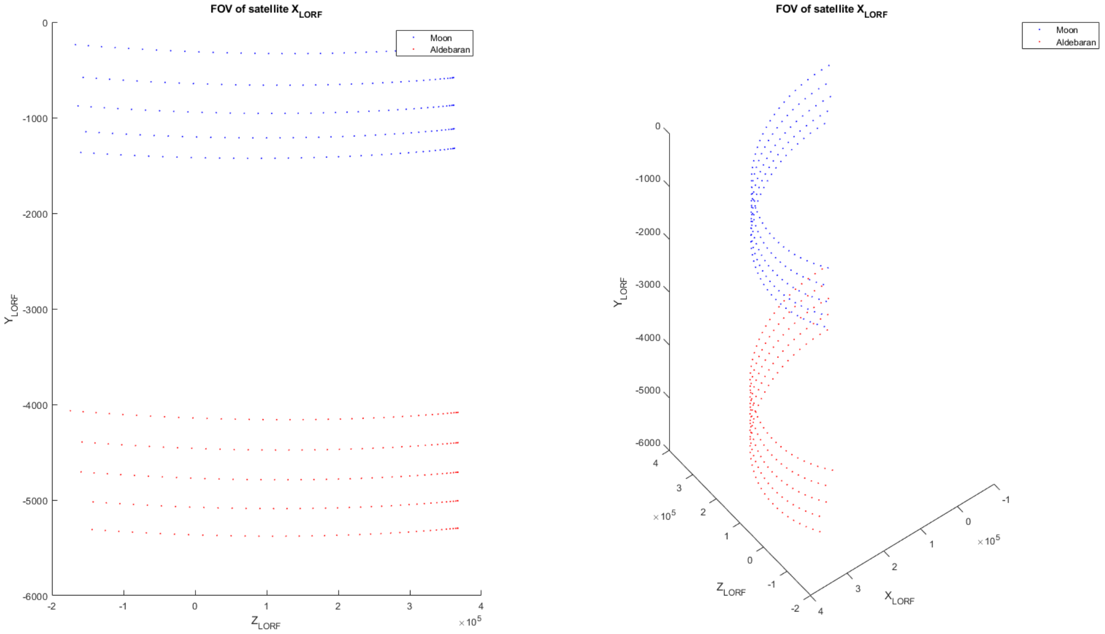

7.5 Observation of the sky

Apart from the study of the occultation of planets and stars while the Moon transits the FOVs of the satellites, what is also interesting is knowing how many stars and planets with their relative names and codes have been occulted by the Moon, when visible, at each time step for Z_{LORF} and X_{LORF}.

Due to the fact that the aim of this routine is not focusing on one precise celestial body but on the entire celestial sphere, it was given the name of "Observation of the sky".

For this kind of analysis, the most important axis to put the telescope on is the Z_{LORF} as it allows a clear view of the sky for the entire orbit. However, the X_{LORF} telescope was also added to this routine as it might give important information in some particular kinds of missions. Nevertheless, the procedures of the two axes are the same, so only the one relative to the Z_{LORF} axis is described.

Once having the coordinates of the Moon in the FOV, whether it is Z_{LORF} or X_{LORF}, the process can start. For each time step, defined by the user, the visibility of the Moon by the telescope is checked: in case of positive answer, the process goes forward and it will be divided into two parts: one considering the planets and one considering the stars.

For the part about the planets, each planet of the Solar System is taken into consideration, except the Earth and the Moon itself; through the SPICE routine *spkezr*, the state vector of the planet from Earth in TOD frame is retrieved and the Cartesian components have been separated from the velocity. By subtracting the satellite's position from the planet's position, the satellite-planet vector is found in TOD. This vector is later transformed into LORF frame.

Talking about planets, it is mandatory to consider them as wide objects in the sky, and thus they have an angular radius calculated as:

$$\gamma = \arcsin\left(\frac{R_P}{\left|\vec{r}_{sat-planet}\right|}\right)$$

where $R_P \rightarrow \quad radius\ of\ the\ planet \quad [km]$.

Now the angle between the satellite-Moon vector and the satellite-planet vector is computed:

$$\psi_P = \arccos\left(\frac{\left(\vec{r}_{sat-Moon} \cdot \vec{r}_{sat-planet}\right)}{\left|\vec{r}_{sat-Moon}\right| \left|\vec{r}_{sat-planet}\right|}\right).$$

If it is less than the sum of the lunar angular radius and the planet angular radius, we are in the case of an occultation and thus a counter is increased by 1 and the name of that planet is put aside.

Once all the planets of the Solar System have been inspected, the focus moves towards the stars. To this end, the entire catalogue called “stardatabase” is loaded and all the stars inside are inspected. First, for each star, the Cartesian coordinates in parsec in J2000.0 are retrieved and transformed into kilometres. Then, having already the position of the satellite, the satellite-star vector is calculated in TOD by subtracting the S/C position from the star position and later transformed into LORF frame.

Now the angle between the satellite-Moon vector and the satellite-star vector is computed:

$$\psi_S = \arccos\left(\frac{\left(\vec{r}_{sat-Moon} \cdot \vec{r}_{sat-star}\right)}{\left|\vec{r}_{sat-Moon}\right| \left|\vec{r}_{sat-star}\right|}\right).$$

The definition of the parameters inside these last equations have been explained before.

The control about the angle ψ_S is done: if it is less than the angular radius of the Moon, it is the case of an occultation. It must be reminded that the angular radius of the stars is hardly ever calculated, due to lack of information explained before, and so they are considered of one dimension in the sky.

When the occultation is proved, the star counter is increased by 1 and the name of the star is set aside. If the name is not present in the database, the routine finds out the related code, whether it is HIP, HD, or HR, to save it.

At the end of the execution, the outputs are, for each telescope:

- A matrix in which, for each time step, there are written the number of planets and stars occulted by the Moon;
- A matrix in which, for each time step, there are written the name of the occulted planets and the names or the codes of the occulted stars.

7.6 Future study occultations

With the previous routine, the study of the single phenomenon of the occultations ended. However, all the routines previously described are intended to be executed inside the main simulation but there are some cases that require the study of the occultations later, after the main analysis and separated from this. Therefore, an entire MATLAB script was written to be launched in a later time. During the main simulation, the code asks the user if he wants to perform the study later and what is calculated is only the passages of the Moon in the FOV of the telescopes, already defined by the user.

When the user needs the study, it is sufficient to launch this routine, without any input arguments. It loads the useful folders and kernels and asks the user to load manually the structure of the desired simulation. Afterwards, the program asks to insert the name of planet and/or the star name-code to perform the study. In fact, there is the possibility to study a planet and a star simultaneously. Thus, there are two sections: one for the planet and one for the star. In each section there are two parts intended for each telescope, on X_{LORF} and on Z_{LORF}. Each section is the repetition of the relative script for the single event previously described, hence they are not described again but it is suggested to look back in the report.

There are included also the scripts to write the outputs as a .txt file at the end of each part relative to the telescope, whether it is of a planet or a star, in order to be created progressively according to what was intended to study.

8 FUTURE IMPROVEMENTS AND CONCLUSION

At the end of this discussion, some final considerations can be made to summarize what was previously found.

Talking about the atmosphere models, significant improvements in empirical density modelling have been obtained using the new JB2008 model incorporating new solar indices, a new semi-annual variation equation, and a new geomagnetic index with respect to the old model (JB2006). This new model, Jacchia-Bowman 2008 (JB2008) provides standard deviations during non-storm periods of approximately 9-10% at 400 km, a significant decrease from 16% previously obtained using the Jacchia 70 model. Other results follow:

1. Use of new global exospheric temperature equations based on EUV and FUV solar indices significantly improves density modelling, especially at solar minimum times.
2. Use of new semi-annual density variation equations using multiple 81-day averaged solar indices accounts for major yearly semi-annual density changes due to changing long term EUV heating.
3. Use of the Dst index as a replacement for a_p greatly reduces density errors, especially during major geomagnetic storm periods. This error reduction is from over 60% for Jacchia 70 and over 35% for NRLMSIS, to 16% for JB2008 during major storms.

On the other hand, the new database underlying the NRLMSISE-00 model incorporates data on total mass density (orbital drag and satellite accelerometers), recent incoherent scatter radar observations covering more than a solar cycle, and satellite-borne FUV occultation measurements of $[O_2]$ from SMM. The model interpolates among newly added and past data sets, often incorporating new features or strengths of each data set. This model uses only $F_{10.7}$ and a_p indices. As a result, the exospheric temperature in NRLMSISE-00 now shows somewhat weaker dependence on $F_{10.7}$ relative to MSISE-90.

The incorporation of satellite-based data on total mass density has allowed the inclusion of a new component (anomalous oxygen) to correct the model estimates of total density at high altitudes (near the exobase). This shows that O+ can dominate drag under particular conditions and, through similar analysis, that hot oxygen could be important to drag. Comparison of NRLMSIS and the standard operational and scientific models to the orbit-based data of Jacchia at high altitudes has revealed significant differences in the seasonal and solar activity dependence of the models. NRLMSISE00 approximates very well the data for altitudes below 600km (data-to-model ratio around 1), above this height it diverges with data-to-model ratio up to 1.3 at 1100km. Standard deviation increases from 0.1 at 250km up to 0.27 at 1100km. The new model appears to provide advantages over both Jacchia-70 and MSISE-90 for estimating total mass density.

The focus of this report then moved towards the forecast methods of the solar indices for the three considered atmospheric models. For both JB2006 and JB2008, real-time and historical indices for this model can be found on this website: http://sol.spacenvironment.net/ and later used in the code to forecast future solar indices at the desired epoch of the simulation. Sometimes, due to lack of forecast, standard tables of indices coming from past solar cycle 23 can be used to make the forecast. NRLMSISE00, instead, uses Marshall Space Flight Center bulletins to forecast solar indices using the Lagrangian Linear Regression Technique of the NASA Technical Memorandum 4759, determining measurements of them at 95, 50 and 5 percentile in contrast with the Jacchia-Bowman's models that provide only one measure.

After this study, the interest moved towards the software code; in particular, the process of how the occultations were implemented in NODES was described, focusing on the passages of the Moon in FOVs of the satellite – directed towards X_{LORF} and Z_{LORF} axes –, on the model of planetary and stellar occultations and on the observation of the sky bringing also two explanatory examples, about Saturn and the star Aldebaran.

At the end, some possible improvements are given to be adopted and implemented in the future.

Regarding the atmosphere models, the latest version of the Space Environment ECSS shall always be checked by the software user to be updated on the ultimate requirements and specifications. Instead, about the NODES, there should be the possibility to add a third FOV directed towards the Y_{LORF} axis, in relation to the type of the mission that requires it. Moreover, the elevation and azimuth angles between the boresight and the LORF axis for the previous analyses were set to zero; it can be chosen to put these angles different from zero and to add also an angular velocity around Y_{LORF} to make the satellite rotate. This angular velocity can be, for example, about $360 \frac{°}{orb}$ in order to point one of the FOVs of the satellite towards the same region of the universe, i.e. for missions of observation of the sky.

In addition to this, a better study on the radiations hitting the satellite's surfaces may also be performed, as well as, the addition of the thermal emission for the spacecraft and the torques acting on the satellite. These torques are caused by differences in forces – of different nature (gravitational, Drag, radiation pressure) – acting on the surfaces of the satellite and having an arm with respect to the center of mass. To this it is added the fact that the satellite is not always symmetrical ($\sum_i \Delta F_i \neq 0$) and that it is not composed of a unique cross-sectional area but it has several hidden surfaces that do not contribute.

9 APPENDICES

9.1 Test on NODES software

Before the beginning of the study of occultations, the NODES software has been deeply studied, examined, controlled for nearly one month and a half in order to find any possible errors or bugs, with the aim also to optimize the code and to improve the graphics and the human-machine interface. Relative to the code, the User Manual and the Technical Note have been updated.

9.1.1 "NONE" in graphics window

The first encountered problem was that of the "NONE" option.

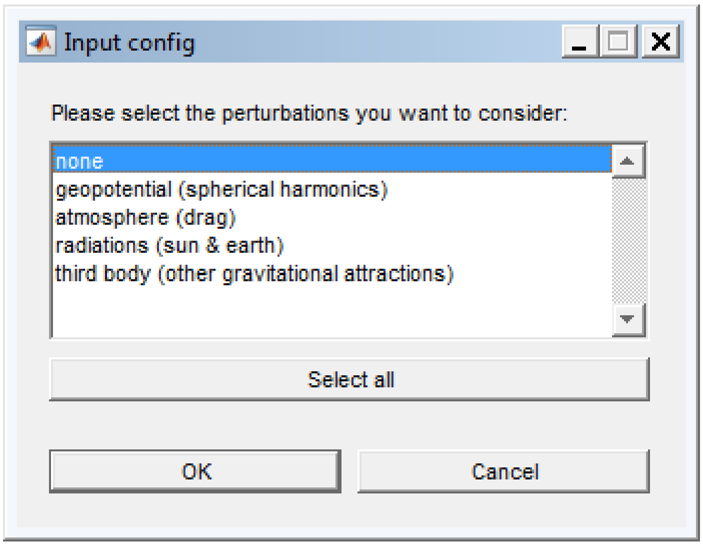

Please select the perturbations you want to consider:

none
geopotential (spherical harmonics)
atmosphere (drag)
radiations (sun & earth)
third body (other gravitational attractions)

Figure 9.1 - Perturbations choice: before correction

With the configuration reported in Figure 9.1 if the user selects the "SELECT ALL" button, as the word says, the program selects all the options in the windows above, including the "NONE". But the "NONE" implies that none of the listed perturbations must be considered and the flags will be set to 0. Thus, instead of selecting all the perturbations and putting all the flags to 1, the user will find no perturbations. This problem was solved acting on the code and removing the "NONE" option from the list but always keeping the option of selecting no perturbations by unchecking the highlighted line while holding "CTRL" on the keyboard and then clicking "OK".

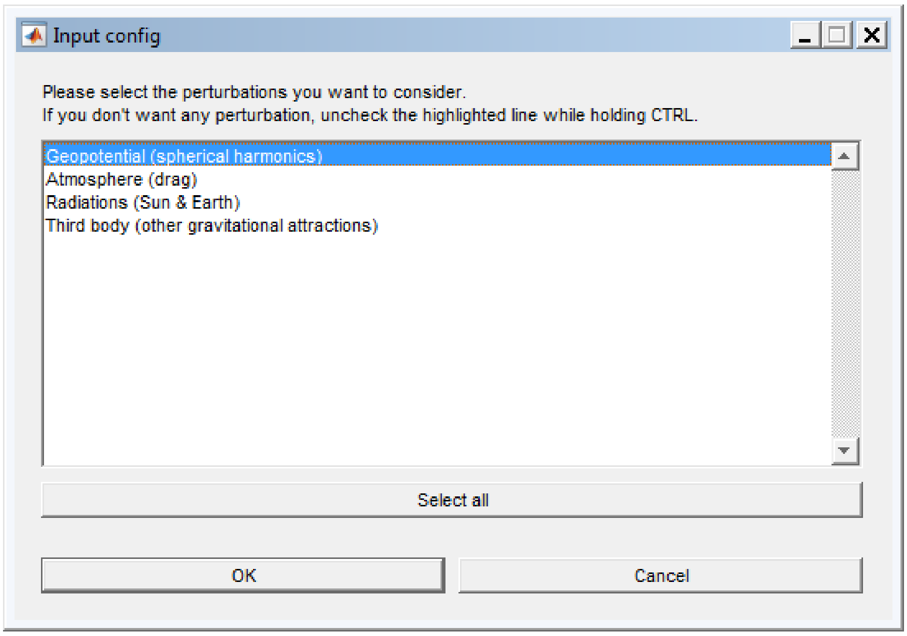

Please select the perturbations you want to consider.
If you don't want any perturbation, uncheck the highlighted line while holding CTRL.

- Geopotential (spherical harmonics)
- Atmosphere (drag)
- Radiations (Sun & Earth)
- Third body (other gravitational attractions)

Figure 9.2 - Perturbations choice: after correction

The same problem was encountered for the "free-force option" and was solved in the same manner as before.

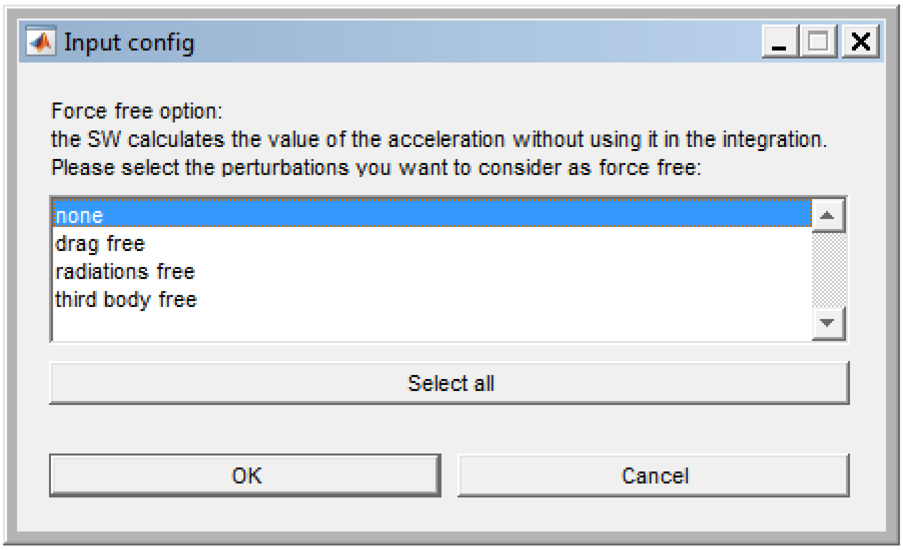

Force free option:
the SW calculates the value of the acceleration without using it in the integration.
Please select the perturbations you want to consider as force free:

- none
- drag free
- radiations free
- third body free

Figure 9.3 - Free-force option: before correction

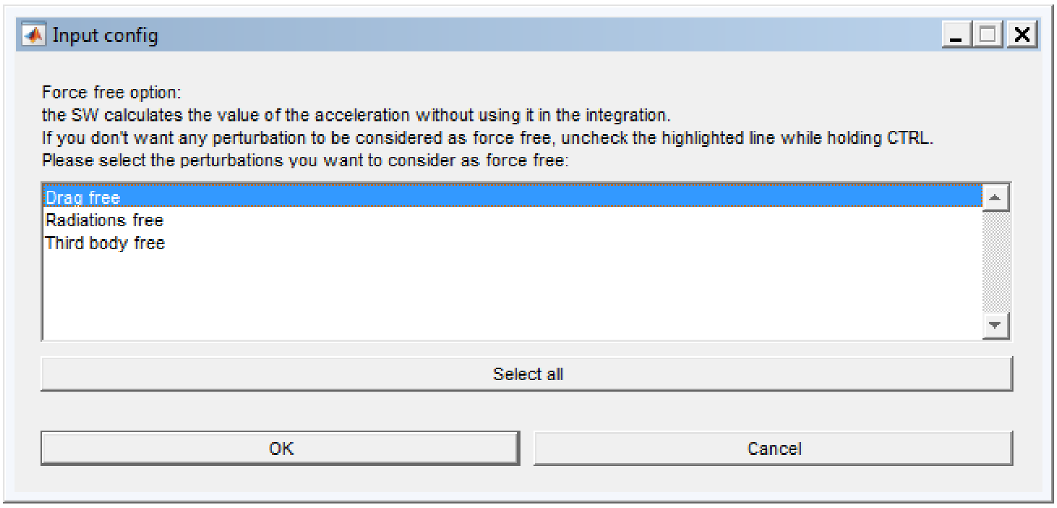

Force free option:
the SW calculates the value of the acceleration without using it in the integration.
If you don't want any perturbation to be considered as force free, uncheck the highlighted line while holding CTRL.
Please select the perturbations you want to consider as force free:

Figure 9.4 - Free-force option: after correction

9.1.2 Ground Stations

It was found that the Ground Stations (GS) database was not up-to-date or even wrong regarding the names of the GS and/or their coordinates; moreover, some GS were no longer available or out of use. In this way, it was necessary to correct them by using the last issue from ESA, the ESA Tracking Stations (ESTRACK) Facilities Manual (EFM), written in reference page.

A second problem issued from code debugging is that the user can insert only one GS to study the visibility of because with more GS the code crashes. This was unacceptable for the study of a real mission. Thus it was fixed so the user can select and study any GS he wants. In addition to this, also the output file generator codes were revised allowing to display the visibility information of each GS. In particular, the file “gs_vistime” shows for each revolution in which the GS is visible from the satellite, the entrance time, the exiting time and the time interval, for each previously selected GS. The file “gs_vislist” shows for each time step if the GSs, placed in column, are all visible, or only some of them, or none. If one is visible, at that time step there is written the GS’s name in the relative column, if it is not visible, a slash (/) is present in the same position. In the end, the file “gs_sataer”, for each GS, for each revolution, indicates explains each time step in which the satellite is visible from the GS along with the relative values of azimuth, elevation and range. To validate these codes, three analyses were done. The first was done by selecting only one GS using the old scripts that worked only with one GS; the second was done by selecting the same GS as before but using the newly correct scripts valid for more GSs; the third selected three GSs included the former GS using the new scripts. These three analyses were compared to each other and it was found that all gave the same results, especially regarding the GS in common: the coverage times were all the same.

A third problem that turned out was that of the angle of elevation of the GS. This angle is calculated between the horizontal plane passing through the GS and the sight line from the GS to the satellite. It is positive when this line is above the horizontal plane, negative when below and this is the phenomenon of the depression of the horizon. It represents the moment in which a link between the GS and the satellite can start.

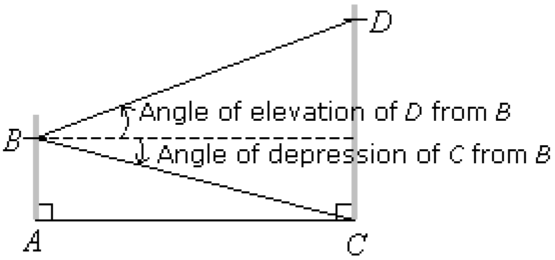

Figure 9.5 - Difference between the elevation and the depression of the horizon

By ESA standards, the angle of elevation was set to 5°. If the user increases its value, it is supposed that the connection time will decrease; on the contrary, if he decreases its value until it becomes negative and beyond, as if the GS is elevated, i.e. on the top of a mountain, it is supposed that the GS sees the satellite earlier and thus the connection time should be increased. Four cases were done by putting different values to the elevation angle of two GSs selected in each analysis: (+5°,+5°) (+5°,-5°) (-5°,+5°) (-5°,-5°). However, the values of the coverage times (entrance time, exiting time, time interval) are always the same. After many other investigations through the code, it has not been understood why the results didn't change; the cause can be found out nested inside other scripts but, it took much time and that was not the aim of the internship, so the study was put aside, leaving to other users the task to verify the cause.

9.1.3 Script "pert-tbdy"

Keeping constant all other parameters, in each mission one perturbation was added to the others.

The constant parameters are:

Table 9.1 - Data mission

Quantity	Value	Unit of measure
Start date and hour	Dec 7th, 2020 @ 12:00:00	
Duration	604800 (7 days)	s
Time step	30	s
Semi-major axis	7000	km
Eccentricity	0.01	
Inclination	60	deg
Right Ascension of the Ascending Node	0	deg
True anomaly	0	deg
Argument of perigee	0	deg

First, we started with a mission with no perturbations inside; the only present force is the central gravity force that leads to a simple Keplerian orbit and the result is in the following figure. It must be said that the central gravity force is always present in all the mission simulations that will be done, even when it is not specified.

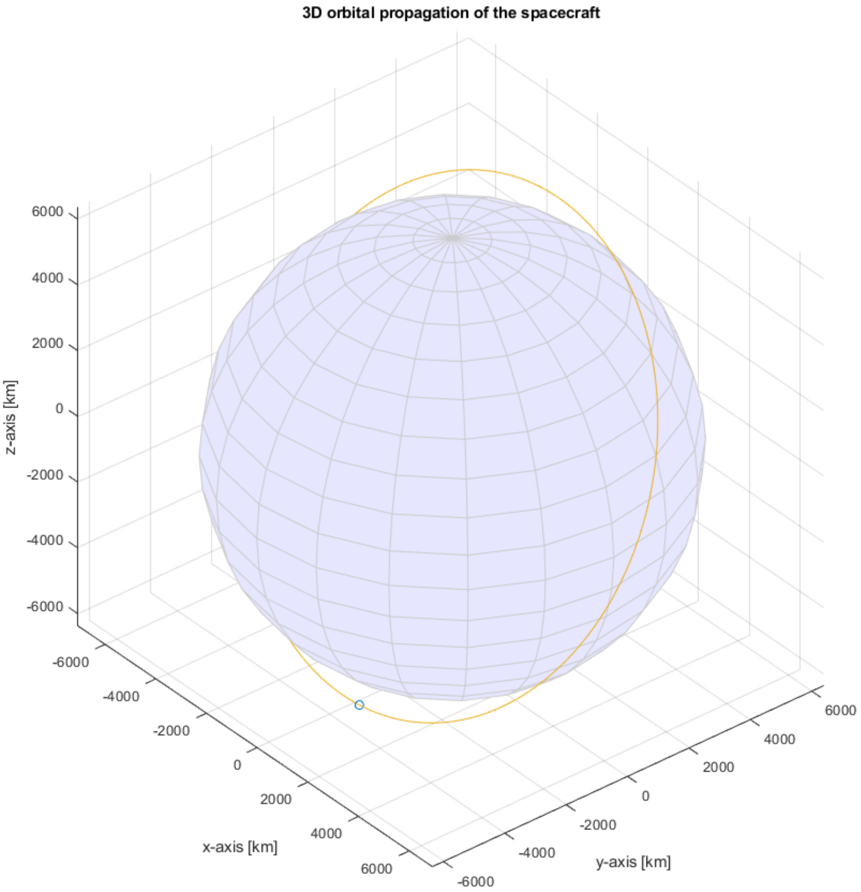

Figure 9.6 - Central gravity field

The second step is adding the first perturbation, that is the geopotential correction, i.e. the spherical harmonic expansion used to correct the gravitational potential for Earth's nonsymmetric mass distribution. The result is shown in the figure below. As you can see, the effect is the precession of the satellite's orbit, leading to a change in the value of the RAAN clockwise as well as of inclination that tends to decrease. This effect is more evident in longer missions.

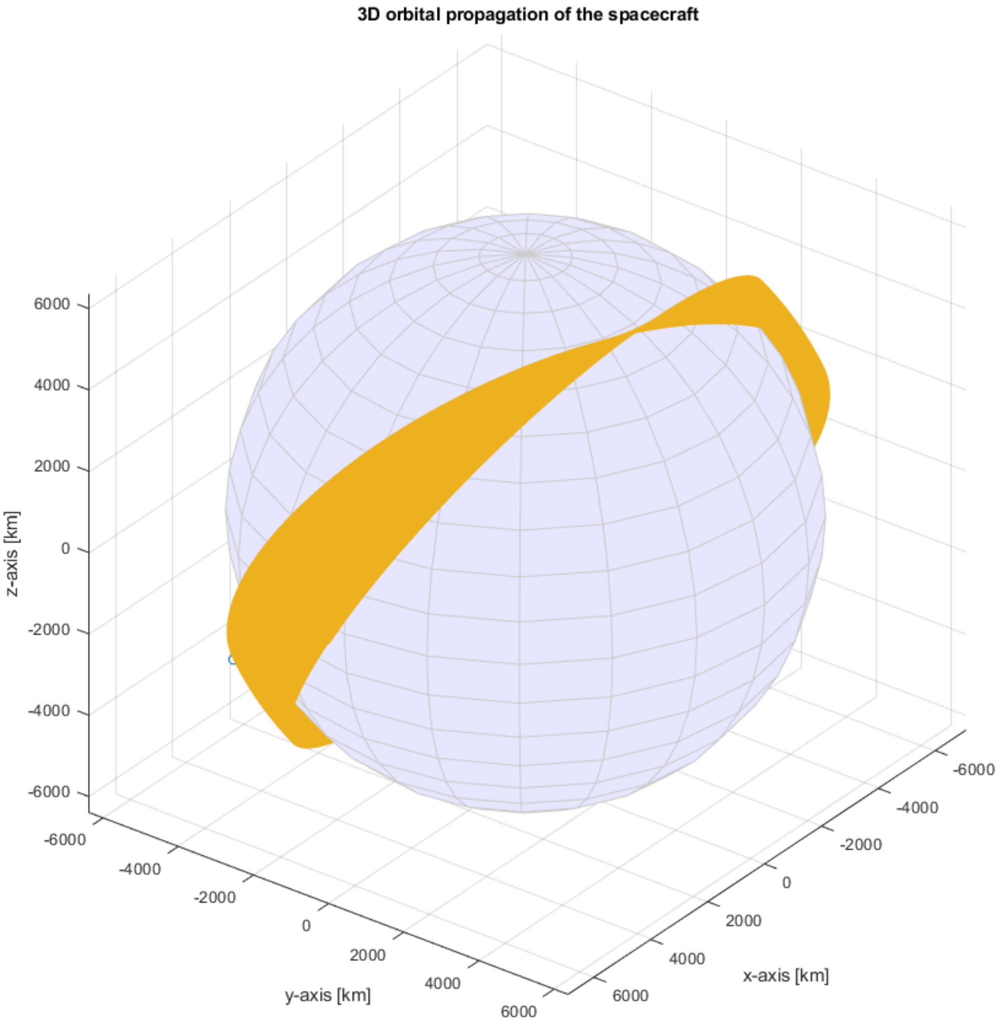

Figure 9.7 - Central gravity field + Geopotential

The following step is adding a second perturbation to the others, that is the effect of third body. As third body, both Sun and Moon were considered because they have a relevant effect on Earth's satellites. Because they apply forces outside the orbital plane, they will change the RAAN and the inclination of the orbital plane. In particular the RAAN moves westward and the inclination tends to decrease. This perturbation depends on both time and space. However, the result is not satisfying as the orbit diverges.

The difference between this analysis and that of Figure 9.7 is the addition of the third body perturbation. In this way, the scripts concerning this perturbation are inspected deeply.

It was found that there were some errors about the signs in the formulation of the perturbative acceleration and about reference system for vectors. The right and complete formulation will be found in paragraph 9.4.2.2.

Once corrected the script, another analysis was done to verify the right behaviour. It had the same parameters and what was found is displayed below.

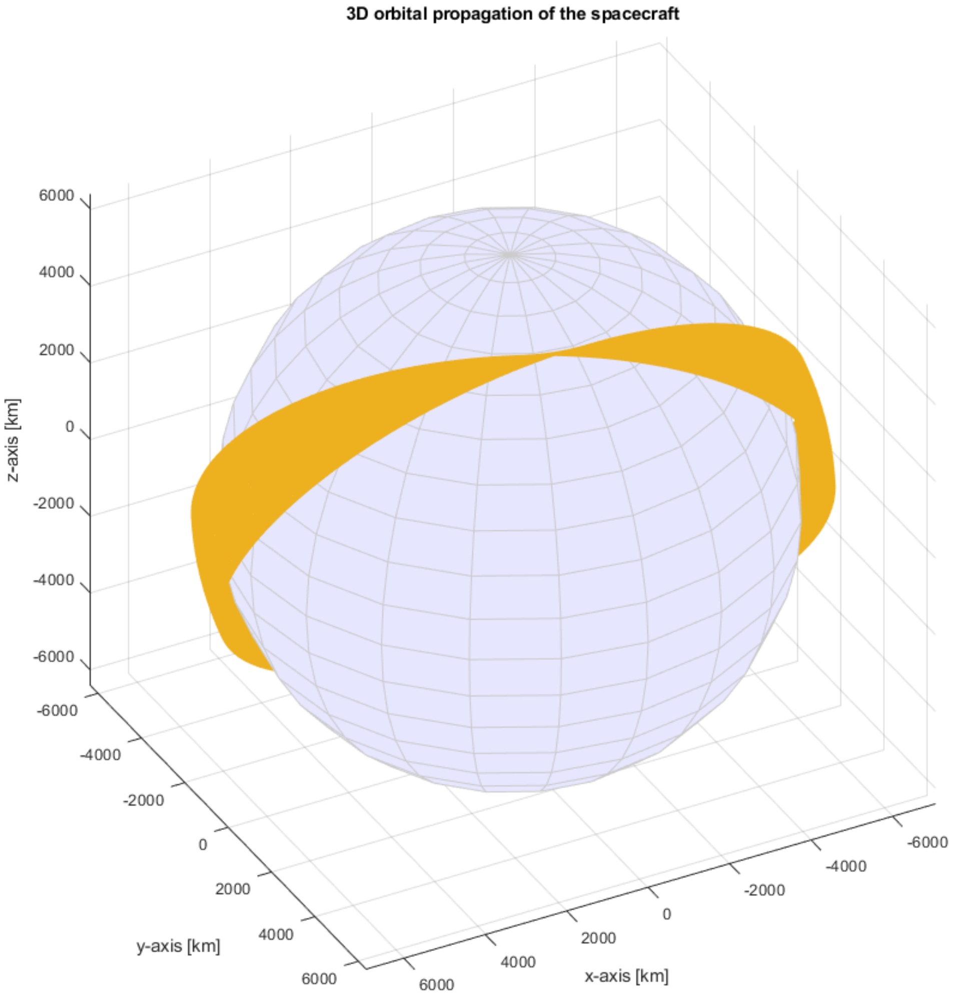

Figure 9.8 - Central gravity field +Geopotential + correct third body

Now it correctly models the behaviour of the satellite under the effects of the two perturbations, geopotential and third body.

To prove that the duration of the mission does not affect the satellite's motion, another analysis was done with mission duration of 86400 s (1 day).

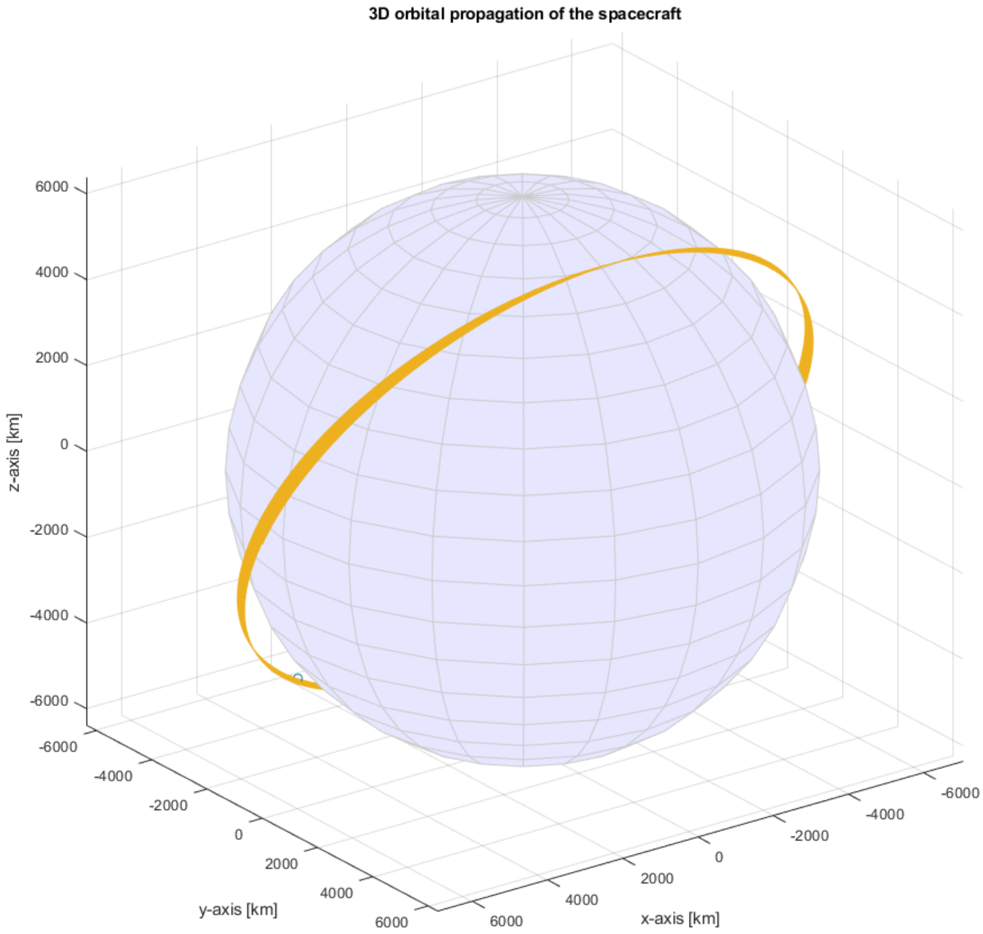

Figure 9.9 – Two perturbations (geopotential and third body), 86400 s (1 day)

As it can be seen, the model correctly represents the motion of the satellite and the orbital plane does not shift of diverge as before. Moreover, the effects of third body perturbation are weak for Low Earth Orbit satellite and thus in the previous analyses they are not much relevant. The bigger the semi-major axis of the satellite's orbit is, the more considerable the third body effects are.

For sake of completeness, another analysis was done and the only parameter that change is the duration; now it lasts 2592000 s (30 days) and the results is below.

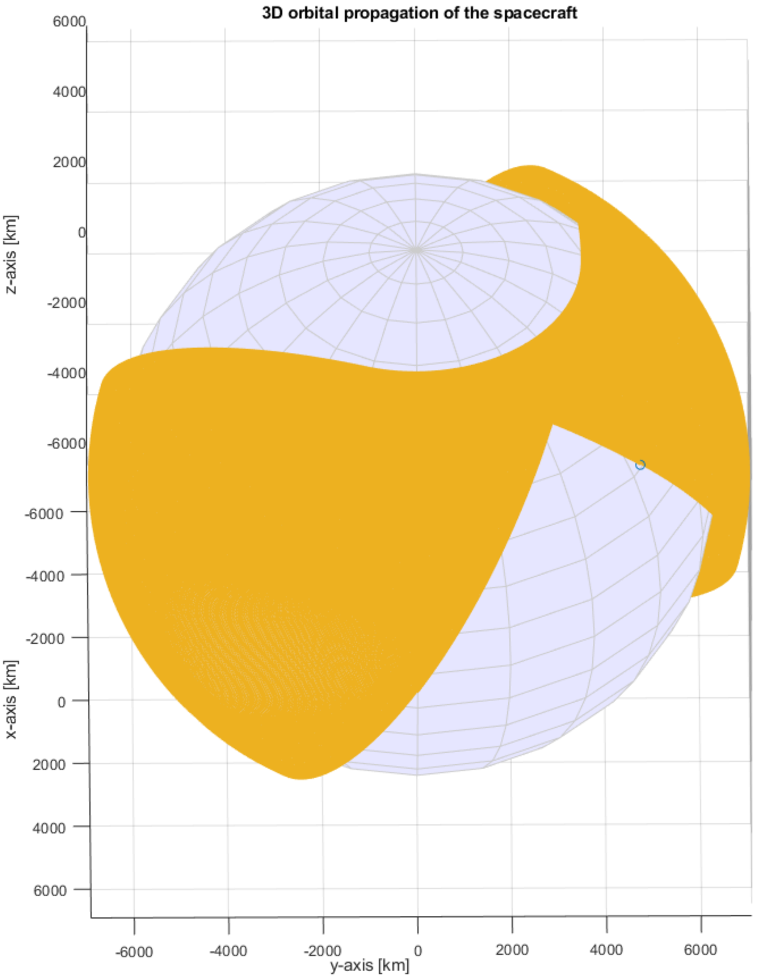

Figure 9.10 – 30 days mission

9.1.4 GEO satellite

To verify the effects of third body perturbation, it was decided to simulate a geostationary satellite. Its semi-major axis is nearly 6 times the previous analysis as well as the mission duration, which is 30 days compared to the previous 7 days. The mission parameters are displayed in the table below.

Table 9.2 - GEO data mission

Quantity	Value	Unit of measure
Start date and hour	Dec 7th, 2020 @ 12:00:00	
Duration	2592000 (30 days)	s
Time step	30	s
Semi-major axis	42378	km
Eccentricity	0.0001	
Inclination	0	deg
Right Ascension of the Ascending Node	0	deg
True anomaly	0	deg
Argument of perigee	0	deg
Perturbations	Geopotential (EIGEN-GL04C)	
	Third body (Sun, Moon)	

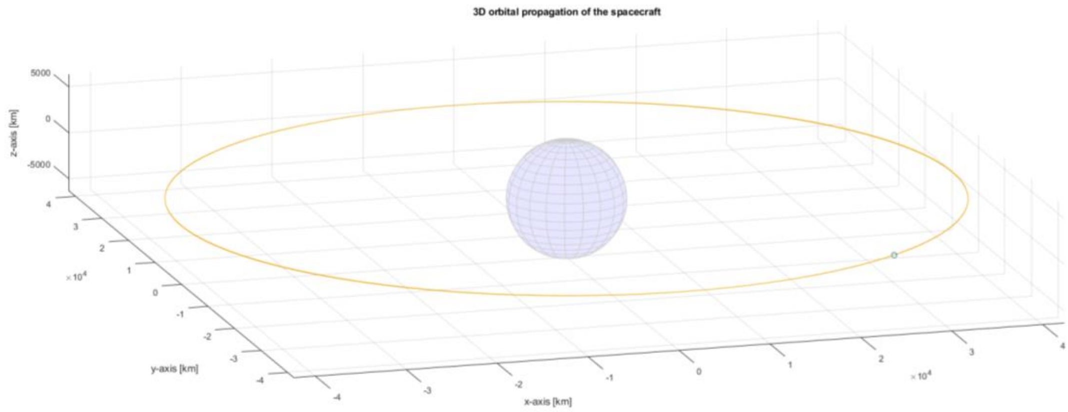

Figure 9.11 - Geostationary satellite

The result of the analysis is shown in Figure 9.11 which depicts a real situation. Through the output text files that the software automatically generates, an Excel spreadsheet was created and the orbital elements of each time step were loaded; then, all values of inclination were plotted as a function of time. The result is an oscillating increasing curve which thus leads to an increasing of the value of inclination up to 0.092° from zero in 30 days. This is strictly connected with the variation of the values of Z coordinate. The change of the other orbital elements (a, e, Ω, ω) exists but is not relevant. Moreover, the fact that the curve is not a smooth oscillation but has little fluctuations inside is due to the variation of all other orbital elements under determinate perturbations.

The plot of the inclination as a function of time for a Keplerian orbit without perturbations would be a constant horizontal line equal to zero, i.e. the initial value. Hence, the effects of the third body perturbation are more prominent in GEO than in LEO satellites and for missions that last longer.

Chart 9.1 - Inclination trend with time

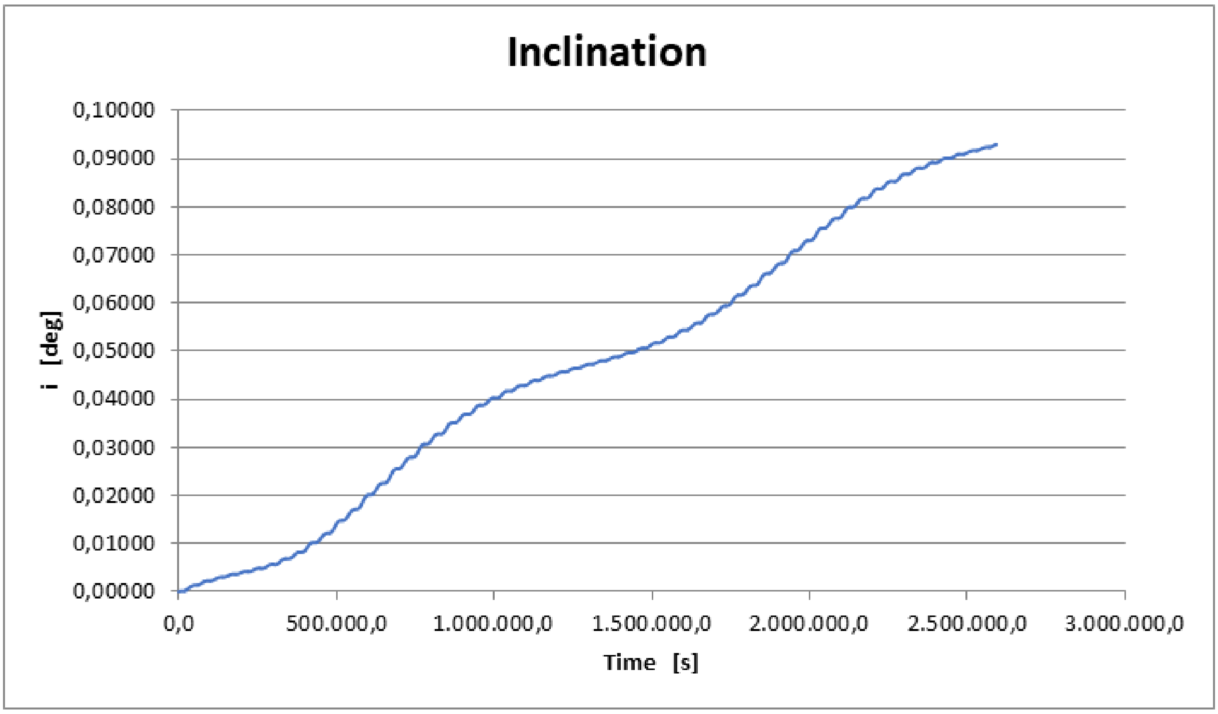

9.1.5 Atmosphere

Several simulations were done to inspect the effects of the atmosphere's models.

9.1.5.1 Duration

The first analyses were done varying only the duration of each mission. The mission parameters are:

Table 9.3 - Mission data

Quantity	Value	Unit of measure
Start date and hour	Dec 7th, 2020 @ 12:00:00	
Time step	30	s
Semi-major axis	7000	km
Eccentricity	0.01	
Inclination	60	deg
Right Ascension of the Ascending Node	0	deg
True anomaly	0	deg
Argument of perigee	0	deg
Perturbation	Atmosphere	
Atmosphere data		
Atmosphere model	NRLMSISE00	
Drag calculation method	Basic formula	
Drag coefficient c_D	2.2	
S/C mass	1000	kg
Winds	no	

With the term "basic formula", the traditional drag formulation is meant $D = -\frac{1}{2}\rho V^2 S c_D$ from which the drag acceleration is computed: $a_D = -\frac{1}{2}\rho V^2 \frac{S}{m} c_D$.

The considered durations are: 86400 s (1 day), 345600 s (4 days), 604800 s (7 days).

In all simulations, the final result is the same:

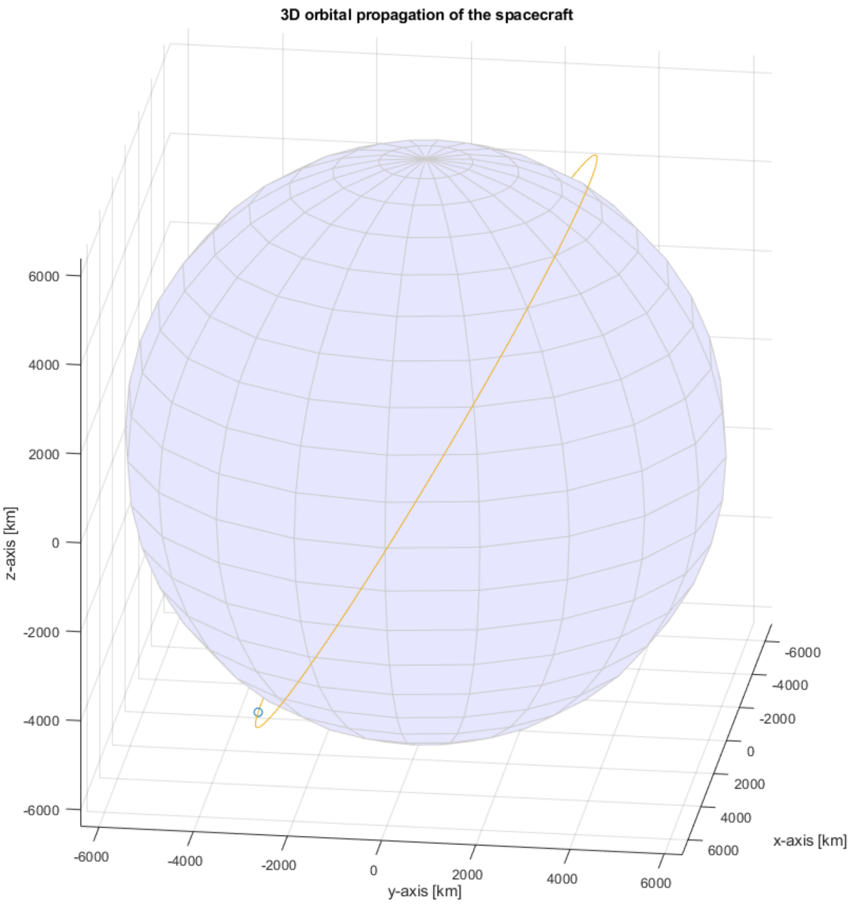

Figure 9.12 - Only atmosphere

With a close inspection, Figure 9.13 and Figure 9.14 , it was seen that all the orbits are in the same plane but with the semi-major axis that gradually lowers as the time passes. This is the consequence of the presence of the atmosphere drag. In Figure 9.13 the Earth is placed behind the lines, as the X-axis tends to decrease leftward, going to the Earth's centre. This zoomed picture was not taken on the Equator but on a different latitude because the X component values span around 6226 km, which is minor than the Earth's mean radius. The drag has a consistent effect on satellites only when they are in LEO orbits; as the height increases, the drag has a minor effect on orbits, i.e. GEO satellites are not influenced by atmosphere drag. Another conclusion is that the atmosphere model NRLMSISE-00 seems to work correctly.

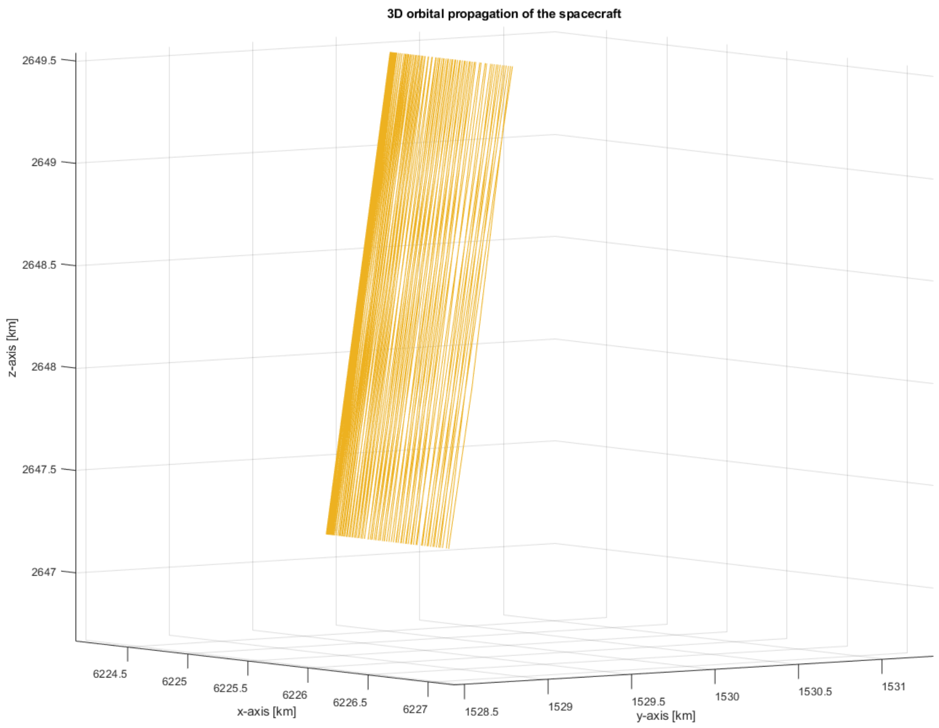

Figure 9.13 – Detail of orbits (the Earth is to the left)

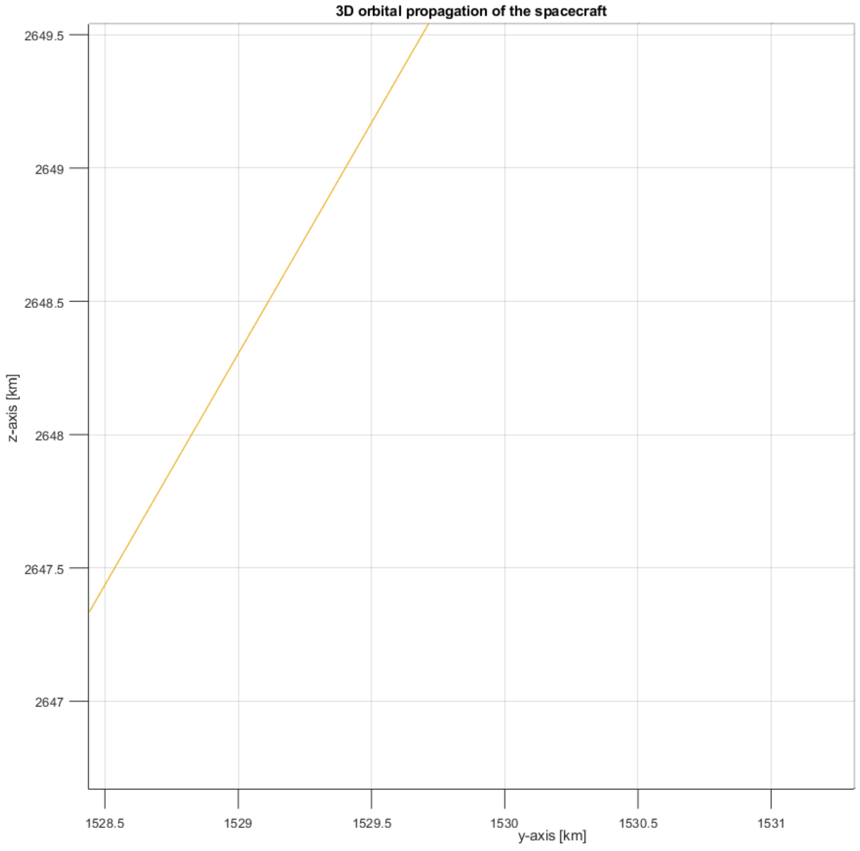

Figure 9.14 – Detail of orbits

In Figure 9.14 it is shown the frontal representation of the previous picture in Figure 9.13, thus the Earth is on the background and the X axis comes out from the sheet. In this figure, the inclination of the orbital plane can be clearly visible, that is the angle between the oblique yellow line and a horizontal line.

The data obtained from the software were then processed in an Excel spreadsheet to see the evolution with time of some orbital elements. The following plots are made for the 604800 s (7 days) analysis.

Chart 9.2 - Semi-major axis trend with time

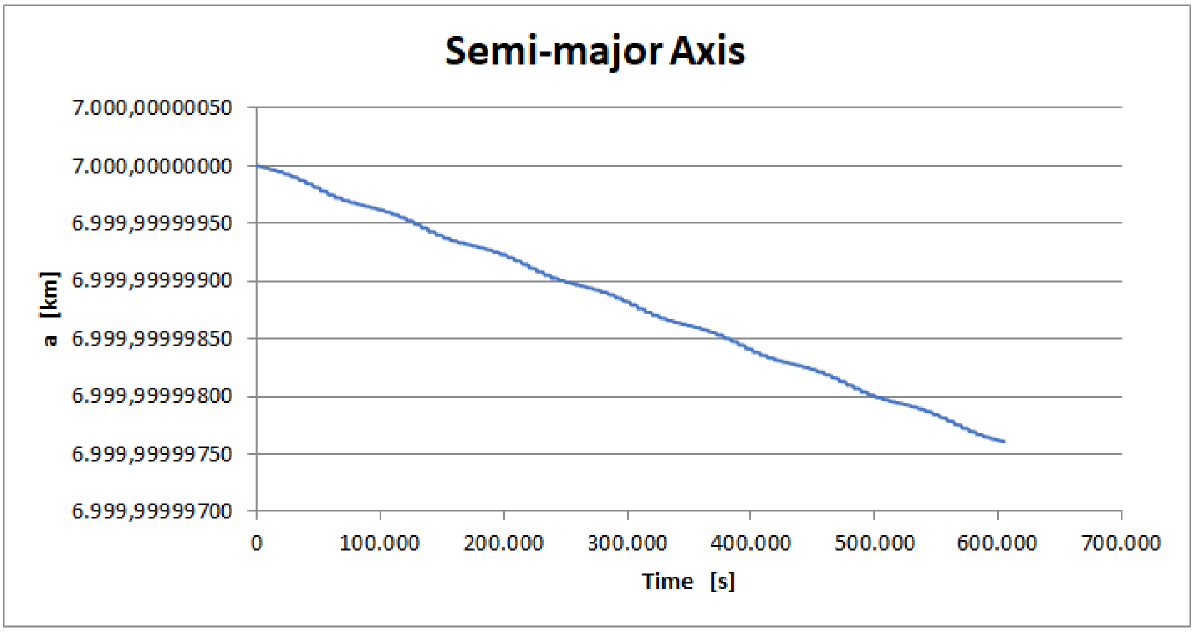

Chart 9.3 - Eccentricity trend with time

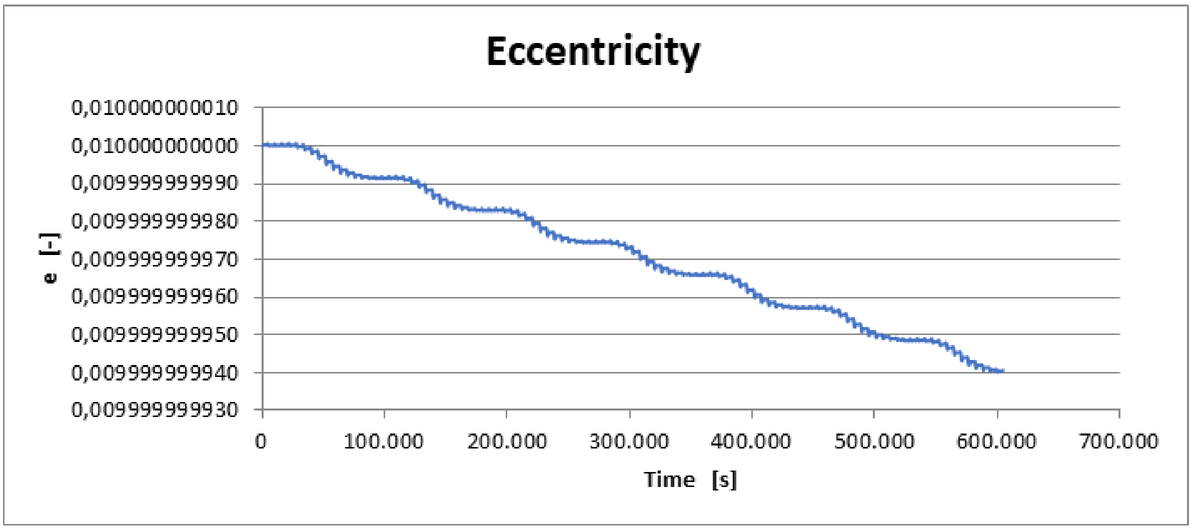

Chart 9.4 - Inclination trend with time

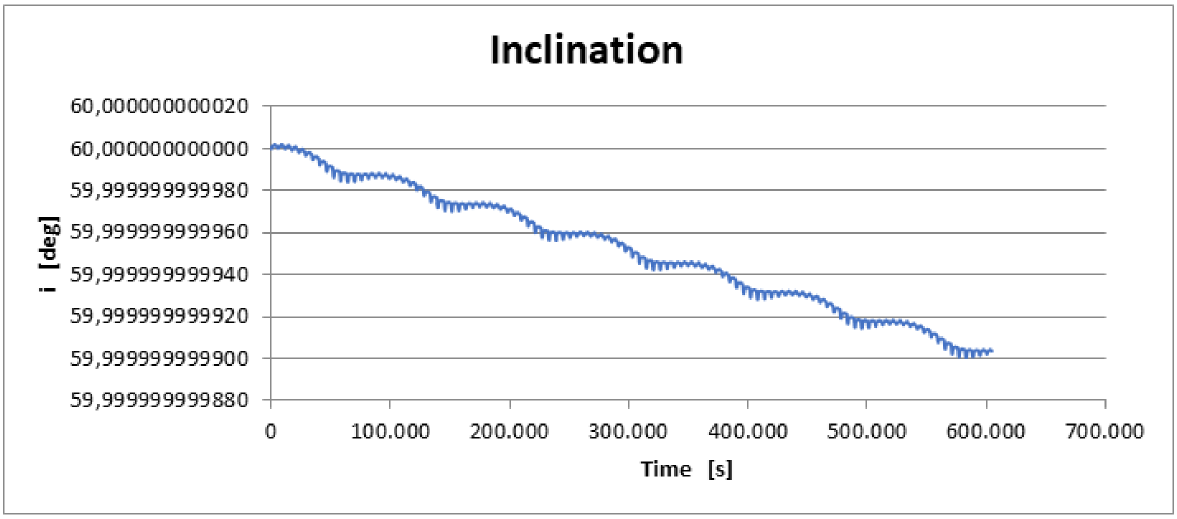

There is a confirmation of that stated before: the semi-major axis decreases and so also the eccentricity and the inclination do. However, the eccentricity and inclination change rate is less than that of semi-major axis: the former are about 10^{-11} instead the second is about 10^{-7}. Moreover, the decreasing of the value of the eccentricity is one of the effects of the drag: it is called "circularization" and consists in changing the semi-major axis by changing the apogee and the perigee altitude. This happens when the perigee is very low inside the atmosphere and the apogee is much higher; in perigee, the drag exerts a force opposite to the velocity vector with the result of lowering the apogee height. This happens in each orbit. The final result is that the orbit tends to be circular, hence the name. This always happens strongly in high-elliptical orbits. In this case, it is a slightly elliptical orbit and the effect is not much pronounced, but it is still present.

9.1.5.2 Time step

In this comparison, all the previous mission parameters (Table 9.3) were left unchanged, the duration is set to 604800 s (7 days) and the time step was varied: it goes from 30 s to 600 s (10 min).

The results are the same, the values at relative time step are equal, the analysis is faster. The conclusion is that the time step does not influence the simulation.

At this point, a clarification about the software is needed. The visualization step is fixed and is given by the user at the beginning of the analysis, i.e. the previous 30 s / 600s. The integration step is variable and depends on the MATLAB solver ODE113 (variable step, variable order). In particular, at the beginning of the integration process, the integration step and the visualization step are equal; later, the solver, being variable step, modifies the integration step to correctly match with the function and its trend. Moreover, the time step should always be balanced by the user in relation to what he is going to simulate, the accuracy of the final results and the performances of the computer.

9.1.5.3 Models

The following analyses were done to compare the atmosphere models, JB2006 and JB2008, because in previous studies the good accuracy and correctness of NRLMSISE00 was already analysed.

The analyses have the following characteristics.

Table 9.4 - Mission data for atmosphere model study

Quantity	Value	Unit of measure
Start date and hour	Dec 7th, 2020 @ 12:00:00	
Duration	1209600 (14 days)	s
Time step	30	s
Semi-major axis (a)	7000	km
Eccentricity (e)	0.01-0.001	
Inclination (i)	60-0	deg
Right Ascension of the Ascending Node (Ω)	0	deg
True anomaly (ν)	0	deg
Argument of perigee (ω)	0	deg
Perturbation	Atmosphere	
Atmosphere data		
Atmosphere model	JB2006/JB2008 for heights > 120 km	
	NRLMSISE00 for heights < 120 km	
Drag calculation method	Basic formula	
Drag coefficient	2.2	
S/C mass	1000	kg
Winds	no	

The first two analyses have eccentricity equal to 0.001 and a null inclination. The other two have the same eccentricity value as before but with an inclination of 60°. The last two analyses have the same inclination but with the eccentricity equal to 0.01. The analyses come in couple because both atmosphere models have been studied. In this way, it will be easy to compare them afterwards.

Chart 9.5 - Old JB2006

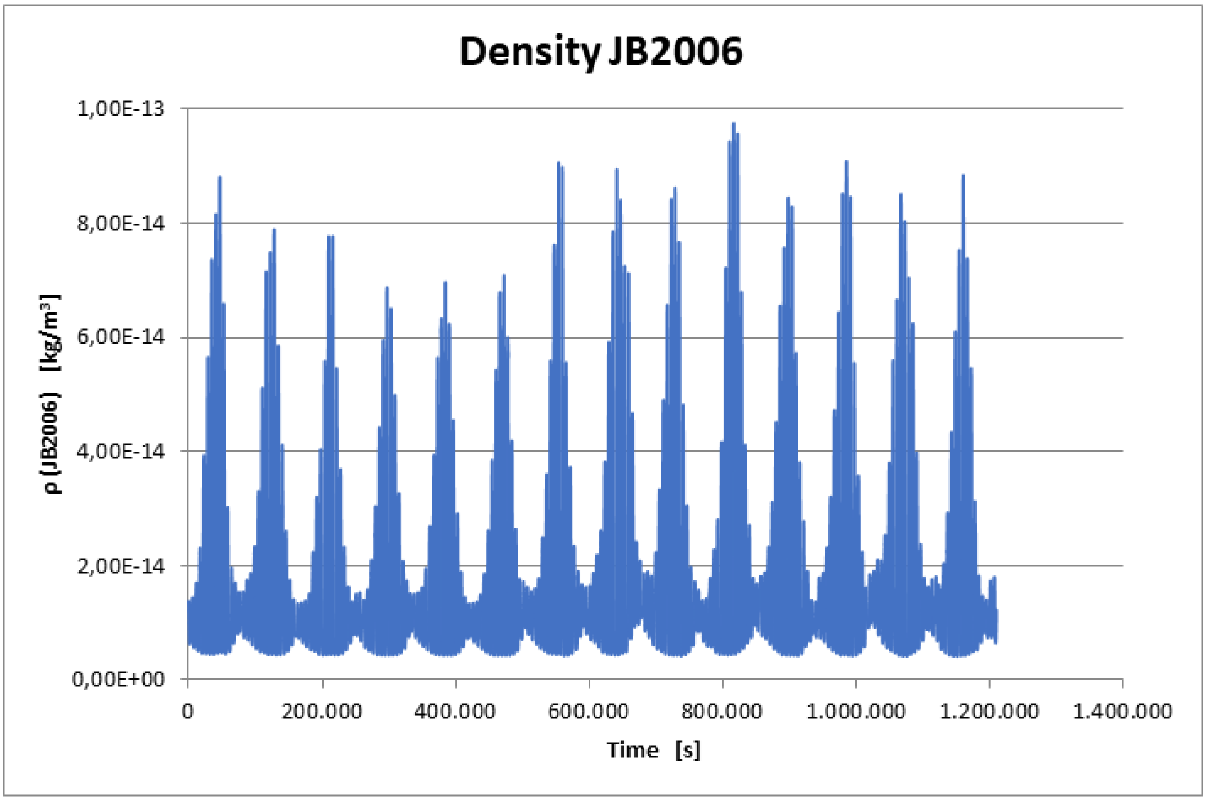

Chart 9.6 - Old JB2008

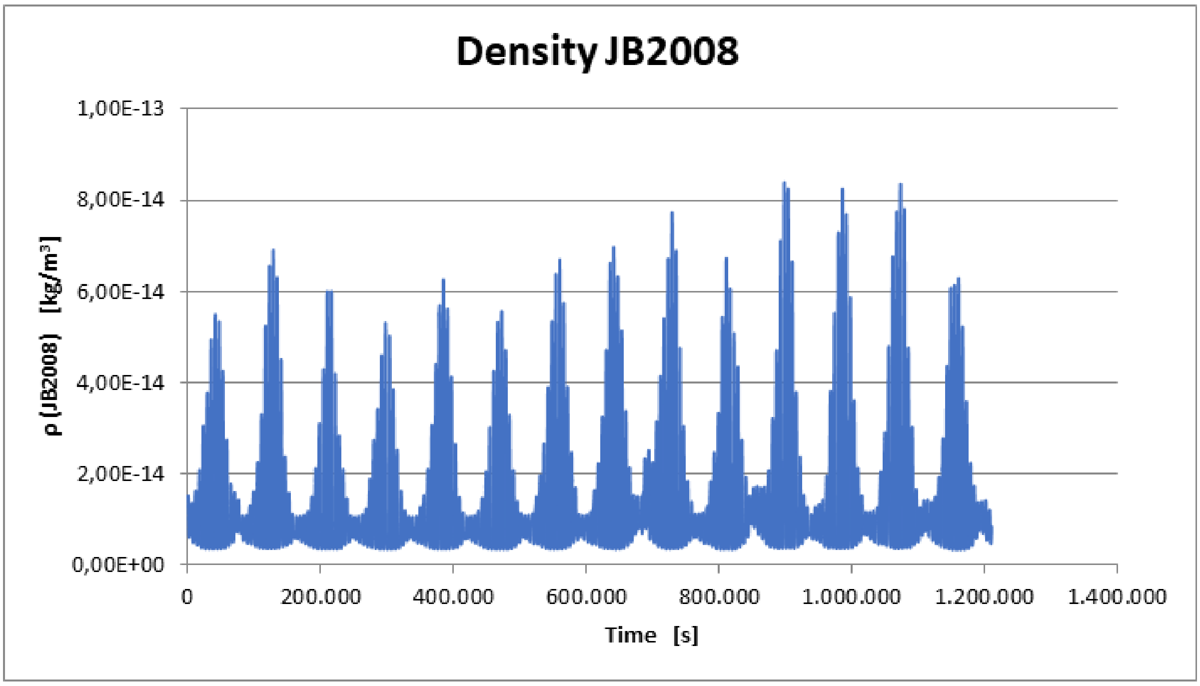

These two charts have been created as results of analyses made with solar indices values that are not up-to-date so they have not been taken into consideration.

Chart 9.7 - New JB2006 (e=0.001 and i=0°)

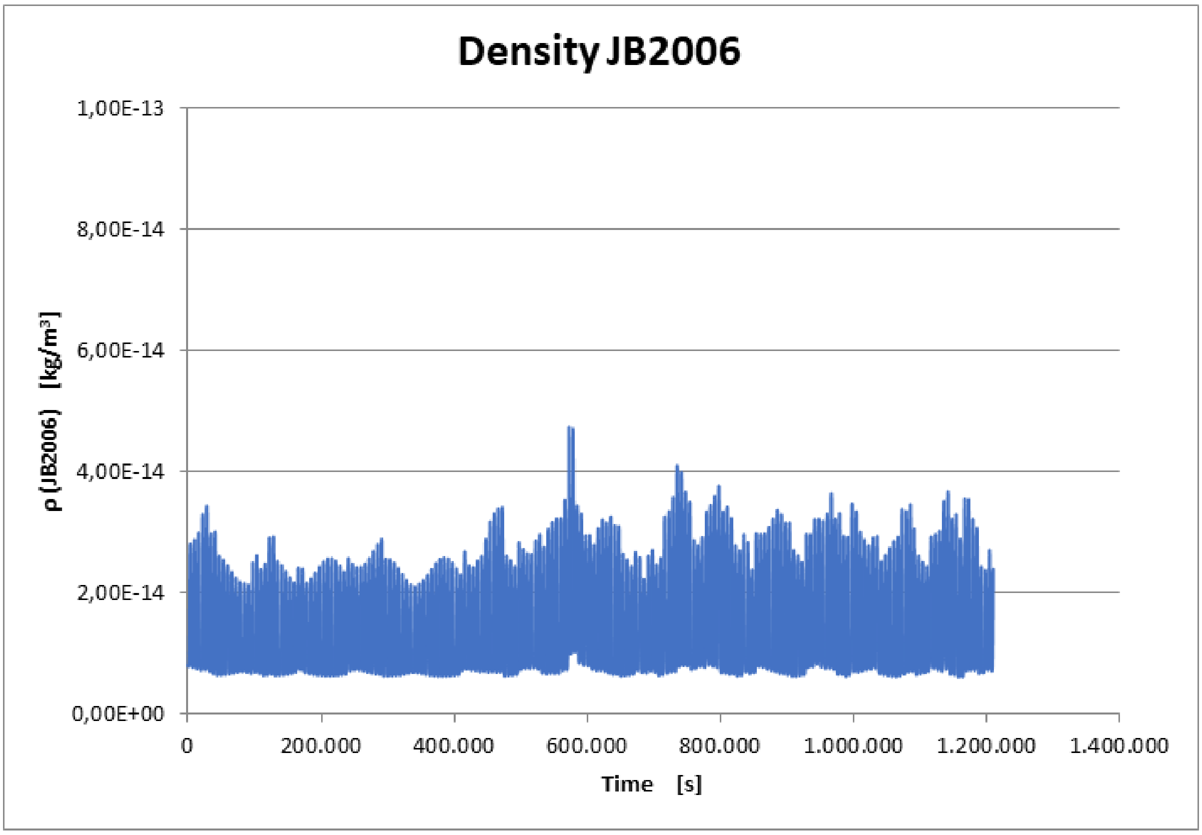

Chart 9.8 - New JB2006 (e=0.001 and i=60°)

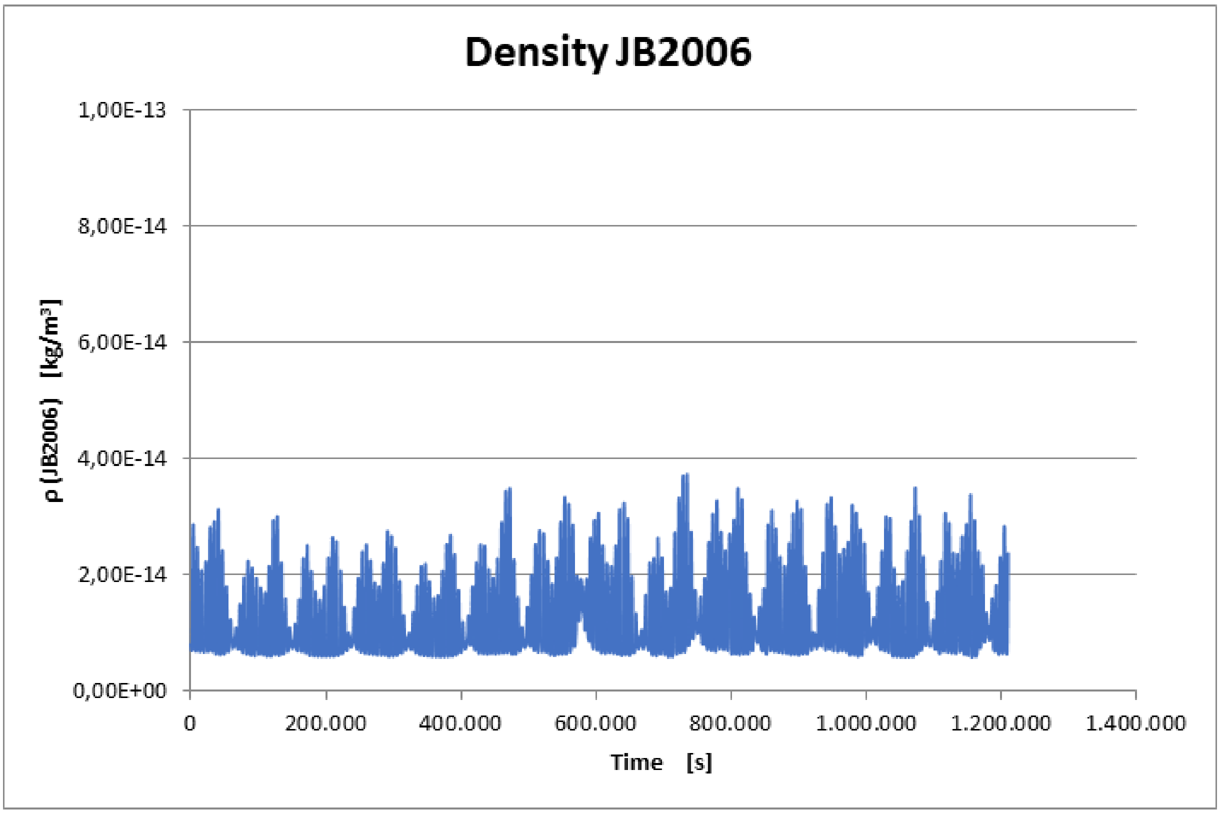

Chart 9.9 - New JB2006 (e=0.01 and i=60°)

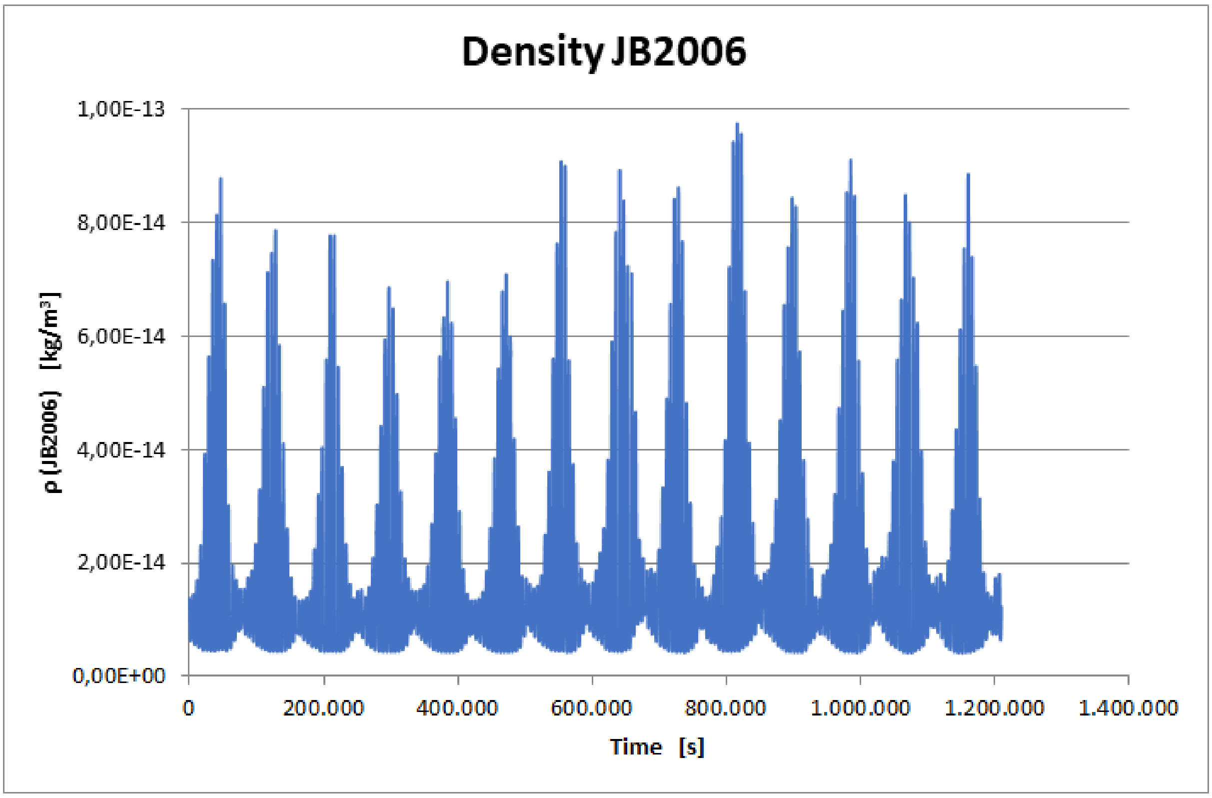

Chart 9.10 - New JB2008 (e=0.001 and i=0°)

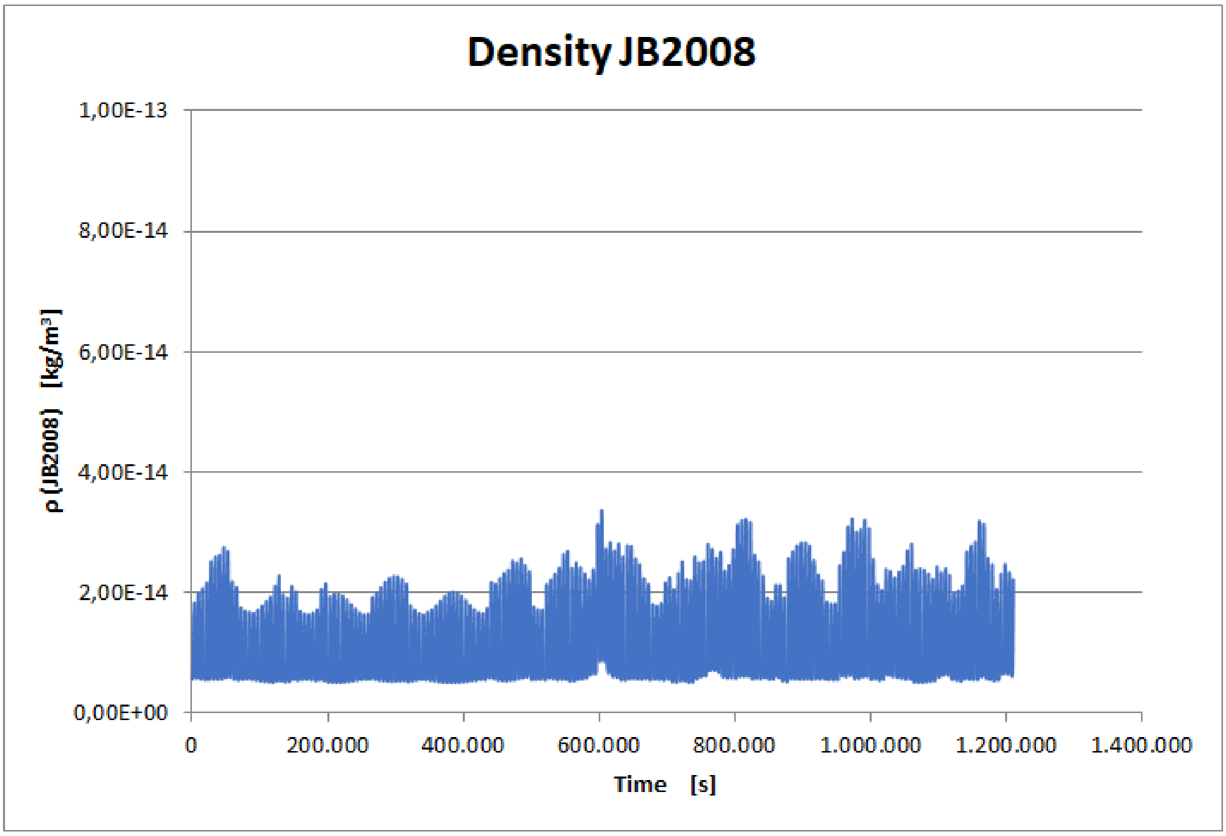

Chart 9.11 - New JB2008 (e=0.001 and i=60°)

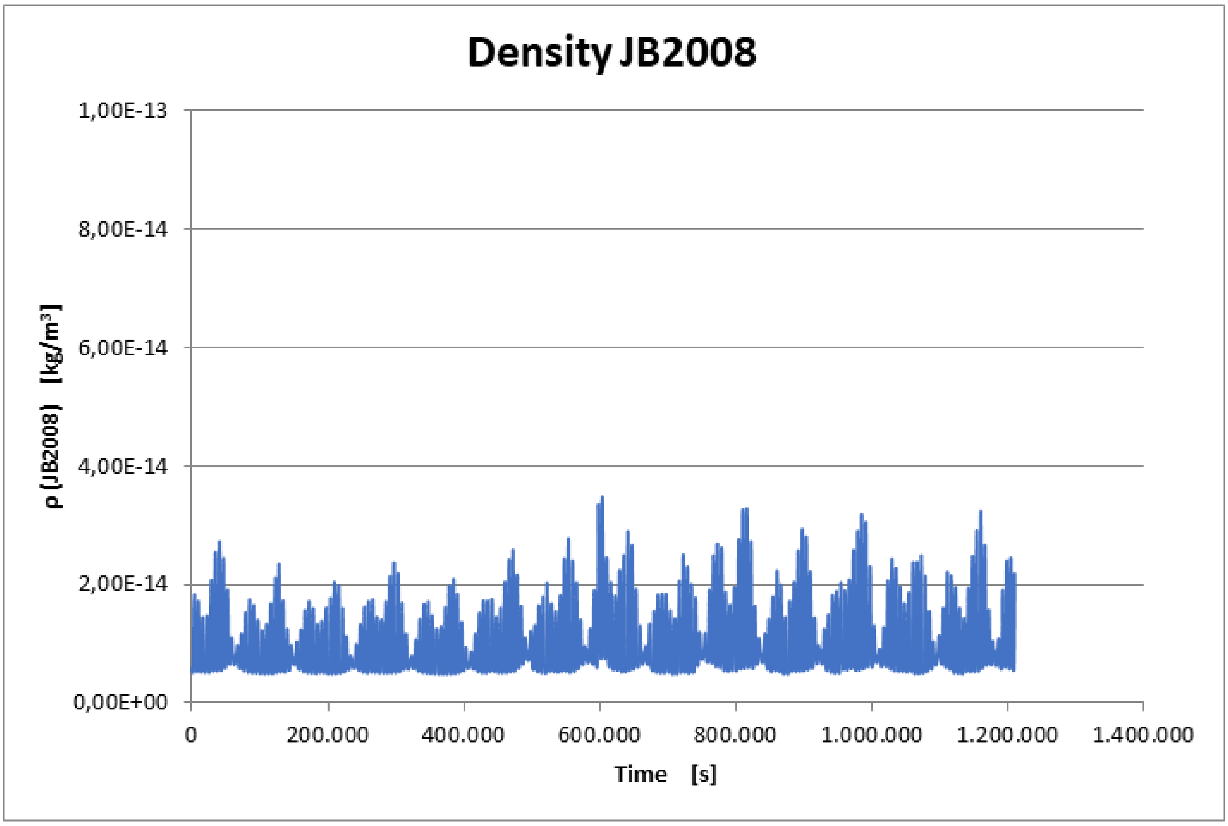

Chart 9.12 - New JB2008 (e=0.01 and i=60°)

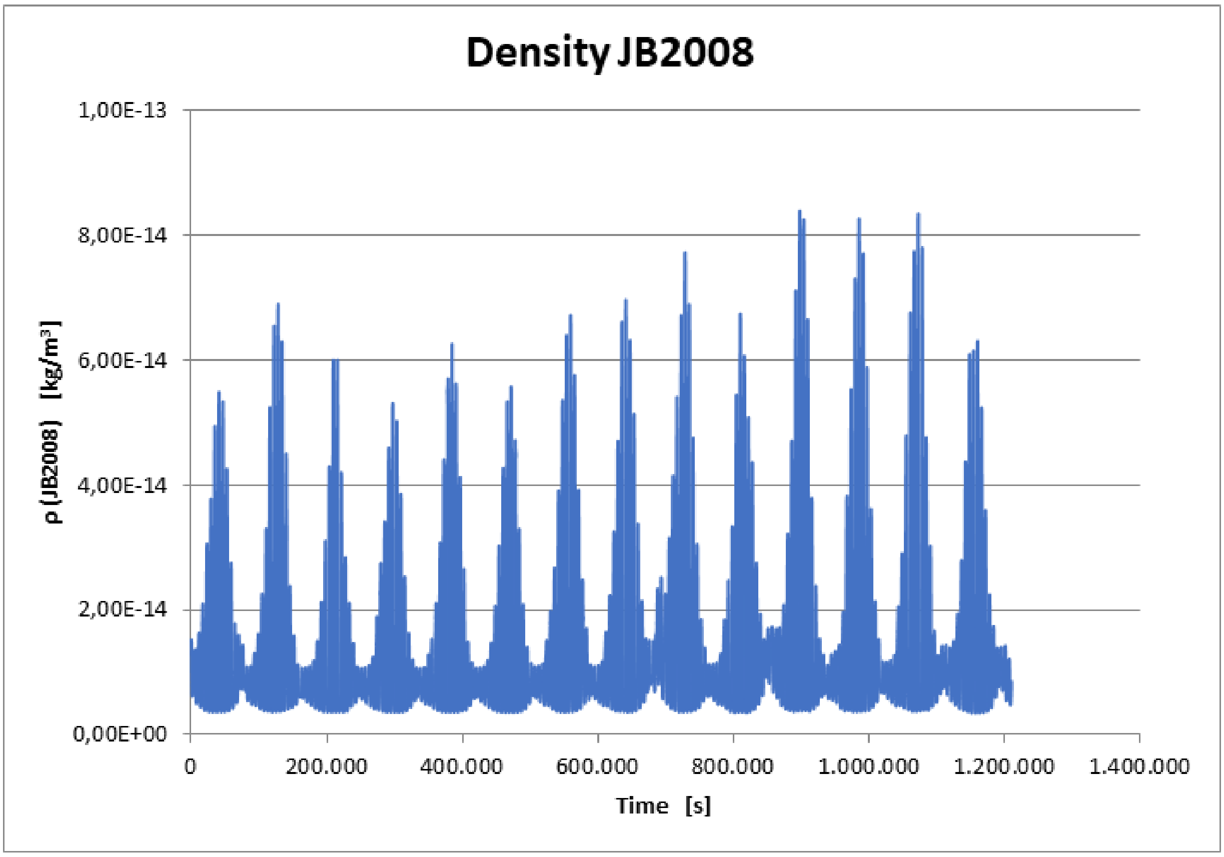

The above charts have been created as results of analyses made with solar indices up-to-date values.

Apparently, comparing the old charts (Chart 9.5 and Chart 9.6) with the relative new ones (Chart 9.9 and Chart 9.12), for both JB2006 and JB2008, we can say that there are no appreciable differences. The reason could be that the last time that the indices have been updated was only one year ago nearly, or less, by another trainee; however, because no solar burst or flare or magnetic storm happened, the indices' values have not greatly varied, leaving unchanged the values of models' density.

For example, Chart 9.10, Chart 9.11 and Chart 9.12 for JB2008 model should be taken into account. This model has been chosen because it proved to be the most accurate in recent years. Considering an orbit with null inclination and eccentricity close to zero (Chart 9.10) leads to a density variation that is quite constant with little oscillations; increasing the inclination up to 60 deg but leaving unchanged the eccentricity (Chart 9.11), leads to have some more prominent peaks of density with the feature of two peaks for each day. However, the values remain below $4 \cdot 10^{-14}$ kg/m^3. Now, increasing the eccentricity up to 0.01, thus having a more elliptic orbit, and leaving the inclination as before, 60 deg, the density peaks increase considerably and reach the value of $8 \cdot 10^{-14}$ kg/m^3 but with only one peak per day.

The previous argument can be adapted also to JB2006 model's charts (Chart 9.7, Chart 9.8 and Chart 9.9).

Moreover, comparing the new JB2006 and JB2008 charts (Chart 9.9 and Chart 9.12), it was noticed that the peaks, the gorges and the minimums occur approximately at the same position in time; the minimums have the same values instead the peaks are more different: for JB2006, there are many points over $8 \cdot 10^{-14}$ kg/m^3 arriving up to $1 \cdot 10^{-13}$ kg/m^3 instead in JB2008 it is hard to find a point above $8 \cdot 10^{-14}$ kg/m^3. The difference between these two models is displayed in Chart 9.15. The Chart 9.13 and Chart 9.14 are for the simulation with $e = 0.001$ and $i = 0°$; these charts have values that are much lower than those in Chart 9.15 with not very high peaks, where present, but in general, there are no peaks compared with those in Chart 9.15.

Chart 9.13 - Difference between JB2006 and JB2008 (e=0.001 and i=0°)

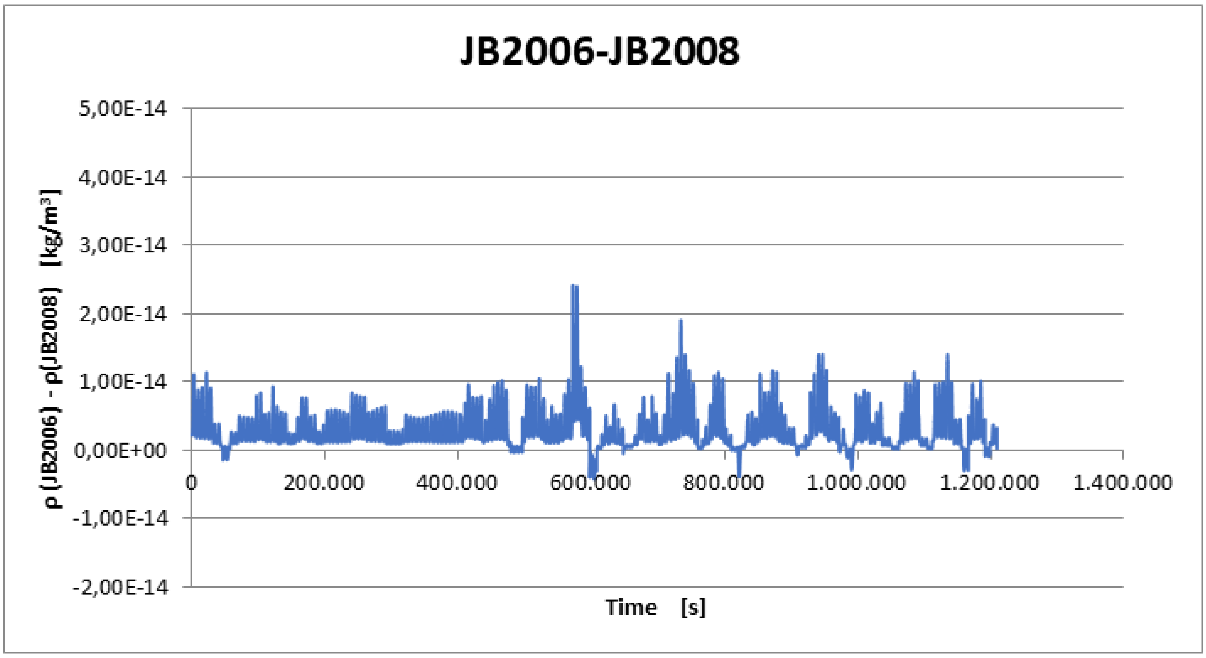

Chart 9.14 - Difference between JB2006 and JB2008 (e=0.001 and i=60°)

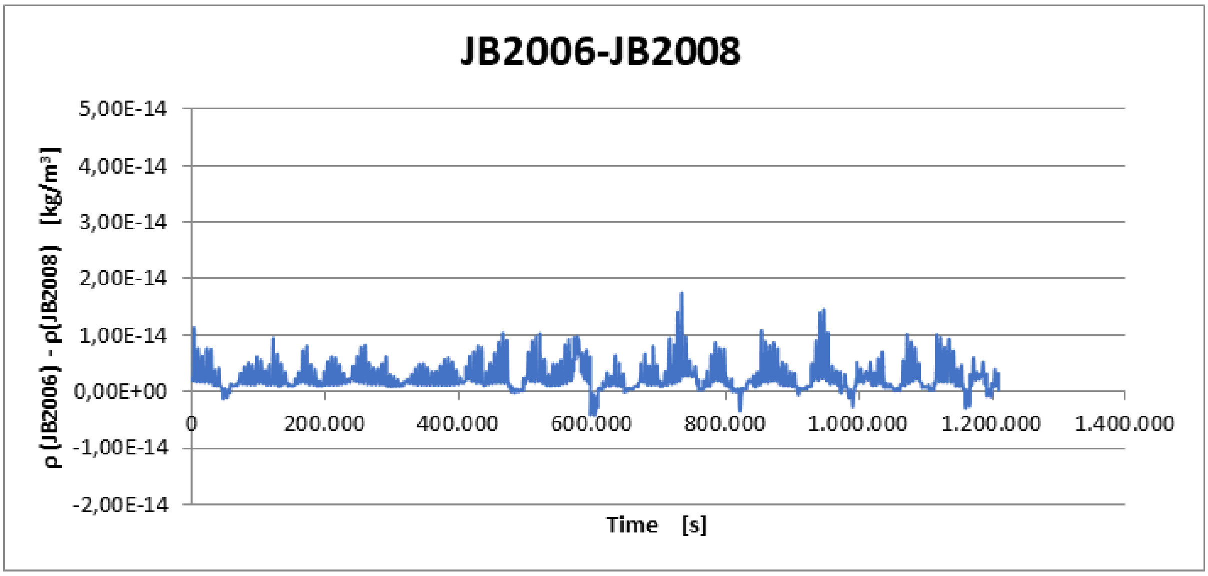

Chart 9.15 - Difference between densities of (new) JB2006 and JB2008 (e=0.01 and i=60°)

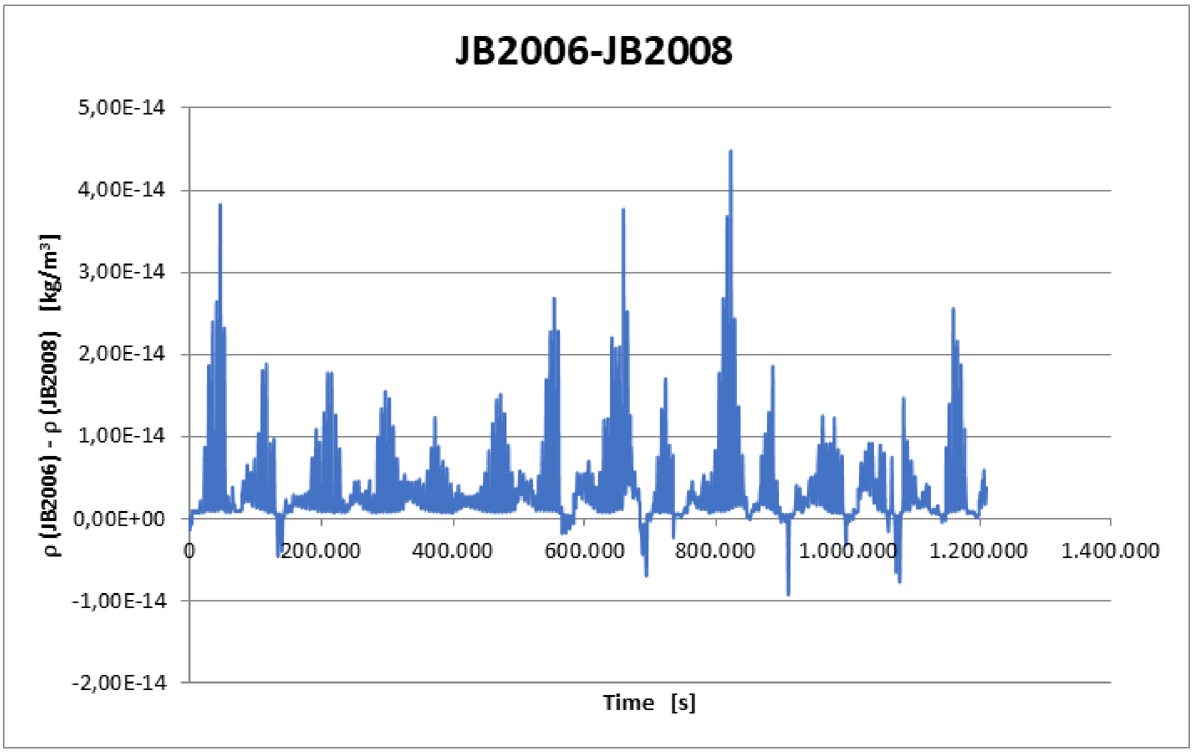

In all charts, if the difference is positive, it means that the density calculated with JB2006 model is higher than that calculated with JB2008 model; on the other hand, if the difference is negative, the JB2008 prevails. If the difference is zero, both models have the same density values. The major differences happen mostly during the peaks, especially in Chart 9.15, instead for the gorges or the minimums, the difference is almost null. In fact, the trend of Chart 9.9, for JB2006, is broadly reproduced.

Taking into account the chart of JB2008 density with updated indices (Chart 9.12), a deeper study was performed upon it. At first sight, 14 minimums and 14 peaks have been noticed. Knowing that the simulation lasts 1209600 s that are equal to 14 days, we can conclude that each minimum and peak together represent one day, i.e. 86400 s. For this reason, only a part of Chart 9.12 was taken, as the other has the same repetitive pattern. The result is shown below. Going deeper and deeper in the trend of one day, it was found that Chart 9.16 has between 14 and 15 maximums and minimums. Knowing that the orbital period of the satellite is

$$T = 2\pi\sqrt{\frac{a^3}{\mu}} = 5828.5\ s$$

where

$$a = 7000\ km \quad semi - major\ axis$$

$$\mu = 398600\,\frac{km^3}{s^2} \quad Earth\ gravitational\ parameter$$

dividing 86400 s by the orbital period T, the number of revolutions per day is found, that is 14.82 rev/day. Rounding this up or down, it is exactly the same number of minimums and maximums in Chart 9.16, as some of them are not very well defined. So we can conclude that the part of the chart peak-peak or gorge-gorge represents one orbit. In Chart 9.17 the trend of true anomaly is plotted. Comparing Chart 9.16 and Chart 9.17, it emerges that at the time when the true anomaly is zero (the satellite is at its perigee), the density is shortly after the peak, whereas, when the true anomaly is at its maximum positive or negative (+180°/-180°, the satellite is at its apogee), the corresponding density value is shortly after the minimum of the gorge. From these considerations, it was found that the orbit, intended as perigee-apogee-perigee, is represented by the gorge, or peak-peak. The fact that the density at perigee is higher than that at apogee is very significant because at perigee the satellite is much more into the atmosphere than at apogee. For this case, the apogee radius is $r_A = a(1+e) = 7070\ km$ instead the perigee radius is $r_P = a(1-e) = 6930\ km$ with a difference of 140 km from apogee to perigee. Moreover, over a day as displayed in Chart 9.16, the density fluctuate due to the variation of the geodetic altitude at which the satellite is, to the variation of the Local Solar Time during an orbit (for which the maximum of the density will be at 3 p.m.) and to the variation of the earthly spherical harmonics, because of the rotation of the Earth below the satellite; its oscillating motion is a superimposition of the effects of variable different elements that affect both the density and the motion of the satellite.

Chart 9.16 - Detail of new JB2008 density (86400 s, 1 day)

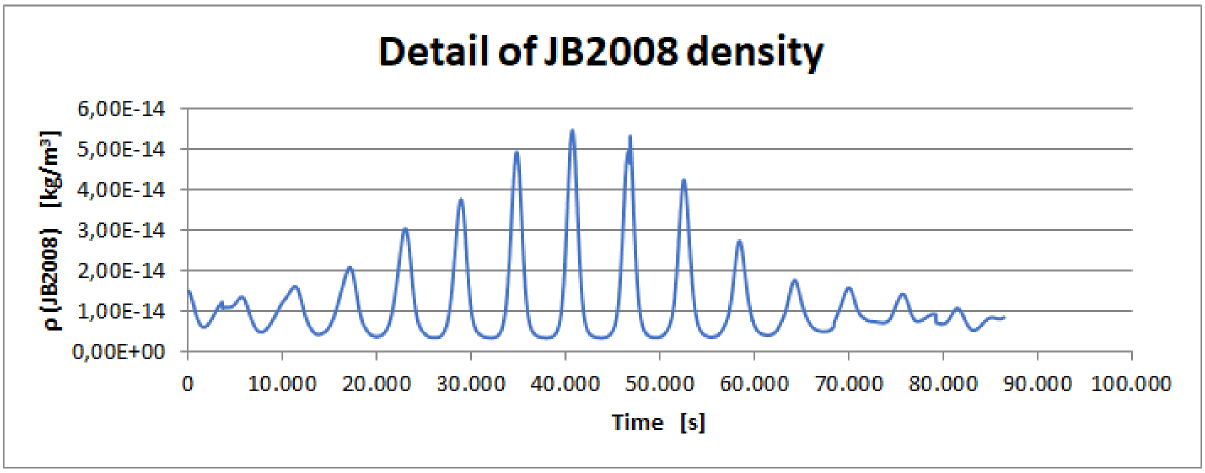

Chart 9.17 - True anomaly

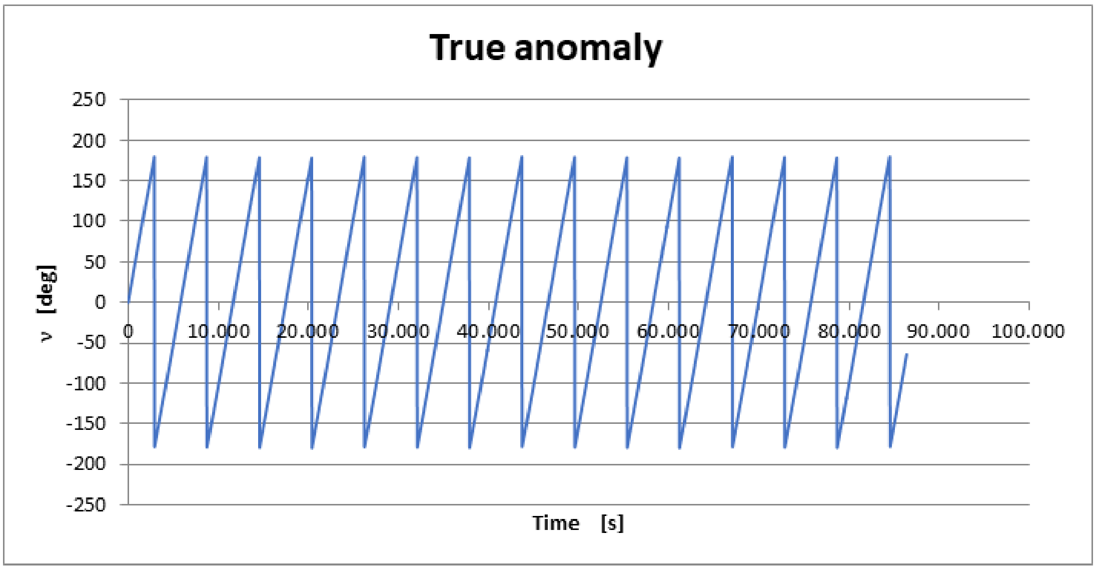

Another case is now taken into consideration; its orbital parameters and simulation features are displayed below:

Table 9.5 - Mission data for atmosphere model study during solar maximum

Quantity	Value	Unit of measure
Start date and hour	Oct 1st, 2025 @ 12:00:00	
Duration	6912000 (80 days)	s
Time step	30	s
Semi-major axis (a)	6643	km
Eccentricity (e)	0	
Inclination (i)	96.6	deg
Right Ascension of the Ascending Node (Ω)	0	deg
True anomaly (ν)	0	deg
Argument of perigee (ω)	0	deg
Perturbation	Atmosphere	
Atmosphere data		
Atmosphere model	JB2006/JB2008 for heights > 120 km	
	NRLMSISE-00 for heights < 120 km	
Drag calculation method	Basic formula	
Drag coefficient	2.2	
S/C cross section	1	m^2
S/C mass	1000	kg
Winds	no	

It was chosen the year 2025 as epoch of the simulation because there will be the maximum of the solar activity; moreover, the month of October was chosen due to the fact that in that period of the year the maximum of density occurs. The duration is longer than the previous one in order to visualize a more evident variation. The inclination angle was taken from the GOCE mission and for altitudes higher than 120 km the JB2006 model was selected to calculate the density.

Chart 9.18 – 2025 mission: JB2006 model density

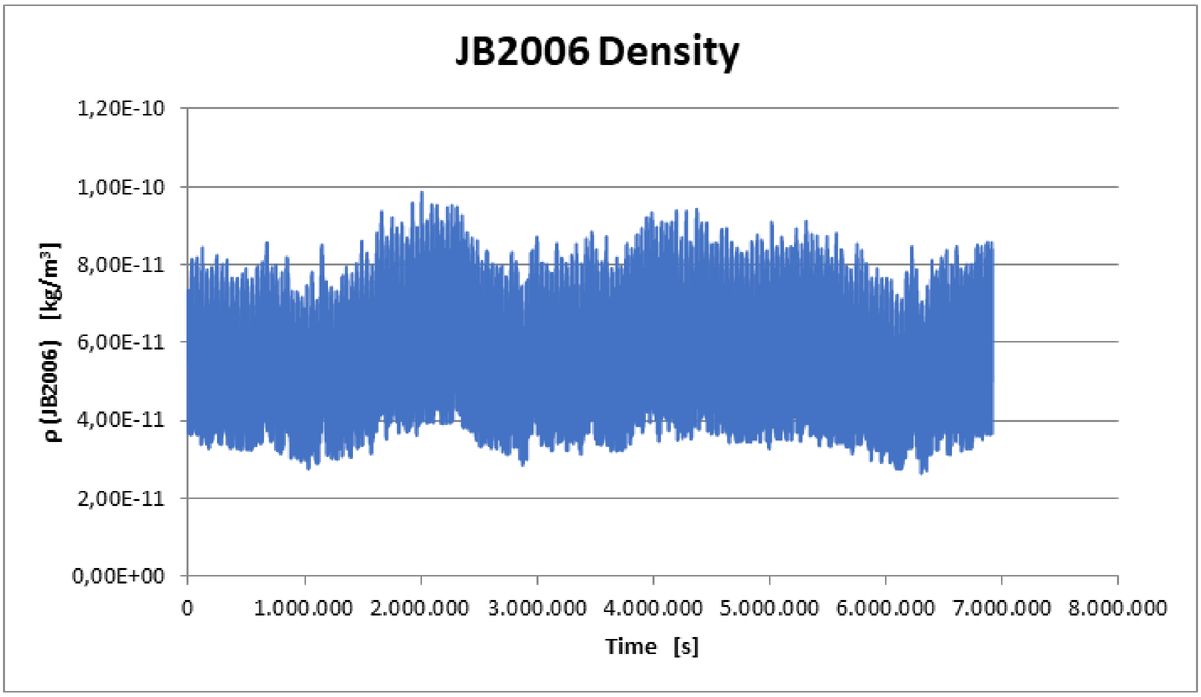

The major difference from the previous density charts is the order of magnitude of the density, that is consistent with the parameters of the simulation: in fact the Chart 9.18 density values are 3 times the density of the previous analyses as the height of the S/C passes from 622 km to 265 km. A typical value of density at this altitude is $5 \cdot 10^{-11}\ kg/m^3$ that is validated by official reports about GOCE mission, which was active in the same range of heights. Moreover, the analysis with the other model of atmosphere was done, in order to compare them.

Chart 9.19 - 2025 mission: JB2008 model density

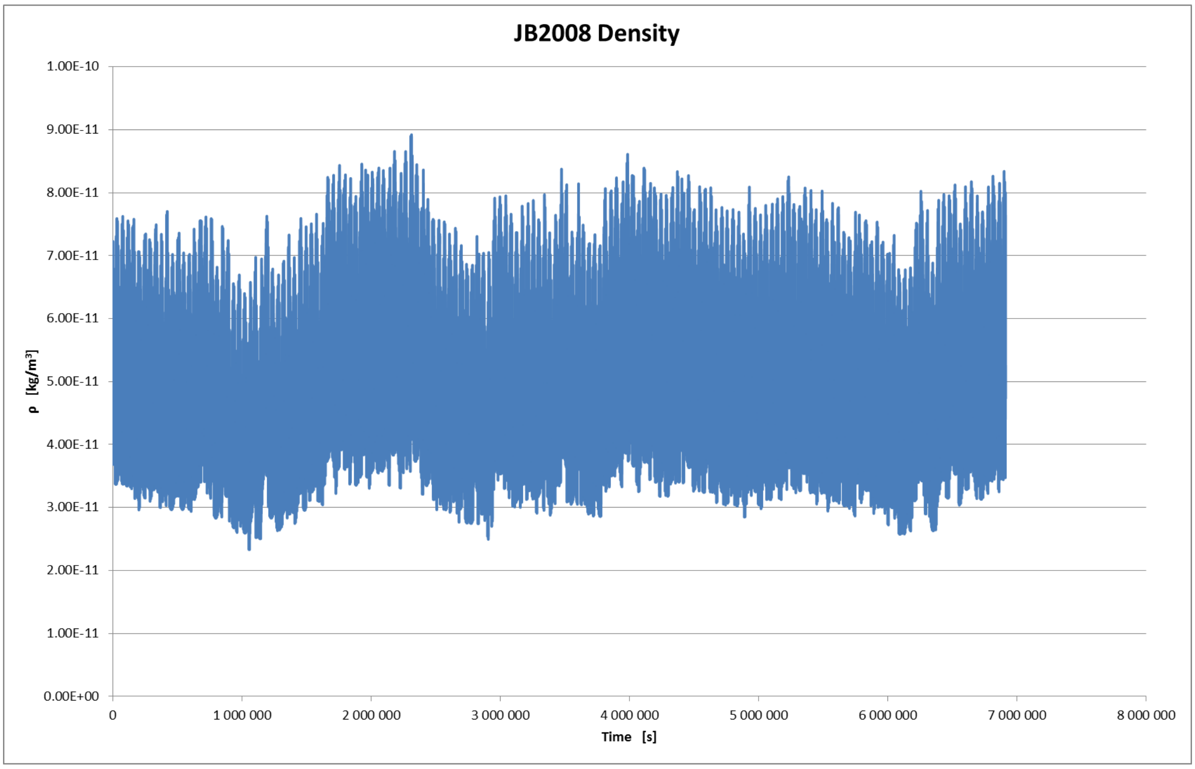

Chart 9.20 – 2025 mission: difference between densities of JB2006 and JB2008

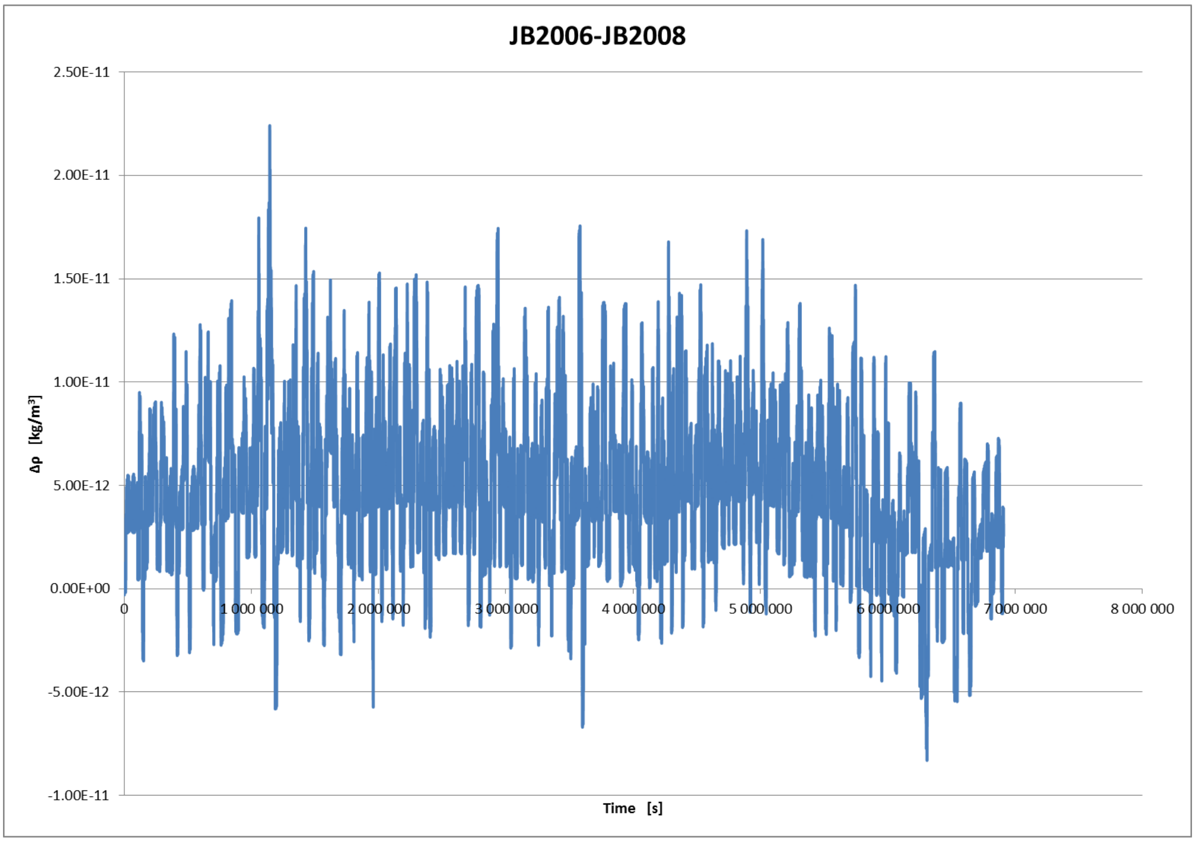

JB2008 seems to have lower values than those in Chart 9.18, which can be seen in Chart 9.20 where the majority of the values are positive. However, both models model the density in a correct way due to the fact that the Δρ has values of about $5.00 \cdot 10^{-12} \frac{km}{m^3}$, which is an order of magnitude smaller that the values of the models, that are approximately around $5.00 - 6.00 \cdot 10^{-12} \frac{kg}{m^3}$. Compared to Chart 9.13, more variation for the density values is evident, to be charged to the period of time in which the simulations develop.

9.1.5.3.1 Geomagnetic storms

To prove that both models correctly take into account strong magnetic storms, two more analyses, one for JB2006 and one for JB2008, were carried out during a particularly active period in the past, magnetically speaking. In this way, no forecast of indices is needed as they are already available for the entire period. This time frame was chosen in the DST file, downloaded from W. K. Tobiska's website, when DST index reached a high negative values, -370 nT. The period was found to be in the first half of November 2004, in particular the storm happened in the period November 8th – 11th, 2004. Thus, the mission data are the same as those in Table 9.4 but the start date was set as November 1st, 2004 @ 00:00:00 UTC and the end is 14 days later, thus covering all the time period in which the storm happens. Along with these analyses, four more simulations have been done to verify the effects of the inclination and of the eccentricity. As in the above part, all the analyses have the same mission data as in Table 9.4 but two of them change the eccentricity by setting it to 0.001 and the other two add the null inclination to the previous eccentricity change; each case has been done for both atmosphere model, JB2006 and JB2008.

Chart 9.21 - Magnetic storm density JB2006 (e=0.001 and i=0°)

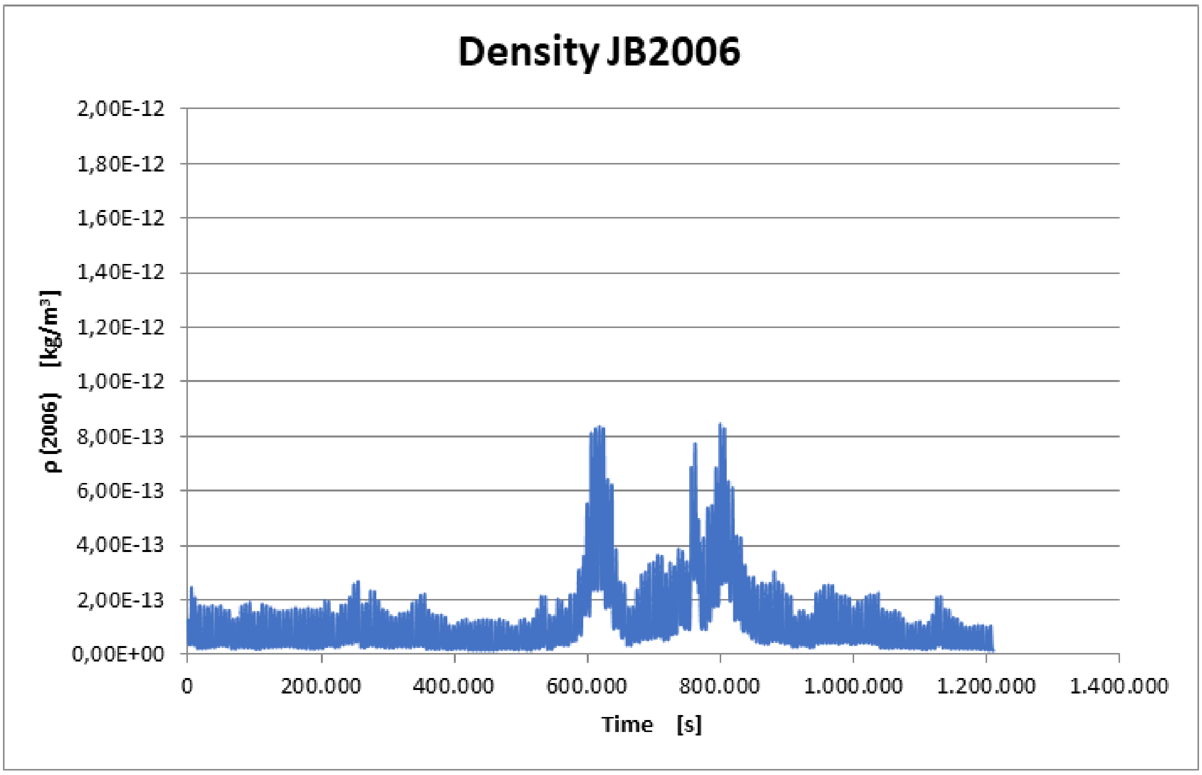

Chart 9.22 - Magnetic storm density JB2006 (e=0.001 and i=60°)

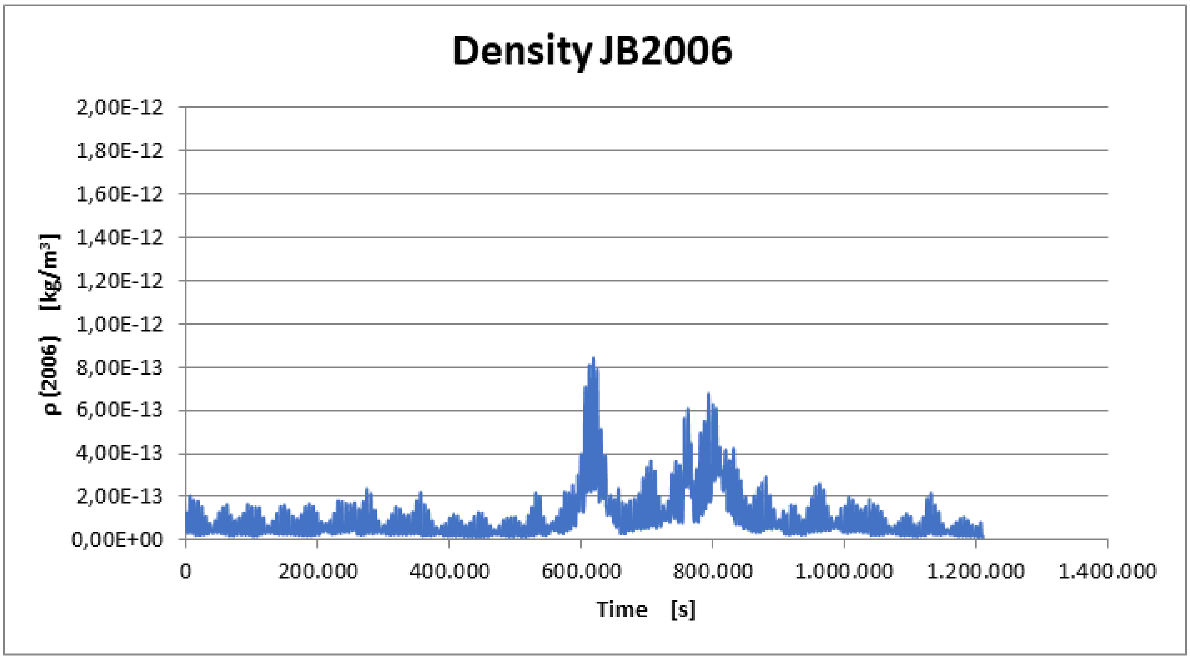

Chart 9.23 - Magnetic storm density JB2006 (e=0.01 and i=60°)

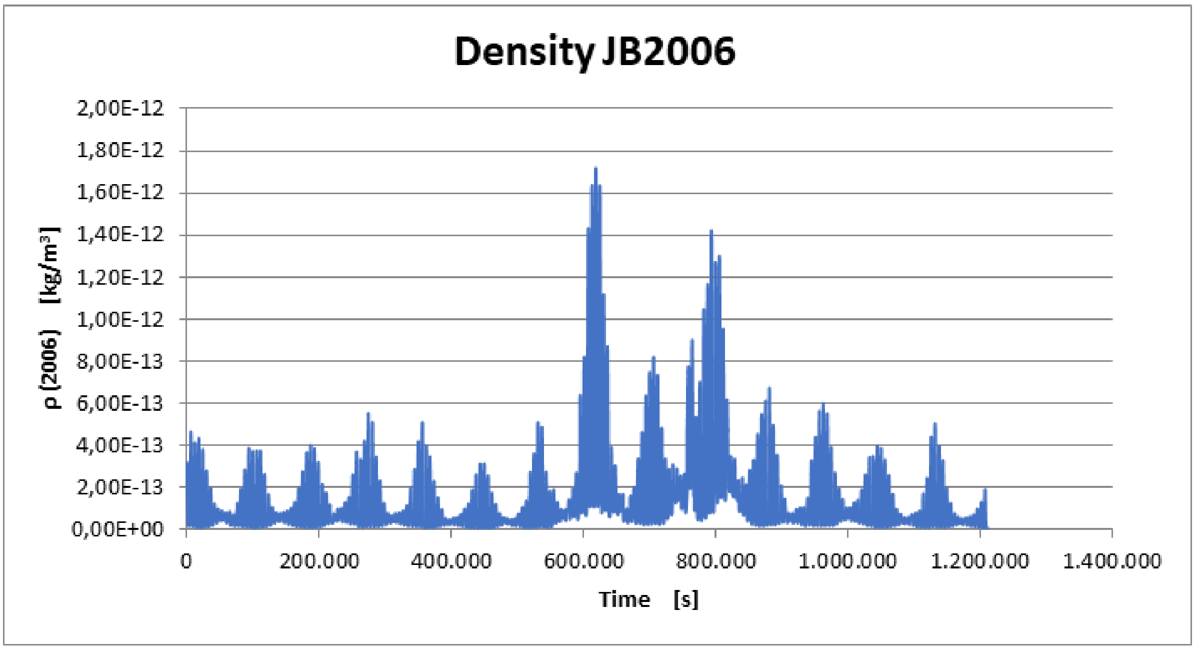

Chart 9.24 - Magnetic storm density JB2008 (e=0.001 and i=0°)

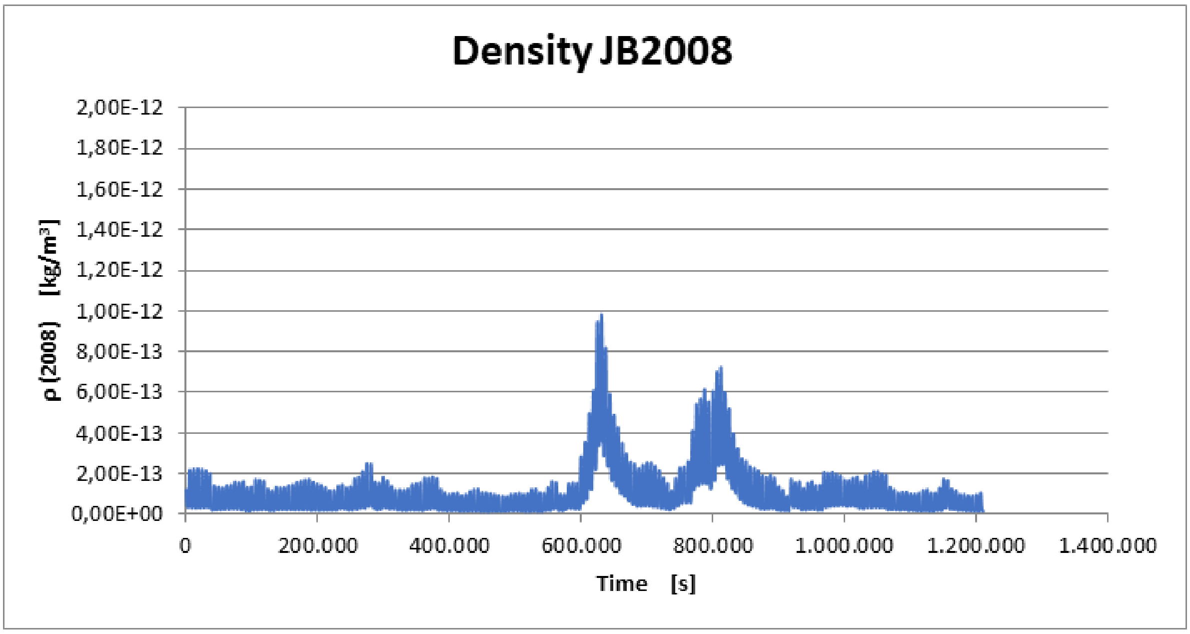

Chart 9.25 - Magnetic storm density JB2008 (e=0.001 and i=60°)

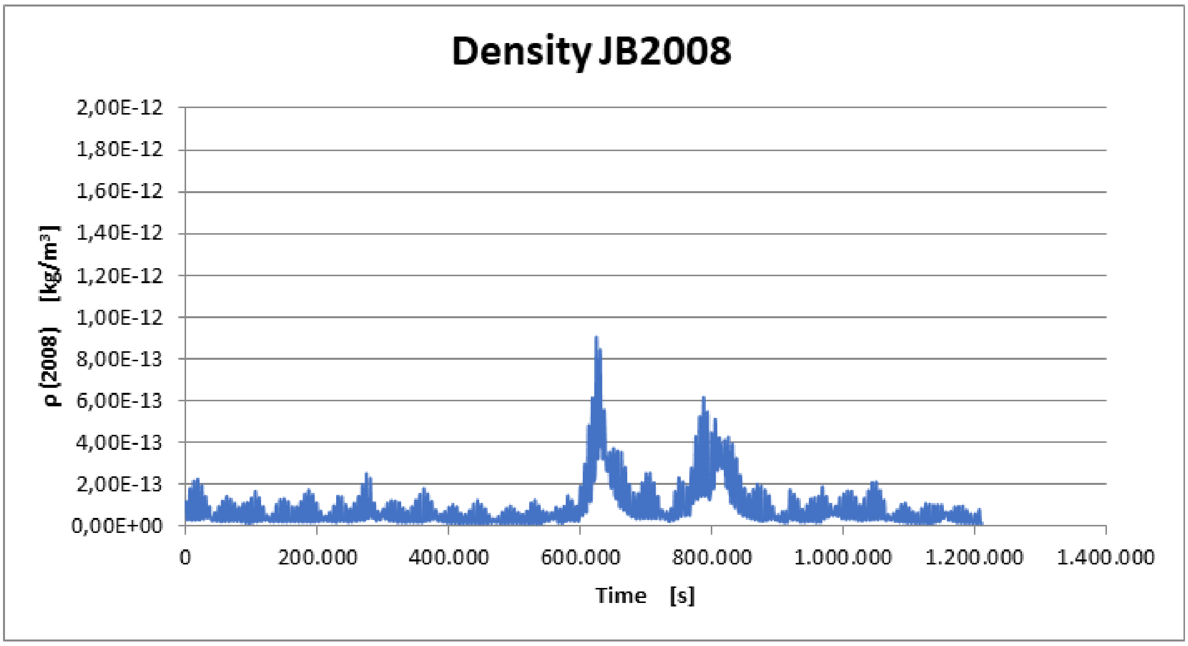

Chart 9.26 - Magnetic storm density JB2008 (e=0.01 and i=60°)

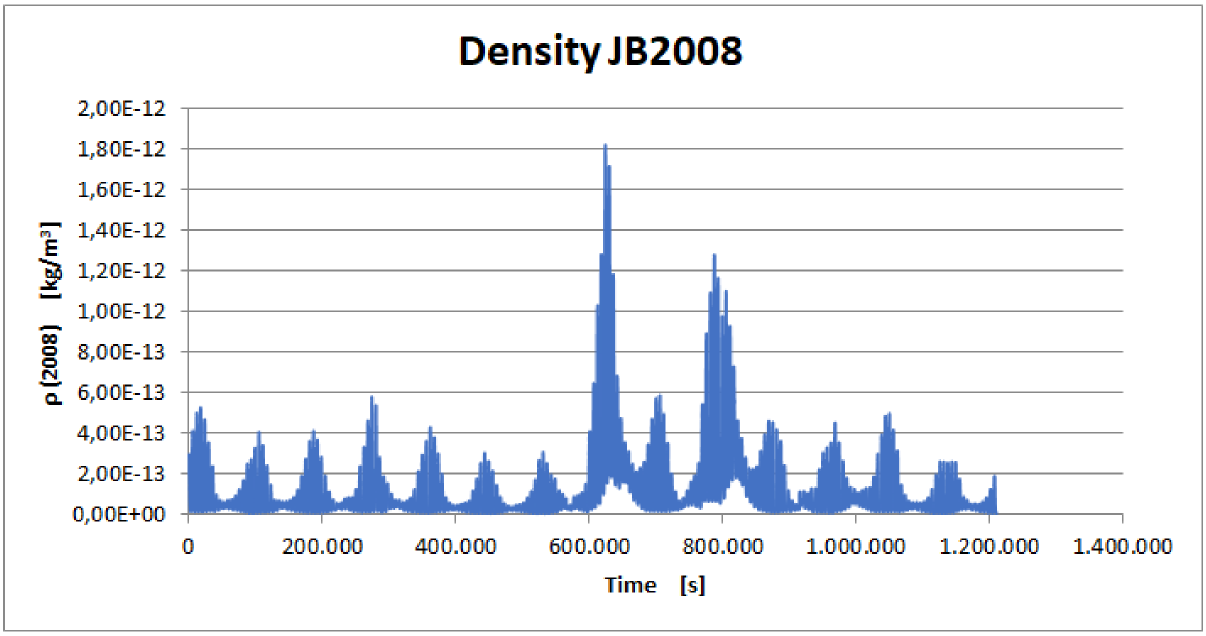

Chart 9.27 - Magnetic storm density difference (JB2006 - JB2008) with e=0.001 and i=0°

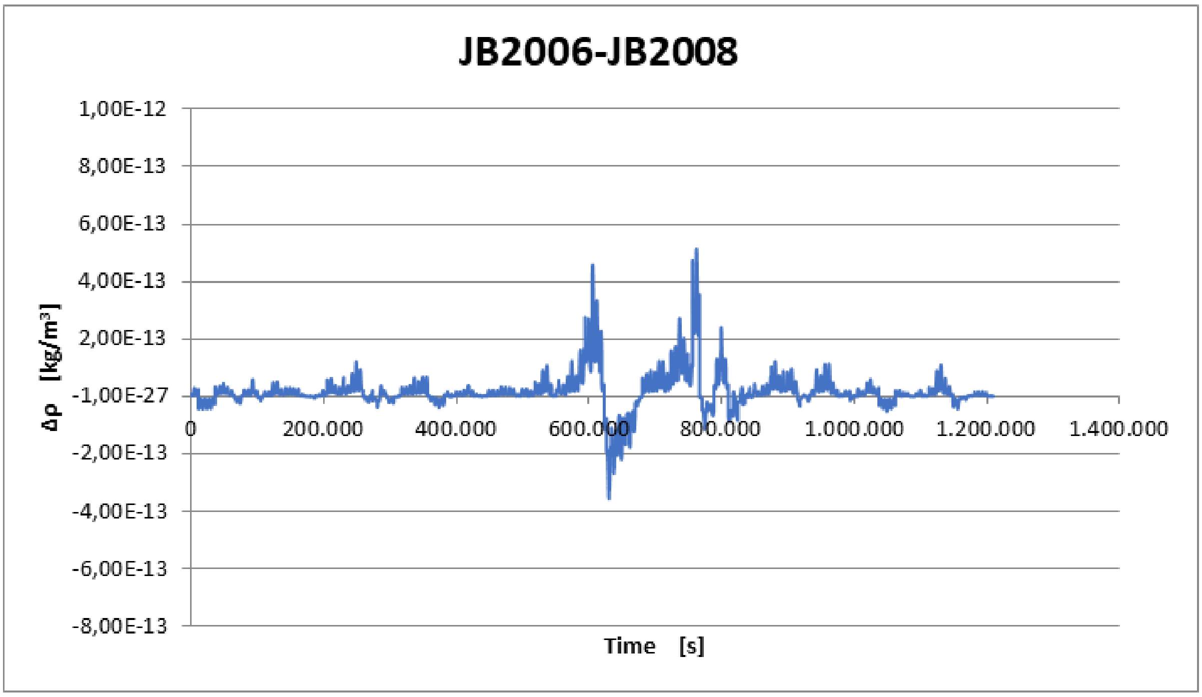

Chart 9.28 - Magnetic storm density difference (JB2006 - JB2008) with e=0.001 and i=60°

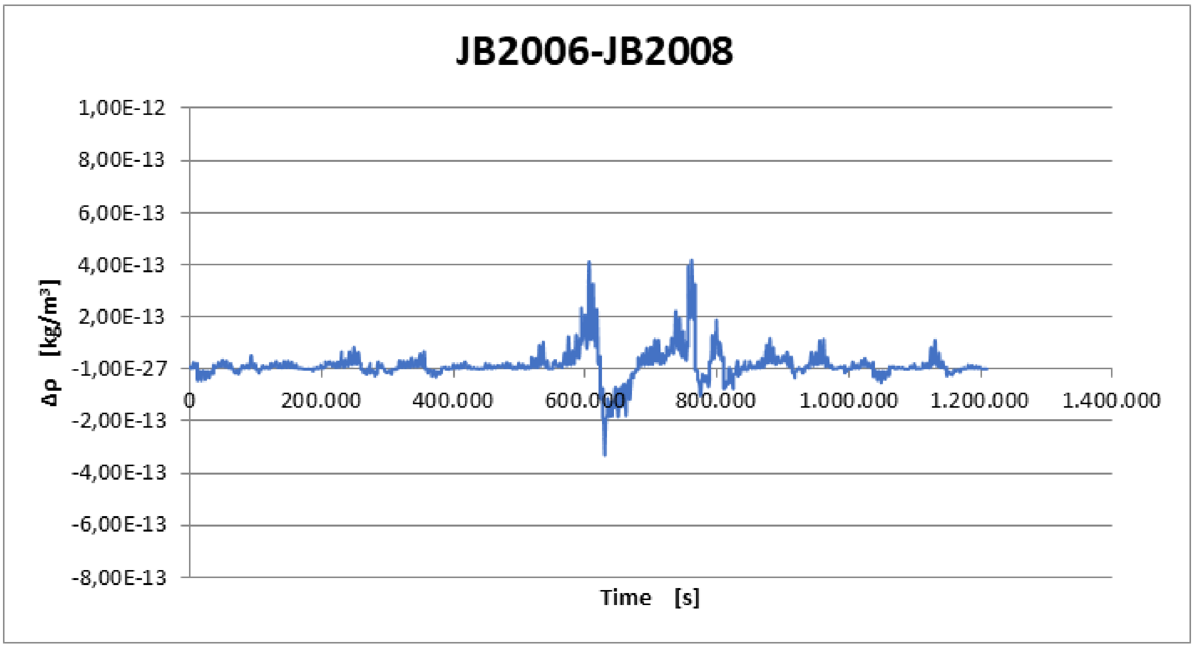

Chart 9.29 - Magnetic storm density difference (JB2006 - JB2008) with e=0.01 and i=60°

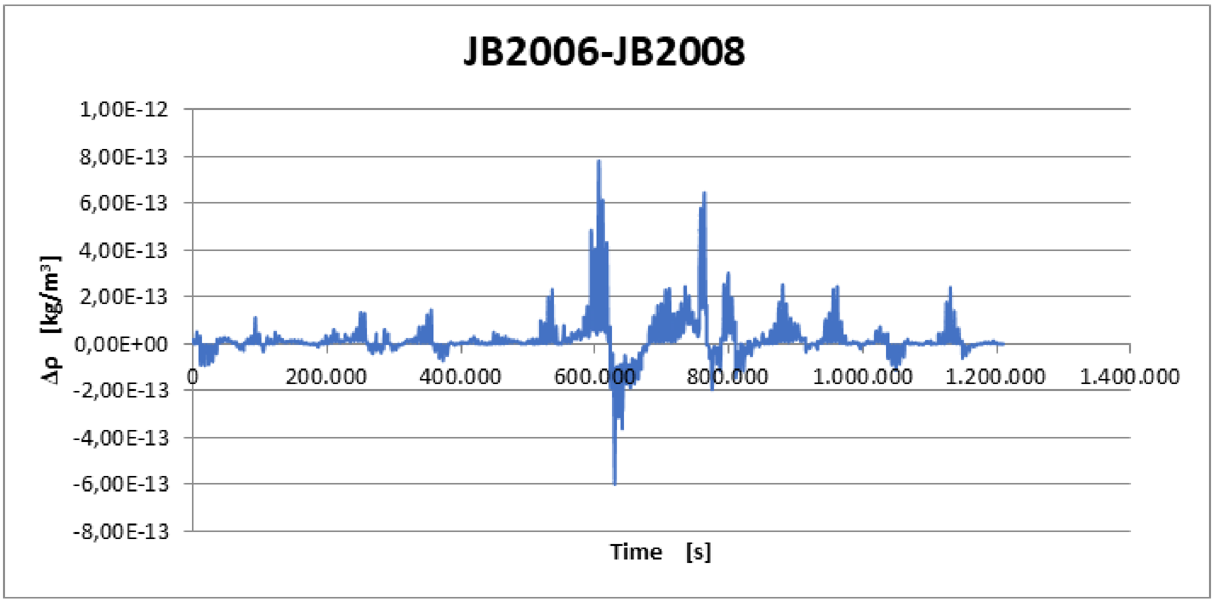

Chart 9.30 - Detail of JB2008 density (kg/m^3) in function of time (s) during storm

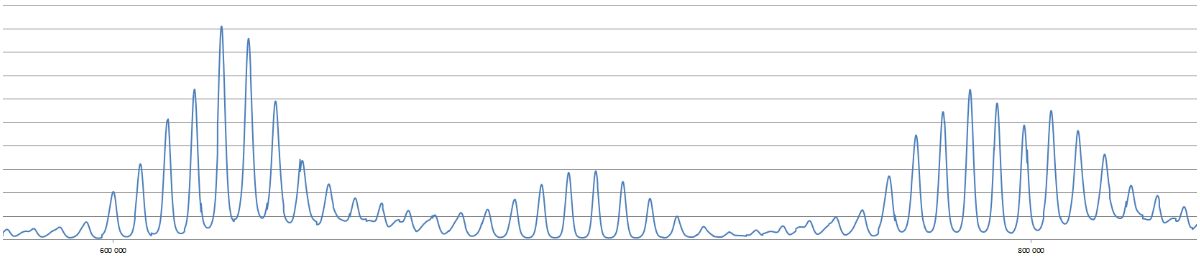

Table 9.6 - DST values November 1st-14th, 2004 with highlighted storm period

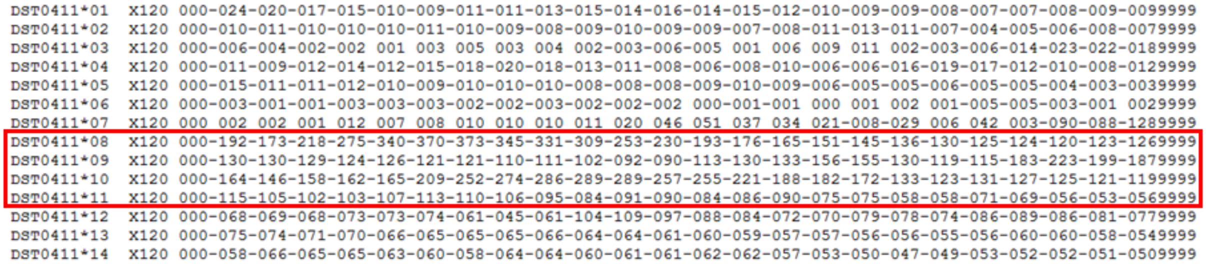

```
DST0411*01  X120 000-024-020-017-015-010-009-011-011-013-015-014-016-014-015-012-010-009-009-008-007-007-008-009-0099999
DST0411*02  X120 000-010-011-010-010-010-011-010-009-008-009-010-009-009-007-008-011-013-011-007-004-005-006-008-0079999
DST0411*03  X120 000-006-004-002-002 001 003 005 003 004 002-003-006-005 001 006 009 011 002-003-006-014-023-022-0189999
DST0411*04  X120 000-011-009-012-014-012-015-018-020-018-013-011-008-006-008-010-006-006-016-019-017-012-010-008-0129999
DST0411*05  X120 000-015-011-011-012-010-009-010-010-010-008-008-008-009-010-009-006-005-005-006-005-005-004-003-0039999
DST0411*06  X120 000-003-001-001-003-003-003-002-002-003-002-002-002 000-001-001 000 001 002 001-005-005-003-001 0029999
DST0411*07  X120 000 002 002 001 012 007 008 010 010 010 011 020 046 051 037 034 021-008-029 006 042 003-090-088-1289999
DST0411*08  X120 000-192-173-218-275-340-370-373-345-331-309-253-230-193-176-165-151-145-136-130-125-124-120-123-1269999
DST0411*09  X120 000-130-130-129-124-126-121-121-110-111-102-092-090-113-130-133-156-155-130-119-115-183-223-199-1879999
DST0411*10  X120 000-164-146-158-162-165-209-252-274-286-289-289-257-255-221-188-182-172-133-123-131-127-125-121-1199999
DST0411*11  X120 000-115-105-102-103-107-113-110-106-095-084-091-090-084-086-090-075-075-058-058-071-069-056-053-0569999
DST0411*12  X120 000-068-069-068-073-073-074-061-045-061-104-109-097-088-084-072-070-079-078-074-086-089-086-081-0779999
DST0411*13  X120 000-075-074-071-070-066-065-065-065-066-064-064-061-060-059-057-057-056-056-055-056-060-060-058-0549999
DST0411*14  X120 000-058-066-065-065-063-060-058-064-064-060-061-061-062-062-057-053-050-047-049-053-052-052-051-0509999
```

As an example for the exposition below, Chart 9.24, Chart 9.25 and Chart 9.26 have been taken into consideration as they are representative of the behaviour of JB2008. It was noticed that for quiet conditions, before and after the storm, the level of density remains quite constant and similar to Chart 9.10, Chart 9.11 and Chart 9.12 respectively and thus, increasingly sharp density maximums are seen as passing from Chart 9.24 to Chart 9.26 through Chart 9.25. Looking on the general trend of the charts, it was noticed that the density values of the analyses under active magnetic conditions are much higher, about one order of magnitude, than those under quiet solar conditions.

Some peaks are much higher than others, exactly during storms, and, comparing them with charts under quiet solar conditions, the two storm peaks were not present but the heights of the quiet condition peaks were almost the same for the entire period of analysis; these features verify that the model feels the effects of the magnetic storms very well, which correspond to a major increase in the density values, for both the maximums and for the minimums. In fact, minimums, during storms, have not the same values as in quiet conditions, but higher, and this depicts once more the effect of the geomagnetic event, as displayed in Chart 9.30. Hence, the first peak happens exactly when the storm has begun, on November 8th; the storm finishes after two peaks, on November 11th, as the values in Table 9.6 confirm.

What previously stated is valid also for the analyses with JB2006 model, which have the same trend as those of JB2008.

For each analyses under storm conditions, we should say that both models have the same values as visualized in Chart 9.27, Chart 9.28 and Chart 9.29 because the differences tend to zero, except for the period of storm when there are the major differences between the models.

All the three charts have the same trend and nearly the same values, except Chart 9.29 that has the sharpest peaks during the storm period.

By the end, we can state that, taking into consideration the fact that JB2008 model is more accurate than JB2006, as described in previous chapter, in Chart 9.27, Chart 9.28 and Chart 9.29 it is displayed that if the difference is positive, the JB2006 has major values than JB2008 and so JB2006 overestimates the atmosphere density for the greatest part of the analysis, as negative differences are very few.

9.1.6 Complete analyses

After some corrections, some analyses were done with three types of perturbations: geopotential, third body and atmosphere drag. Hereunder the mission data are shown.

Table 9.7 - Mission data for complete analyses

Quantity	Value	Unit of measure
Start date and hour	Dec 7th, 2020 @ 12:00:00	
Duration	604800 (7 days)	s
	2592000 (30 days)	s
	15552000 (180 days/6 months)	s
Time step	60	s
Semi-major axis	7000	km
Eccentricity	0.01	
Inclination	60	deg
Right Ascension of the Ascending Node	0	deg
True anomaly	0	deg
Argument of perigee	0	deg
Perturbations	Geopotential (EIGEN-GL04C)	
	Atmosphere	
	Third body (Sun, Moon)	
Atmosphere data		
Atmosphere model	NRLMSISE00	
Drag calculation method	Basic formula	
Drag coefficient	2.2	
S/C mass	1000	kg
Winds	no	

The resulting plots are displayed below.

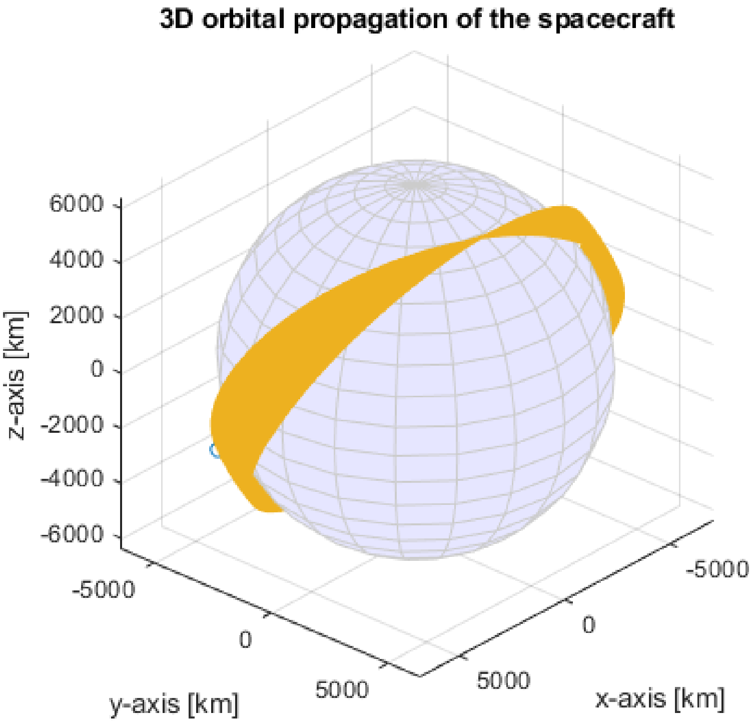

Figure 9.15 – 7 days

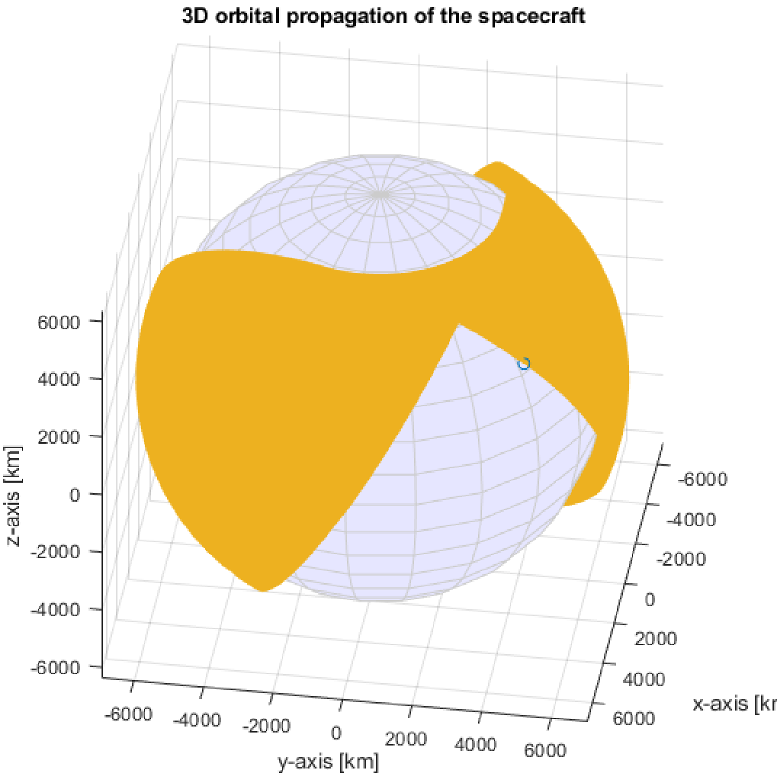

Figure 9.16 – 1 month

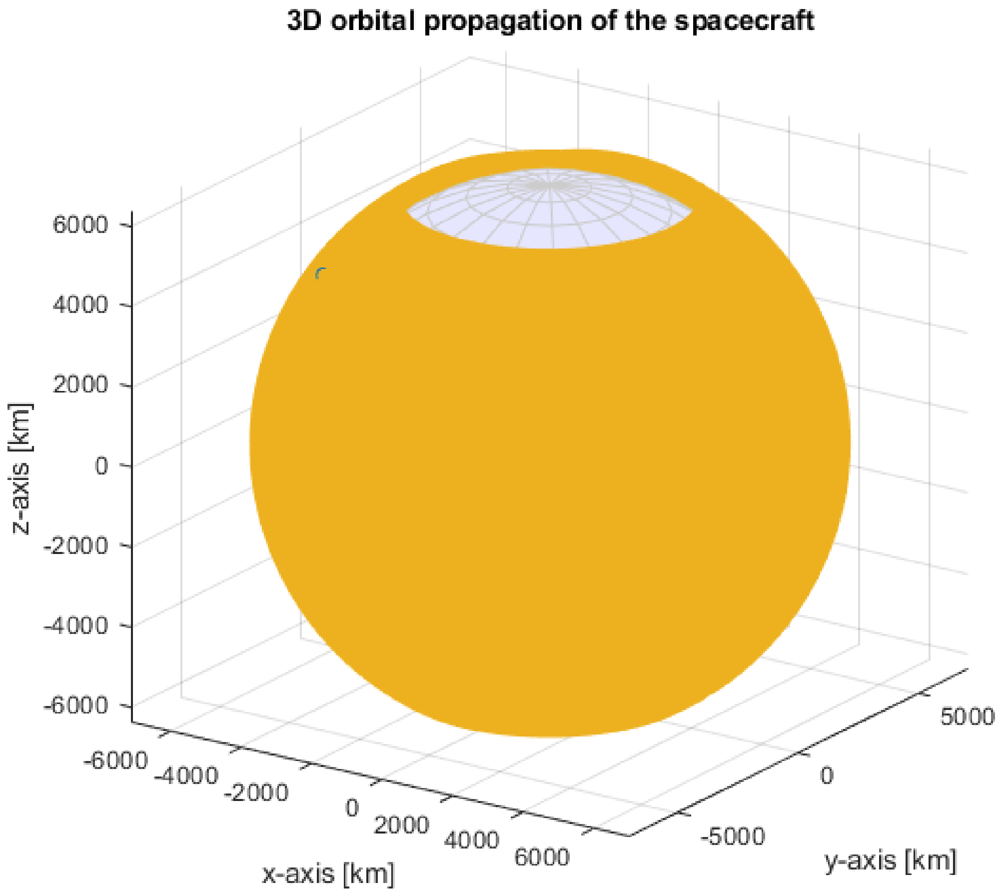

Figure 9.17 – 6 months

Later, using an Excel spreadsheet, the trends of some important orbital elements have been visualized.

Chart 9.31 - 7 days semi-major axis

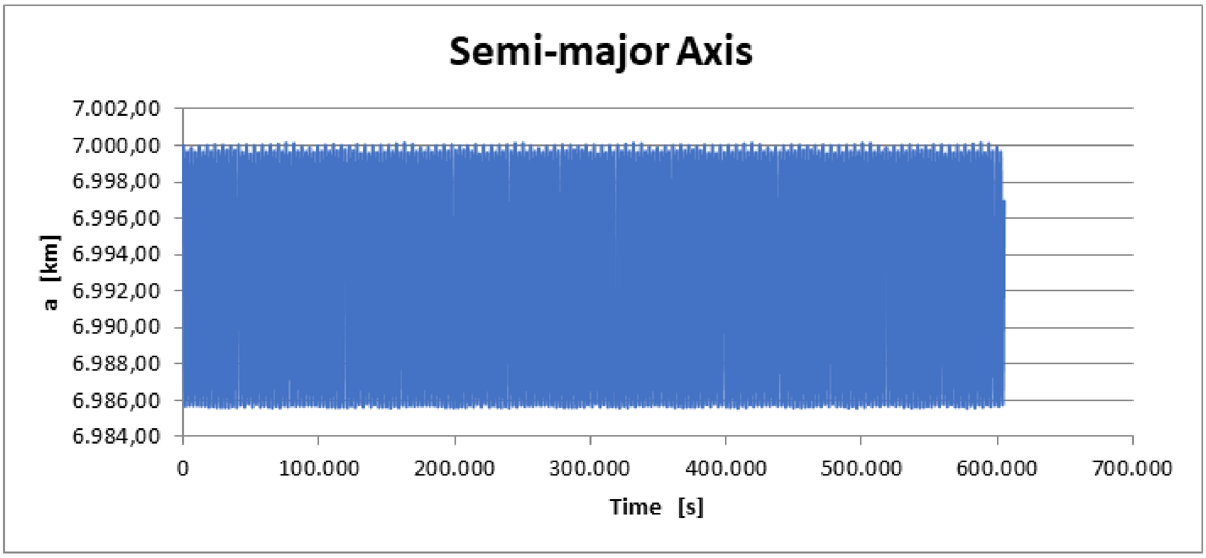

Chart 9.32 - 1 month semi-major axis

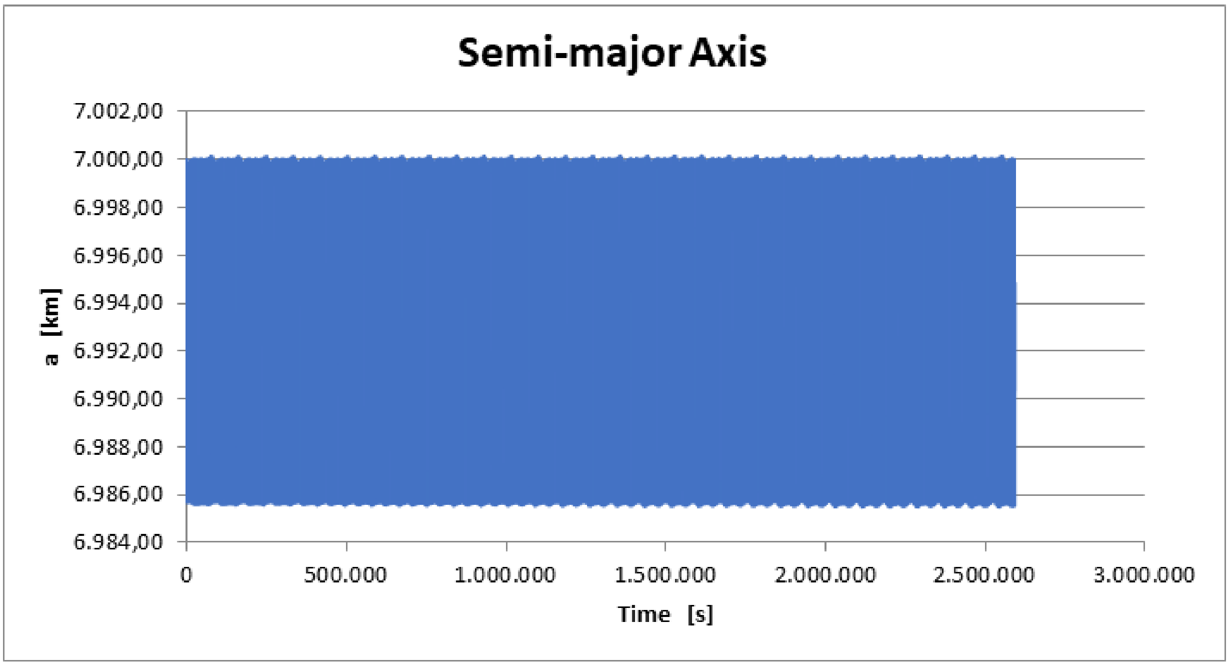

Chart 9.33 - 6 months semi-major axis

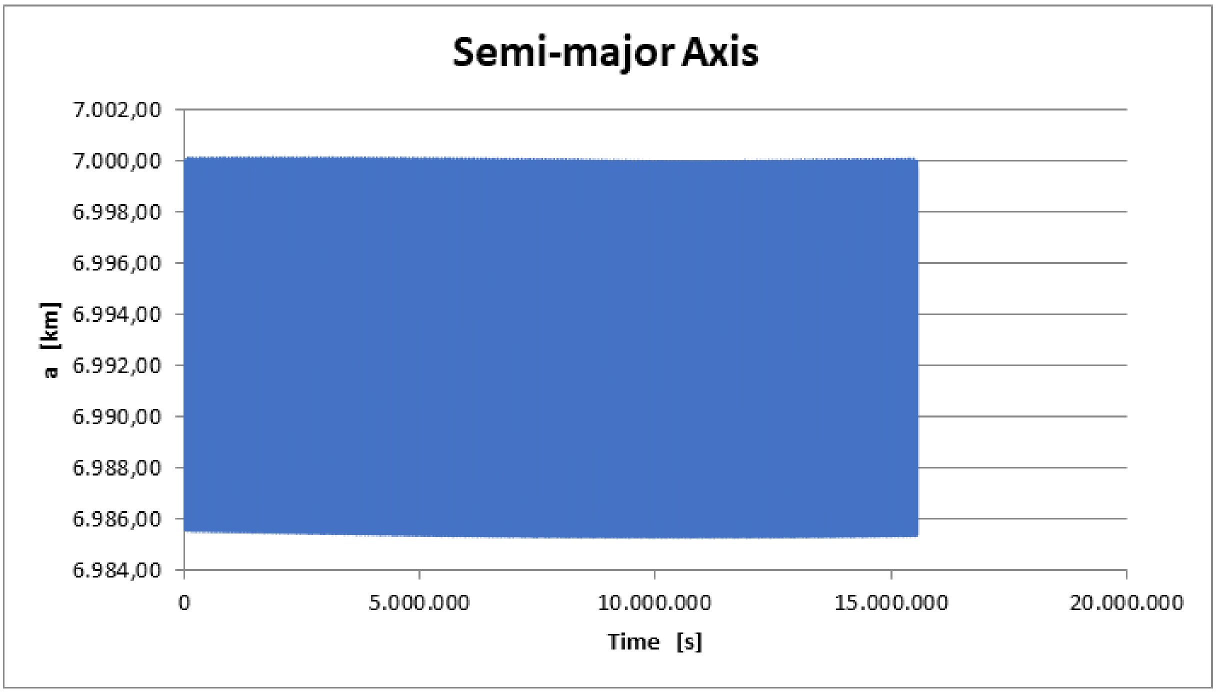

The semi-major axis trend is quite constant in time with a vertical displacement of about 14 km.

Chart 9.34 - 7 days inclination

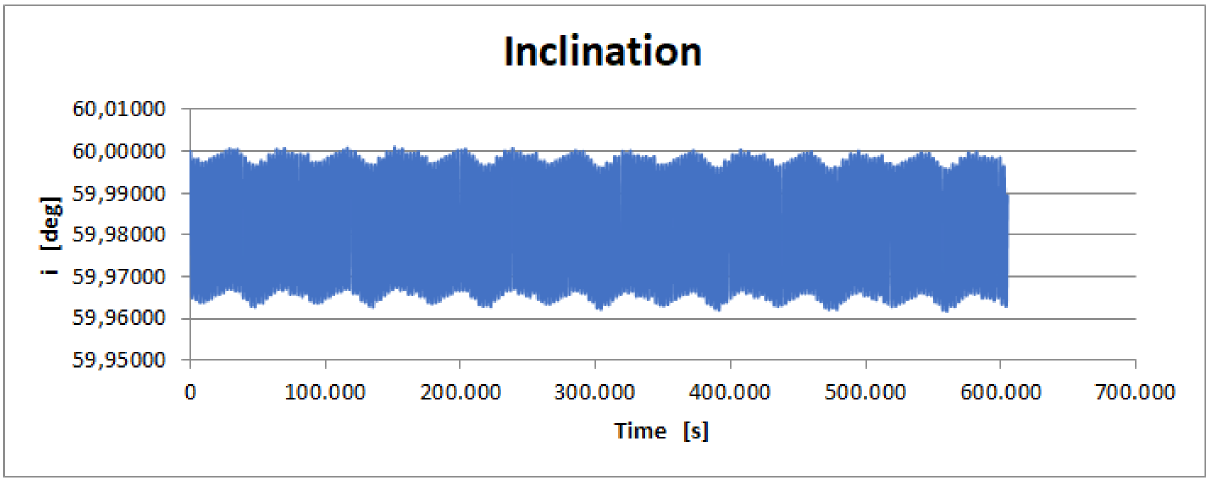

Chart 9.35 - 1 month inclination

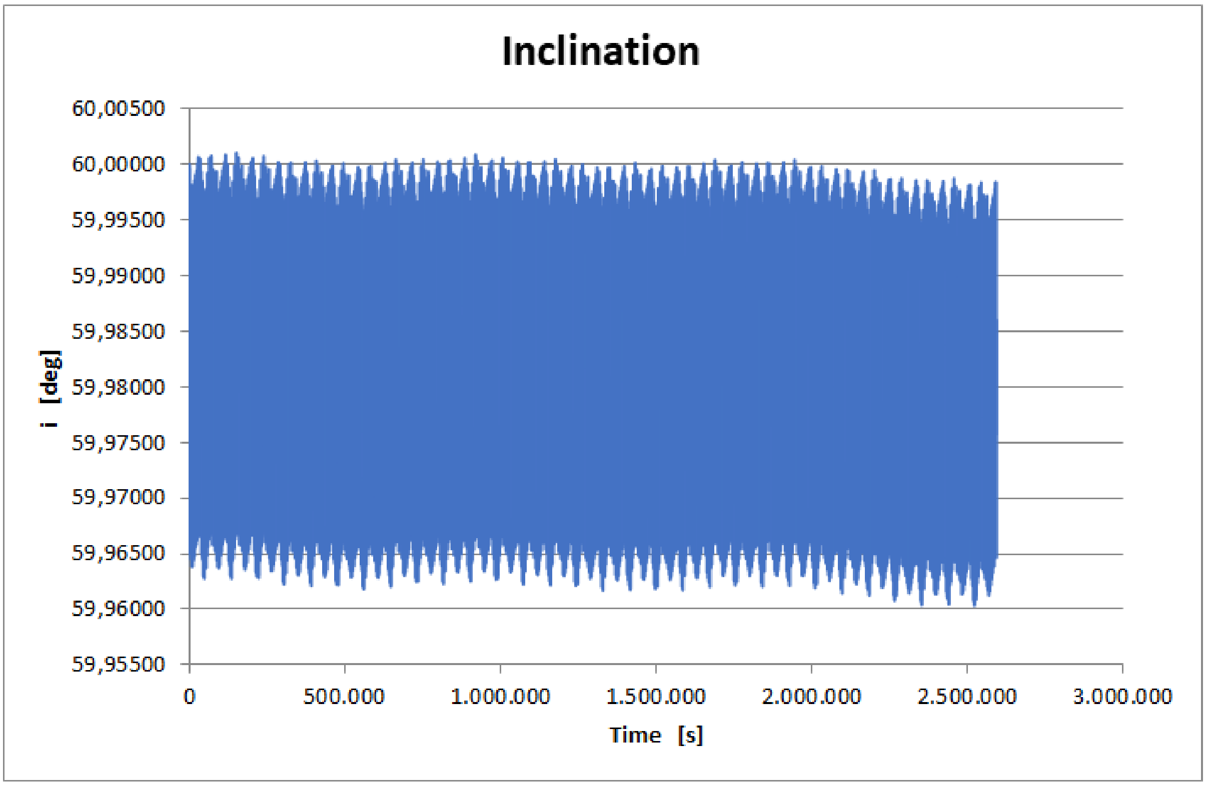

Chart 9.36 - 6 months inclination

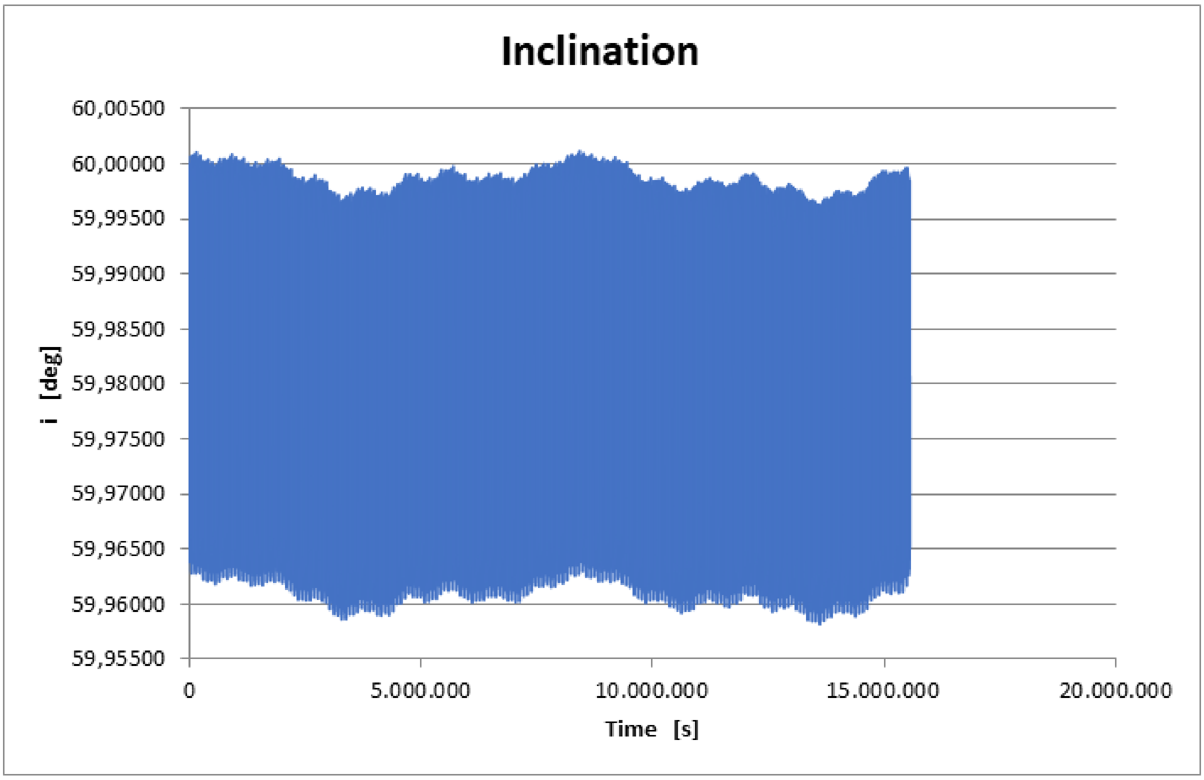

The inclination values are constant too with a maximum displacement of about 0.04°.

Chart 9.37 - 7 days eccentricity

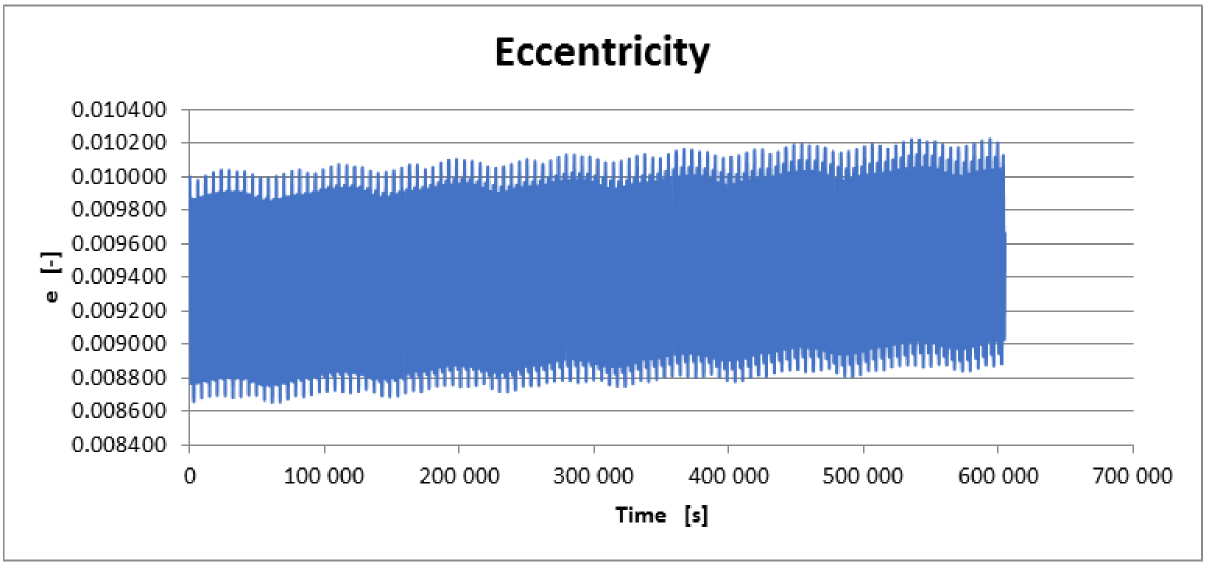

Chart 9.38 - 1 month eccentricity

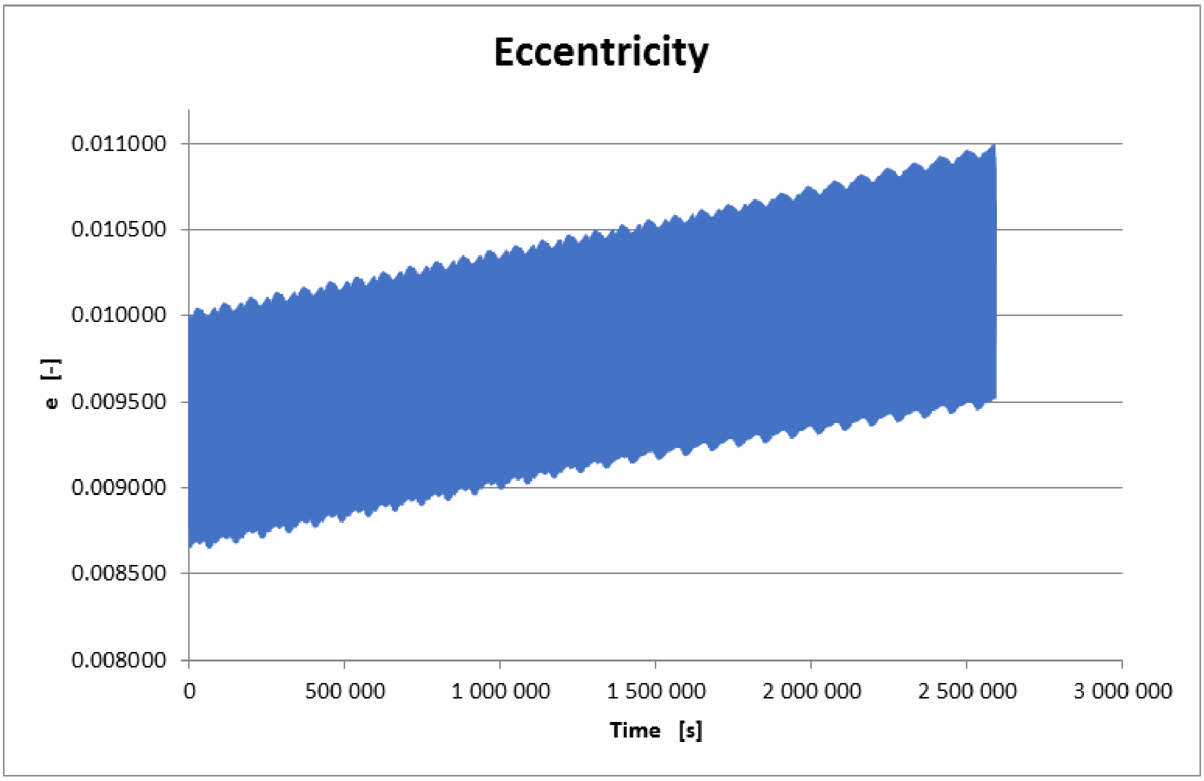

Chart 9.39 - 6 months eccentricity

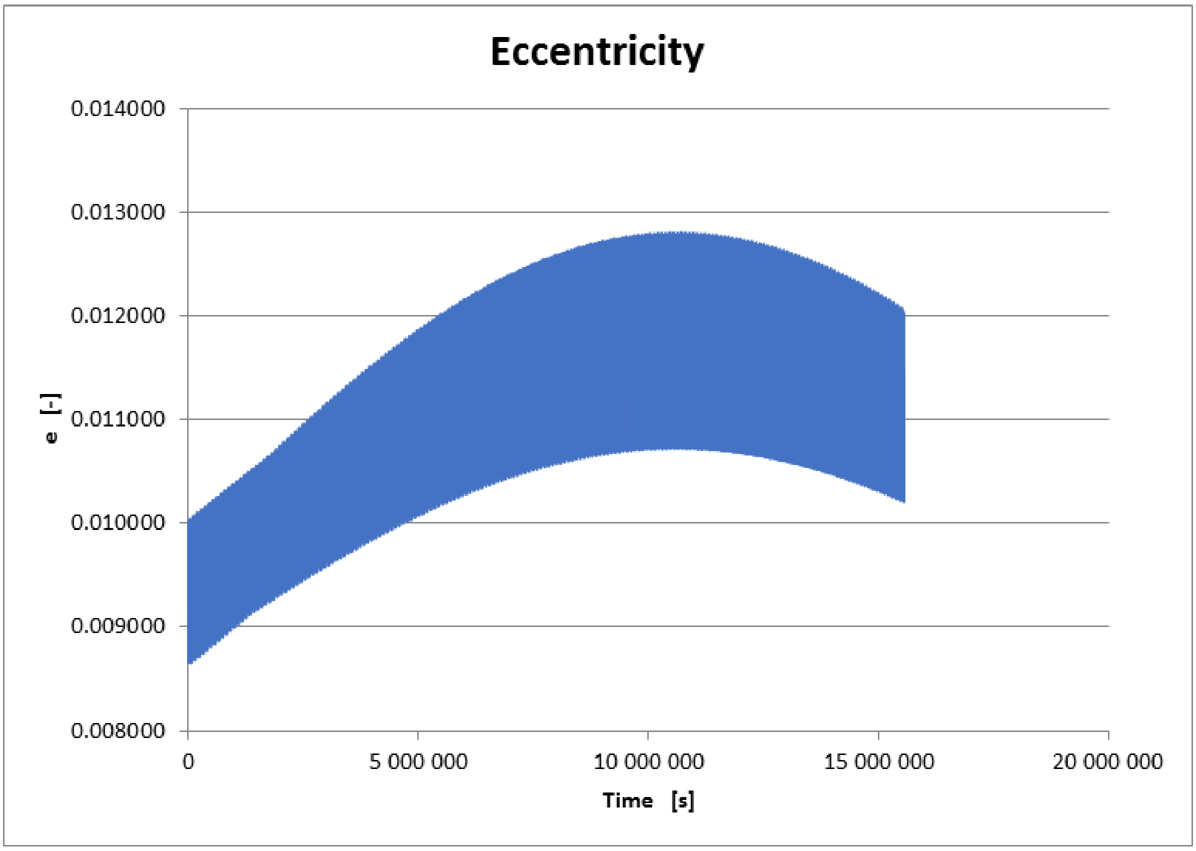

The eccentricity is increasing its value more and more with the time. This effect is more visible as the time of simulation increases. In the 6 months simulation, the reader can see that the chart has a maximum with a value of nearly 30% more than the initial value. So, the conclusion is that the eccentricity would have a periodic trend, but to visualize that, a longer analysis should be done, nearly about $4 \cdot 10^7\ s$.

Chart 9.40 - 1 month RAAN

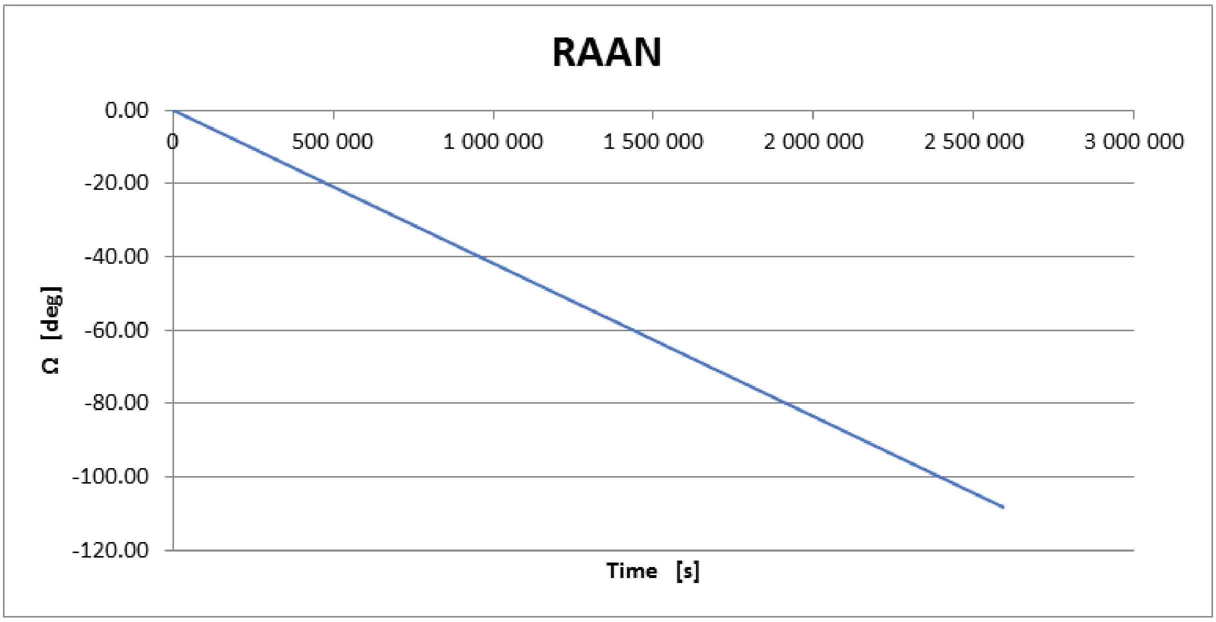

Chart 9.41 - 6 months RAAN

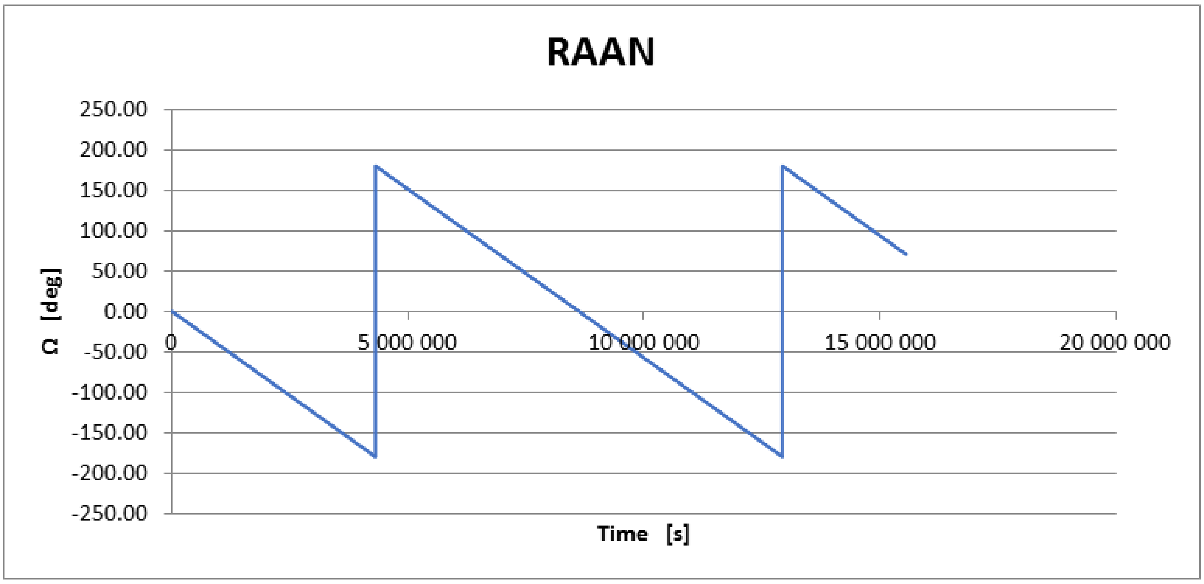

The RAAN evolution for the 7-days simulation has the same trend as the 1-month RAAN, so only the last was reported. To better visualize the trend of the RAAN in time, the chart of 6-months RAAN was included. To understand the change rate of RAAN in time, some calculations have been done. In Chart 9.41, the values of some interesting points have been taken: the first maximum and the second minimum. The first has coordinates (4320000 s, 180°) as (time, RAAN), the second has (12926310 s, -180°), thus Ω has made a 360° rotation.

The Δt between the two points is 8606310 s and so the change rate of RAAN is $\frac{\Delta\Omega}{\Delta t} = \frac{360°}{8606310\,s} = 4.1830 \cdot 10^{-5} \frac{°}{s}$ that corresponds to $\frac{\Delta\Omega}{\Delta t} = 3.6141 \frac{°}{day}$. It is a regression motion because the slope of the curve is negative.

To compare this value with a theoretical value, a general formulation was found in Astrodynamics manuals.

$$\frac{\Delta\Omega}{\Delta t} = -3\pi J_2 \left(\frac{R_\oplus}{a(1-e^2)}\right)^2 \frac{\cos(i)}{\tau} \frac{180}{\pi} \qquad \left[\frac{°}{s}\right]$$

Where

$$\begin{gathered} J_2 = 1082.6 \cdot 10^{-6} \quad \textit{first zonal harmonic} \\ R_\oplus = 6378\,km \quad \textit{Earth radius} \\ a = 7000\,km \quad \textit{semi-major axis} \\ e = 0.01 \quad \textit{eccentricity} \\ i = 60° \quad \textit{inclination} \\ \tau = 2\pi\sqrt{\frac{a^3}{\mu}} = 5828.5\,s \quad \textit{orbital period} \\ \mu = 398600 \frac{km^3}{s^2} \quad \textit{Standard gravitational parameter} \end{gathered}$$

The result is $\frac{\Delta\Omega}{\Delta t} = -4.1642 \cdot 10^{-5} \frac{°}{s}$. Compared to the previous value, it can be said that they are close at the $10^{-7} \frac{°}{s}$; the minus before the number reveals that it is a regression motion, as stated before.

Moreover, the evolution of the X-Y-Z axis have been plotted for 30 days and 6 months. The charts for 7 days evolution are not so explanatory.

Chart 9.42 - 1 month X-axis trend

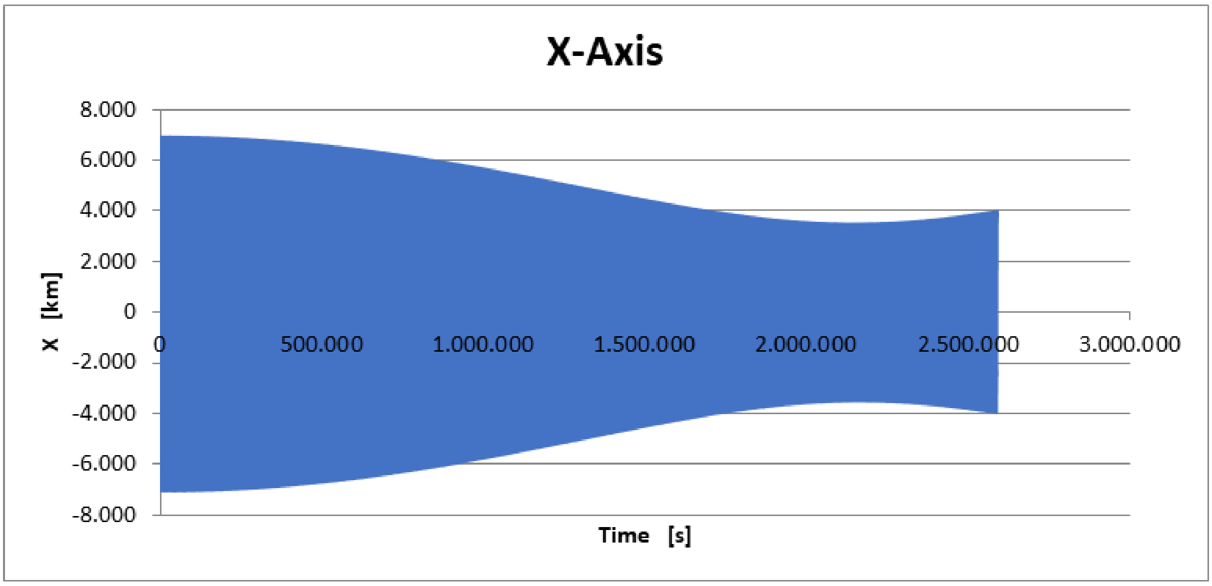

Chart 9.43 - 1 month Y-axis trend

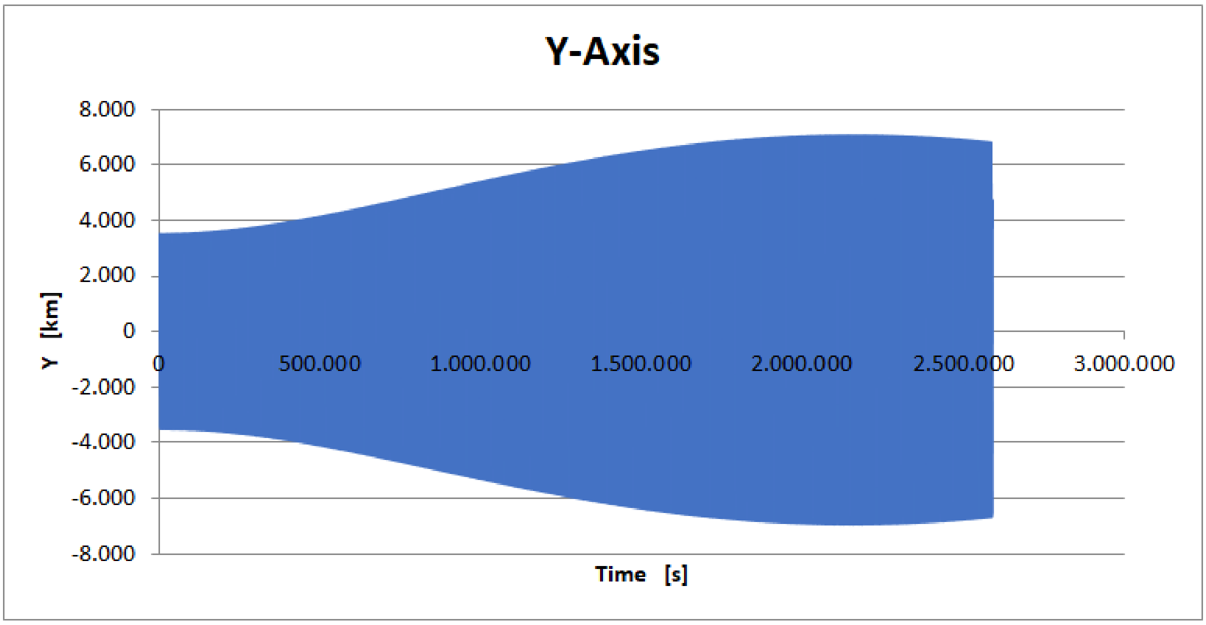

Chart 9.44 - 1 month Z-axis trend

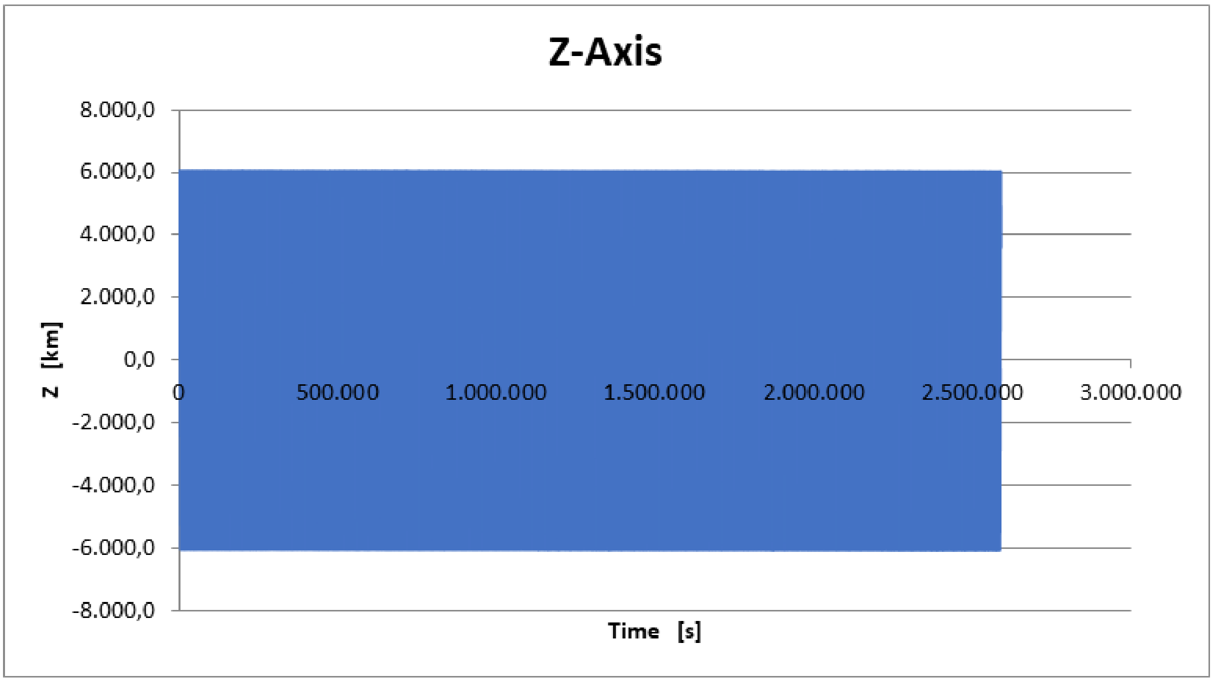

Chart 9.45 - Comparison between 1 month X-axis and Y-axis trends

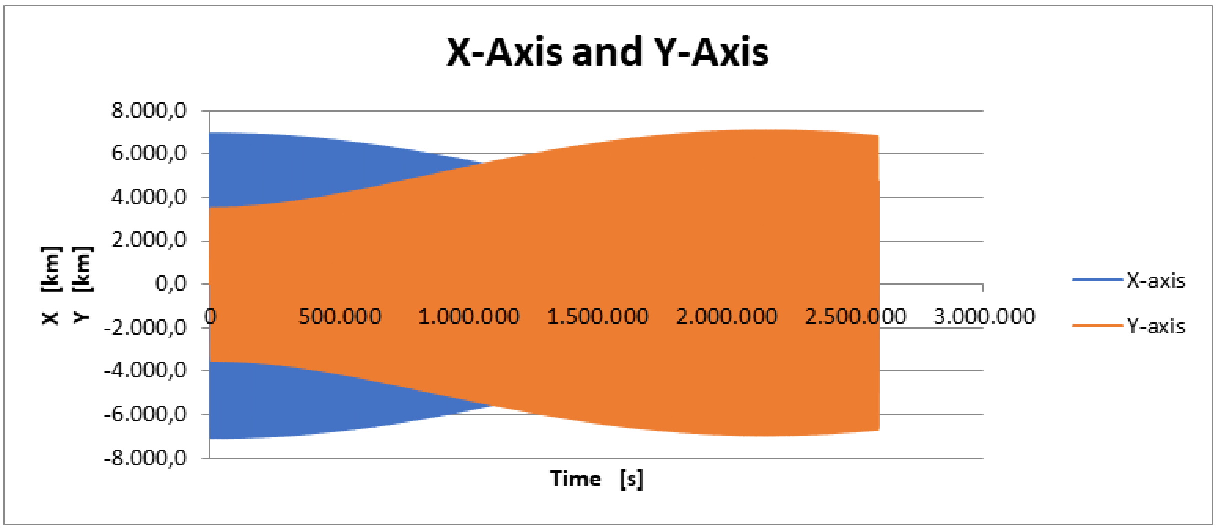

Chart 9.46 - 6 months X-axis trend

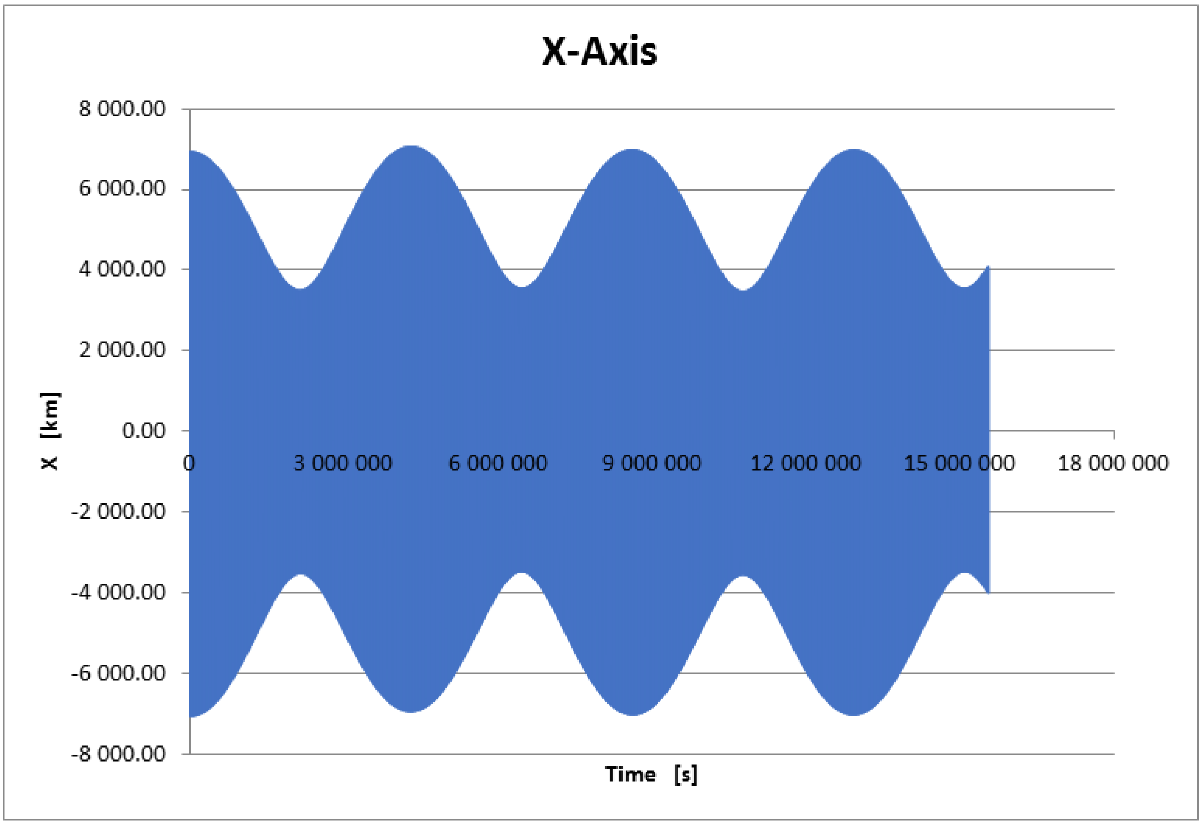

Chart 9.47 - 6 months Y-axis trend

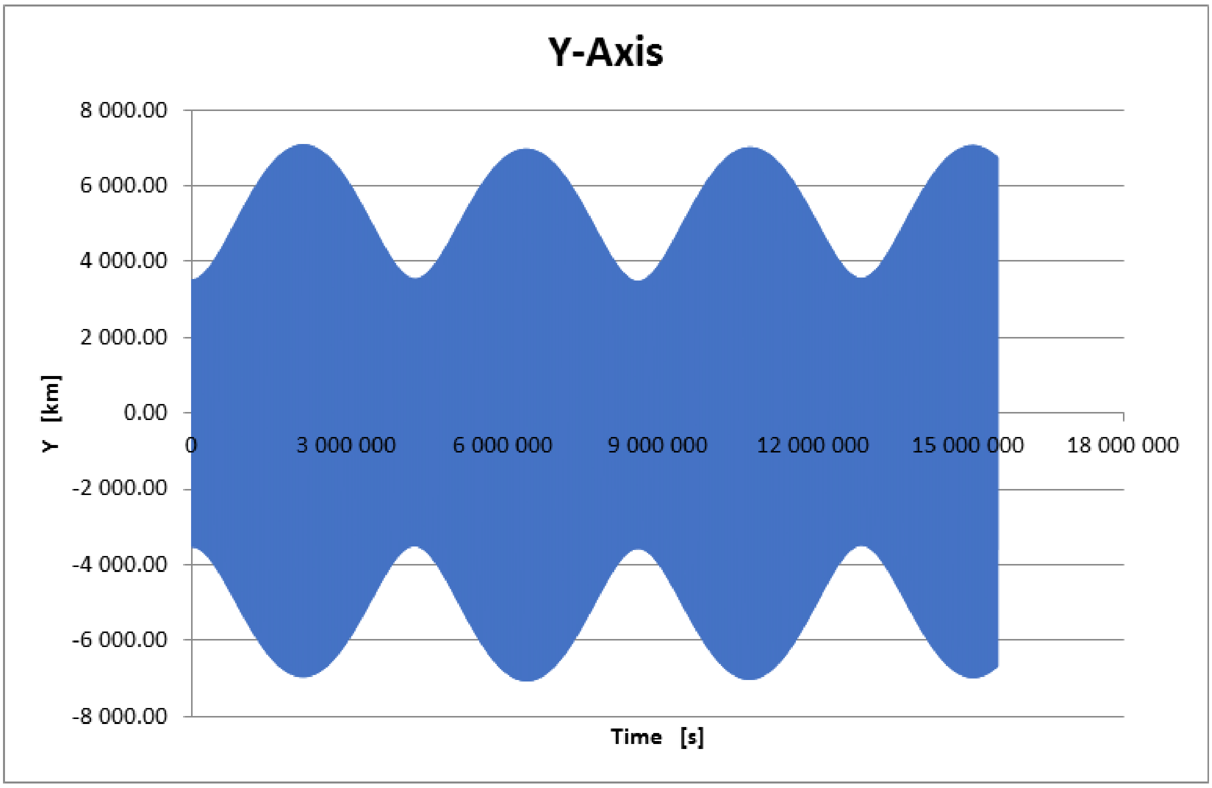

Chart 9.48 - 6 months Z-axis trend

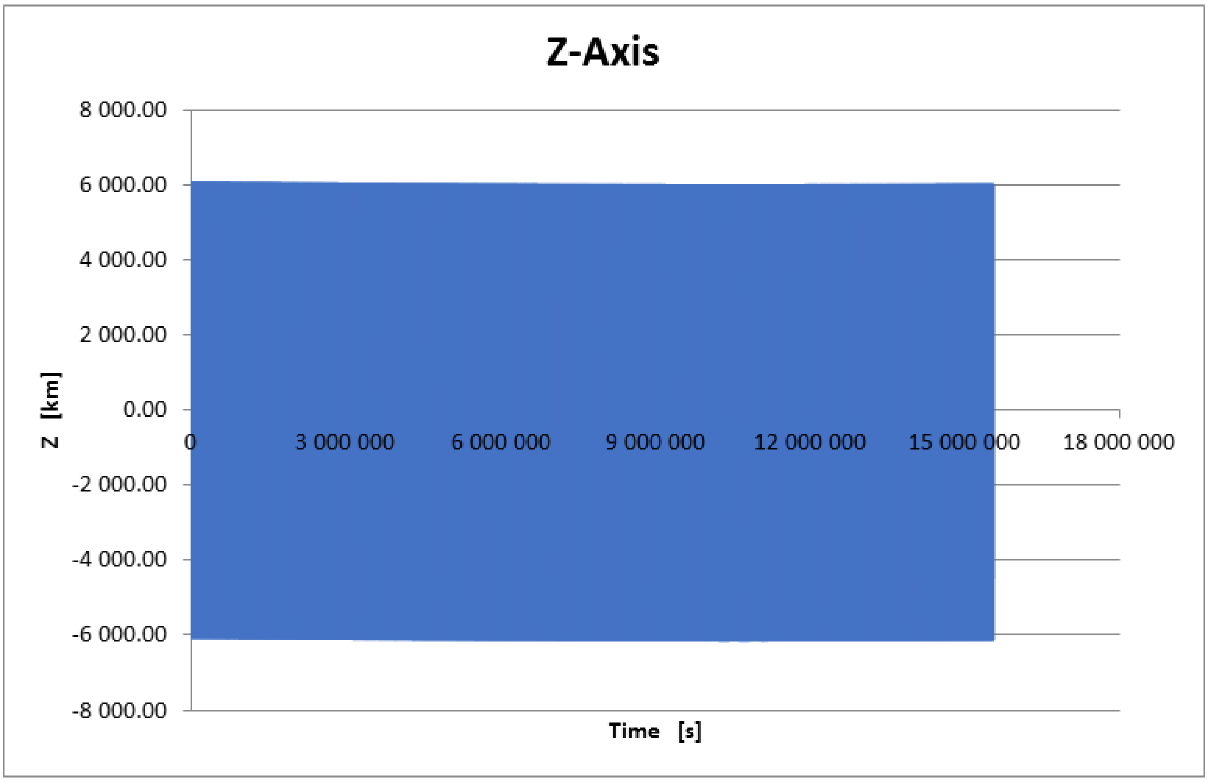

Chart 9.49 - Comparison between 6 months X-axis and Y-axis trends

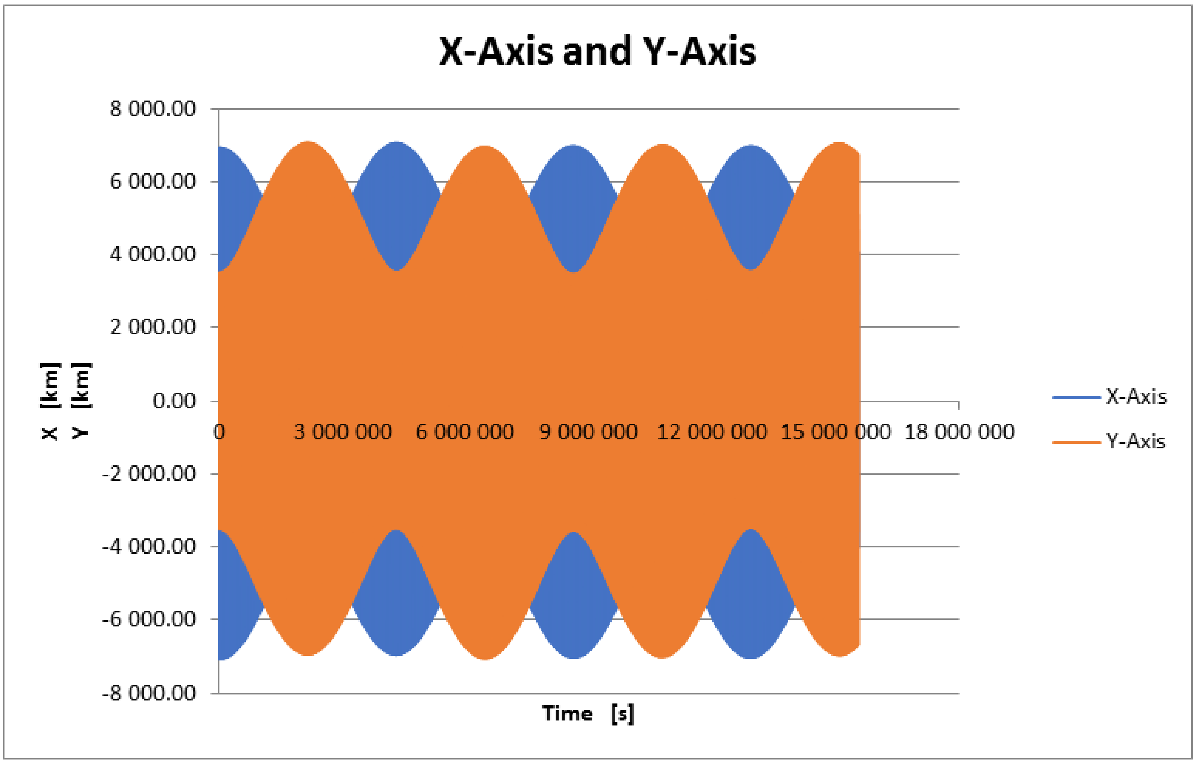

Both the 1 month and the 6 months analysis have the same trend for X-Y-Z axes. In particular, Z-axis (Chart 9.44 and Chart 9.48) has a constant trend, although during each orbit, it changes its value going from the positive maximum to the negative minimum. This movement is always present in all charts, but it is not noticed as the curves are compacted, so only the overall trend is seen. In Chart 9.50 a detail of the evolution in time of the values of the X-axis is shown. Considering the last assertion, we can say that the X-axis (Chart 9.42 and Chart 9.46) and Y-axis (Chart 9.43 and Chart 9.47), for both analyses, have an undulating general trend in time for both positive and for negative values. For example, the X-axis passes from a minimum displacement (3200, -3200) to a maximum displacement (6900, -6900). Moreover, the X and Y axis have an opposite trend, where one is positive maximum, the other is positive minimum and vice versa as Chart 9.45 and Chart 9.49 prove.

Chart 9.50 - Detail of X-axis evolution

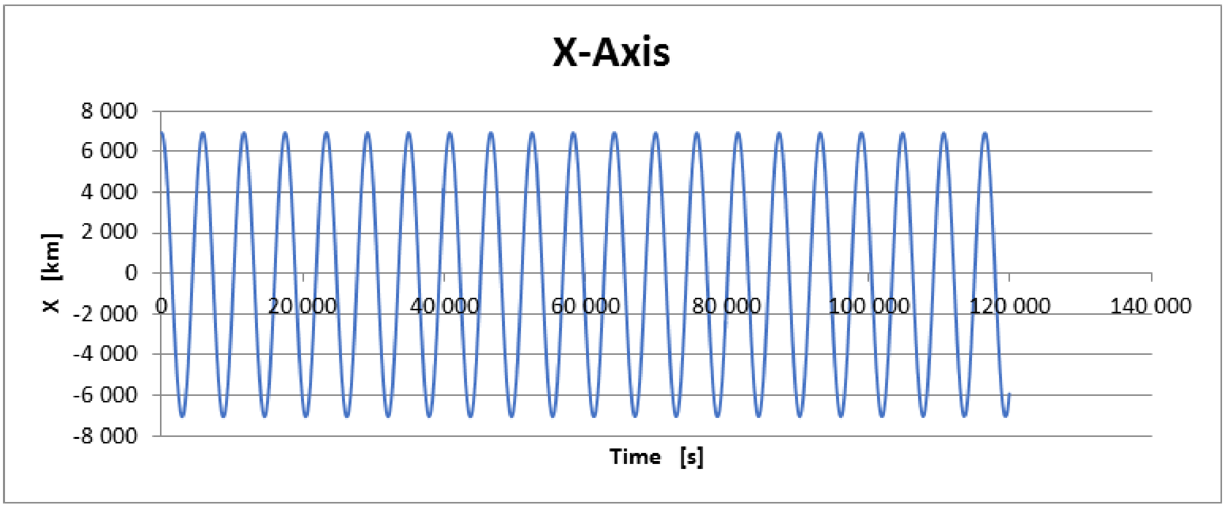

9.1.7 Radiation

An additional test was made to verify the correctness of another perturbation: the radiation. It can come from Sun in two ways: directly or reflected by Earth and is called “albedo”. In this way some simulations were done to evaluate if it works or not. The mission data are the following.

Table 9.8 - Mission data for radiation study

Quantity	Value		Unit of measure
Start date and hour	Dec 7th, 2020 @ 12:00:00		
Duration	172800 (2 days)		s
Time step	60-30-5		s
Semi-major axis (a)	6778		km
Eccentricity (e)	0.01		
Inclination (i)	60		deg
Right Ascension of the Ascending Node (Ω)	0		deg
True anomaly (ν)	0		deg
Argument of perigee (ω)	0		deg
Perturbation	Radiation	Sun	
		Earth	
S/C mass	1000		kg

The first two analyses used only the Sun as a source of radiation but with a different time step, the first 60 s and the second 30 s. The simulations worked perfectly, so both the time step and the source of radiation worked very well. The third analysis added the Earth to the Sun as source of radiation, with a time step of 60 s: this analysis stopped functioning while writing an output file. A fourth test was done, similar to the last but with a time step of 5 s; here again the code suddenly crashed without any explanation. It was understood that the problem was the albedo from the Earth, so it was left apart in future simulations, leaving to others the task of fixing this bug as it was not one of the aims of the present thesis.

9.1.8 Creation of helpful scripts

Some scripts were created as they were necessary for the success of the code.

9.1.8.1 conv_units

It converts values in input from and to the following units of measure: parsec (pc), light-year (ly), km, astronomical unit (au); also from hours (h), from degrees (deg), from radians (rad) to h, to deg, to rad, to degrees/minutes/seconds (dms) and to hour/minutes/seconds (hms);

9.1.8.2 conv_hmsdms

It converts the input values that are in the format (hh, mm, ss) from and to the following units of measure:

- from hour, minutes, seconds (hms) to hours (h), to degrees (deg), to radians (rad);
- from degree, minutes, seconds (dms) to degrees (deg), to radians (rad).

9.1.8.3 vectornorm

This function was created for MATLAB versions prior to R2017b, version in which The Mathworks introduced it, with the name "vecnorm" in the MATLAB library. It calculates the Euclidean norm of matrix.

The input arguments are: y (matrix), p = 2, dim.

- y is a m-by-n matrix
- p = 2 means the Euclidean norm of a vector. The Euclidean norm of a vector v of N elements is defines by

$$\|v\| = \sqrt{\sum_{k=1}^{N} |v_k|^2}$$

- dim can be 1 or 2. If it is 1, the function calculates the norm of each column returning a row vector (1 x n); if it is 2, it calculates the norm of each row returning a column vector (m x 1).

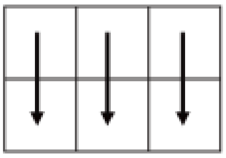

Figure 9.18 - vecnorm(y, p, 1)

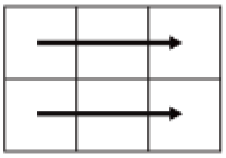

Figure 9.19 - vecnorm(y, p, 2)

9.2 SPICE

SPICE (Spacecraft Planet Instrument C-matrix Events) is a NASA ancillary information system used to compute geometric information used in planning and analysing science observations obtained from robotic spacecraft. SPICE was developed at NASA's Navigation and Ancillary Information Facility (NAIF), located at the Jet Propulsion Laboratory, to assist NASA scientists in planning and interpreting scientific observations from space-borne instruments, and to assist NASA engineers involved in modelling, planning and executing activities needed to conduct planetary exploration missions. The use of SPICE extends from mission concept development through the post-mission data analysis phase, including help with correlation of individual instrument data sets with those from other instruments on the same or on other spacecrafts. It has become the de facto standard for handling much of the so-called observation geometry information on NASA's planetary missions, and it is now widely used in support of science data analysis on planetary missions of other space agencies as well. SPICE, that is given freely to everyone worldwide, is focused on solar system geometry and some of its capabilities are used on a variety of astrophysics, solar physics and earth science missions. SPICE consists of both data and software. [W5]

9.2.1 Data

SPICE data files are usually referred to as "kernels." These files provide information such as spacecraft trajectory and orientation; target body ephemeris, size and shape; instrument field-of-view size, shape and orientation; specifications for reference frames; and tabulations of time system conversion coefficients. SPICE data are archived in a national archive centre such as the NASA Planetary Data System archives.

Information inside SPICE has been structured and formatted for easy access and correct use by the planetary science and engineering communities. SPICE kernels are produced by the most knowledgeable sources of such information, usually located at a mission operations centre.

The SPICE system's logical components and the actual data files—the kernels—used to realize those components are summarized below.

S - Spacecraft ephemeris, given as a function of time. (SPK)

P - Planet, satellite, comet, or asteroid ephemerides, or more generally, location of any target body, given as a function of time. (also SPK)

The P component also logically includes certain physical, dynamical and cartographic constants for target bodies, such as size and shape specifications, and orientation of the spin axis and prime meridian. (PCK)

I - Instrument information containing descriptive data peculiar to the geometric aspects of a particular scientific instrument, such as field-of-view size, shape and orientation parameters. (IK)

C - Orientation information, containing a transformation, traditionally called the "C-matrix," which provides time-tagged pointing (orientation) angles for a spacecraft bus or a spacecraft structure upon which science instruments are mounted. The C component may also include angular rate data for that structure. (CK)

E - Events information, summarizing mission activities – both planned and unanticipated. Events data are contained in the SPICE E-kernel file set, which consists of three components: Science Plans, Sequences, and Notes. (EK) (Note: the Events kernel is rarely used.)

Some additional data products are also important components of the SPICE system, even if not contained in the "SPICE" acronym.

A frames kernel (FK) contains specifications for the assortment of reference frames that are typically used by flight projects. This file also includes mounting alignment information for instruments, antennas and perhaps other structures of interest.

Spacecraft clock (SCLK) and leap seconds (LSK) kernels are also part of SPICE; these are used in converting time tags between various time measurement systems.

A digital shape model kernel (DSK), with separate designs for both small, irregularly shaped bodies such as asteroids and comet nuclei, and for large, more uniformly shaped bodies such as the moon, earth and Mars, offers the possibility of using higher fidelity shape models within SPICE for those (few) bodies for which scientists have calculated detailed shape. When they exist, a DSK can often be used in place of the size and shape portion of a PCK. [W5]

9.2.2 Software

The SPICE system includes software referred to as The SPICE Toolkit, used for reading the SPICE data files and computing geometric parameters based on data from those files.

The SPICE Toolkit is comprised of several items.

1. A large collection of user-level application program interfaces (APIs) and underlying subroutines and functions, provided as source code with extensive user-focused documentation (code headers).
2. A ready-to-use library made from the APIs, subroutines and functions described in 1.

3. A small set of ready-built utility (application) programs, along with their associated User Guides. These are programs thought to be of use to many SPICE users. (Additional utility programs are available from the Utilities link on the NAIF website.)
4. A set of technical reference documents – one for each major SPICE functional area.
5. A few additional documents that describe the contents and structure of a Toolkit package, highlight and provide small usage examples of the most popular APIs, and provide a permuted index based on the abstracts for all modules.

These tools are provided as subroutine libraries in four programming languages: C, FORTRAN, IDL, MATLAB and Java Native Interface. For example, the MATLAB version of SPICE is called MICE and it includes, in addition to files, a folder with all the routines written as MATLAB scripts and so readily to be used in user's MATLAB session, as long as he loads the path of MICE location first. Third parties offer Python and Ruby interfaces to the C-language Toolkit. The Toolkits also include a number of utility and application programs. The SPICE Toolkits are available for most popular computing platforms, operating systems and compilers. Extensive documentation accompanies each Toolkit. Moreover, a set of tutorials is available to help users understand the SPICE data and software. Some "open book" programming lessons useful in learning how to program using Toolkit subroutines are also available. [W5]

The current SPICE Toolkit version is N0066, released April 10, 2017. [W6] To keep the software up-to-date, it is advisable for future users to look up for new releases on NAIF website, that can be found in the websites list.

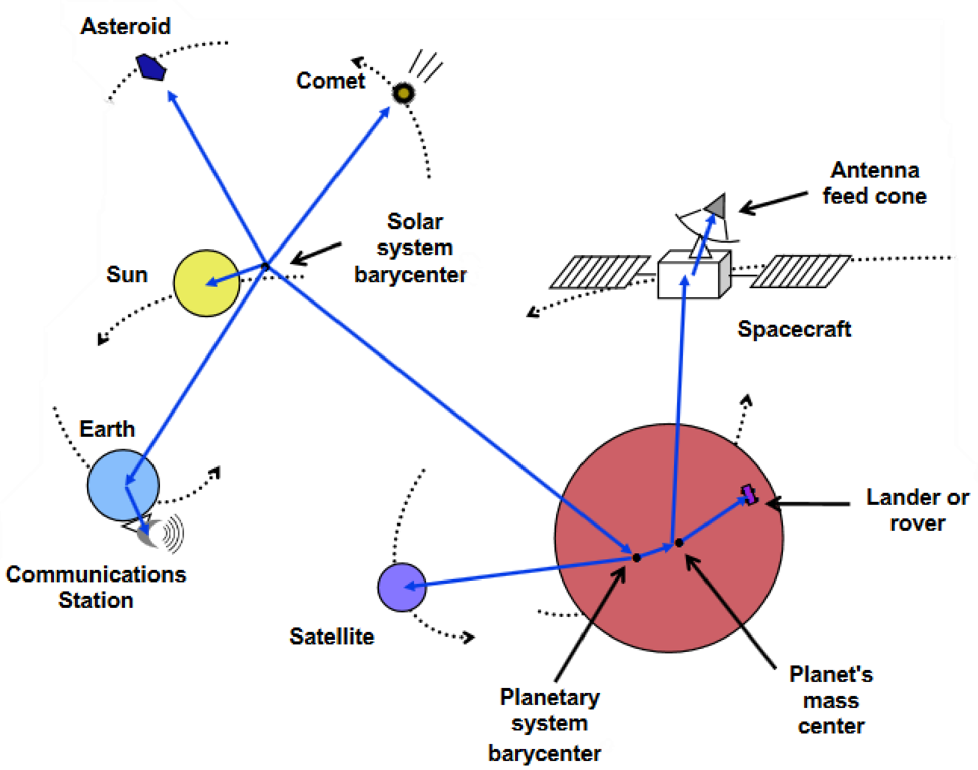

Figure 9.20 - Example of possible interactions in SPICE

9.3 Standard deviation

In statistics, the standard deviation (SD, also represented by the lower case Greek letter sigma σ for the population standard deviation or the Latin letter s for the sample standard deviation) is a measure that is used to quantify the amount of variation or dispersion of a set of data values. A low standard deviation indicates that the data points tend to be close to the mean (also called the expected value) of the set, while a high standard deviation indicates that the data points are spread out over a wider range of values.

The standard deviation of a random variable, statistical population, data set, or probability distribution is the square root of its variance. It is algebraically simpler, though in practice less robust, than the average absolute deviation. A useful property of the standard deviation is that, unlike the variance, it is expressed in the same units as the data.

In addition to expressing the variability of a population, the standard deviation is commonly used to measure confidence in statistical conclusions. For example, the margin of error in polling data is determined by calculating the expected standard deviation in the results if the same poll were to be conducted multiple times. This derivation of a standard deviation is often called the "standard error" of the estimate or "standard error of the mean" when referring to a mean. It is computed as the standard deviation of all the means that would be computed from that population if an infinite number of samples were drawn and a mean for each sample were computed. In statistics, the standard deviation of a feature over a population of N units is defined as

$$\sigma = \sqrt{\frac{\sum_{i=1}^{N}(x_i - \bar{x})^2}{N}}$$

where $\bar{x} = \mu = \frac{1}{N}\sum_{i=1}^{N} x_i$ is the arithmetic mean (the blue line).

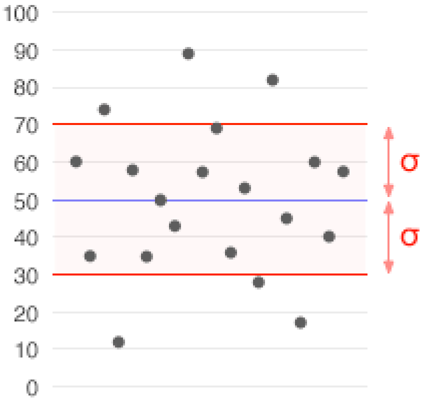

Figure 9.21 - Standard deviation representation

The standard deviation of a population and the standard error of a statistic derived from that population (such as the mean) are quite different but related (related by the inverse of the square root of the number of observations). The reported margin of error of a poll is computed from the standard error of the mean (or alternatively from the product of the standard deviation of the population and the inverse of the square root of the sample size, which is the same thing) and is typically about twice the standard deviation – the half-width of a 95 percent confidence interval.

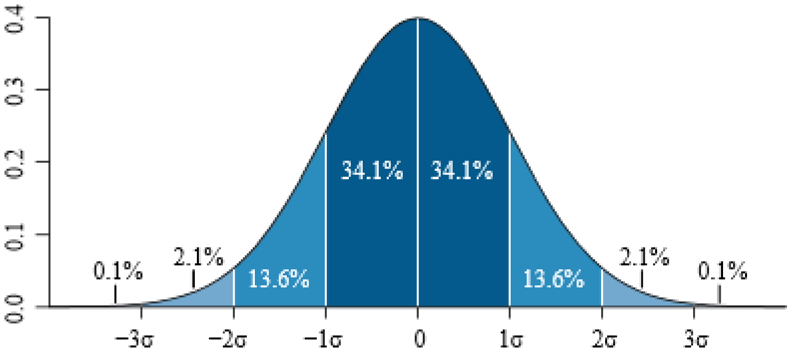

Figure 9.22 - Gaussian distribution

If a data distribution is approximately normal then about 68 percent of the data values are within one standard deviation of the mean (mathematically, $\mu \pm \sigma$, where μ is the arithmetic mean and it is placed in 0), about 95 percent are within two standard deviations ($\mu \pm 2\sigma$), and about 99.7 percent lie within three standard deviations ($\mu \pm 3\sigma$). This is known as the 68-95-99.7 rule, or the empirical rule. The two points of the curve that are one standard deviation from the mean are also the inflection points. [W7]

9.4 Perturbed orbits

As a first approximation, the ideal Keplerian orbits can be treated under the basic assumption that the motion of a body in these orbits is a result of the gravitational attraction between two bodies. This situation does not exist in reality. In fact, the two-body problem of motion of each individual planet of the solar system is an idealization and additional forces acting on any moving body must be taken into account. The gravitational attraction among planets is a conservative force. In case of geostationary satellites, which have high-altitude orbits, the effects of the conservative perturbing forces of Sun and Moon on the motion of these satellites cannot be ignored because they tend to change the inclination of the orbits. Moreover, there are also nonconservative perturbing forces, such as solar pressure. In case of geostationary orbits, solar pressure tends to change the eccentricity of the orbit. Another nonconservative force is the atmospheric force, also called atmospheric drag, which is pertinent to low-altitude orbits. Such forces tend to decrease the semi-major axis of the orbit, eventually causing the satellite to fall down to the Earth's surface. In the following sections, these perturbations are better described and explained. [14]

9.4.1 The perturbed equation of motion

The basic dynamical equation of motion for a Keplerian orbit (or for a two-body problem) is

$$\ddot{\vec{r}} + G(m_1 + m_2)\frac{\vec{r}}{r^3} = 0$$

that can be rewritten in the following form:

$$\frac{d^2\vec{r}}{dt^2} = -\mu\frac{\vec{r}}{r^3} = \vec{\gamma}_k$$

with initial conditions $\vec{r}(0), \vec{v}(0)$. The orbital elements (a = semi-major axis, e = eccentricity, i = inclination, Ω = longitude of the ascending node, ω = argument of the perigee, ν = true anomaly) do not depend on time except for the true anomaly ν, which identifies the position of the S/C during its motion on the orbit plane

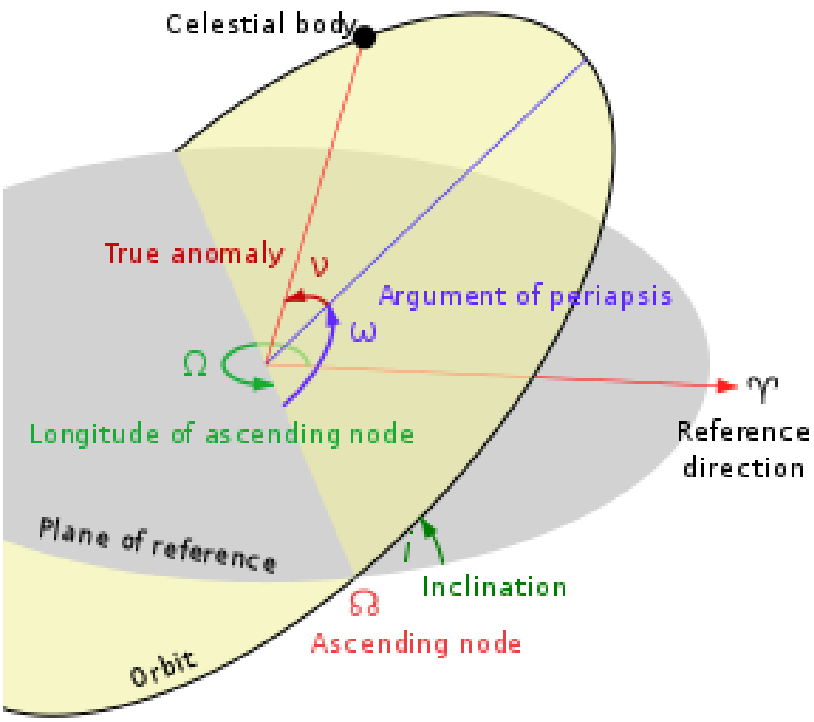

Figure 9.23 - Orbital elements

For the general case, including perturbing forces of any kind, the equation of motion of the satellite becomes:

$$\frac{d^2\vec{r}}{dt^2} = \vec{\gamma}_k + \vec{\gamma}_p$$

with initial conditions $\vec{r}(t_0) = \vec{r}_0, \vec{v}(t_0) = \vec{v}_0$.

Here $\vec{\gamma}_k$ and $\vec{\gamma}_p$ stand respectively for the Keplerian and the perturbing accelerations caused by the Keplerian and perturbing forces.

The last equation is the general equation for the motion of a body in any orbit. In the following analysis the perturbation acceleration $\vec{\gamma}_p$ is appreciably smaller than the Keplerian acceleration $\vec{\gamma}_k$. Here the orbit parameters are dependent also on time; thus the perturbing acceleration is dependent on the radius vector $\vec{r}$, the velocity $\vec{v}$ and the time: $\vec{\gamma}_p = \vec{\gamma}_p(\vec{r}, \vec{v}, t)$; for example, the Moon's perturbing acceleration on the S/C depends on the Moon's position in its orbit relative to the Earth. In this way all the six orbital elements of the S/C change step by step on the orbit and the Keplerian orbit do not coincide with the perturbed orbit. Suppose that at any time t_0 the perturbing acceleration $\vec{\gamma}_p$ is removed. The S/C keeps moving around the Earth with the last orbital parameters it had at the time when the perturbing acceleration was removed; this orbit is a Keplerian orbit, called *osculating orbit*, and it can be found by knowing $\vec{r}(t_0)$ and $\vec{v}(t_0)$. [14]

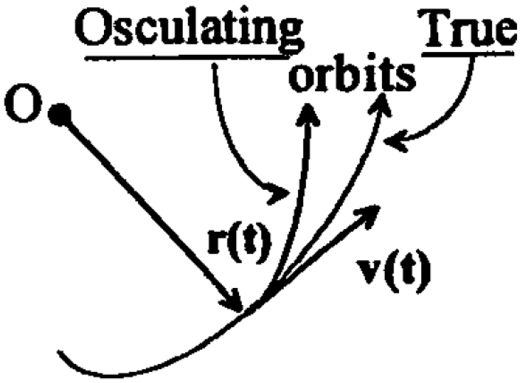

Figure 9.24 - Definition of true and osculating orbits

9.4.2 Perturbing forces and their influence on the orbit

One of the most important perturbing forces on Earth-orbiting satellites arises from the nonhomogeneity of the Earth. The Earth globe is not a perfect sphere, and neither is its mass distribution homogeneous. These physical facts produce perturbing accelerations on the moving body. The consequences of these accelerations are variations of the orbital parameters of earth-orbiting satellites.

As already mentioned, a true Keplerian orbit is obtained for a two-body system. The existence of additional celestial bodies produces perturbing forces with the heavy consequences that a three (or more)-body problem must be solved. For such problems, a closed-form analytical solution might not exist. Moreover, it will be described that the gravitational perturbing forces of the Sun and the Moon cause serious complications in high-altitude geostationary orbits.

The solar pressure exerted by the Sun on large satellites can be ignored in low-altitude orbits where aerodynamic perturbing forces predominate. For high-altitude orbits where aerodynamic forces are negligible, the perturbing solar pressure forces cannot be ignored. On the other hand, for interplanetary voyages, the solar pressure may be used to obtain accelerating forces on the satellite, and this is called the “solar sail” mode. [14]

9.4.2.1 Nonhomogeneity and oblateness of the Earth

Because the force exerted by the Earth on a body outside its sphere is a conservative force, it can be derived from a gradient of a scalar potential function $U(r) = -\frac{\mu}{r}$ and the value of gravity is constant. This would be completely true if the Earth were modelled as a mass concentrated in a single point, or as a homogeneous sphere; in this way, the only geometrical constraint would be the Earth radius, under which the satellites cannot fly. Unfortunately, this is not the case: the Earth is an oblate body and its mass distribution is not homogeneous, so the gravity is not constant but depends on this nonhomogeneity from point to point. Correction factors must therefore be added to the scalar potential function.

It is convenient to express the corrected potential of the Earth in the following form:

$$U(r,\phi,\lambda) = -\frac{\mu}{r} + B(r,\phi,\lambda)$$

where $B(r,\phi,\lambda)$ is the appropriate spherical harmonic expansion used to correct the gravitational potential for the Earth's nonsymmetric mass distribution.

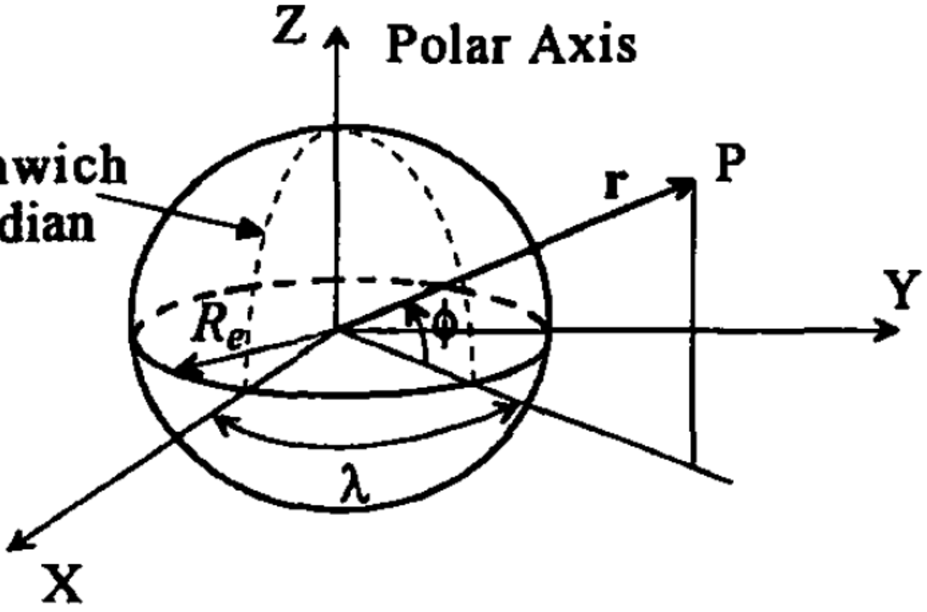

Figure 9.25 - Coordinates for the derivation of the Earth's external gravitational potential

If R_e is defined as the mean radius of the Earth at the equator, then

$$B(r,\phi,\lambda) = \frac{\mu}{r}\left\{\sum_{n=2}^{\infty}\left[\left(\frac{R_e}{r}\right)^n J_n P_n sin(\phi) + \sum_{m=1}^{n}\left(\frac{R_e}{r}\right)^n (C_{nm}\, cos(m\lambda) + S_{nm}\, sin(m\lambda))P_{nm}\, sin(\phi)\right]\right\}$$

This equation is the infinite series of the geopotential function at any point P outside the Earth's sphere where r, ϕ, λ are its spherical coordinates.

The parameters are defined as follows:

r – geocentric distance of point P

ϕ – geocentric latitude

λ – geographical longitude

R_e – mean equatorial radius of the Earth

$cos(m\phi)$ and $sin(m\lambda)$ – harmonics in λ

n – degree

m – order

$\mu = GM$ – Earth gravity constant

J_{nm} – zonal harmonic coefficients

J_n – zonal harmonic coefficients of order 0

P_{nm} – associated Legendre polynomial

P_n – Legendre polynomial of degree n and order 0

C_{nm} – tesseral harmonic coefficients for $n \neq m$

S_{nm} – sectoral harmonic coefficients for $n = m$

From the last equation, it can be noticed that the zonal harmonics depend on the latitude only. These coefficients are a consequence of the Earth's oblateness. The tesseral harmonics represent longitudinal variations of the Earth’s shape. Values of the listed coefficients are obtained from satellite observations and appropriate measurements and they are time dependent. The equation of $B(r, \phi, \lambda)$ written before and the following list of values are valid for the EGM 96 (Earth Geopotential Model 1996) based on the reference ellipsoid WGS 84 (World Geodetic System 1984).

Table 9.9 - Spherical coefficients for EGM 96

Zonal harmonic coefficients	Tesseral harmonic coefficients	Sectoral harmonic coefficients
$J_2 = 1082 \cdot 10^{-6}$	$C_{21} = 0$	$S_{21} = 0$
$J_3 = -2.53 \cdot 10^{-6}$	$C_{22} = 1.57 \cdot 10^{-6}$	$S_{22} = -0.9 \cdot 10^{-6}$
$J_4 = -1.61 \cdot 10^{-6}$	$C_{31} = 2.19 \cdot 10^{-6}$	$S_{31} = 0.27 \cdot 10^{-6}$
	$C_{32} = 0.31 \cdot 10^{-6}$	$S_{32} = -0.21 \cdot 10^{-6}$

The gravity field model used in NODES is the EIGEN-GL04C, for which the following formulation for the geopotential and the listed values are valid.

$$U(r, \phi, \lambda) = \frac{\mu}{r}\left\{1 + \sum_{l=2}^{N}\left(\frac{R_e}{r}\right)^{l}\sum_{m=0}^{l}\left(C_{lm}\cos(m\lambda) + S_{lm}\sin(m\lambda)\right)P_{lm}(sin\phi)\right\}$$

Table 9.10 - Spherical coefficients for EIGEN-GL04C

Zonal harmonic coefficients	Tesseral harmonic coefficients	Sectoral harmonic coefficients
$C_{20} = -484.165 \cdot 10^{-6}$ $C_{30} = 0.957205 \cdot 10^{-6}$ $C_{40} = 0.539992 \cdot 10^{-6}$ $C_{50} = 0.68683615 \cdot 10^{-7}$	$C_{21} = -0.2552149 \cdot 10^{-9}$ $C_{22} = 2.43936 \cdot 10^{-6}$ $C_{31} = 2.03045 \cdot 10^{-6}$ $C_{32} = 0.9047817 \cdot 10^{-6}$	$S_{21} = 0.144095 \cdot 10^{-8}$ $S_{22} = -1.4002858 \cdot 10^{-6}$ $S_{31} = 0.2482048 \cdot 10^{-6}$ $S_{32} = -0.618986 \cdot 10^{-6}$

It is important to realize that the successive coefficients C_{nm} and S_{nm} do not necessarily decrease; however, the factor $\left(\frac{R_e}{r}\right)^l$ or $\left(\frac{R_e}{r}\right)^n$ tends to diminish each term of the series. Comparison of these coefficients, whatever the model is, shows that the magnitude of J_2 is hundreds (400-500) times larger than other J_n coefficients, which can be disregarded for many engineering purposes. In fact, the J_2 plays a major role in changing the shape of the orbit locally. This is because the gravity depends only on space and on what is below the satellite step by step in its orbit but not on time and how long the gravity force is exerted. At the end, taking the geopotential function, simplifying it and performing some calculations, important results are obtained.

It is found that the average change of the parameters *a*, *e*, and *i* per orbit is null:

$$\frac{da}{dt} = 0; \quad \frac{de}{dt} = 0; \quad \frac{di}{dt} = 0.$$

Moreover, it was found that some orbital parameters change with time; this is the case of the longitude of the ascending nodes Ω, the argument of the perigee *ω* and the true anomaly *v*.

$$\frac{d\Omega}{dt} = -\frac{3}{2}\frac{\pi J_2 \cos(i)}{(1-e^2)^2}\left(\frac{R_e}{a}\right)^2 \qquad \frac{d\omega}{dt} = \frac{3}{4}\frac{\pi J_2\left[5\cos^2(i)-1\right]}{(1-e^2)^2}\left(\frac{R_e}{a}\right)^2$$

$$\frac{dv}{dt} = \pi + \frac{3}{4}\frac{\pi J_2\left[3\cos^2(i)-1\right]}{(1-e^2)^{\frac{3}{2}}}\left(\frac{R_e}{a}\right)^2$$

These effects can be useful for some kind of satellites. The $\frac{d\Omega}{dt}$ is used by low-orbit nadir-pointing satellites with Earth-scanning instrumentation in Sun-synchronous orbit, to achieve the best Sun-satellite-target conditions, i.e. having the sun behind the satellites. The idea is to obtain an orbit with the secular rate of the Right Ascension of the Ascending Node *Ω* equal to the Right Ascension rate of the mean Sun. For a satellite with an altitude of 800 km and null eccentricity, this is achieved for an inclination *i* of 98.6°.

The second effect $\frac{d\omega}{dt}$ is used by telecommunications satellite systems based on high-elliptic orbits, i.e. Molniya orbits. For them, it is important that the perigee remains constant relative to the line of nodes, so that the apogee remains above the region of communication. This condition is achieved by setting $\frac{d\omega}{dt} = 0$ that corresponds to $i = 63.4°$ or $i = 116.6°$, which are called “critical inclinations”. [14]

9.4.2.2 Third-body perturbing force

A third body, like the Sun or the Moon, creates a perturbing force with respect to an Earth-orbiting satellite that can change appreciably the parameters of its nominal Keplerian orbit. The lunisolar perturbation – the most considered effect for this kind of problem – has a periodic trend which combines the effect of the Moon and the effect of the Sun; in one year, it accounts for one period for the Sun and twelve periods for the Moon, due to the revolution of the Earth around the Sun, which it is once per year, and to the revolution of the Moon around the Earth, which is twelve times per year. The effects of the third-body perturbing force are time and space dependant. The Sun exerts a stronger influence of the spacecrafts that perform long orbital manoeuvres whereas the Moon influences Earth’s satellites with very high semi-major axis, thus closer to it. The lunisolar perturbation exerts a force outside the orbital plane, thus leading to a change in the inclination’s and RAAN’s values. The two-body problem can be generalized to the much more difficult n-body problem in the following way.

In a system consisting of n bodies, the sum of the forces acting on the ith body is

$$\vec{F}_i = G \sum_{j=1}^{j=n} \frac{m_i m_j}{r_{ij}^3} (\vec{r}_j - \vec{r}_i) \ , \qquad i \neq j.$$

According to Newton’s second law of motion – $\vec{F} = \frac{d\vec{p}}{dt} = \frac{d(m\vec{v})}{dt}$ where m is the mass of the body and $\vec{v}$ is the velocity vector – for constant masses $\vec{F}_i = m_i \frac{d^2\vec{r}_i}{dt^2}$, from which it follows that

$$\frac{d^2\vec{r}_i}{dt^2} = G \sum_{j=1}^{j=n} \frac{m_j}{r_{ij}^3} (\vec{r}_j - \vec{r}_i), \qquad i \neq j.$$

In Figure 9.26, m_1 stands for the Earth and m_2 for the satellite. Extracting these two masses from the summation in the previous equation, the accelerations for m_1 and m_2 become

$$\frac{d^2\vec{r}_1}{dt^2} = G \frac{m_2}{r_{12}^3} (\vec{r}_2 - \vec{r}_1) + G \sum_{j=3}^{j=n} \frac{m_j}{r_{1j}^3} (\vec{r}_j - \vec{r}_1)$$

$$\frac{d^2\vec{r}_2}{dt^2} = G \frac{m_1}{r_{21}^3} (\vec{r}_1 - \vec{r}_2) + G \sum_{j=3}^{j=n} \frac{m_j}{r_{2j}^3} (\vec{r}_j - \vec{r}_2)$$

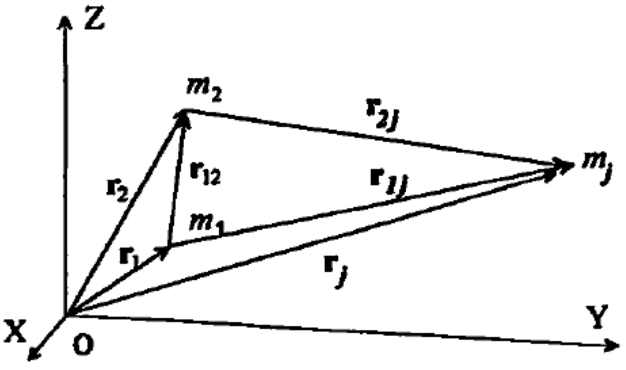

Figure 9.26 - Simplified model for the n-body dynamics perturbing function

These are the equations of the motion with respect to the inertial coordinate axes. It is defined $\vec{r} = \vec{r}_2 - \vec{r}_1 = \vec{r}_{12}$, $\vec{r}_{2j} = \vec{\rho}_j$, and $\vec{r}_{1j} = \vec{r}_{pj}$. If we choose $m_1 = M_e$ to be the mass of the Earth, $m_2 = m_s$ to be the mass of the satellite and $m_j = m_{pj}$ to be the mass of the *j* perturbing body, and if the origin of the inertial frame is located at the centre of the Earth ($\vec{r}_1 = 0$), then subtracting the first equation from the second in the last set of equations leads to the final result:

$$\frac{d^2\vec{r}}{dt^2} + G\frac{\vec{r}}{r^3}(M_e + m_s) = G\sum_{j=3}^{j=n} m_{pj}\left[\frac{\vec{\rho}_j}{\rho_j^3} - \frac{\vec{r}_{pj}}{r_{pj}^3}\right].$$

This equation is identical to the basic equation of motion for the two-body problem – $\vec{r} + G(m_1 + m_2)\frac{\vec{r}}{r^3} = 0$ – if no third body exists. In this way, the perturbing acceleration due to the *n-2* perturbing bodies becomes

$$\vec{\gamma}_p = \sum_{j=3}^{j=n} \mu_{pj}\left[\frac{\vec{\rho}_j}{\rho_j^3} - \frac{\vec{r}_{pj}}{r_{pj}^3}\right], \qquad \text{where } \mu_{pj} = Gm_{pj}.$$

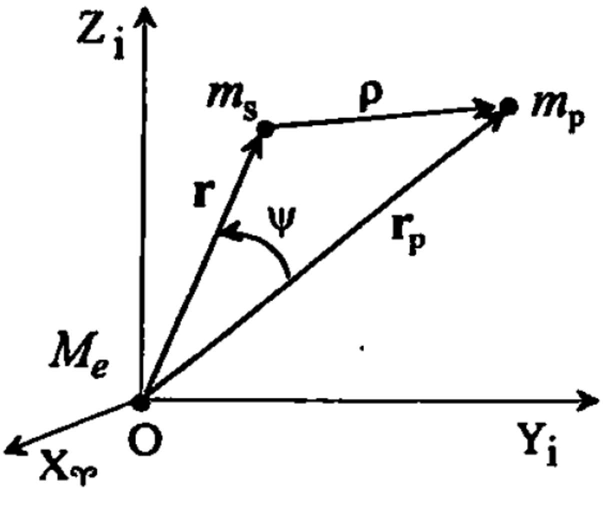

Figure 9.27 - Three-body problem representation

Figure 9.27 represents the special case of the three-body problem, adapted from the Figure 9.26. The Earth is at the origin O, ψ is the angle between the radius vectors to the satellite m_s - $\vec{r}$ - and to the perturbing body m_p - $\vec{r}_p$ - and $\vec{\rho}$ is the vector from the satellite to the perturbing body. The perturbing acceleration becomes

$$\vec{\gamma}_p = \mu_p \left(\frac{\vec{\rho}}{\rho^3} - \frac{\vec{r}_p}{r_p^3} \right),$$

where $\mu_p = Gm_p$ is the gravity constant of the *j*th perturbing body. Thus, the equation of the three-body problem becomes:

$$\ddot{\vec{r}} + G(M_e + m_s)\frac{\vec{r}}{r^3} = \vec{\gamma}_p.$$

It can be shown that the perturbing acceleration satisfies the equality $\vec{\gamma}_p = -\frac{\partial U_p}{\partial \vec{r}}$, where U_p has the form

$$U_p = \mu_p \left(\frac{1}{\rho} - \frac{1}{r_p^3} \vec{r} \cdot \vec{r}_p \right).$$

With some calculations and knowing that $\frac{r}{r_p} \ll 1$, it is obtained that the potential has the form

$$U_p = \frac{\mu_p}{r_p} \left[1 - \frac{1}{2} \left(\frac{r}{r_p} \right)^2 + \frac{3}{2} \left(\frac{r}{r_p} \right)^2 \cos^2 \psi \right].$$

It is interesting to mention these two values for the Moon and the Sun:

$$\left.\frac{\mu_p}{r_p^3}\right|_{Moon} = 8.62 \cdot 10^{-14}\ s^{-2} \qquad \left.\frac{\mu_p}{r_p^3}\right|_{Sun} = 3.96 \cdot 10^{-14}\ s^{-2}$$

This is relevant because the Moon, with a much lower mass than that of the Sun, has a higher value of the ratio, due to the great proximity to the Earth of the Moon – nearly 384.400 km – with respect to the Sun, which is $1AU \cong 1.5 \cdot 10^8\ km$. [14]

9.4.2.3 Solar pressure and solar wind

Solar radiation comprises all the electromagnetic waves radiated by the Sun with wavelengths from X-rays to radio waves. The solar wind consists mainly of ionized nuclei and electrons. Both kinds of radiation may produce a physical pressure when acting on any surface of a body. This pressure is proportional to the momentum flux (momentum per unit area per unit time) of the radiation. The solar radiation momentum flux is greater than that of the solar wind by a factor of 100 to 1000, so the solar wind pressure is of secondary importance.

The mean solar energy flux of the solar radiation is proportional to the inverse square of the distance from the Sun. The mean integrated energy flux at the Earth's position is given by

$$F_e = \frac{1358}{1.0004 + 0.0334\cos(D)} \quad \left[\frac{W}{m^2}\right]$$

where the value 1358 W/m^2 is the solar constant and D is the phase of the year, which is calculated starting on July 4th, the day of the Earth aphelion. This is equivalent to a mean momentum flux, also called solar radiation pressure, of

$$P = \frac{F_e}{c} = 4.5 \cdot 10^{-6}\, kg\, m^{-1}\, s^{-2} = 4.5 \cdot 10^{-6}\, Pa$$

where c is the velocity of light. [14]

Hereunder there is a summary table of the solar radiation pressure at different distances from the Sun in astronomical units.

Table 9.11 - Solar radiation pressure values at different distances from Sun

Distance from Sun	Radiation pressure in µPa
0.20 AU	113.5
0.39 AU (Mercury)	30.3
0.72 AU (Venus)	8.7
1.00 AU (Earth)	4.54
1.52 AU (Mars)	1.955
3.00 AU (typical asteroid)	0.505
5.20 AU (Jupiter)	0.17

The effect of the solar radiation pressure consists in a change of the eccentricity of the orbit as it applies a constant strain to the satellite in the same direction around the orbit, i.e. leading to a movement of the eccentricity vector in a perpendicular direction. Moreover, this effect is time and space dependant and it affects the values of the Right Ascension of the Ascending Node and the inclination because it applies a force out of the orbital plane.

The force $|\vec{F}_R|$, connected to the solar radiation pressure, that hits the spacecraft is proportional to P, to the cross-sectional area A of the satellite perpendicular to the Sun line, and to a coefficient C_P that is dependent on the absorption characteristic of the spacecraft: $|\vec{F}_R| = PAC_P$.

The value of C_P lies between 0 and 2: $C_P = 1$ is for a black body, a perfectly absorbing material, whereas $C_P = 2$ is for a body reflecting all light back to the Sun.[W9]

9.4.2.3.1 Albedo

Albedo is the measure of the diffuse reflection of solar radiation out of the total solar radiation received by an astronomical body, e.g. a planet like Earth. It is dimensionless and measured via an albedometer on a scale from 0 – corresponding to a black body that absorbs all incident radiation – to 1 – corresponding to a body that reflects all incident radiation. Surface albedo is defined as the ratio of radiosity – the radiant flux leaving a surface per unit area – to the irradiance – the radiant flux received by a surface per unit area. The reflected proportion is not only determined by properties of the surface itself, but also by the spectral and angular distribution of solar radiation reaching the Earth's surface. These factors vary with atmospheric composition, geographic location and time, connected to the position of the Sun. While bi-hemispherical reflectance – the effectiveness of a surface of a material in reflecting radiant energy – is calculated for a single angle of incidence for a given position of the Sun, albedo is the directional integration of reflectance over all solar angles in a given period. The temporal resolution may range from seconds, as obtained from flux measurements, to daily, monthly, or annual averages.

Unless given for a specific wavelength (spectral albedo), albedo refers to the entire spectrum of solar radiation. Due to measurement constraints, it is often given for the spectrum in which most solar energy reaches the surface, between 0.3 and 3 μm. This spectrum includes visible light (0.4–0.7 μm), which explains why surfaces with a low albedo appear dark, e.g., trees absorb most radiation, whereas surfaces with a high albedo appear bright, e.g., snow reflects most radiation. Albedo is an important concept in climatology, astronomy, and environmental management. The average albedo of the Earth from the upper atmosphere, its planetary albedo, is 30–35% because of cloud cover, but widely varies locally across the surface because of different geological and environmental features.

In particular, the albedos of planets, satellites and minor planets such as asteroids can be used to infer much about their properties. The study of albedos, their dependence on wavelength, lighting angle – "phase angle" – and variation in time comprises a major part of the astronomical field of photometry. For small and far objects that cannot be resolved by telescopes, much of what we know comes from the study of their albedos. For example, the absolute albedo can indicate the surface ice content of outer Solar System objects, the variation of albedo with phase angle gives information about regolith properties, whereas unusually high radar albedo is indicative of high metal content in asteroids.

Enceladus, a moon of Saturn, has one of the highest known albedos of any body in the Solar System, with an albedo of 0.99. Another notable high-albedo body is Eris, with an albedo of 0.96. Many small objects in the outer Solar System and asteroid belt have low albedos down to about 0.05. A typical comet nucleus has an albedo of 0.04. Such a dark surface is thought to be indicative of a primitive and heavily space weathered surface containing some organic compounds. Coming closer to Earth, the overall albedo of the Moon is measured to be around 0.14. Although such reflectance properties are different from those of any terrestrial terrains, they are typical of the regolith surfaces of airless Solar System bodies.

Two common albedos that are used in astronomy are the V-band geometric albedo – measuring brightness when illumination comes from directly behind the observer – and the Bond albedo – measuring total proportion of incident electromagnetic energy reflected back into space. Their values can differ significantly, which is a common source of confusion.

Table 9.12 - Geometric and bond albedo for planets

Planet	Geometric albedo	Bond albedo
Mercury	0.14	0.09
Venus	0.69	0.76
Earth	0.43	0.31
Mars	0.17	0.25
Jupiter	0.54	0.50
Saturn	0.50	0.34
Uranus	0.49	0.30
Neptune	0.44	0.29

Moreover, the correlation between astronomical (geometric) albedo, absolute magnitude and diameter of a celestial object is:

$$A = \left(\frac{1329 \cdot 10^{-\frac{H}{5}}}{D} \right)^2$$

where A is the astronomical albedo, D is the diameter in kilometres and H is the absolute magnitude. [W8]

9.4.2.4 Atmospheric drag

In orbital mechanics, decay is a gradual decrease of the distance between two orbiting bodies over many orbital periods. These orbiting bodies can be a planet and its satellite, a star and any object orbiting it, or components of any binary system. For bodies in low-Earth orbit, the most significant effect, and the major cause of orbital decay, is atmospheric drag. It results in the reduction in the altitude of a satellite along its orbit and thus a reduction of the semi-major axis. Orbits do not decay without some friction-like mechanism which transfers energy from the orbital motion; in fact, atmospheric drag at orbital altitude is caused by frequent collisions of gas molecules with the satellite. However, atmospheric drag can also be useful for a mission because, lowering the semi-major axis, it leads to a circularization of the orbit without any propulsive manoeuvre at the expense of time as the perigee height rises and the density decreases. For the case of Earth, atmospheric drag resulting in satellite re-entry can be described by the following sequence:

lower altitude → denser atmosphere → increased drag → increased heat → usually burns on re-entry

Orbital decay thus involves a positive feedback effect, where the more the orbit decays, the lower its altitude drops, and the lower the altitude, the faster the decay. Decay is also particularly sensitive to external factors of the space environment such as solar activity; for example, during solar maxima the Earth's atmosphere causes significant drag up to a hundred kilometres higher than during solar minima. Moreover, the effects of the atmospheric drag are time and space dependant.

Atmospheric drag exerts a significant effect at the altitudes of space stations, space shuttles and other manned Earth-orbit spacecraft, and satellites with relatively high "low-Earth orbits" such as the Hubble Space Telescope. Space stations typically require a regular altitude boost to counteract orbital decay, also called orbital station-keeping. Uncontrolled orbital decay brought down the Skylab space station, and relatively controlled orbital decay was used to de-orbit the Mir space station. Due to atmospheric drag, the lowest altitude above the Earth at which an object in a circular orbit can complete at least one full revolution without propulsion is approximately 150 km; under this altitude, the re-entry is unavoidable.

Talking about analytical equation, atmospheric drag depends on the properties of the atmosphere and on the size, shape, and speed of the satellite. One way to express this is by means of the drag equation:

$$F_D = \frac{1}{2}\rho v^2 C_D S$$

where F_D is the drag force, ρ is the density of the atmosphere, v is the in-track speed of the satellite around the Earth, C_D is the drag coefficient and S is the cross-sectional area.

In the first chapter of this thesis, a complete discussion about the latest atmosphere's models and how to find the numeric value of atmospheric density together with the explanation of solar indices' forecast is provided. [W10] [W11]

9.5 Celestial Equatorial Coordinates

9.5.1 Right Ascension

In astronomy, Right Ascension (often referred to by the initials RA, or with the first Greek letter α) is a term associated to the equatorial coordinate system. Right Ascension is analogous to longitude, but projected onto the celestial sphere rather than the Earth's surface. It is defined as the angular distance between the fundamental meridian (the equinoctial colure) and the meridian passing through the chosen object, measured eastward along the celestial equator. The zero corresponds to the first point of Aries (point of the boreal vernal equinox, γ). Right Ascension is measured in hours (h), minutes (m) and seconds (s), corresponding to the Earth's rotation: 24 hours of Right Ascension are a complete revolution. Note that 1 hour equals to 15 degrees and that Right Ascension uses sidereal time and not solar civil time. Right Ascension can be used to find the position of a star and to calculate how long it will take to find itself at a certain point in the sky. For example, if a star with RA = 01h 30m 00s is at the zenith, a star with RA = 10h 00m 00s will be on the vertical in 8 hours and 30 sidereal minutes. [W12]

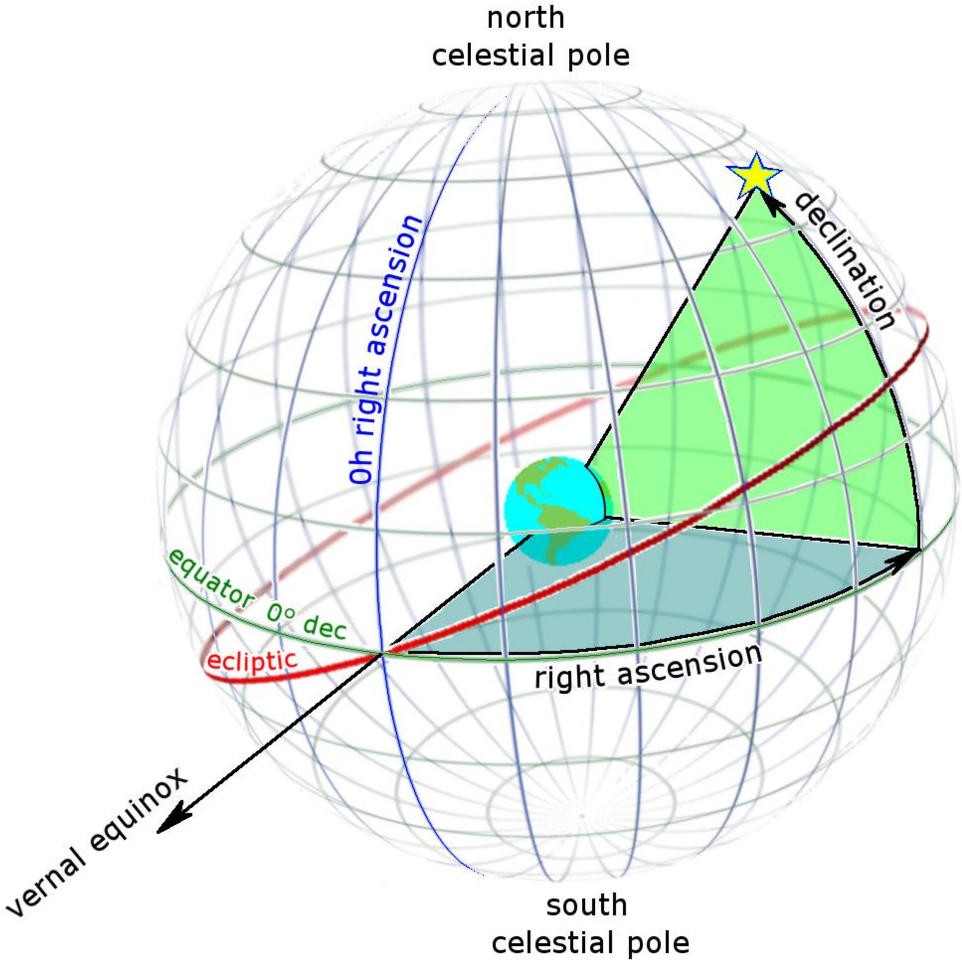

Figure 9.28 - Definition of Right Ascension and Declination

9.5.2 Declination

In astronomy, the declination δ (often abbreviated to Dec) represents one of the equatorial coordinates that serves, together with Right Ascension, to determine the height of a star on the celestial sphere. Specifically, it is the celestial angle at the centre of the Earth subtended by an arc of the celestial meridian between the celestial equator and the parallel passing through the object, i.e. it is the latitude projected on the celestial sphere rather than on the Earth's surface. By convention the points north of the celestial equator have a positive declination, while those below have a negative declination.

Any units of angular measure can be used for declination, but it is customarily measured in the degrees (°), arcminutes (′), and arcseconds (″) of sexagesimal measure, with 90° equivalent to a quarter circle. Declinations with magnitudes greater than 90° do not occur, because the poles are the northernmost and southernmost points of the celestial sphere.

Some examples are of particular interest:

- The celestial equator has a declination of 0°
- The north celestial pole has a declination of +90°
- The south celestial pole has a declination of −90°

Because of the slow movements of the Earth, first of all the precession of the equinoxes, the coordinate system on which the Right Ascension and the Declination are based changes slowly over time and it is necessary to specify the astronomical epoch to which we refer. [W13]

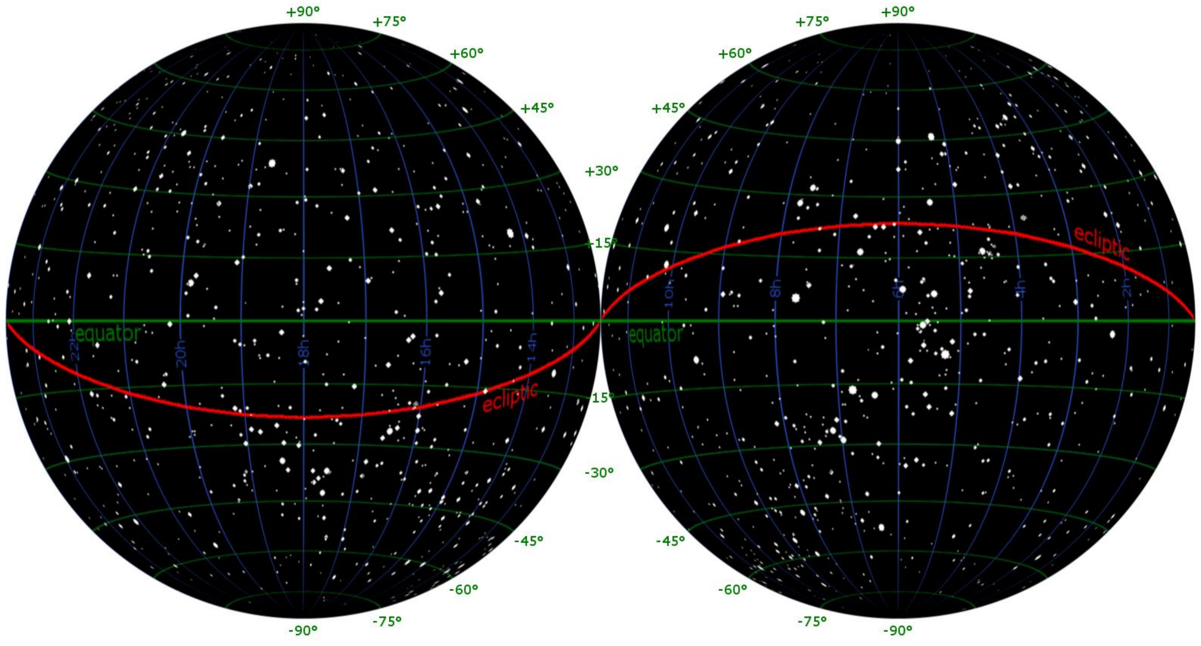

Figure 9.29 - Celestial sphere evenly divided by Declination and Right Ascension with ecliptic on the background

10 ACRONYMS AND DEFINITIONS

$\bar{A}_p$	13-month smoothed geomagnetic index
$\bar{F}_{10.7}$	13-month smoothed 10.7cm solar radio noise flux
$F_{10.7}$	Daily or monthly mean value of 10.7cm solar radio noise flux
$\bar{R}$	13-month smoothed sunspot number
a_P	3-hourly value of geomagnetic index
A_p	Daily or monthly mean value of geomagnetic index
Dst	Disturbance storm time
FOV	Field of View
$GCRF$	Geocentric Celestial Reference Frame
IS	International System of Units
$ITRF$	International Terrestrial Reference Frame
R	Wolf's relative sunspot number
$RAAN$	Right Ascension of the Ascending Node
S/C	Spacecraft
SW	Software
$TAS\text{-}I$	Thales Alenia Space Italia
TOD	True of Date (reference system)
σ	Standard deviation

11 LIST OF FIGURES

12 LIST OF TABLES

13 LIST OF CHARTS

14 BIBLIOGRAPHY

[1] Thales Alenia Space, *Internal documents (NODES' Power Point presentation, Technical Note, User Manual).*

[2] ECSS-E-ST-10-04C, 15 November 2008.

[3] ECSS-E-ST-10-04C Rev.1 DIR1, 30 January 2019.

[4] L. G. Jacchia, "New static models of the thermosphere and exosphere with empirical temperature profiles," *Smithsonian Astrophysical Observatory,* no. 313, 1970.

[5] B. R. Bowman, W. K. Tobiska, F. A. Marcos and C. Valladares, "The JB2006 Empirical Thermospheric Density Model," *Journal of Atmospheric and Solar-Terrestrial Physics,* vol. 70, no. 5, pp. 774-793, 2008.

[6] B. R. Bowman, W. K. Tobiska, F. A. Marcos, C. Y. Huang, C. S. Lin and W. J. Burke, "A New Empirical Thermospheric Density Model JB2008 Using New Solar and Geomagnetic Indices," *AIAA/AAS Astrodynamics Specialist Conference,* no. 6438, 2008.

[7] J. M. Picone, A. E. Hedin, D. P. Drob and A. C. Aikin, "NRLMSISE-00 Empirical Model of the Atmosphere: Statistical Comparisons and Scientific Issues," *J. Geophys. Res.,* p. 1468, 2002.

[8] H. Wang and C. Zhao, "Effects of various solar indices on accuracy of Earth's thermospheric neutral density models," *Science in China Series G Physics Mechanics and Astronomy,* vol. 52, no. 7, pp. 1120-1128, July 2009.

[9] F. A. Marcos, B. R. Bowman and R. E. Sheehan, "Accuracy of Earth's thermospheric neutral density models," vol. AIAA, no. 6167, 2006.

[10] W. K. Tobiska, S. D. Bouwer and B. R. Bowman, "The development of new solar indices for use in thermospheric density modeling," *Journal of Atmospheric and Solar-Terrestrial Physics,* vol. 70, 2008.

[11] W. K. Tobiska, R. B. Bowman and D. Bouwer, "Solar and geomagnetic indices for thermospheric density models," January 2012.

[12] K. O. Niehuss, H. C. J. Euler and W. W. Vaughan, Statistical Technique for Intermediate and Long-Range Estimation of 13-Month Smoothed Solar radio flux and Geomagnetic Index, September 1996.

[13] AA.VV., Ephemeris Subsystem SPK Tutorial, Vols. NAIF-Spice Tutorials, JPL/NASA,

June 2019.

[14] M. Sidi, Spacecraft Dynamics and Control: A Practical Engineering Approach, vol. Cambridge Aerospace Series, Cambridge: Cambridge University Press, 1997, pp. 28-41.

[15] J. T. Emmert, H. P. Warren, A. M. Segerman, J. M. Byers and J. M. Picone, "Propagation of atmospheric density errors to satellite orbits," *Advances in Space Research,* vol. 59, no. 1, pp. 147-165, 2017.

[16] M. Snow , M. Weber, J. Machol, R. Viereck and E. Richard, "Comparison of Magnesium II core-to-wing ratio observations during solar minimum 23/24," *J. Space Weather Space Clim.,* 2014.

[17] J. L. Lean, J. M. Picone and J. T. Emmert, "Quantitative forecasting of near-term solar activity and upper atmospheric density," *J. Geophys. Res.,* 2009.

[18] ESA Tracking Stations (ESTRACK) Facilities Manual, 2.0 ed., 25 July 2017.

[19] W. M. Smart and R. M. Green, Textbook on Spherical Astronomy, Sixth ed., Cambridge University Press, 1977.

15 WEBSITE LIST

[W1] https://it.wikipedia.org/wiki/Thales_Alenia_Space

[W2] https://en.wikipedia.org/wiki/Atmosphere

[W3] https://en.wikipedia.org/wiki/Atmosphere_of_Earth

[W4] https://en.wikipedia.org/wiki/Occultation

[W5] https://naif.jpl.nasa.gov/naif/

[W6] https://naif.jpl.nasa.gov/naif/toolkit.html

[W7] https://en.wikipedia.org/wiki/Standard_deviation

[W8] https://en.wikipedia.org/wiki/Albedo

[W9] https://en.wikipedia.org/wiki/Radiation_pressure

[W10] https://en.wikipedia.org/wiki/Orbital_decay

[W11] https://en.wikipedia.org/wiki/Drag_(physics)

[W12] https://it.wikipedia.org/wiki/Ascensione_retta

[W13] https://it.wikipedia.org/wiki/Declinazione_(astronomia)

[W14] https://en.wikipedia.org/wiki/Hipparcos

[W15] https://en.wikipedia.org/wiki/Henry_Draper_Catalogue

[W16] https://it.wikipedia.org/wiki/Catalogo_BS

[W17] https://ccmc.gsfc.nasa.gov/modelweb/

[W18] http://www.dem.inpe.br/~val/atmod/default.html

[W19] https://sol.spacenvironment.net/jb2008/index.html

[W20] http://www.spacewx.com/

[W21] https://www.nasa.gov/msfcsolar

[W22] https://arc.aiaa.org/

[W23] https://en.wikipedia.org/wiki/NRLMSISE-00

[W24] https://occultations.org/ International Occultation Timing Association (IOTA)

[W25] http://www.iota-es.de/

[W26] https://ssd.jpl.nasa.gov/?horizons

[W27] https://aa.usno.navy.mil/index.php

[W28] https://naif.jpl.nasa.gov/pub/naif/toolkit_docs/Tutorials/pdf/individual_docs/18_spk.pdf

[W29] http://simbad.u-strasbg.fr/simbad/

[W30] https://www.swift.psu.edu/secure/toop/convert.htm

[W31] http://icgem.gfz-potsdam.de/tom_longtime

[W32] http://icgem.gfz-potsdam.de/ICGEM/ICGEM.html

[W33] ftp://ssd.jpl.nasa.gov/pub/eph/planets/ascii/de430

[W34] ftp://ssd.jpl.nasa.gov/pub/eph/planets/

[W35] ftp://ssd.jpl.nasa.gov/pub/eph/planets/bsp/de430.bsp

[W36] http://sail.msfc.nasa.gov/

[W37] http://sol.spacenvironment.net/~JB2006/indices.html

[W38] https://en.wikipedia.org/wiki/Spacecraft_Planet_Instrument_C-matrix_Events

[W39] https://www.swpc.noaa.gov/content/space-weather-glossary